Electronic Theses and Dissertations   Graduate School

1-1-2015

Microtremor recordings in Northern Mississippi: Evaluating site effect and correlating with wave climate

Zhen Guo
University of Mississippi

Follow this and additional works at: https://egrove.olemiss.edu/etd

Part of the Geology Commons

Recommended Citation

MICROTREMOR RECORDINGS IN NORTHERN MISSISSIPPI:

EVALUATING SITE EFFECT AND CORRELATING WITH WAVE CLIMATE

A Thesis
presented in partial fulfillment of requirements
for the degree of Ph.D. of Engineering Science
in the Department of Geology and Geological Engineering
The University of Mississippi

by

ZHEN GUO

May 2015

ABSTRACT

Site effects is considered as one of the main reasons that cause enormous damages in earthquakes and it is mainly controlled by the local geological condition. The main research area, Northern Mississippi, is located in Mississippi Embayment (ME) where is mainly composed of unconsolidated sediments which can be as thick as 1400m along the Mississippi River floodplain, and is favorable to have significant site effects. Meanwhile Northern Mississippi is also located in the moderate to heavy potential damage area of the New Madrid Seismic Zone, which is in the northern section of ME. Therefore, it is very necessary to evaluate the site effect in Northern Mississippi area in order to prepare for the earthquake.

In this research, microtremor recordings are used to evaluate the site effects. A total of 14 continuous long-term microtremor recordings (LTRs), each lasting at least 6 hours, at 8 selected locations in Mississippi (MS), Louisiana (LA) and Alabama (AL) states, and a large number (305) of systematic single-point short-term recordings (STRs), each lasting 15-30 minutes, in Northern Mississippi area are collected using a LE-3D/20s seismometer with Eigen-frequency of 0.05Hz and RefTek 130-01/3 data logger with a sampling rate of 100Hz.

With these recordings, the horizontal to vertical spectral ratio (HVSR) method is applied to find the predominant frequency (f_0) and roughly estimate amplification factor as HVSR value at f_0 (HVSR@f_0). Within Northern Mississippi area, the f_0 is tightly correlated with

unconsolidated sediments thickness (UST) and average shear wave velocity (Vs) are also estimated.

Within the low frequency range (<0.2Hz), high HVSRs are observed in most LTRs and STRs, which is possibly caused by the wind either directly blow on the seismometer or on the buildings around the recording location, or human's activities.

The spectra of these recordings all show high power spectral density (PSD) energy level at frequency of around 0.2Hz, which is known as double-frequency peak based on observations on ocean bottom. By correlating the PSD level at DF peaks (PSD@f_p) of LTRs with the simultaneous ocean data (significant ocean wave frequency, significant ocean wave height, wind speed, and atmosphere pressure) of Atlantic Ocean and Gulf of Mexico as well as the local wind speed and atmosphere pressure, it is concluded that the DF peaks observed in Northern Mississippi are combined impact of wave climate in both Atlantic Ocean and Gulf of Mexico. The particle motion analysis and calculation of vibration angle strengthen this conclusion. The plots of DFs and PSD@f_p of STRs vs. UST in horizontal plane are significantly different from the plots in vertical direction, which indicated that the shear wave resonance in thick sediments modifies the DF microseism more obviously in horizontal direction than in vertical direction.

From this research in Northern Mississippi, it can be observed that the predominant frequency of the area where UST > 200m are within DF range, and it can be concluded that DF microseisms are strongly influenced by ocean activities. Therefore, the possible influence from ocean activities on the estimation of f_0 and amplification factor using HVSR method is examined by correlating the HVSR@f_0 to the ocean wave climate (significant wave height, wind speed and atmosphere pressure) and projecting the microtremor spatial spectral vectors on stereographic net.

These analysis show that the estimation of f_0 value is not related to either the vibration direction or the energy level of the ocean wave, but the HVSR@f_0 values are significantly affected by the energy level of ocean wave climate.

To improve the estimation of amplification factor, a modified HVSR method is proposed, with which, a more reliable amplification factor is obtained by calculating the average spatial spectral vector based on the stereographic projection method.

Three main strong conclusions can be drawn from this research: 1) the HVSR method is a fast and reliable method to estimate the predominant frequency; 2) the double-frequency microseism in northern Mississippi is a combined impact of both Atlantic Ocean and Gulf of Mexico; and 3) the estimated amplification factor by HVSR method should be modified according to the microtremor recording condition especially the noise level at around predominant frequency.

DEDICATION

This dissertation work is dedicated to my mother Lv Mingxiang and my father Guo Zhanlu who have been supporting me all the time.

LIST OF ABBREVIATIONS AND SYMBOLS

$A(t)$	Significant measured wave height or wind speed as measured at the NDBC stations
A_m	A more reliable amplification factor
A_{mH}	Amplification factor in horizontal direction
A_{mV}	Amplification factor in vertical direction
$A_\parallel(t)$	The component of wave or wind vector aligned with the noise stations
a,b	Major and minor axes of the $V(t)$-$R(t, \varphi_m)$ elliptical or centrally symmetric cluster
DF	Double-frequency
DFT	Direct Fourier transforms
DWF	Double ocean wave frequency
$EW(t)$, $EW(f)$	Amplitude time series, spectral amplitude in East-West direction
FFT	Fast Fourier transforms
f	Frequency
f_c	Center frequency of the spectral peak
f_p	Representative peak frequency of HVSR
f_{ps}	Frequencies of peaks in PSD(f)
f_f	Flattening factor of $V(t)$-$R(t, \varphi_m)$ elliptical or centrally symmetric cluster

f_r	Resonant frequencies of a two-layer model (unconsolidated sedimentary layer over lying bedrock)
f_0	Predominant frequency
$f_1.f_2$	The first and second harmonic peak frequency shown on HVSR
$\vec{H}$	A spatial vector defined by a single pick of microtremor time series at two directions on horizontal plane (N-S and E-W)
$H(f)$	Resultant horizontal spectral amplitude at research site
H_b	Horizontal vibration amplitude at bedrock
HVSR	Horizontal to vertical spectral ratio
$HVSR_R$	Average HVSR values of a LTR calculated by averaging spatial spectral vectors of a LTR
HVSR@f	HVSR values at a specified frequency f, e.g. HVSR@f_0 is the HVSR values at predominant frequency f_0
L	Length of times series data window in unit of second
l	One of the three transfer factors in calculation of the angles (β_R and δ_R) for finding average spatial vector of a group of spatial vectors corresponding to times series segments
$lat1$, $lon1$	Latitudes and longitudes of ambient noise recording station
$lat2$, $lon2$	Latitudes and longitudes of ocean wave observation station
LPDF	Long-period DF
LTA	Long-term average amplitude
LTR(s)	Long-term recording

$\vec{M}$	A spatial vector defined by a single pick of microtremor time series at three directions (vertical, N-S and E-W)
m	One of the three transfer factors of calculating the angles (β_R and δ_R) for finding average spatial vector of a group of spatial vectors corresponding to microtremor times series segments
N	The number of sample in each selected time series segment in PSD calculation
Ns	Total number of segments that is divided in a LTR, or the number of STRs in a STR group
n	One of the three transfer factors of calculating the angles (β_R and δ_R) for finding average spatial vector of a group of spatial vectors corresponding to microtremor times series segments
NDBC	National Data Buoy Center
NHNM	New high-noise model
NLNM	New low-noise model
NMSZ	New Madrid Seismic Zone
$NS(t)$, $NS(f)$	Amplitude time series, spectral amplitude in North-South direction
PSD(t,f)	Power spectral density in time-frequency domain
PDF	Probability density function
PSD@f_{ps}	PSD levels at peak frequencies f_{ps}
$R(t, \varphi)$	Radial amplitudes time series at back azimuth angle φ in horizontal plane
$R(t, \varphi_m)$	Radial amplitudes time series at back azimuth angle φ_m in horizontal plane
Ra_m	Maximum ratio of radial to transvers components in horizontal plane

$Ra(\varphi)$	Radial to transvers ratio at back azimuth angle φ in horizontal plane
SD	Standard deviation of spatial spectral vectors of a LTR or a STR group
SPDF	Short-period DF
STA	Short-term average amplitude
STR(s)	Short-term recording(s)
STR-I(s)	STR(s) with seismometer exposed to the wind
STR-II(s)	STR(s) with seismometer protected from the wind by a plastic box
$T(t, \varphi)$	Transvers amplitudes time series at back azimuth angle φ in horizontal plane
$Tr(f)$	Transfer function between HVSR value and ocean data
UST	Unconsolidated sediment thickness
V_b	Vertical vibration amplitude on bedrock
Vs	S-wave velocity
$V(t)$, $V(f)$	Amplitude time series, spectral amplitude in vertical direction
α	The bearing angle between the north and the line connecting the ambient noise and ocean observation stations and measured towards the ocean observation station
β	The angle from the resultant horizontal vector $\overrightarrow{H}$ to the north, $\beta = 90° - \varphi_e$
β_R	The angle β of average spatial vector of a group of vectors
Δt	Sample interval of microtremor recording (0.01s)
δ	The angle from the resultant horizontal vector $\overrightarrow{H}$ to the spatial vector $\overrightarrow{M}$
δ_R	The angle δ of average spatial vector of a group of vectors

$\theta(t)$	The azimuth of the ocean wave at dominant frequency or wind as measured at the NDBC stations
φ	Back azimuth angle between the north and the radial direction towards the source in horizontal plane
$\varphi_e(f)$	Estimated vibration angle as a function of f
$\varphi_e(t,f)$	Estimated vibration angle in time-frequency domain
φ_m	Back azimuth angle corresponding to the maximum radial to transvers ratio Ra_m

ACKNOWLEDGMENTS

I wish to thank my committee members who were more than generous with their expertise and precious time. A special thanks to my advisor Dr. Adnan Aydin for his countless hours of reflecting, reading, encouraging, and all patience throughout the entire process of pursuing my Ph.D degree. Thank you Drs. Joel Kuszmaul, Terry Panhorst, and Roger Waxler for agreeing to serve on my committee.

TABLE OF CONTENTS

LIST OF TABLES

LIST OF FIGURES

INTRODUCTION

0.1. STATEMENT OF THE PROBLEM

Early research on earthquake damage demonstrated that the intensity of earthquake damage is not only related to the magnitude of earthquake, but also strongly controlled by the site conditions. This requires determining those aspects of site that influence site response to earthquakes.

0.1.1. Site effects

For a given earthquake event, damage caused by that earthquake can be totally different within the influenced areas, some may be free from damage while others suffer heavy damage. Such differences were observed in many earthquakes including Mexico 1985 (Singh et al, 1988a and b), Spitak 1988 (Borcherdt et al, 1989), Loma Prieta 1989 (Hough, 1990) and Kobe 1995 (Bard, 1999). Site effects (closely related to the local surface geological settings; Arai and Tokimatsu, 2004) are the main reason for considerably varying damage from an equal intensity earthquake at different locations (Ma, 2009; Borcherdt, 1976; Nakamura, 1989; Jiang, 2005). This was confirmed by many related studies, such as Dravinski et al (1991), Wenzel and Achs (2006), Bonnefoy-Claudet *et al*. (2008), Zaharia *et al*. (2007), and Kaláb and A.Lyubushin (2008).

As a well-known example, in Mexico earthquake of 1985, the intensities of shaking and associated building damage were enormously different across the Mexico City due to changing soil conditions. The western part of the city is underlain by rock and hard soil deposits experienced much less significant damage than that of the eastern part located on soft clay deposits filling the former lake bed (Seed et al, 1988).

Nakamura (1989) summarized numerous earthquakes occurred in Japan and compared the acceleration waveforms of each earthquake recorded at various seismic observation stations installed in Japan, as shown in Figure 1. The seismic acceleration waveforms at an observation point are generally quite similar without much variation between different earthquakes. In other words, it may be said that the effect of surface layers is most critical among the three main characteristics influencing dynamic response of a site (i.e. characteristics of surface layers, radiation and propagation).
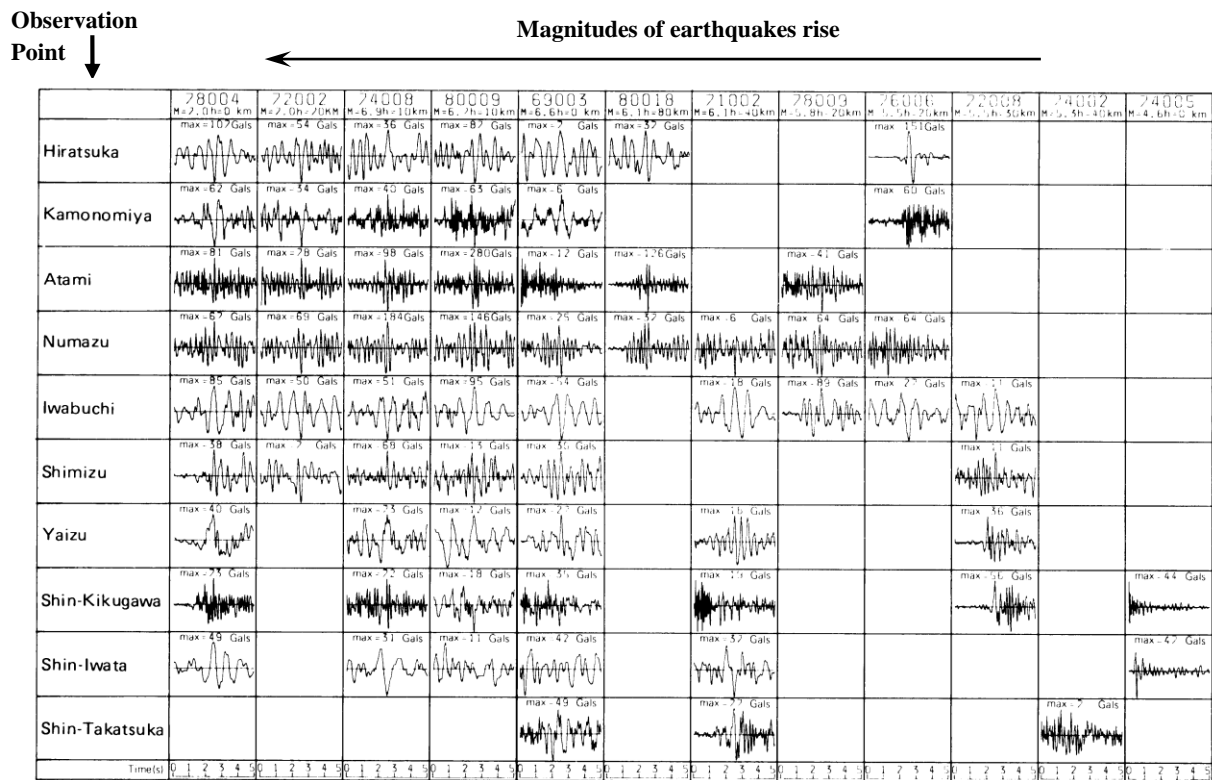
Figure 1. Comparison of seismic waveforms of various earthquakes recorded at several observation stations in Japan (Nakamura, 1989).

0.1.2. Evaluation of site effects

Present approaches to evaluate site effects are either empirical or theoretical. The empirical approaches were very popular in recent years, especially in regions of high seismicity,

3

where it is possible to record frequent (Lermo and Chávez-Garcá, 1994), which leads to a large record of earthquake observations in sites of different local geology. In areas of moderate to low seismicity, an alternative empirical method can be used based on microtremor recordings obtained by simple and low cost measurements at any place and any time, without a need for other geological information to evaluate the site effects (Nakamura, 2000).

One of the popular techniques of using microtremor recordings is based on calculating the spectral ratio of simultaneous recordings of microtremors across a site underlain by unconsolidated sediments (usually forming thick sequences) to those at a nearby reference station (usually located on a bedrock outcrop) (Lermo and Chávez-Garcá, 1992). However, it is not always possible to obtain reliable simultaneous records on both stations due to a variety of uncertainties, for example local interruptions.

Single point microtremor recording and horizontal to vertical spectral ratio (or Nakamura) method (HVSR) (Nakamura, 1989) were introduced to address these issues, which popularized the use of microtremor recordings in site effects evaluation. Reliability of the HVSR method in estimating the site effect parameters (especially predominant frequency f_0) is now supported by two decades of countless research worldwide, especially in Japan and Europe (Nakamura 2008a; Bard and SESAME-Team, 2005).

0.1.3. Wave climate influence on microtremor

When microtremor was studied more, another problem about the source of the microtremor, especially which related to the predominant frequency of a site, was raised. Both ocean bottom and inland based observations on microtremor reported that vibrations with relatively strong energy level within a low frequency band are related to the ocean wave climate,

4

which led to an emphasis on correlation between microtremor and wave climate. The more detailed background about this correlation will be explained in introduction part of Part II which is because the results of Part I are helpful for understanding that.

0.2. MICROTREMOR

0.2.1. Definition

Microtremor, also known as ambient noise, was originally introduced in the aspects of theoretical interpretation and practical engineering application by Kanai and Tanaka (1954). Its definition can be found in many literatures and can be expressed in such ways below:

Kanai and Tanaka (1954) defined microtremor as persistent ground vibrations at minute amplitudes about 1 micron. Kanai and Tanaka (1961) defined ambient seismic noise or microtremors as feeble ground motions with amplitudes of about 0.1-1 micrometer and periods of 1/10-10s.

Microtremor was defined by Nakamura (1996) as a mixture of natural ground oscillations and artificial ground vibrations. He suggested that natural oscillations can be caused by wind, rainfall, sea waves, volcanic activity and little magnitude earthquakes, while the artificial vibrations can arise from various human activities, such as transportations (road and railway), factories, constructions, industrial noise, etc.

Microtremor can also be defined as small amplitude (several to dozens of micrometers) weak vibration (having no particular source and generation time) that can be detected by high sensitive instrument at any time and place on the earth surface (Xu, 2003).

Lermo and Chávez-García (1994) defined microtremor as part of ambient seismic noise referring to low-period seismic (< 2 sec) noise which could be used as an alternative to earthquake records to evaluate local site effect.

According to Dravinski et al (1991), microtremor is the continuous ground vibrations of less than several micrometers with periods ranging from several tenths of a second to several seconds. Compared to the seismic waves, microtremors are considered as seismic noise, ambient seismic noise or ambient vibration over a wide frequency range.

Okada (2003) suggested that the ubiquitous, weak, low amplitude vibrations which may be recorded on the surface of the Earth are commonly called microtremor.

In the context of this thesis, microtremor is understood to be uninterrupted and imperceptible ambient vibrations of the ground due to a multitude of natural and anthropogenic sources of disturbances, strengths of which vary in time and space (Guo et al, 2014).

0.2.2. Characteristics

Microtremor has a wide frequency range which is hard to be defined. Recent observations have shown that the lower limit of its frequency band can be as low as 10^{-5} Hz (Peterson, 1993) while 10^{-3} Hz (Stephen et al, 2003) is more common. The upper limit of the frequency band can be as high as 40 Hz (Young et al, 2013). In terms of frequency and vibration source, microtremor can be classified as: 1) long period microtremor with frequency lower than 1 Hz, also known as microseism, mainly generated by natural sources such as ocean waves or wind, which is composed of mainly surface waves including Rayleigh wave and Love wave; and 2) short period microtremor with frequency higher than 1 Hz generated mainly by artificial activities such as traffic and running machines etc. (Bard, 1999; Seo et al, 1990).

The applications of microtremor recordings are based on the following mathematical characteristics:

*1.	Stationary stochastic process*

Microtremor recorded at a certain location is expressed as a stationary stochastic process over a certain finite time span (Okada, 2003). The observed microtremor recordings at a certain location may exhibit time dependent variations, since the characteristics of both the locations and energy of the vibration sources are random and uncertain. However, during the propagation through the geological materials, the microtremor is modified since the materials perform as a filter. Thus, the recorded microtremor at a random location might be already different from its sources and suggests the inherent characteristics of the media which is not variable in time. Therefore, the statistic property of the recorded microtremor is considered stable over a relatively long time period.

*2.	Stationary ergodic signal*

Microtremor is stationary ergodic signal, which means a microtremor time series recorded during a relative short time (might be several minutes) at a location is a representative sample at this location over a longer time range (might be several days or months). However, this characteristic is questioned by some researchers as the density function of vibration sources (the amount of vibration source/area) varies along with time (monthly or seasonally). Therefore, the multiple microtremor recordings are needed to reflect the real dynamic characteristics of the surface soil (Wang, 2001).

*3.	White noise*

The source spectrum of microtremor is characterized by white noise. White noise is a random signal (or process) with a flat power spectral density, i.e. the signal contains equal power

within a fixed bandwidth at any center frequency (see Wikipedia). The flat spectrum of white noise without any significant peak is the assumption of Kanai's research of microtremor in 1954. However, the spectrum of microtremor on the surface is not white noise due to the resonance effect in the soft layers overlaying the bedrock. Thus microtremor recorded only on the hard rock site or on the bedrock is assumed as white noise (Lermo, 1994), which is used as a reference spectrum to evaluate the site effects.

0.3.   STUDY AREA AND DATA ACQUISITION

0.3.1.   Study area

The study area mainly covers Northern Mississippi (largely situated within the Mississippi Embayment, Figure 2). The stratigraphic sequence of the area mainly consists of unconsolidated sediments with thicknesses reaching 1400 m along the Mississippi River floodplain whereas the bedrock is exposed along the eastern boundary. Figure 2 shows the geological map of the main research area and the description of geological units are summarized in Table 1.

The northern section of Mississippi Embayment includes the New Madrid Seismic Zone (NMSZ) which is the most seismically active area in the central part of North America (Schweig, 1996) and the earthquake potential and potential damage of which is high (Johnston, 1985). The New Madrid earthquakes of 1811-12, a sequence of three events with moment magnitudes as large as 8.0 (Johnston, 1996), are estimated to have affected an area of approximately 2.5 million km^2 with an intensity of V or greater (Nuttli, 1974) due to strong site effects. Northern Mississippi, about 160 km to the south of the estimated epicenter of these earthquakes, experienced intensities ranging from VII to IX (Stover and Coffman, 1993).

Covering that part of the Upper Mississippi Embayment (Figure 2) area to the north of the Mississippi-Tennessee state line, there are excellent studies utilizing microtremors to determine f_0 using the HVSR method and estimate shear wave velocity V_s profile by empirical relations between f_0, unconsolidated sediment thickness (UST) and V_s (Bodin and Horton, 1999; Bodin et al, 2001; Park and Hashash, 2005; Rosenblad and Goetz, 2010; Langston and Horton, 2011). Bodin and Horton (1999) recorded microtremors at six locations along the southern state

line of Tennessee covering a UST range of 0 to 950 m. Bodin et al. (2001) correlated UST with f_0 in and around Shelby County, TN where UST ranges from about 300 m to 1050 m. To date, there are no similar studies to the south of the state line, i.e. Northern Mississippi, though the area also suffered a significant damage during the New Madrid earthquakes of 1811-1812, and witnessed an extensive infrastructure and population growth in the last two decades. The lack of strong ground motion records in Northern Mississippi eliminates chances for independent estimates of site-effect parameters at nearby recording points.
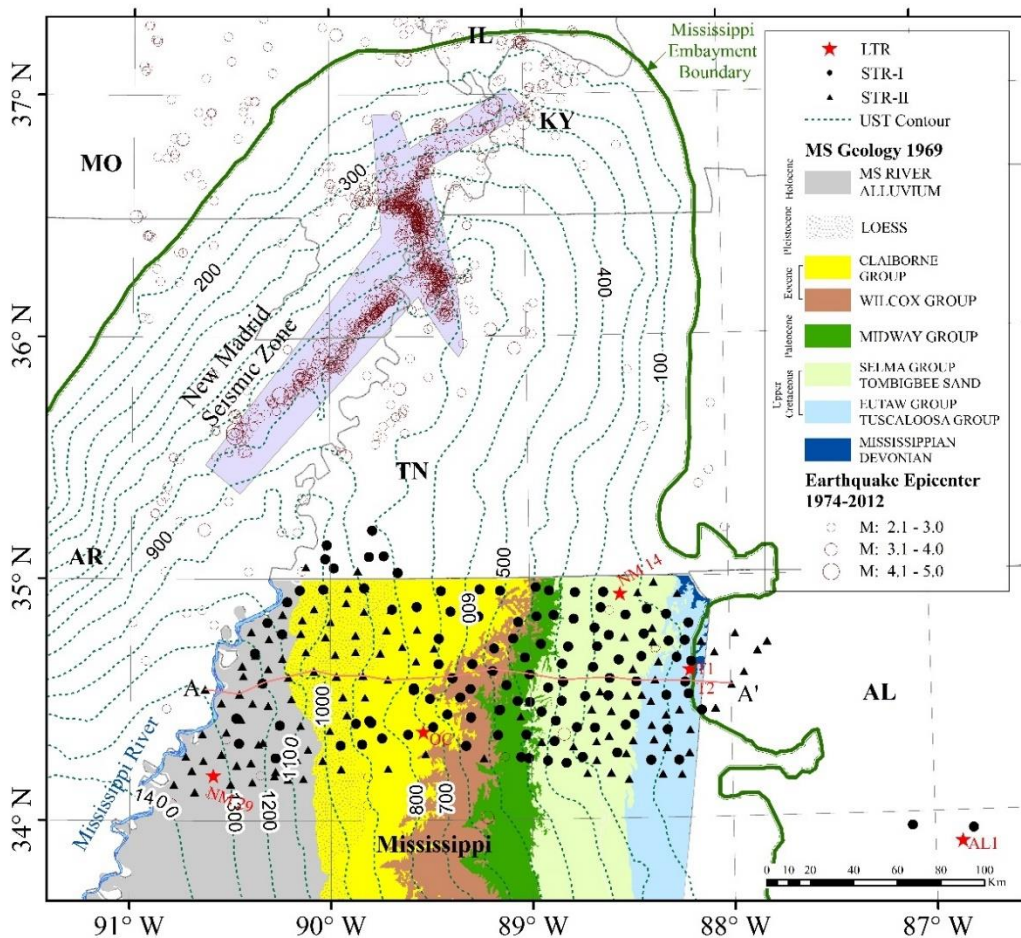
Figure 2. Geological map of the main study area (Northern Mississippi) (MDEQ) and locations of short-term microtremor recordings within the regional setting of the Upper Mississippi Embayment. Note the isopachs of unconsolidated sediments (UST) within Mississippi Embayment (based on Bodin et al, 2001) and the epicenters of earthquakes in the New Madrid Seismic Zone during 1974 – 2012 (from Center for Earthquake Research and Information at http://www.memphis.edu/ceri/seismic/catalogs/index.php).

Table 1. General stratigraphic sequence of Northern Mississippi (based on MDEQ)

SERIES	GROUP	FORMATION	DESCRIPTION
Holocene	Alluvium		Loam, sand, gravel and clay
	Loess		Grayish to yellowish-brown massive silt
Eocene	Claiborne	Kosciusko	Irregularly bedded sand, clay and some quartzite
		Tallahatta	Predominantly sand, locally glauconitic, containing clay stone and clay lenses and abundant clay stringers
	Wilcox		Irregularly bedded fine to coarse sand, more or less lignitic clay, and lignite
Paleocene	Midway	Porters Creek	Dark-gray clay containing slightly glauconitic, micaceous sand lenses
		Clayton	Greenish-gray coarsely glauconitic sandy clay and marl The lower part is crystalline sandy limestone and loose sand
Upper Cretaceous	Selma		Prairie Bluff chalk: compacted chalk, sandy chalk, and calcareous clay
		Ripley	Gray to greenish-gray glauconitic sand, clay and sandy limestone
			Demopolis chalk: chalk and marly chalk containing fewer impurities than underlying and overlying formations
			Mooreville chalk: marly chalk and calcareous clay
			Coffee sand: light-gray cross-bedded to massive glauconitic sand, sandy clay and calcareous sandstone.
			Tombigbee sand: massive fine glauconitic sand
		Eutaw	More or less cross-bedded and thinly laminated glauconitic sand and clay
		Tuscaloosa	Light and vari-colored irregularly bedded sand, clay and gravel
Mississippian			Lime stones, chert and shale of Meramec, Osage and Kinderhook age
			Chattanooga shale and underlying lime stones of early Devonian age

0.3.2. Data acquisition

As shown in Figure 2 and Figure 3, this study is based on three types of ambient noise recordings: long-term recording (LTR), short-term recording with seismometer exposed to wind (STR-I) and short-term recording with seismometer protected from natural wind by a plastic box (STR-II).

1. Long-term Recordings

A total of 15 continuous LTRs were carried out at 8 selected locations in Mississippi (MS), Louisiana (LA) and Alabama (AL) states as shown in Figure 3. The ambient conditions during each LTR are summarized in Table 2. Of these locations, AL 1 (Pickwook Caverns State Park) is in Alabama; T-1/T-2 (Tishomingo State Park), NM 14 (Corinth), OC (Oxford campus of University of Mississippi) and NM 29 (Clarksdale) are in Northern Mississippi, 500-600km north of Gulf of Mexico, and SM 1 (Collins) is in Southern Mississippi, around 150km north of Gulf of Mexico. At point OC (Figure 4), of the seven recordings, 1) six were made at base floor of Brevard Hall (OC 37) numbered from 1 to 6, and one was made at basement of Coulter Hall (OC 38); 2) five were made with seismometer exposed to A/C generated air current and two with seismometer protected from air current in the room by a plastic box. LTR at point SM 2 (Biloxi) is located in the coastal zone of Mississippi, about 10 km from the Gulf of Mexico, while LA 1 (New Orleans, LA) is only 2 km to the south of Lake Pontchartrain (Figure 3) and about 100km from the coastline. Except AL 1, T-1 and T-2, which are located on bedrock, all other LTR points lie within Mississippi Embayment area, which is composed of weakly- to un-consolidated sediments filling a broad and gently southwestward plunging trough underlain by Paleozoic bedrocks (Cushing et al, 1964).
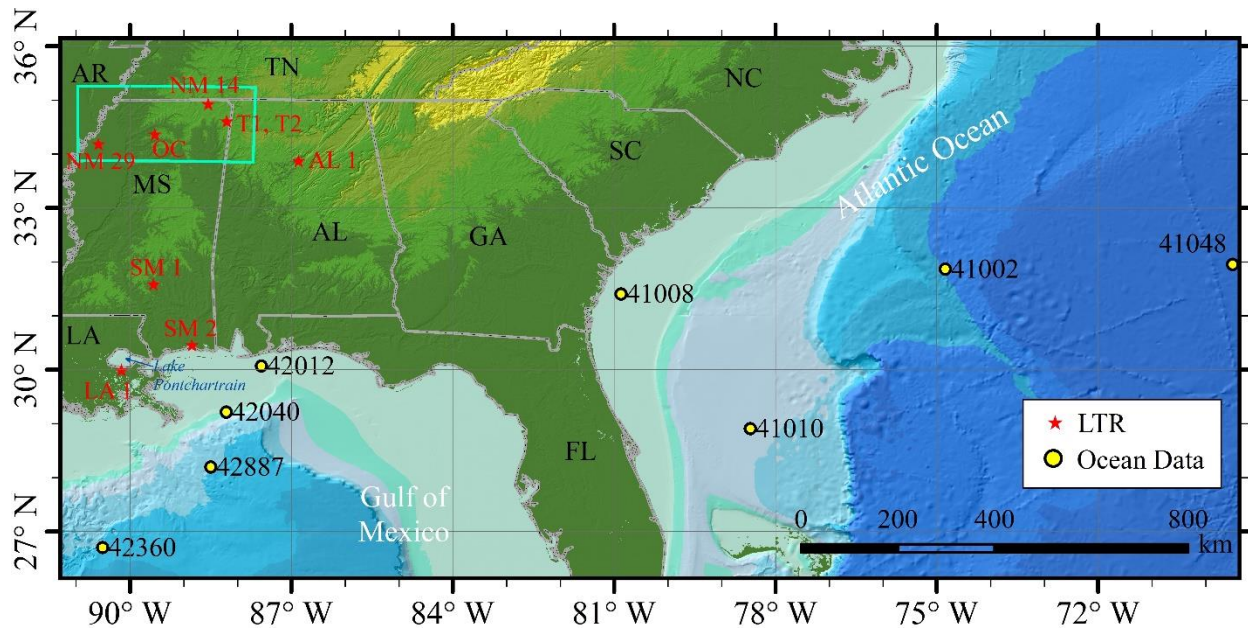
Figure 3. Locations of a) the main research area (Northern Mississippi) outlined by blue rectangle, b) long-term recordings (LTRs) in Mississippi (MS), Louisiana (LA) and Alabama (AL) states shown by red stars and c) ocean wave climate (ocean wave height, ocean wind speed and pressure) observation stations (marked as "Ocean data" in the legend, from National Data Buoy Center at http://www.ndbc.noaa.gov/) in Atlantic Ocean and Gulf of Mexico. The relative changes in the relief continental and sea floor) are represented by color gradient on the base map.

2. Short-term Recordings

A large number (305) of systematic single-point short-term recordings (STRs), each lasting 15-30 minutes, were collected over an extensive area covering Northern Mississippi, where the UST increases from 0 at the eastern state boundary to as large as 1400 m at the western boundary as shown in Figure 2. At OC, 54 closely spaced (500-1000 ft apart) STRs were carried out (Figure 4).

In order to show sampling bias in representation of UST intervals within this large UST range, the survey area was divided into 14 zones defined by 100 m UST contours (Figure 2), and the percentages of STR-I and STR-II points in each interval to total number of STRs were plotted in Figure 5. It can be seen that where UST is thinner than 200 m or thicker than 800 m,

the STRs are dominantly STR-II type but where UST ranges from 200 m to 800 m, STR-I type recordings are much more abundant.
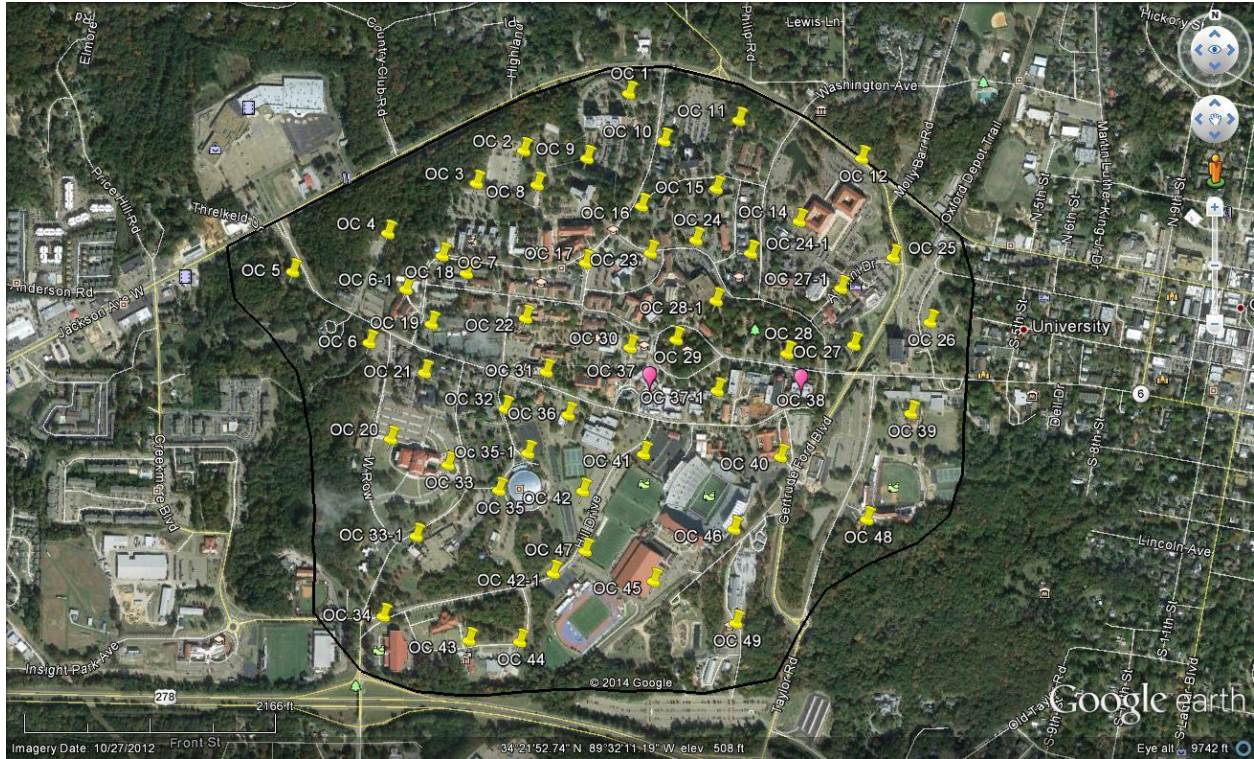
Figure 4. Layout of microtremor recording locations in Oxford campus of University of Mississippi (OC).

To capture and record the ambient noise, a LE-3D/20 s seismometer with Eigen-frequency of 0.05 Hz and RefTek 130-01/3 data logger with a sampling rate of 100 Hz were used.

A data sheet used for describing field conditions of recording location and its instruction are attached in Appendix A. All the recording conditions of STRs are summarized in Appendix B.

Table 2. General information about the LTR points and summary of the recording conditions (see Figure 3 for the locations).

Recording point		Recording time (YYYY.DDD)	Recording length (hr)	Latitude	longitude	UST[1] (m)	Ground type[2]	Exposure[3]	Possible noise sources[4]
AL1		2011.106	6	N 33°52.523'	W 86°51.890'	0	S	N	Wind
T-1		2011.302	8	N 34°36.684'	W 88°12.048'	10.2	C	A/C	F, T
T-2		2012.301	8	N 34°36.682'	W 88°12.060'	10.2	C	A/C	F, T
NM 14		2012.148	11	N 34°55.799'	W 88°32.704'	133.7	CT	A/C	S
OC 37	-1	2011.059-060	28	N 34°21.862'	W 89°32.160'	726.0	C	A/C	F
	-2	2011.072-073	43						F
	-3	2011.093-095	47.5						F
	-4	2013.015-018	66						F
	-5	2013.226-227	22					P	F
	-6	2014.074-077	70						F
OC 38		2011.272-273	16	N 34°21.862'	W 89°31.898'	729.0	C	A/C	F
NM 29		2012.149	12	N 34°11.203'	W 90°35.029'	1334.5	CT	A/C	T, S
SM 1		2013.053	14.5	N 31°35.112'	W 89°33.557'	unknown	CT		T
SM 2		2013.054	10.5	N 30°27.450'	W 88°50.771'	unknown	CT	A/C	T, S
LA 1		2013.082	12	N 29°59.756'	W 90°09.549'	unknown	CT	A/C	T, S

1) UST values are read based on Figure 2.
2) Ground type: **S** - Soil; **C -** Concrete; **CT -** Ceramic Tile
3) Exposure: **N** - Natural wind; **A/C -** Air conditioner; **P -** Protected by plastic box
4) Possible noise sources: **F -** Footsteps; **T -** Traffic; **S** - Sewer line
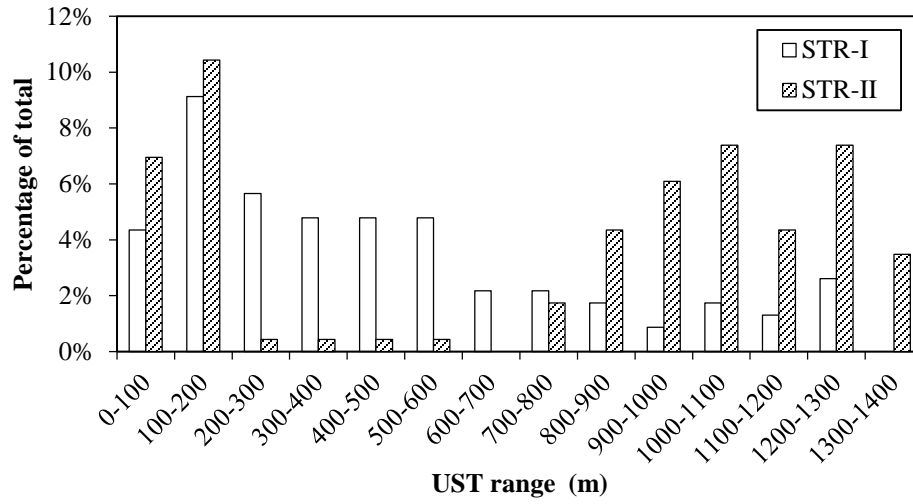
Figure 5. Percentage of STR-I and STR-II recordings to total number of STRs in each 100 m UST range.

0.4. THESIS STRUCTURE

This thesis is organized in three parts with different emphasized topics: evaluating site-effects (Part I), correlating double-frequency microseism with wave climate (Part II) and proposing a modified HVSR method to estimate amplification factor (Part III).

0.4.1. Part I

In this part, the HVSR method is applied to LTRs (T-1, T-2, NM 14, OC 37-1 to 4, OC 38, NM 29) and to all STRs collected in Northern Mississippi to determine distributions of the site-effect parameters (predominant frequency f_0 and amplification factor roughly estimated as HVSR value) and their relation with UST as well as estimated average shear wave velocity V_s across Northern Mississippi. The seismometer used in this research enables stable recording of low frequency (down to 0.05 Hz) noise which is mainly caused by natural sources, and thus help identifying f_0 in areas with thick unconsolidated sedimentary sequence. Utilizing this property, the low frequency band (0.05-0.2 Hz) of the recordings were analyzed to gain insight into the time variability of noise spectra, HVSR and vibration direction, and how these variations correlate with direction and speed of wind.

0.4.2. Part II

This part presents the power spectral density (PSD) of double-frequency (DF) microseisms of 12 continuous single point LTRs at 5 inland and 2 coastal locations selected in Mississippi and Louisiana states and 234 single point STRs. By correlating PSD of LTRs with the simultaneous ocean data (including significant ocean wave frequency, significant ocean wave height, ocean wind speed, above ocean atmosphere pressure) of Atlantic Ocean and Gulf of

Mexico, as well as local atmosphere pressure and wind speed, DF microseisms observed in Northern Mississippi were shown to be shaped by a combined impact of both wave climates of Atlantic Ocean and Gulf of Mexico. Particle motion analysis and calculation of vibration angle defined separately for LTRs and STRs strengthen this conclusion. The DF and PSD level at DF of STRs plots in horizontal direction vs. UST show significant differences from the plots in vertical direction, which indicates that the shear wave resonance in thick sediments modifies the DF microseisms more obviously in horizontal direction than in vertical direction.

0.4.3. Part III

The analysis in Part I and Part II reveals that the predominant frequency (f_0) of most Northern Mississippi area where UST > 200 m is within DF range, moreover, the DF microseism is strongly related to ocean waves. Therefore in this part, firstly, a good correlation between HVSR@f_0 and ocean data (wave height, wind speed and pressure) is observed by correlation analysis and building transfer function between them, which indicated that the HVSR@f_0 within the area where UST > 200 m is affected by the ocean activities. Then the stereographic projection is applied to project the spatial spectral vectors of time series segments of each LTR and STRs within each 100 m UST group. The average vector of each LTR and STR group are calculated and plotted. In order to improve this estimation, the transfer functions between HVSR@f_0 and ocean data observed at various stations are calculated and plotted. Finally, in order to improve the estimation of amplification factor by HVSR method, a modified HVSR method applying stereographic projection is proposed.

PART I:

MICROTREMOR RECORDINGS IN NORTHERN MISSISSIPPI

AND SITE EFFECT PARAMETERS

1.1. INTRODUCTION

In this part, we present (a) estimates of the predominant frequency (f_0) and amplification factors in Northern Mississippi by applying horizontal to vertical spectral (HVSR) method on the selected microtremor recordings; (b) correlations between f_0 and unconsolidated sediment thickness (UST); and (c) estimates of the average shear wave velocity (V_s) of the sediments in this area. In addition we discuss our observations on the wind effects on HVSR within low frequency (< 0.2 Hz).

1.2.   DATA PROCESSING

The recording conditions of LTRs (indicated by *) used in this part are summarized in Table 3. LTRs in Northern Mississippi are differ on bedrock depth (or UST), specifically exposed at AL 1, shallow at T-1, T-2 and NM 14, moderately deep at OC 37and OC 38 and deep at NM 29 (see locations in Figure 2).

1.2.1.   Data preparation

Microtremor recordings are time series of small amplitude ground vibrations in three orthogonal directions, aligned to Vertical ($V(t)$), North-South ($NS(t)$) and East-West ($EW(t)$).

In this part, LTRs were split into 15-20 min time series segments without overlap, comparable to the length of STRs (15-30 min). And each STR was treated as a whole times series segment. Then each time series segment was transferred to zero mean values and linear trend is removed.

After the above data preparation, the data processing was performed according to the following steps by Geopsy, a freeware software suit developed for the analysis of ambient vibrations (www.geopsy.com).

1.2.2.   Windowing and window selecting

The time series segments were first filtered by an anti-triggering algorithm based on a prescribed range of short- to long-term average amplitude ratios (0.2 < STA/LTA < 2.5) to avoid occasional energy bursts (Bard, 1999; Bard and SESAME-Team, 2005) and determine appropriate sampling intervals (data windows with quasi-stationary signal amplitude) for the

spectral analysis (www.geopsy.org).

Then the filtered time series were divided into several windows with a window length of 50s simultaneously in all three directions. A sample of time series in three components with selected windows is shown in Figure 6.
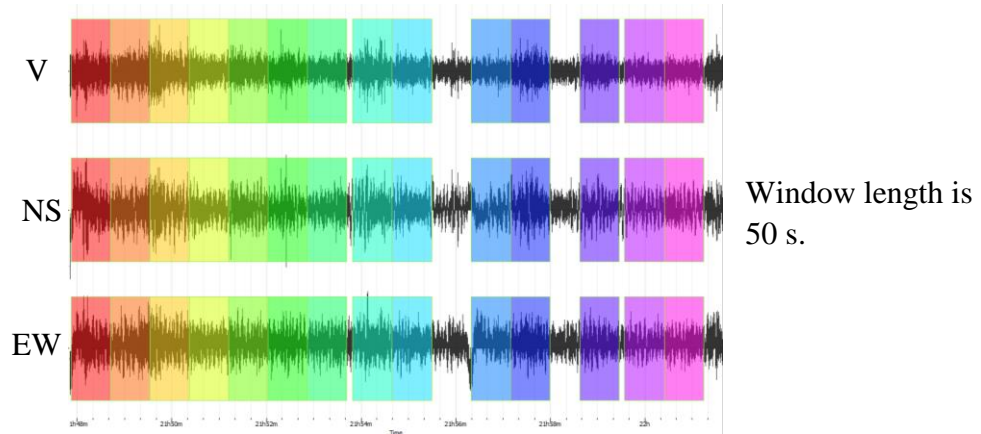
Figure 6. A sample of microtremor time series with its selected windows.

1.2.3. Fast Fourier transform (FFT)

Direct Fourier transform (DFT) or Cooley-Tukey method (Cooley and Tukey, 1965), a finite-range FFT of the original time series, is applied on the time series of three components after the data preparation to obtain the samples' amplitude-frequency spectra within a frequency band of 0.02-15 Hz, which are then smoothed using a Konno-Ohmachi function with the bandwidth coefficient set to 40 to get smoothed spectra of three components $V(f)$, $NS(f)$ and $EW(f)$. The resultant horizontal spectrum $H(f)$ for each sample was computed from quadratic mean as Eq. (1), which was then used for determining HVSR of each window:

$$H(f) = \sqrt{\frac{NS^2(f) + EW^2(f)}{2}} \tag{1}$$

Table 3. Summary of recording conditions and site effect parameters of LTR (*) and nearest STR points in Figure 9.

Point	UST (m)	Fundamental frequency f_0	Distance to nearest LTR point (km)	Ground type[1]	Exposure [2]	Recording period (STR in min)	Possible noise sources[3]	Wind direction	Wind speed (mph)
AL 1*	0	NO	0	S	N	6 hr			
AL 2	0	NO	7.6 NE	B	N	15	T		
AL 3	0	NO	24.2 NWW	B	N	15	T		
T-1*	10.2	2.018	0	C	A/C	8 hr	F, T		
T-2*	10.2	2.466	0	C	A/C	8 hr	F, T		
NM 10	0.1	NO	19.5 SSE	A	N	15	HT	Calm	Calm
NM 11	9.1	1.034	3.7 N	S	N	15	LT		
NM 46	26.4	0.904	6.4 S	A	N	18	HT	SSE	8
NM 47	10.9	2.157	11.3 S	A	N	15	MT, A/C	SE	8
NM 140	0.1	7.686	55.0 NE	C	P	15	T	S	4
NM 141	0.1	10.043	37.7 NEE	C	P	15	R, HT	SSE	4
NM 142	0.1	7.189	26.0 NE	C	P	19	T, RM	S	13
NM 144	0.1	NO	13.6 N	GS	P	15	T	SSE	7
NM 14*	133.7	0.967	0	CT	A/C	11 hr	S	Calm	Calm
NM 13	102.6	NR	14.1 SE	A	N	15	HT	Calm	Calm
NM 15	173.0	0.846	7.8 W	S	N	15	G	Calm	Calm
NM 112	130.5	NR	10.2 S	F	N	15		Calm	Calm
NM 113	179.3	0.846	11.3 SW	C	N	15	MT	Calm	Calm
NM 164	82.7	1.544	16.2 NE	A	P	15	LT	Calm	Calm
NM 165	100.0	0.791	7.9 E	C	P	15	MT	Calm	Calm

Table 3 Cont.

Point	UST (m)	Fundamental frequency f_0	Distance to nearest LTR point (km)	Ground type[1]	Exposure [2]	Recording period (STR in min)	Possible noise sources[3]	Wind direction	Wind speed (mph)
OC 37-1~4*	726.0	0.290	0	C	A/C	28+43+47.5+66 hr	F		
OC 38*	726.0	0.290	0.4 E	C	A/C	16 hr	RM		
NM 34	763.8	0.271	7.1 W	A	N	15		SE	4
NM 93	674.2	0.310	5.1 NE	A	N	15		Calm	Calm
NM 181	753.8	0.237	18.0 S	C	P	15	T	S/SE	9
NM 29*	1334.5	0.170	0	CT	A/C	12 hr	S	Calm	Calm
NM 28	1267.9	NR	28.2 NNE	A	N	15	MT	Calm	Calm
NM 159	1387.6	0.159	18.7 W	C	P	19	MT	NW	15
NM 160	1370.8	0.170	11.4 SW	C	P	8		NNW	16.5
NM 210	1300.0	0.194	8.7 SE	GS	P	15	R	SWW	19.6

Refer to Figure 2 for the locations of recording points.

Abbreviations: **NO -** not observed; **NR -** not recognized

1) Ground type: **C -** Concrete; **A -** Asphalt; **S -** Soil; **G -** Gravel; **CT -** Ceramic Tile; **F -** Farmland
2) Exposure: **A/C -** Air conditioner; **N -** Natural wind; **P -** Protected by plastic box
3) Possible noise sources: **F -** Footsteps; **RM -** Running machines; **T -** Traffic; **HT -** Heavy traffic; **MT -** Moderate traffic; **LT -** Light traffic; **R -** River; **A/C -** Air conditioner unit; **S** - Sewer line; **G -** Grass

1.2.4. Horizontal to vertical spectral ratio (HVSR) method

Figure 7 shows a two-layer model with unconsolidated sediments ("Soft") overlaying on bedrock ("Hard") proposed by Nakamura (2008b), in which, H and V are the horizontal and vertical spectral amplitudes of microtremor measured on research site (soft sediment surface), and H_b and V_b are those on bedrock (hard layer).

On the surface of soft sediment, the vibration is largely affected by surface wave (mostly Rayleigh waves), while on bedrock, this effect should not be include. From the hard layer to soft layer, the amplification factor in horizontal direction is estimated by:

$$A_{mH} = H/H_b \tag{2}$$

And the amplification factor in vertical direction, as well as the degree of Rayleigh wave effect is estimated by:

$$A_{mV} = V/V_b \tag{3}$$

If there is no surface wave, A_{mV} should have a value close to 1.0.

Assuming that the effect of surface wave are identical in horizontal and vertical directions, then a more reliable amplification factor can be wrote as:

$$A_m = A_{mH}/A_{mV} \tag{4}$$

$$= \frac{H/H_b}{V/V_b} \tag{5}$$

$$= \frac{H/V}{H_b/V_b} \tag{6}$$

It is supported by measured microtremor and earthquake data that the vibration in hard ground is uniform for each frequency and direction. Therefore, on bedrock, $H_b \approx V_b$.

Finally, the amplification factor is just the horizontal to vertical spectral ratio (HVSR) of

research site as a function of frequency f :

$$HVSR(f) = H(f)/V(f) \qquad (7)$$

The HVSR(f) spectra are calculated for all samples of each short-term and segmented long-term recordings according to Eq. (7) within frequency band 0.02-15.0 Hz.
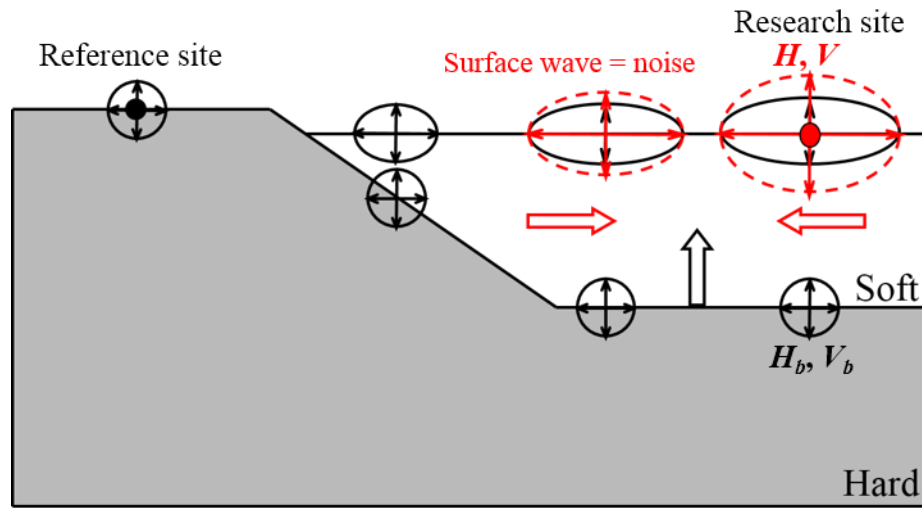
Figure 7. Two-layer model of HVSR method (Nakamura, 2008b).

1.2.5. Predominant frequency (f_0) and amplification factor

The HVSR are plotted vs. frequency and geometrically averaged to find the representative peak frequency f_p considered as f_0 and the corresponding value of HVSR considered as estimated amplification factor. The following criteria were used to determine f_0 (Bard and SESAME-Team, 2005):

1) HVSR should be > 2 at f_p;

2) In the frequency range [$f_p/4$, $4f_p$], minimum value of HVSR should be < ½ HVSR at f_p; and

3) Standard deviation of HVSR at f_p should be less than the threshold values of corresponding frequency ranges within which f_p is located, as shown in Table 4.

Table 4. Frequency dependent threshold values of HVSR standard deviation (Bard and SESAME-Team, 2005).

Frequency Range (Hz)	< 0.2	0.2-0.5	0.5-1.0	1.0-2.0	> 2.0
Threshold value	3.0	2.5	2.0	1.78	1.58

1.2.6. Vibration directions

When the instantaneous amplitudes of the two orthogonal horizontal components (EW and NS) of ambient vibrations in the horizontal plane are plotted against each other, they form an essentially elliptical cluster (Figure 8a), demonstrating the stochastic nature of the vibrations. As this ellipse appears to be stationary, its major axis should be aligned with steady and dominant vibration direction, which is modulated and rotated by the local geological and environmental conditions. Resultant or dominant vibration angle φ_e can be estimated by taking the pairs of spectral amplitudes and calculating their resultant vector and the acute angle this vector makes with the east direction (Figure 8b). This can be refined by filtering out the outliers and particular frequency bands that represent known transient and intermittent sources. Note that the actual vibration directions may be aligned in the NW-SE quadrangles, whereas this representation projects all directions onto the NE-SW quadrangles (Figure 8b).

The procedure to calculate vibration angle φ_e is described as below:

1) Obtain the amplitude spectra in NS and EW directions within frequency band 0.02-15Hz by FFT (see section 1.1.3), and then simply estimate the vibration angle φ_e as a function of f by Eq. (8):

$$\varphi_e(f) = atan \frac{NS(f)}{EW(f)} \tag{8}$$

where $NS(f)$ and $EW(f)$ are the amplitude spectra in NS and EW directions respectively.
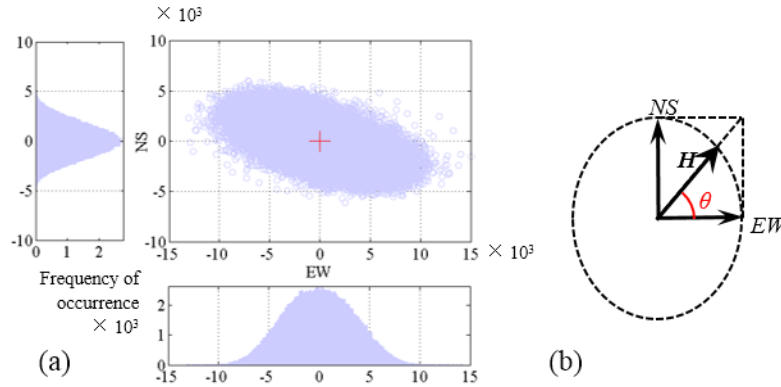
Figure 8. a) Polar scatter chart of vibration directions in the horizontal plane and amplitude frequency distributions of the horizontal components of vibrations. Note the amplitude frequencies have normal distributions centered at zero; and b) definition of the vibration direction angle φ_e.

2) Plot the calculated vibration angles, noting that since these spectra consist of positive values, the estimated vibration angles vary between 0 and 90° and all fall into the first (N-E) quadrant of a compass. This means that the actual vibrations in the other quadrants of the horizontal plane are all folded onto the first quadrant. However, this simplified picture can still reveal main vibration direction: a) N-S (±45 from N or S) if $45° \leq \varphi_e < 90°$; and b) E-W (±45 from E or W) if $0° < \varphi_e \leq 45°$; and

3) Finally, calculate the vibration angles of finely spaced frequency bands and plot the temporal changes in a continuous format across all bands as a function of time producing a color gradient map in time-frequency domain, $\varphi_e(t,f)$.

1.3. RESULTS

All spectral and HVSR curves were presented within a wide range frequency bandwidth (0.02-20 Hz) in order to facilitate discussion of possible trends at the lower end of the spectrum. It should be noted, however, that the stable response frequency of the seismometer extends only down to 0.05 Hz, and hence observed trends may not be as reliable below this frequency (0.02-0.05 Hz).

1.3.1. Long-term recordings (LTR)

Ambient conditions during each LTR and the site effect parameters calculated for that LTR point were summarized in Table 2 and Table 3.

In Figure 9, the HVSR curves from LTR are shown in the first column. Paired variations of HVSR at f_0 and (a) mean sea level air pressure (Pressure, inHg) and (b) wind speed (mph) during the entire recording period are shown in the second and third columns, respectively. The pressure and wind speed data were downloaded from "http://www.weather underground.com". A summary of observations on the HSVR curves of each LTR point is provided below:

1. *AL1 (Figure 9-a; Pickwood Caverns State Park, Warrior, AL)*

- Continuous overnight (01:10-07:10) recording made after a tornado on April 16, 2011.

- The sensor was placed on soil ground in a forest.

- Instantaneous wind speed reached 17 mph at midnight.

- The HVSR curves for all 20 min. segments of the recording plotted in Figure 9-a: 1) the curves have broad flat peaks over a broad frequency band of 0.35-3.0 Hz with a likely average peak f_p at 1.03 Hz; 2) except during 3:30 am-4:30 am when the wind was strongest,

the peaks are mostly unidentifiable due to low (< 2) HVSR ; 3) the minimum HVSR value within frequency range [f_p/4: 0.25, $4f_p$: 4.12] is 1.21, which is $> ½$ HVSR at f_p, i.e. $f_p \neq f_0$ at this site.

2. *T-1 & T-2 (Figure 9-b; Tishomingo State Park, MS)*

- Two continuous day time (08:45-17:20) recordings at the same point in Tishomingo State Park on October 29, 2011 (T-1) and October 27, 2012 (T-2).

- The sensor placed on concrete ground inside the park gatehouse.

- The HVSR curves for 20 min segments of T-1 and 15 min segments of T-2 plotted in Figure 9-b with the overall average (thick solid line) and one standard deviation (thin dashed lines): 1) the curves have broad flat peaks over a broad frequency band of 1.35-3.0 Hz with an average peak f_p at 2.31 Hz; 2) the one standard deviation range at f_p is +/- 0.43 , which is $<$ 1.58 (threshold value for $> f_p = 2.0$); thus this peak satisfies all three criteria of f_0; 3) variations of HVSR at f_0 has a low correlation coefficient with wind speed for both T-1 and T-2.

3. *NM 14 (Figure 9-c; Corinth, MS)*

- Continuous overnight (21:20-08:20) recording on May 26-27, 2012.

- The sensor placed indoor and influenced by occasional door movements and footsteps.

- The HVSR curves for 20 min segments plotted in Figure 9-c: 1) within the frequency range of 0.02-0.2 Hz, the HVSR curves display remarkable variations with time; HVSR is significantly low during the small hours (00:00-05:00), but reaches very high levels as artificial activities in the early morning hours intensify; 2) within the frequency range $>$ 0.5Hz, the first ($f_{p1} = f_0$) and second ($f_{p2} = f_1$) peaks are easily identifiable; 3) at f_0, time

dependency of HVSR is obvious with a significant difference between daytime and nighttime values; 4) nighttime curves show slightly higher values in both f_0 and HVSR; 5) HVSR at f_1 also display time dependency but the value of f_1 is stable; 6) HVSR at f_0 has a very low correlation with wind speed in the recording period.

4. *OC 37-1~4 & OC 38 (Figure 9-d-h; University, MS)*

- Four continuous recordings made in the basement of Brevard Hall (OC 37-1~4) and one recording in Coulter Hall (OC 38) both located in Oxford Campus of the University of Mississippi.

- The sensor placed on concrete ground and exposed to the influence of A/C in the room.

- The HVSR curves plotted in Figure 9-d-h: 1) at nighttime, within the frequency range of 0.02 – 0.2 Hz, HVSR fluctuates roughly within 1-5; during daytime, HVSR is much higher especially on March 1st when the campus was busy; 2) the first peak ($f_{p1} = f_0$) is sharp and stable with time around 0.29 Hz; 3) the second peak ($f_{p2} = f_1$) is located at 0.79 Hz during nighttime; 4) from the first two recordings, the third peak ($f_{p3} = f_2$) can also be able to be identified around 1.6 Hz; 5) correlations between HVSR at f_0 and both pressure and wind speed are medium-to-low for recordings at OC 37 and very low for those at OC 38.

5. *NM 29 (Figure 9-i; Clarksdale, MS)*

- Continuous (20:00-08:20) indoor recording on May 27, 2012.

- The HVSR curves plotted in Figure 9-i: 1) within 0.02-0.14 Hz range, HVSR fluctuates within 4 to 20+ during night (20:00-0:00) and early morning (05:00-08:20), but in a relatively low and narrow range (2-4) during the small hours (00:00-05:00); 2) during nighttime, f_0 is easily identified at around 0.170 Hz; 3) within 0.5-2 Hz range, HVSR changes

slightly with time but there is no traceable separation between daytime and nighttime curves; 4) the likely second and third peaks ($f_{p2} = f_1$ and $f_{p3} = f_2$) are identifiable at around 0.52 Hz and 1.0 Hz respectively; 5) for $f > 2$ Hz, HVSR is very small and almost fixed in time; 6) HVSR at f_0 shows a low correlation with pressure.
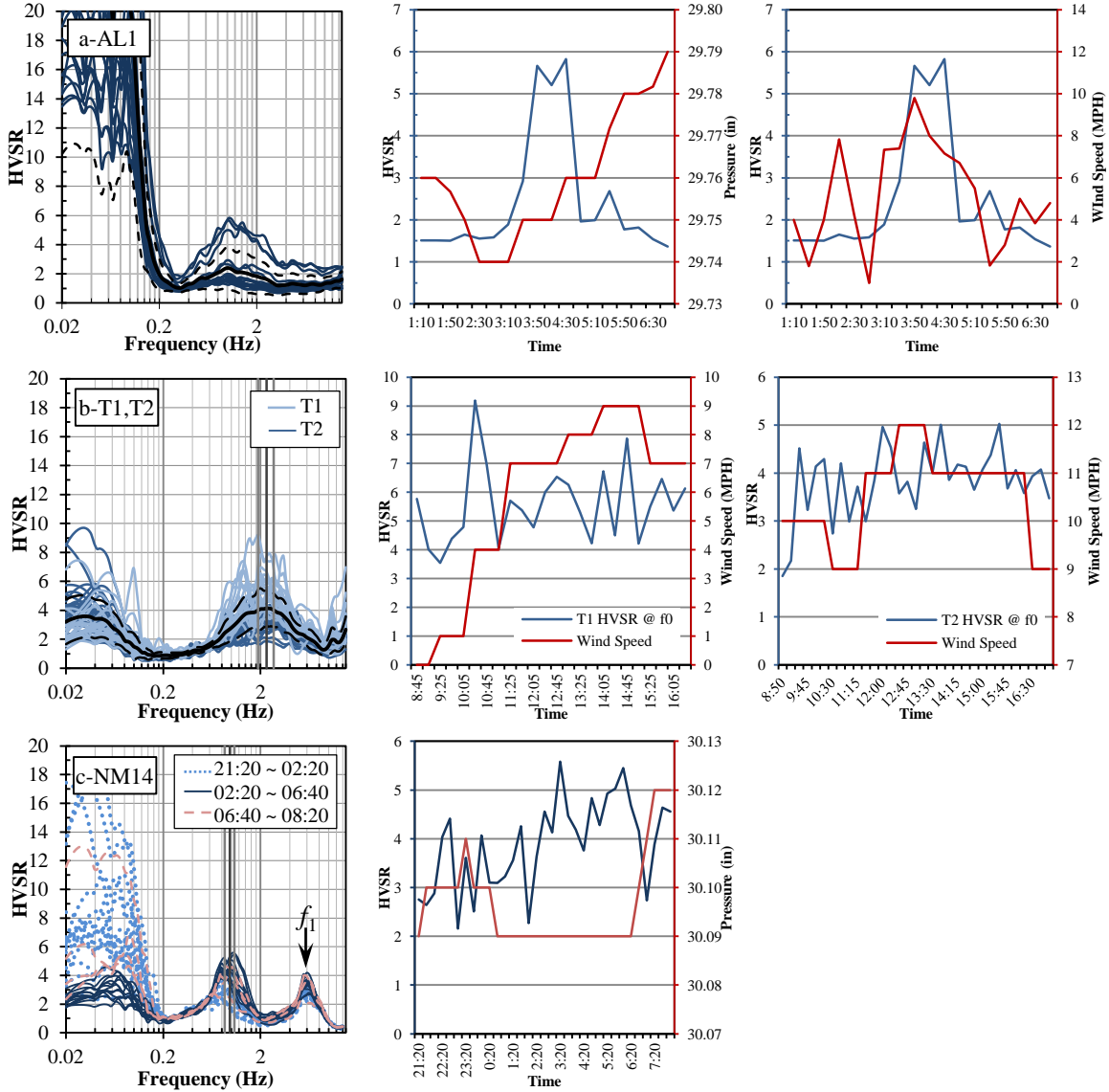
Figure 9. First column of graphs depicts the HVSR curves of LTR, while the second and third columns shows the paired variations of HVSR at f_0 (blue lines) and mean sea level air pressure or wind speed, respectively, during recording period. Each row of the graphs represent an LTR: a) AL 1; b) T-1 & T-2; c) NM 14;
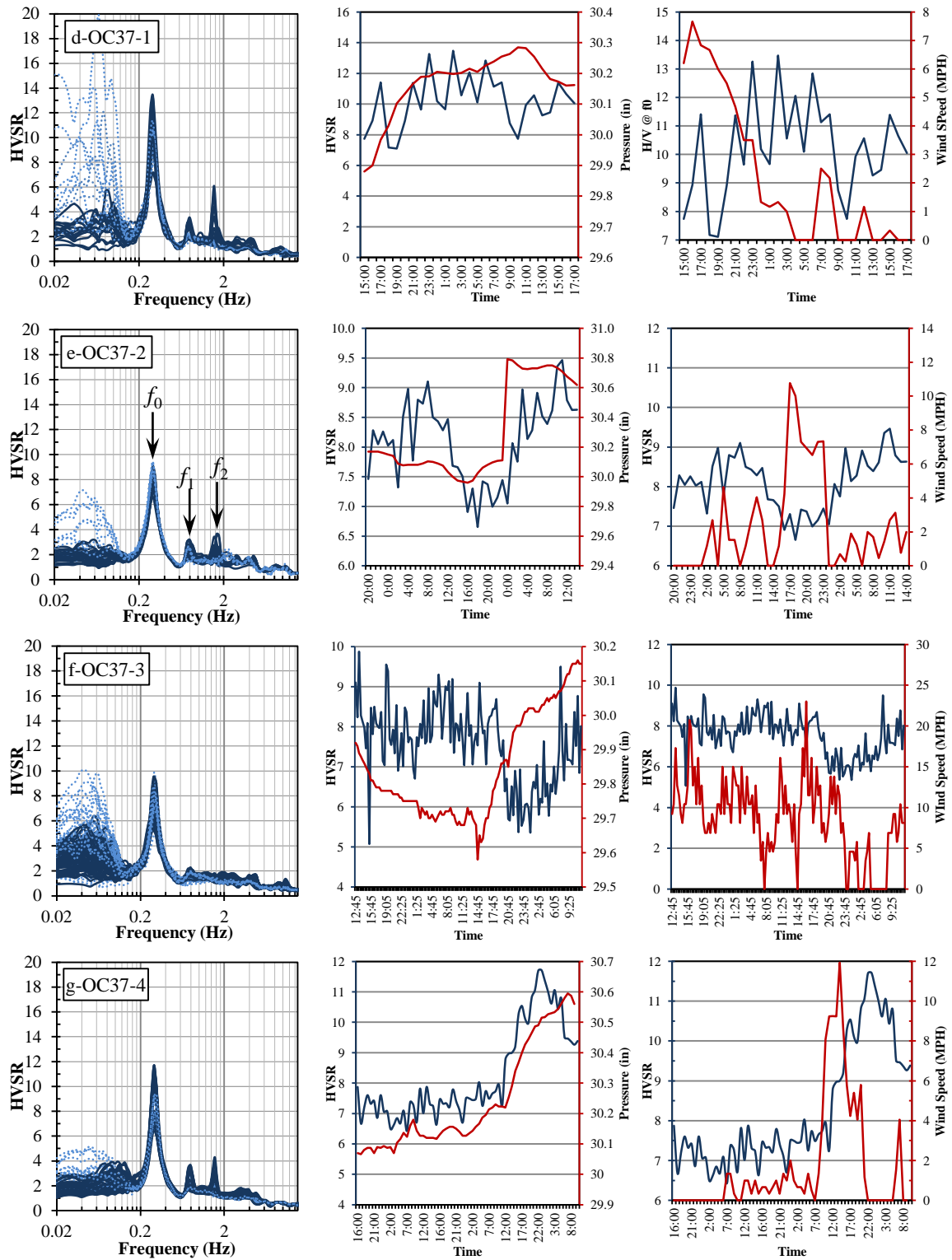
Figure 9. Cont. d) OC 37-1 (11:00-12:00 Feb. 28; 15:00 Feb. 28-18:00 Mar. 1, 2011);e) OC 37-2 (20:00 Mar. 12-15:00 Mar. 14, 2011); f) OC 37-3 (11:45 Apr. 3-12:05 Apr. 5, 2011); g) OC 37-4 (16:15 Jan. 15-10:20 Jan. 18, 2013);
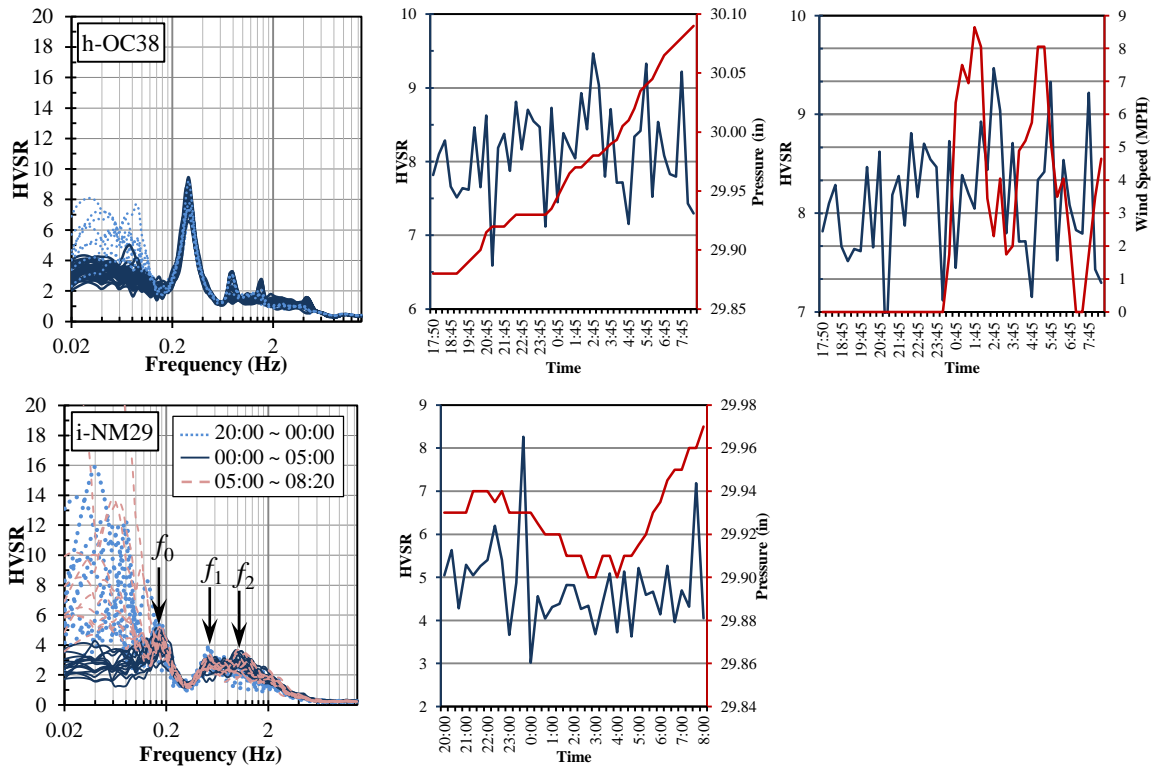
Figure 9. Cont. h) OC 38 (Coulter Hall, Oxford Campus, MS) (17:45 Sep. 29-09:00 Sep. 30, 2011); i) NM 29. Note: in rows c-g, dashed lines represent daytime (09:00-18:00) and solid lines represent the evening to morning hours (18:00-9:00).

1.3.2. Wind Effect

In Figure 9, some of the HVSR curves in the low frequency range (0.02-0.2 Hz) have much higher peaks than those considered as f_0. For example, at AL 1, which is an outdoor LTR point, the HVSR values in this low frequency range are much higher than in the rest of the frequency spectrum. At other LTR points, which are all indoors, the daytime HVSR values in the low frequency range are generally higher than those of the night time values. These high peaks in the low frequency range are caused by the natural wind directly blowing on the sensor and by human activities (Mucciarelli et al, 2005; Chatelain et al, 2008; Bard, 1999). Our observations during this study supported these cause-effect relationships as discussed below.

35

The graphs in Figure 10 depict the HVSR curves of the LTR points (red lines) and those of nearby STR-I (blue lines) and STR-II (green lines) points where UST is similar. The ambient conditions of these recordings are summarized in Table 3. For the points strongly influenced by local noise sources, shorter data windows than usual 50 s ones were required to extract sufficient number of valid samples across the recording period. Because the HVSR values at longer periods than the length of data window (L) (or at smaller frequencies than 1/L Hz) cannot be uniquely determined, the HVSR curves for those points with shorter data windows are truncated as for NM 13 below 0.033 Hz (Figure 10).
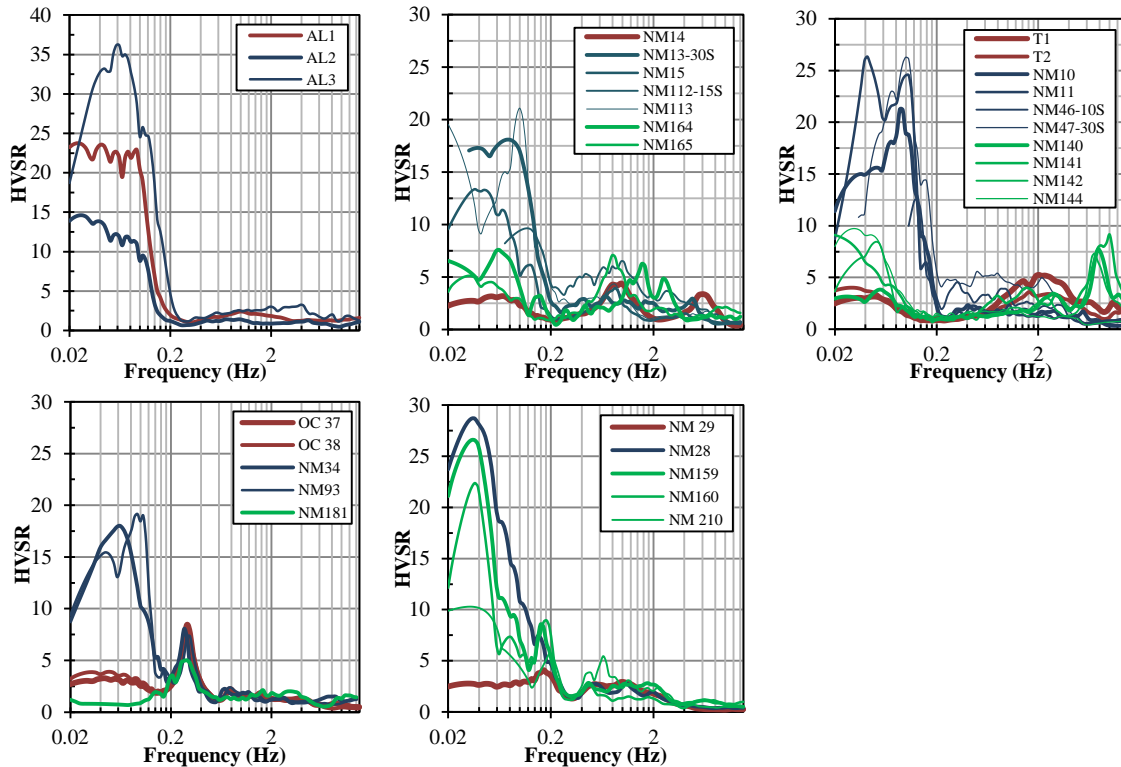
Figure 10. Comparison of the HVSR curves of LTR (red lines), STR-I (blue lines) and STR-II (green lines) points (see description in Table 3).

Chatelain et al. (2008) pointed that the wind effect is related to the ground type, i.e. wind modifies the HVSR when there are grass or trees around the sensor but no wind effect is evident when the sensor is placed on asphalt or cement ground. In this study, however, as Figure 10

reveals, the HVSR values of STR-I within the low frequency band (0.02-0.2 Hz) are all significantly higher than those of LTR and STR-II regardless of the ground type. This suggests that the effect of natural wind can be largely eliminated with the protection of the sensor by a plastic box. Note, however, among the STR-II points, NM159, NM160 and NM210 display high HVSR values in the low frequency band, possibly because of strong winds (with speeds reaching as high as 15 MPH) during the recordings at these points. Despite this complication, f_0 at these sites was more readily identifiable compared to that at NM 28, which is an STR-I point.

Bard and SESAME-Team (2005) and Angelis (2012) pointed out that the wind can have significant influence on HVSR in the frequency band less than 1 Hz. The results of this study (Figure 10) show that this influence is not identifiable at frequencies above 0.2 Hz. This observation may be strictly valid for the study area but it is supported by the vibration directions (Figure 11), as discussed in the next section.

a) AL1   b) NM 14
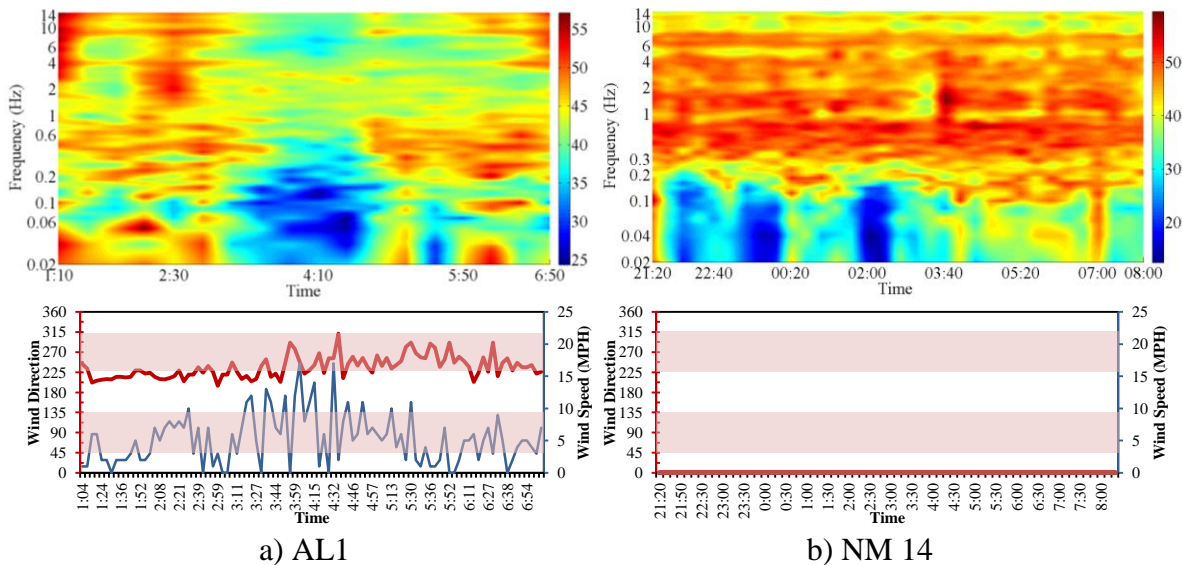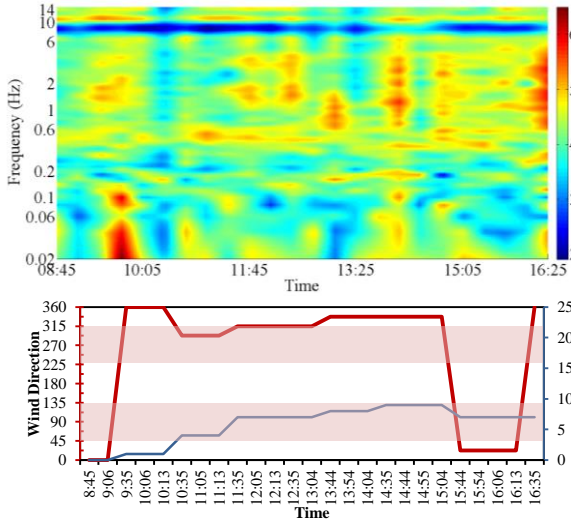
c) T-1
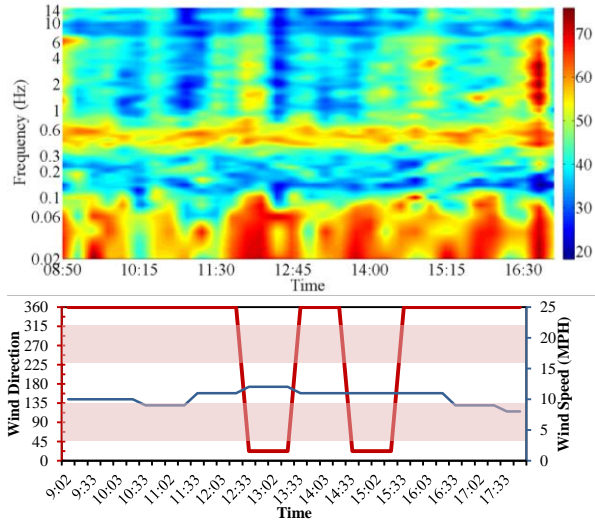
d) T-2
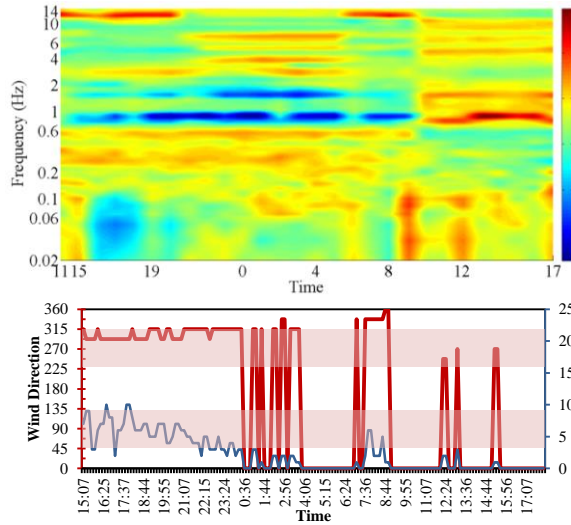
e) OC37-1, Feb 28, 2011
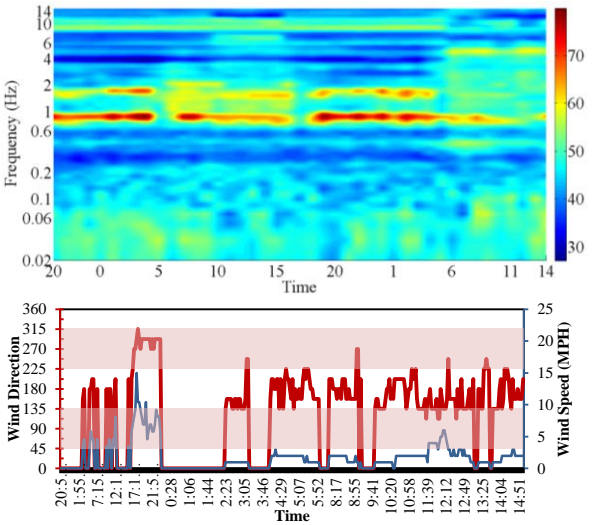
f) OC 37-2, Mar. 12, 2011
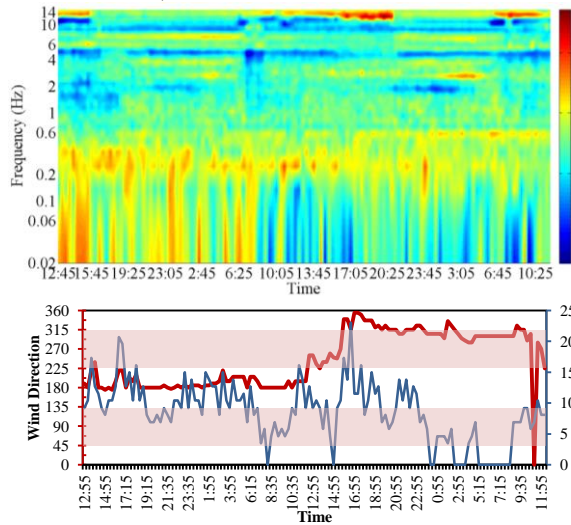
g) OC37-3, Apr. 3, 2011

h) OC37-4, Jan. 15, 2013

i) OC38   j) NM 29
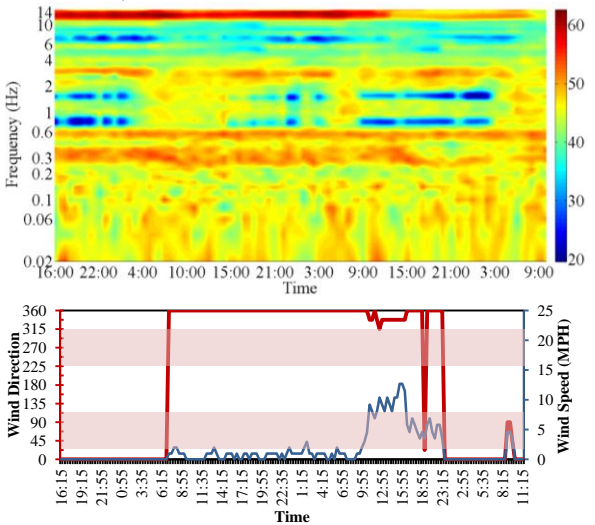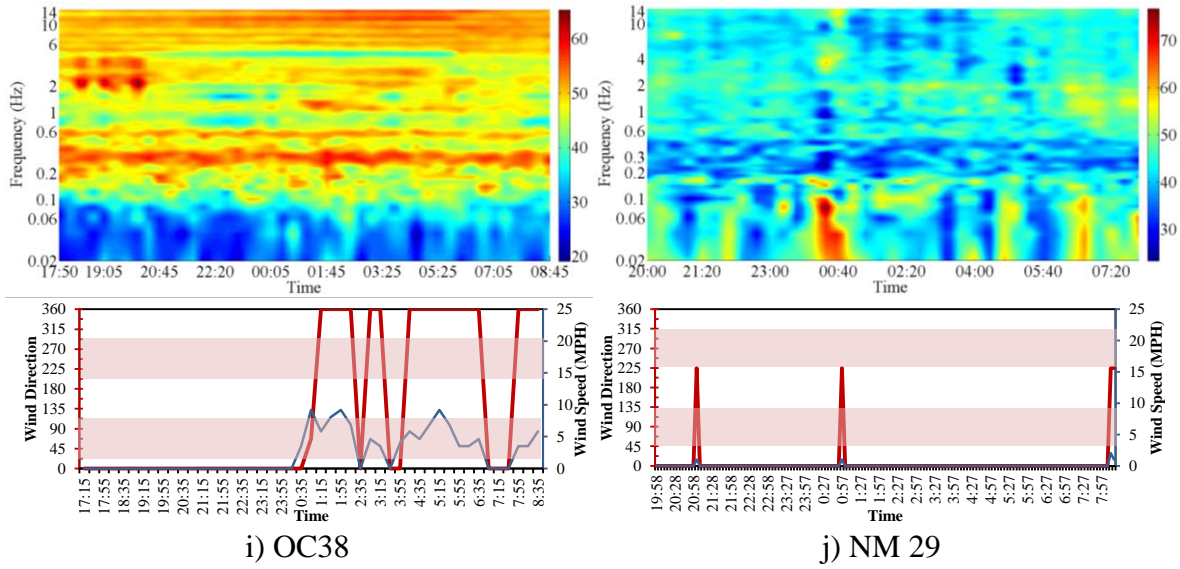
Figure 11. Color gradient map of the vibration angle φ_e of the LTR points in frequency-time space (upper), and corresponding variations in wind direction (red line) and wind speed (blue line) (lower). Note the color bar legends for the values of the vibration angle on the right-hand-side of the gradient maps. The pink shaded ranges on the wind direction axes represent $\pm 45^o$ from E-W direction.

1.4.   DISCUSSION

1.4.1. Vibration directions

The vibration angle φ_e (Figure 8) was calculated here across the frequency spectrum for each LTR. It was then mapped in frequency-time space as shown in Figure 11. The resulting color gradient maps reveal time-dependent nature of φ_e. In the frequency range of roughly > 0.2 Hz, φ_e also exhibits strong frequency-dependency. For the range < 0.2 Hz, φ_e is primarily time-dependent but occasionally also frequency-dependent. These observations suggest that microtremors at the low frequency range are of different origin(s). The significant correlation between φ_e of the low frequency band and the wind direction suggests strong influence of wind even though the sensor was situated indoor.

1.4.2. Correlation between UST and f_0

The UST at each recording point was determined from the isopach map of the Mississippi Embayment (Bodin et al, 2001) (Figure 2) and was plotted against f_0 observed at that location (Figure 12). The best-fit nonlinear regressions of UST vs. f_0 are presented in Figure 12 [labeled as B-1 for $0 < UST(m) < 1400$ (Figure 12a) and A-4 and B-4 for $100 < UST(m) < 1400$ (Figure 12b)]. Figure 12a also presents the best-fit regression models of UST and f_1 data pairs (labeled as A-5 fitted for $100 < UST(m) < 1400$). The other lines represent regression equations derived by earlier studies. All these regression models and values of their fit-parameters are summarized in Table 5. The f_0, HVSR@f_0, f_1 and HVSR@f_1 at each STR location are summarized in Appendix B (Note f_1 is not identifiable at lots of locations).

The regression models produced in this study for both f_0 and f_1 have the same general

expression as the previous models and produce very similar trends. While at large UST values (> 200 m), UST-frequency data pairs form a narrow band, as UST decreases, impact of the errors in predicting actual UST (due to smoothing during preparation of the isopach map and interpolation in reading the UST at each microtremor recording point) gradually becomes more visible (in data scatter). The scarcity of the data in the small UST range prevents a more detailed analysis of the nature of the relationship UST and frequency.
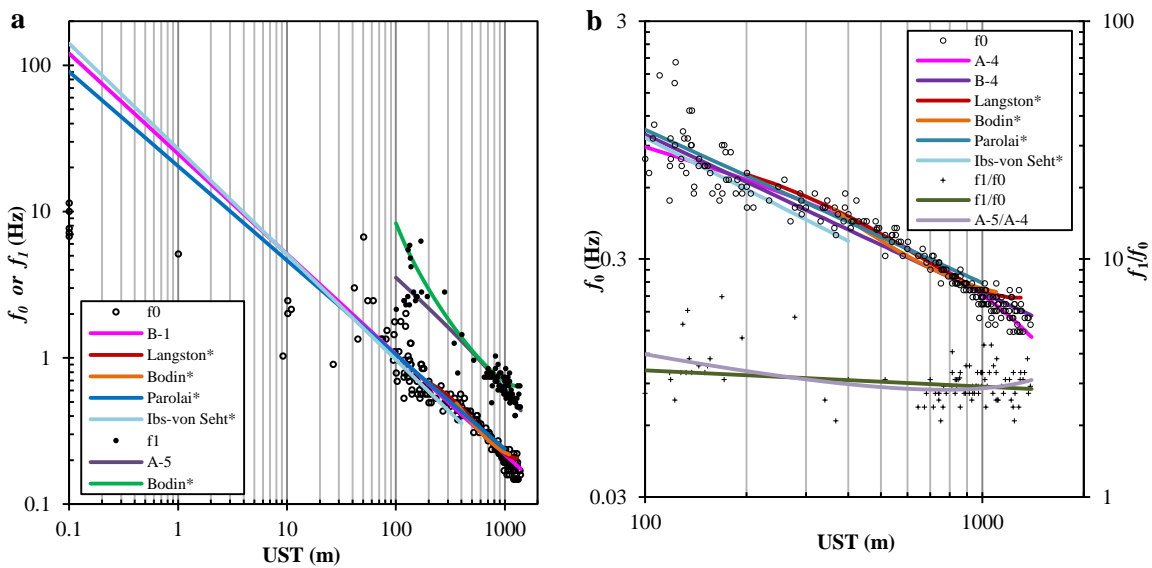
Bodin*: Bodin *et al* (2001): Memphis, Tennessee, U.S.A.
Langston*: Langston and Horton (2011): Upper Mississippi Embayment down to Memphis City, Tennessee, U.S.A.
Parolai*: Parolai *et al* (2002): Cologne, Germany
Ibs-von Seht*: Ibs-von Seht and Wohlenberg (1999): Lower Rhine Embayment, Europe

Figure 12. Regression models of (a) UST (0-1400 m) vs. f_0, and UST (100-1400 m) vs. f_1, and (b) UST (100-1400 m) vs. f_0, and UST (100-1400 m) vs. f_1/f_0. (See Table 5 for parameters of all the regression models)

Figure 13a shows the variation of UST along profile A-A' (Figure 2) while Figure 13b gives the smoothed HVSR spectra at each recording point along this profile. As UST decreases, f_0 peaks gradually become flatter and diminishes at the bedrock, and the values of f_0 and f_1 in general increase while the trend line for f_0 is expected to become strongly nonlinear.

41

Table 5. Regression models of UST vs. f_0 and UST vs. f_1, data pairs, and model parameter values.

Source	Regression method	R^2	SSE	a	b	c	Equation	UST range (m)
UST vs. f_0								
A-4 (This study)	R-LAR	0.991	0.162	4.789	-0.2368	-0.7206	$f_0=a\,(UST)^b+c$	> 100
B-4 (This study)	R-LAR	0.996	0.074	21.26	-0.6635		$f_0=a\,(UST)^b$	> 100
B-1 (This study)	R-BW	0.996	1.783	24.87	-0.6852		$f_0=a\,(UST)^b$	0-1400
Langston (2011)				1.04E-06	-2.64E-03	0.10108	$\ln f_0=a\,(UST)^2+b\,(UST)+c$	200-1300
Bodin (2001)				-3.06E-06	7.89E-03	-0.39899	$f_0=1/[a\,(UST)^2+b\,(UST)+c]$	350-1100
Parolai (2002)				20.466	-0.6447		$f_0=a\,(UST)^b$	Based on < 402, estimate > 1000
Ibs-von Seht (1999)				26.801	-0.722		$f_0=a\,(UST)^b$	< 1219
UST vs. f_1								
A-5 (This study)	LAR	0.976	3.303	70.74	-0.6339	-0.2796	$f_1=a\,(UST)^b+c$	> 100
Bodin (2001)							$f_1=1/[a\,(UST)^2+b\,(UST)+c]$	
R-LAR: Robust regression with least absolute residuals approach R-BW: Robust regression with bisquare weights approach								

The frequency f_1 may be interpreted as the first harmonics of f_0 if the latter is taken as the fundamental frequency. The resonant frequencies f_r of a two-layer model (unconsolidated sedimentary layer overlying bedrock) can be written as (Ibs-von Seht and Wohlenberg, 1999):

$$f_r = \frac{n \cdot V_s}{4 \cdot (UST)} \qquad n = 1, 3, 5,..$$ (9)

where V_s is the shear wave velocity which is a function of depth. When n is 1, $f_r = f_0$, and n is 3, $f_r = f_1$. Therefore, theoretically $f_1/f_0 = 3$ which is consistent with the results obtained at the majority of the recording points. Because f_2 is unidentifiable at most STR points, the ratio f_2/f_0 was calculated only for OC 37, OC 38 and NM 29 and the values are between 5.32 and 6.08 which are also close to the theoretical value of 5.
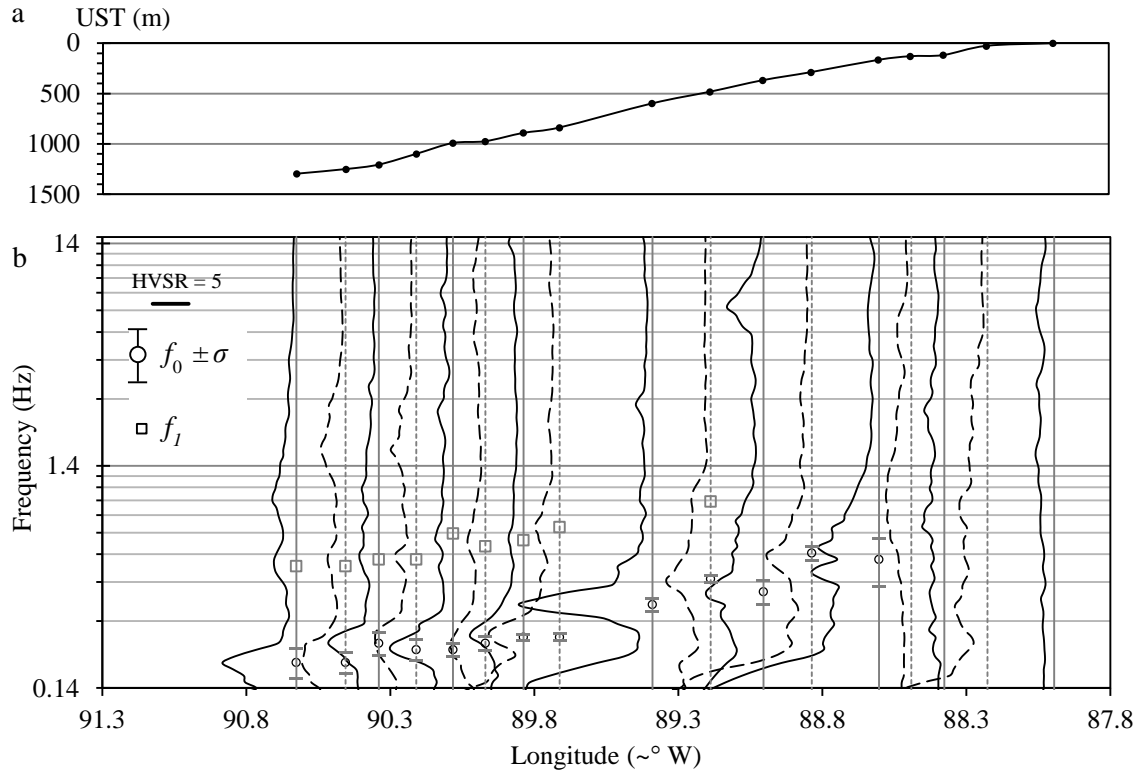
Figure 13. (a) UST along the profile A-A' (Figure 2) and (b) STR HVSR spectra at recording points along the profile. The solid red and blue lines indicate the values of f_0 and f_1 respectively.

Distribution of predominant frequency values f_0 in the study area is presented by a

contour map (Figure 14) based on those recording points at which "reliable" identification of f_0 was possible. Different contour intervals are used for different frequency ranges to account for and benefit from f_0 distributions across the area. These contour lines are clearly consistent with the geological boundaries and the basin morphology.
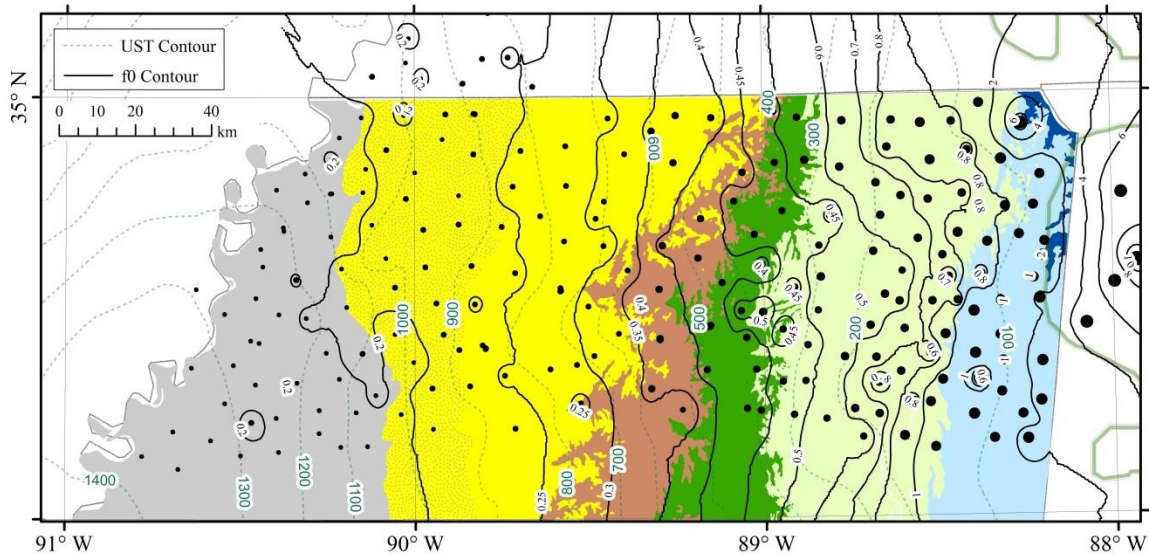
Figure 14. Predominant frequency (f_0) contours in Northern Mississippi.

1.4.3. Average shear wave velocity and its variation with UST

According to Ibs-von Seht and Wohlenberg (1999), average shear wave velocity (V_s) of unconsolidated sediments at each microtremor recording point can be estimated by fundamental mode of Eq. (9), in which $n = 1$ and $f_r = f_0$. These estimates of V_s were plotted against UST values at corresponding recording points (Figure 2) as shown in Figure 15. The resulting data scatter may be interpreted as displaying two distinct trends in UST ranges roughly below and above 500 m. Also shown on this figure are the trends predicted by B-1 (this study), Langston* (Langston et al., 2011) and Bodin* (Bodin et al., 2001) regression models (Figure 12 and Table 5). The model B-1 coincides very well with Bodin* in UST range 500-900 m. In addition to

these predicted trends, Figure 15 also gives a measured V_s profile in Memphis, TN area by Romero and Rix (2005). The similarity of this measured profile and V_s-UST trends (especially B-1) is encouraging in terms of the validity of the microtremor approach and reveals that average Vs of the unconsolidated sediments varies a great deal at shallow depth and reaches that of engineering bedrock (> 600 m/s) around 400-500 m in Northern Mississippi. Large scatters at depths less than 200 m may be attributed to instability of HVSR and increased error in predicting UST from the contours (Figure 2). The significant scatter above 1000 m may also be related to both accuracy of UST contours (Figure 2) and strong influence of local geological and environmental conditions on f_0 in these ranges.
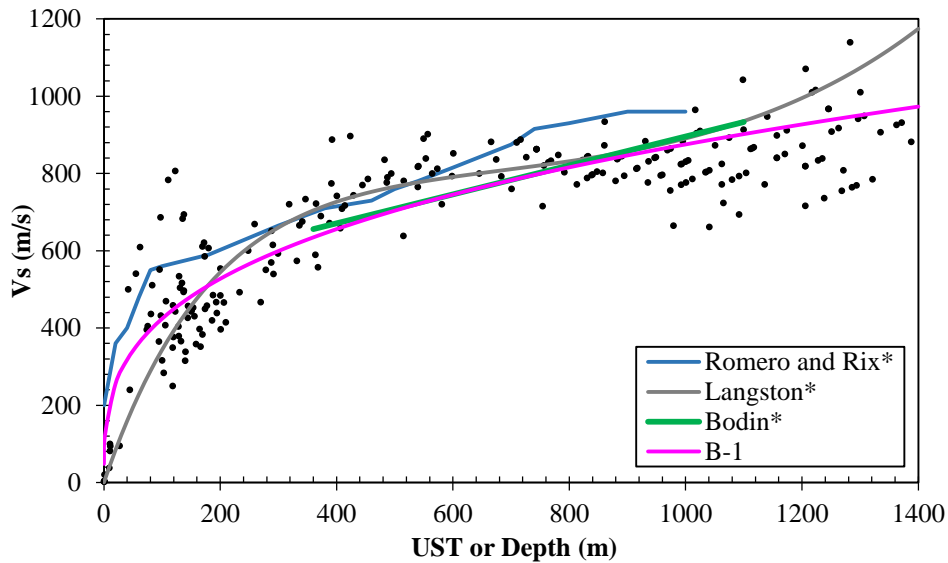
Figure 15. Estimates of average shear wave velocity V_s as a function of UST (or Depth). Note: B-1 recalculates V_s from Eq. (9) using f_0-UST pairs (Figure 12 and Table 5) whereas Langston* and Bodin*are direct relationships of V_s vs. UST. Romero and Rix* is a measured shear wave profile (V_s vs. Depth) in Memphis, TN area.

1.5. CONCLUSIONS

General conclusions that can be drawn from this study are:

1) Microtremor, as a stationary stochastic process, can provide a stable and reliable estimation of the predominant frequency.

2) Wind as a natural source and human activities can significantly influence the microtremor in low frequency band (< 0.2 Hz). Wind effect can be significantly reduced by preventing direct exposure of the sensor.

3) Predominant frequency correlates well with unconsolidated sediment thickness.

4) Average shear wave velocity and its variation as a function of UST across a sedimentary basin can be established from systematic microtremor surveys.

Specific conclusions that may be valid only for the Mississippi Embayment area and in particular for Northern Mississippi are:

1) High peaks on HVSR curves in low frequency range (0.02-0.2 Hz) are caused by wind and human activities.

2) Vibration direction is strongly frequency-dependent above 0.2 Hz and time-dependent below this value.

3) The observed values of the first and second harmonics of the predominant frequencies are consistent with their theoretical values.

4) Average shear wave velocity appears to vary more closely with the UST in 200-1000 m range.

PART II:

DOUBLE-FREQUENCY MICROSEISMS IN AMBIENT NOISE IN

NORHTERN MISSISSIPPI

2.1.   INTRODUCTION

The term "ambient noise" is used in various contexts emphasizing its origin, magnitude and continuity (Webb, 1998; Bard, 1999; Seht and Wohlenberg, 1999; Seo et al, 1990; Schimmel et al., 2011). Ambient noise, also known as microtremor, is understood as "uninterrupted and imperceptible ambient vibrations of the ground due to a multitude of natural and anthropogenic source of disturbance, strength of which vary in time and space" (Guo et al, 2014). Lower part of the ambient noise spectrum (frequency range < 1 Hz) is often referred to as microseism, emphasizing its natural causes such as ocean activities and wind (Seo et al., 1990; Dravinski et al., 1991; Beroya et al., 2009; Bard, 1999). The microseism noise band also has a lower bound, which is often defined as 0.04 Hz (Cessaro, 1994; Traer et al, 2012), sometime 0.1 Hz (Webb, 1998). The double-frequency (DF) microseism (also known as "secondary microseism", Essen et al., 2003; Rhie and Romanowicz, 2006; Schimmel et al., 2011; Ebeling 2012) that manifests itself as a spectral peak at twice the frequency of ocean waves were observed in ambient noise recordings on the deep ocean floors, coastal seafloors and the continents worldwide (Peterson, 1993; Webb, 1998; McNamara and Buland, 2004). The mechanism behind the DF microseism energy involves "the interaction of opposing wave fields having nearly the same wave number, generating a pressure excitation pulse nearly unattenuated to the ocean floor (Bromirski et al., 2005)". For this reason, most of the research on DF microseism is based on data collected on coastal seafloors or coastal land (Babcock et al., 1994; Sun et al., 2013; Stephen et al., 2003; Webb, 1998; Brooks et al., 2009). In terms of the generation mechanism and frequency range, two classes of DF microseism were recognized: 1) long-period DF (LPDF) microseism (f = 0.085-0.2 Hz), which is generated by swells from distant storms, and 2) short-period DF (SPDF)

microseism (f = 0.2-0.5 Hz), which is excited by local storms (Dorman et al., 1993; Webb, 1998; Stephen et al., 2003; Bromirski et al., 2005).

The global observations suggest that microseism recordings, especially at DF, contain relevant information about the atmosphere, hydrosphere and lithosphere (Ebeling, 2012). Bromirski et al. (1999) reconstructed the "wave climate" offshore San Francisco based on coastal DF microseism data recorded at University of California, Berkeley. Their efforts resulted in a possibility of very realistic real-time estimates of deep water "significant wave height" of swells (from distance storms/waves) with peak frequency lower than 0.085 Hz. However, their estimates of the associated peak wave period were mostly conservative (but limited to the upper limit of fluctuations) throughout the duration of the observations. DF microseism observations by Essen et al. (2003) in northern and central Europe revealed that the microseism energy is mainly related to the significant wave height in distinct and identifiable generation regions, supporting the notion that historical records of DF microseism can be used to estimate the wave climate.

Significant but a few researches on DF microseism were carried out based on inland recordings. Peterson (1993) presented the spectra of ambient noise collected all around the world but mostly from continental observation stations, from which the DF peaks can be easily identified. Cessaro (1994) determined source locations of DF microseisms recorded simultaneously on three land-based long-period arrays by wide-angle triangulation, using the azimuths of approach obtained from frequency-wave number analysis. McNamara and Buland (2004) found that the frequency and spectral amplitude of DF microseism vary temporally and spatially within United States. Chevrot et al. (2007) determined precise locations of DF

microseism sources using individual and array microseism recordings at coastal and inland stations in Western Europe.

The study presented in this paper is also based on inland recordings of the ambient noise. Figure *3* shows the recording locations (in red) covering Northern Mississippi (blue box) and the coastal zone of Gulf of Mexico. The research area is situated in a region which is potentially influenced by both Atlantic Ocean and Gulf of Mexico, making it an ideal location to conduct ambient noise measurements with the purpose of exploring the possibility of estimating the wave climates of Atlantic Ocean and Gulf of Mexico.

2.2. DATA PROCESSING

2.2.1. Data preparation

In order to show sampling bias in representation of UST intervals within this large UST range, the survey area was divided into 14 zones defined by 100 m UST contours (Figure 2), and the percentages of STR-I and STR-II points in each interval to total number of STRs were plotted in Figure 4. It can be seen that where UST is thinner than 200 m and thicker than 800m, the STRs are dominantly STR-II type but where UST ranges from 200 m to 800 m, STR-I type recordings are much more abundant. Therefore the results of STR-II in the latter UST range will not be utilized in the analysis of the DF peak.

2.2.2. Power spectral density (PSD)

To directly compare our data to new low-noise model (NLNM) and new high-noise model (NHNM) proposed by Peterson (1993), PSDs of all ambient noise recordings are calculated within frequency band from 0.02 to 15 Hz. The calculation mostly followed the procedure proposed by McNamara and Buland (2004) with a slight difference which is noted below.

In order to investigate variations of the noise spectra with time in greatest possible detail, each times series of the three components (V, NS and EW) of LTRs is parsed into 20-min segments continuously without overlap. This differs from McNamara and Buland's (2004) treatment dividing time series into 1-hr segments overlapping by 50% and then further dividing each 1-hr segment into 13 smaller segments overlapping by 75%. After this preparation, the data is processed using the following procedure:

1) Transfer the time series to zero mean value and remove any linear trend in each segment;

2) Filter each segment by an anti-triggering algorithm based on a prescribed range of short (1 s)- to long (30 s)-term average amplitude ratios (0.2 < STA/LTA < 2.5) to avoid occasional energy bursts (Bard, 1999; Bard and SESAME-team, 2005), which is not part of McNamara and Buland's (2004) treatment;

3) Compute the amplitude spectrum of filtered segments by Fast Fourier transform (FFT) with a 10% cosine taper applied to smooth the FFT;

4) Smooth the spectrum using Konno-Ohmachi function with the bandwidth coefficient set to 40, which is a third difference from McNamara and Buland (2004);

5) Obtain the PSD by simply squaring the amplitude spectrum and multiplying with a normalization factor $2\Delta t/N$, where Δt is the sample interval (0.01 s) and N is the number of samples in each selected times series segment;

6) Further modify the PSD by multiplying with a factor of 1/0.825 to obtain the correct scale since 10% cosine taper were used (Bendat et al., 1971);

7) Present the modified PSD, as a function of frequency, in units of decibels, $(m/s^2)^2/Hz$.

Unlike LTRs, each STR is treated as a whole without segmentation using the same set of procedures outlined above. The process of estimating PSD is repeated for all three components of LTRs and STRs. After step 4), the resultant horizontal spectrum is calculated as Eq. (1), such that steps 5 to 7 are run only on the resultant horizontal spectrum to estimate the horizontal PSD.

2.2.3. Probability density function (PDF)

Following the procedure by McNamara and Buland (2004), the PDF of each LTR and all STRs are calculated within frequency band from 0.02 to 15 Hz.

2.2.4. Particle motion

There are two goals of the particle motion analysis: to find the propagation azimuth of maximum energy and to identify wave type of microseisms ($f < 1$ Hz) within several frequency bands corresponding to several spectral peaks in vertical direction. Particle motion analysis is run on all LTRs and STRs according to the following procedure modified from Ali et al (2010):

1) Each LTR time series of three components (V, NS and EW) is divided into 20-min segments (30 minutes segments for SM 2 and LA 1) continuously without overlap and each STR time series of three components is treated as a whole;

2) Mean amplitude of each segment is subtracted from the waveform and linear trend of each segment is removed;

3) A band-pass filter with a frequency band of [f_c-0.001, f_c+0.001] (f_c being the center frequency of the spectral peak) is applied to each segment, producing filtered amplitude time series $V(t)$, $NS(t)$ and $EW(t)$;

4) Two horizontal components are rotated by an angle φ into radial (R) and transverse (T) components according to Eq. (10) (Havskov and Ottemöller, 2010):

$$\begin{cases} R(t,\varphi) = -NS(t)\cos\varphi - EW(t)\sin\varphi \\ T(t,\varphi) = NS(t)\sin\varphi - EW(t)\cos\varphi \end{cases} \tag{10}$$

where φ is defined as back azimuth angle between the north and the radial direction towards the source;

5) Calculate the root-mean-square of $R(\varphi)$ and $T(\varphi)$ and their ratio $Ra(\varphi)$;

6) Repeat steps 4 and 5 each time increasing angle φ by 1 °until the full circle is completed;

7) Plot $Ra(\varphi)$ vs. φ and find the maximum ratio Ra_m and corresponding azimuth angle φ_m, and finally plot $V(t)$ vs. $R(t, \varphi_m)$.

2.2.5. Estimated vibration angle φ_e

Even though particle motion method is an accurate way to estimate the propagation azimuth of the maximum energy, it is relatively time consuming. Therefore, an estimated vibration angle is calculated following the procedure provided in section 1.2.6. Vibration directions.

2.3. RESULTS

2.3.1. PSD and PDF of Long-term recordings (LTRs)

For LTRs of T-1/T-2, OC 37-4, OC 37-6 and LA 1, values of PSDs across fine frequency bands for each separately processed time series interval are plotted in time-frequency domain to produce color gradient maps, hereafter $PSD(t,f)$ maps (Figure 16a-d). And PDF plots in frequency and PSD domain for all LTRs are presented in Figure 17. These maps at all LTR points clearly show presence of a single or a pair of DF peaks within DF ranges (as defined in the introduction). In this paper, these peaks are called 1st-DF peak (roughly < 0.3 Hz) and 2nd-DF peak (roughly > 0.3 Hz) (as indicated in Figure 16 and Figure 17), frequency ranges and PSD levels of which are summarized in Table 6. From this table, it appears that 2nd-DF peak is more stable within a narrow frequency band whereas 1st-DF peak oscillates even at a given station.

1. Northern Mississippi LTRs (T-1, T-2, NM 14, NM 29 and OC 37)

LTR points located in Northern MS all but OC 37 show a single DF peak in both horizontal and vertical directions. The DF peaks in horizontal and vertical directions appear at the same frequency band. Horizontal PSD at T-1, T-2 and NM14 are slightly lower than vertical PSD, but the opposite holds true for OC 37 (2, 3 and 4) and NM 29.

Unlike others, most of the OC 37 recordings show 2nd-DF peaks in both horizontal and vertical directions. The 1st-DF peaks display a shift during recording time usually from frequency band of LPDF (0.085-0.2 Hz) to SPDF (0.2-0.5 Hz) and occasionally backwards. However frequency ranges in horizontal direction are slightly higher and wider than in vertical direction. This shift in frequency ranges is accompanied by changes in PSD magnitudes. The 2nd-DF peaks

can be easily identified at around 0.36 Hz in vertical direction of most OC 37 recordings. In horizontal direction, some show a single sharp peak, or a single shifting peak, or flat peak, all at a lower frequency than vertical direction. When identified, 2nd-DF peaks in horizontal direction have higher PSD levels than in vertical direction.

The $PSD(t,f)$ maps of T-1 and T-2, OC 37-4 and OC 37-6 are given in Figure 16-a, b and c. Since these are all located in Northern Mississippi (Table 2 and Figure 3) 500-600 km from Gulf of Mexico, differences among them might be related to the UST at each recording point. This will be further discussed later in the section on DF vs. UST.

2. *Southern Mississippi LTRs (SM 1, SM 2 and LA 1)*

LTR at SM 1 (Figure 17f) shows a broad flat DF peak in vertical direction with relatively stable PSD level and a sharp peak in horizontal direction with variable PSD levels. PSD level in horizontal direction is higher than in vertical direction.

For LTRs at SM 2 and LA 1, 1) two clear peaks appear stable with an exception that 1st-DF peak at SM 2's vertical direction is flat; 2) the frequency of each DF peak in horizontal direction is slightly lower than in vertical direction; 3) the horizontal PSD of 1st-DF peak is higher than that in vertical direction; 4) the frequencies of 2nd-DF peaks in both directions are about twice as those of 1st-DF peaks; and 5) the PSD level of 2nd-DF peak are almost identical in both directions. The PDF plot of SM 2 is given in Figure 17g and the $PSD(t,f)$ map of LA 1 is given in Figure 16d.

Table 6. Summary of frequency ranges, PSD levels and estimated vibrations angles of double-frequency peaks at LTRs.

Point	1st-DF peak					2nd-DF peak				
	Vertical		Horizontal		φ_e	Vertical		Horizontal		φ_e
	f	PSD	f	PSD		f	PSD	f	PSD	
T-1	0.18	-119	0.18	-120	41.9 °					
T-2	0.18	-106	0.18	-110	39.5 °					
NM 14	0.25	-124	0.25	-125	41.7 °					
OC 37-1	0.16-0.22	-120 - -130			46.4 °	0.36	-127 - -135	0.29	-109 - -120	47.6 °
OC 37-2	0.17-0.24	-121 - -134	0.18-0.33	-115 - -120	44.0 °	0.36	-132 - -138			42.9 °
OC 37-3	0.12-0.19	-114 - -120	0.13-0.20	-108 - -122	47.5 °	0.31-0.35	-123 - -131	0.29-0.31	-110 - -118	50.8 °
OC 37-4	0.17-0.24	-117 - -134	0.18-0.30	-105 - -120	45.0 °	0.36	-124 - -134			48.7 °
OC 37-5	0.22	-130 - -134			46.4 °	0.36	-128	0.31	-114	52.6 °
OC 37-6	0.13-0.22* 0.20	-125 - -130 -112 - -119			47.9 °	0.36	-120 - -133	0.33 0.20-0.33*	-115 - -120 -100 - -110	49.7 °
NM 29	0.25	-112	0.25	-108	37.2 °					
SM 1	0.16-0.25*	-119	0.14	-105 - -113	44.3 °					
SM 2	0.13-0.21*	-118	0.14	-106	37.6 °	0.29	-113	0.27	-111	45.7 °
LA 1	0.17	-110	0.16	-103	49.8 °	0.33	-110	0.31	-110	44.9 °

1) f: frequency, Hz; PSD: Power spectral density, $(m/s^2)^2$/Hz dB.
2) Frequency range: Usually, the given frequency range means that the DF peak is shifting within this range, but
3) *: the peak covers a broad frequency range.

2.3.2. Correlation of double-frequency (DF) peaks with ocean data and local weather

To investigate the possible sources of DF peak, LTRs at T-2, OC 37-4, OC 37-6 and LA 1 (see Table 2 for ambient conditions) are selected as examples to represent variations in horizontal and vertical components of PSD as shown in the first and second $PSD(t,f)$ maps in Figure 16a-1~d-1. A total of 8 ocean observation stations in Gulf of Mexico and Atlantic Ocean (see Figure 3 for locations) are selected to retrieve the relevant ocean data from the National Data Buoy Center (NDBC) database (http://www.ndbc.noaa.gov/). The four stations in Gulf of Mexico include one coastal station (42012) that is 22 km seaward from the shoreline and three far ocean stations (42040, 42887 and 42360) installed along the edge of continental shelf in Gulf of Mexico. The stations in Atlantic Ocean also include one coastal station (41008) that is 32 km from shoreline, one (41010) installed within continental shelf and two (41002 and 41048) installed in deep ocean area. Temporal changes in the double ocean wave frequency (DWF), simply taken as twice the frequency of the dominant ocean wave, are shown in the uppermost scatter graphs in Figure 16a-1~d-1.

The second and third scatter graphs in these figures represent temporal changes in ocean wave height and ocean wind speed respectively. The signs of the values of wave height and wind speed in these graphs differentiate between opposite propagation directions of ocean wave with maximum energy and ocean wind relative to the ambient noise station, i.e. positive being towards and negative away from the ambient noise station respectively. These quantities are obtained from decomposition of the resultant vectors according to Eq. (11):

$$A_\parallel(t) = A(t)cos(\theta(t) - \alpha) \tag{11}$$

where $A(t)$ is the significant measured wave height or wind speed; $A_\parallel(t)$ is the component of wave or wind vector aligned with the noise stations; and $\theta(t)$ is the azimuth of the ocean wave at

dominant frequency or wind as measured at the NDBC stations. The angle α is the bearing angle between the north and the line connecting the ambient noise and ocean observation stations and measured towards the ocean observation station:

$$\alpha = atan2[cos(lat1)\,sin(lat2)) - sin(lat1)\,cos(lat2)\,cos(lon2 - lon1),$$

$$sin(lon2 - lon1)cos(lat2)] \tag{12}$$

where *lat*1 and *lon*1, and *lat*2 and *lon*2 are latitudes and longitudes of ambient noise recording and ocean wave observation stations respectively. The fourth and fifth scatter graphs in Figure 16a-1~d-1 are atmospheric pressure above ocean and atmosphere pressure and wind speed at each ambient noise station. To capture the time delay between microseisms and ocean conditions, these graphs show ocean data several hours prior to the ambient noise recording started.

The correlation analysis were carried out according to the following procedures:

1) Delimit the frequency band(s) that appear to include the highest PSD levels within DF band 0.085-0.5 Hz;

2) The lowest of these bands includes the 1st-DF peaks, the PSD levels and most likely frequencies of which vary within that band;

3) Each map is then divided into several time zones boundaries of which are defined based on the visually identifiable linear trends in either the PSD levels of the 1st- or 2nd-DF peaks or in one or more sets of ocean data as shown in Figure 16b-1~d-1;

4) Visually select the best match between the double wave frequency (DWF) at each ocean observation station and the 1st or 2nd DF peaks; e.g. at OC 37-4 (Figure 16b-1), the 1st-DF peak matches DWF at station 41010 within time zones ①, ② and part of ④. This pairing is shown on the first two columns of the tables in Fig. 3 and is used as the basis for our

correlation analysis. For those stations that could be paired with both 1st- and 2nd-peaks in different time zones, correlations were shown for both peaks.

5) As the time zones were defined with reference to at least one linear trend (see Step 3), the presence (+) or absence (-) of correlations were assigned according to the behavior of the other time series data as summarized in the inset tables on the right columns of Figure 16b-2~d-2. For example, if the time zone is identified based on a linearly increasing PSD level, then any linear trend recorded at an ocean observation station would be recorded as "correlated or +".

1. *T-1 and T-2 (*Figure *16a-1&-2)*

    PSD(t,f) maps at T-2 as well as the ocean and local weather data are presented in in Figure 16a-1. *PSD*(t,f) maps at T-1 are given in in Figure 16a-2. Due to the lack of synchronous ocean data from the Atlantic Ocean stations and loose correlation between DF of T-1 and ocean data at Gulf of Mexico, the ocean data for recording period at T-1 are not presented.

    The ocean wave and ocean wind speed are relatively stable (consistently high) during T-2 recording period, and therefore, are processed without segmentation for the correlation analysis. DWF at stations 41002, 41008 and 41010 in Atlantic Ocean coincide well with DF at T-2. The wave height at 41002 and wind speed at 41002 and 41010 were unusually high. The PSD levels of the DF peak at T-2 was about 10 dB higher than that of T-1 (which is recorded earlier at the same location) and even higher than those of SM 2 and LA 1 recordings (although located at the coastal area and recorded while both oceans were much quieter).

2. *OC 37-4 (Figure 16b-1&-2)*

    In time zone ①, DWF at station 41002 in Atlantic Ocean coincides well with 1st-DF, and

both wave height and the PSD level decrease. DWFs at stations 42012, 42040 and 42360 in Gulf of Mexico are very close to 2nd-DF. In this time zone, ocean wind speed, pressure and local weather conditions are all positively correlated with DF peaks as summarized in the insert tables in Figure 16b-2.

In time zone ②, wave height decreases and DWF at station 41002 increases while the PSD level at 1st-DF continuously decreases. DWF at station 41002 rises to a frequency close to 2nd-DF while DWF at station 41010 continue to correlate well with 1st-DF. DWF at station 42012 suddenly increases and wave propagation switches direction during the second half of this time zone while the PSD level at 2nd-DF can be seen to undergo a faint decrease around the same time.

In time zones ③ and ④, the PSD levels of both DF peaks increase. DWFs at stations 41002 and 41010 generally shift from the frequency range of 2nd-DF to 1st-DF, whereas wave height (at station 41002) increases. At stations 42012 and 42040, wave height increases in negative direction but only DWF at station 42040 coincides well with 2nd-DF. DWF at station 42012 rises to as high as 0.5 Hz accompanied with a slight decrease in the PSD levels of both DF peaks.
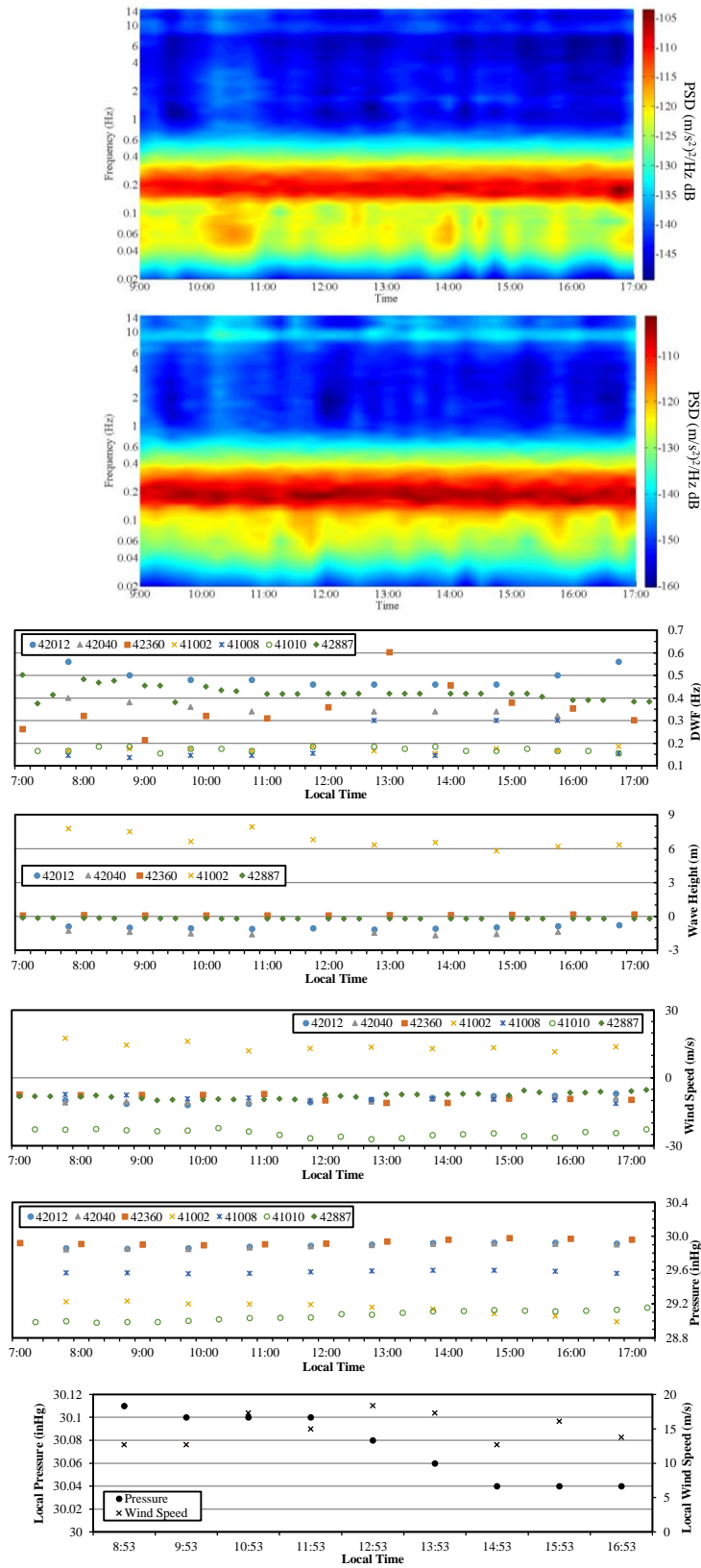
a)-1
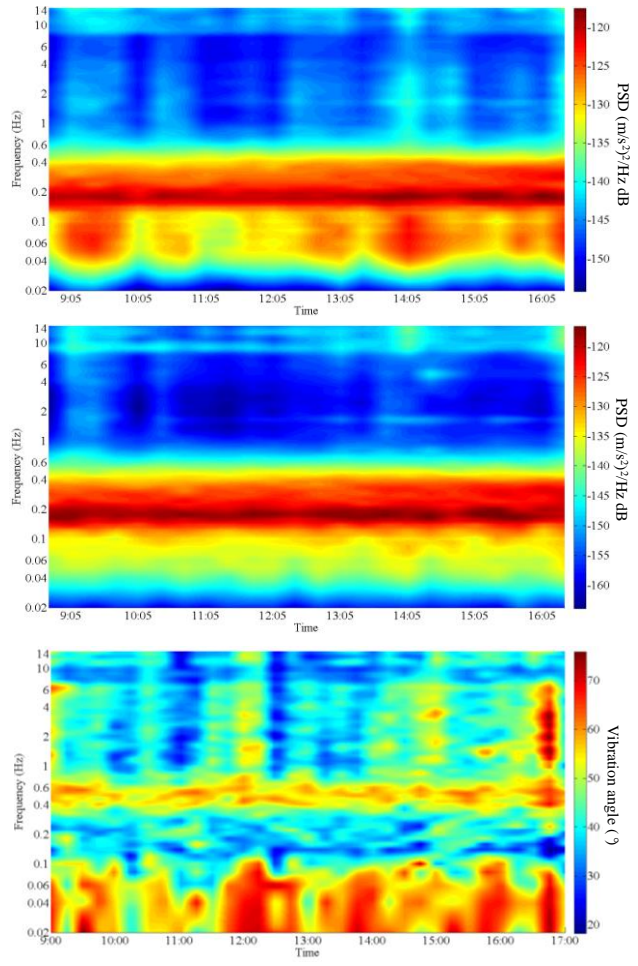
a)-2
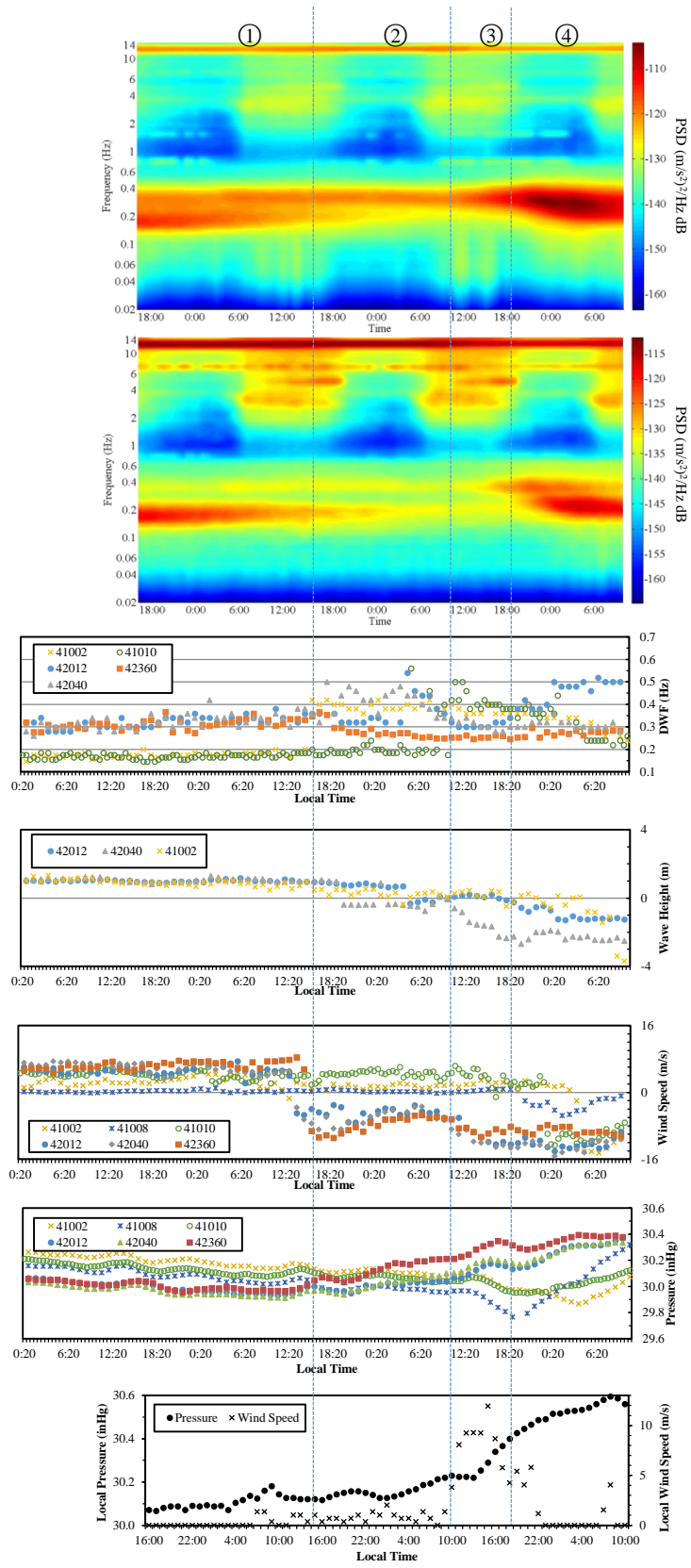
b)-1
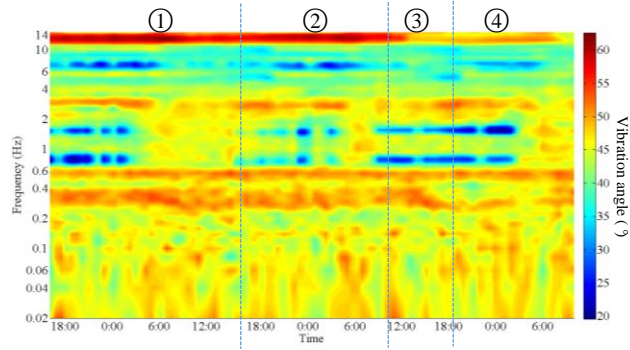
Wave height

Station	Peak	①	②	③	④
41002	1st-DF	+	+	+	+
41010	1st-DF	+	+	-	+
42012	2nd-DF	+	+	+	+
42040	2nd-DF	+	+	+	+
42360	Both	+	-	-	-

Wind Speed

Station	Peak	①	②	③	④
41002	1st-DF	+	+	+	+
41008	2nd-DF	+	+	+	+
41010	2nd-DF	+	+	+	+
42012	2nd-DF	+	+	+	+
42040	2nd-DF	+	+	+	+
42360	Both	+	-	-	-

Ocean pressure

Station	Peak	①	②	③	④
41002	1st-DF	+	+	-	-
41008	1st-DF	+	+	-	+
41010	2nd-DF	+	+	-	+
42012	2nd-DF	+	+	+	+
42040	2nd-DF	+	+	+	+
42360	2nd-DF	+	-	+	+

Local

	Peak	①	②	③	④
Pressure	2nd-DF	+	+	+	+
Wind	2nd-DF	+	+	-	-

b)-2

65
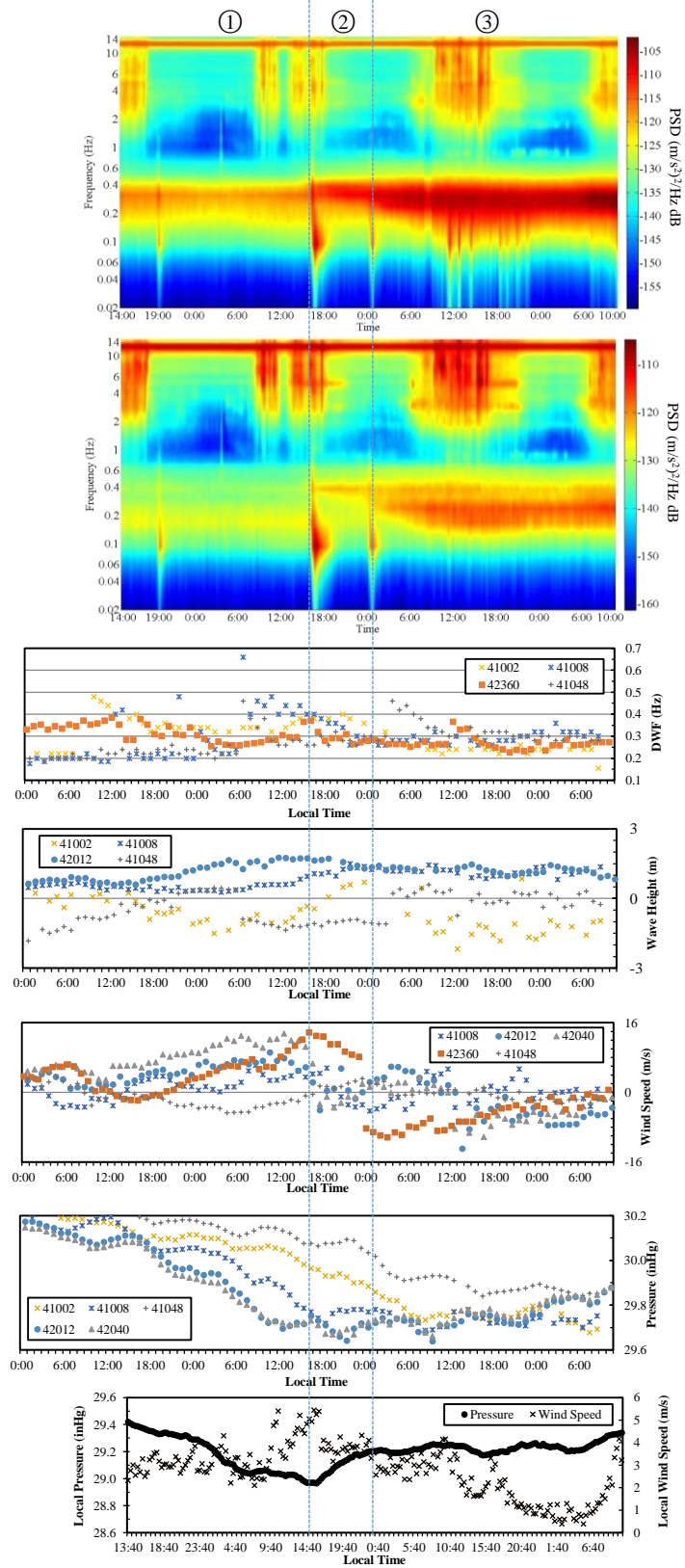
c)-1
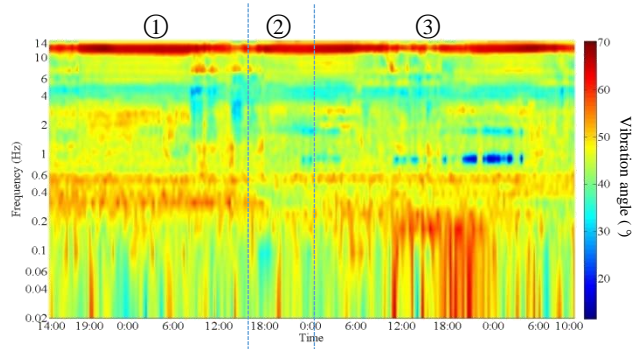
Wave height

Station	Peak	①	②	③
41002	1st-DF	+	-	+
	2nd-DF	-	+	-
41008	1st-DF	+	-	+
	2nd-DF	-	+	-
41048	1st-DF	+	+	+
42012	Both	-	-	-
42360	1st-DF	+	+	+

Wind Speed

Station	Peak	①	②	③
41008	1st-DF	+	+	+
41048	Both	-	-	-
42012	Both	-	-	-
42040	Both	-	-	-
42360	1st-DF	+	+	+

Ocean pressure

Station	Peak	①	②	③
41002	Both	+	-	-
41008	Both	+	-	-
41048	Both	-	-	-
42012	Both	+	-	-
42040	Both	+	-	-

Local

	Peak	①	②	③
Pressure	2nd-DF	+	+	+
Wind	2nd-DF	+	+	-

c)-2

d)-1

68
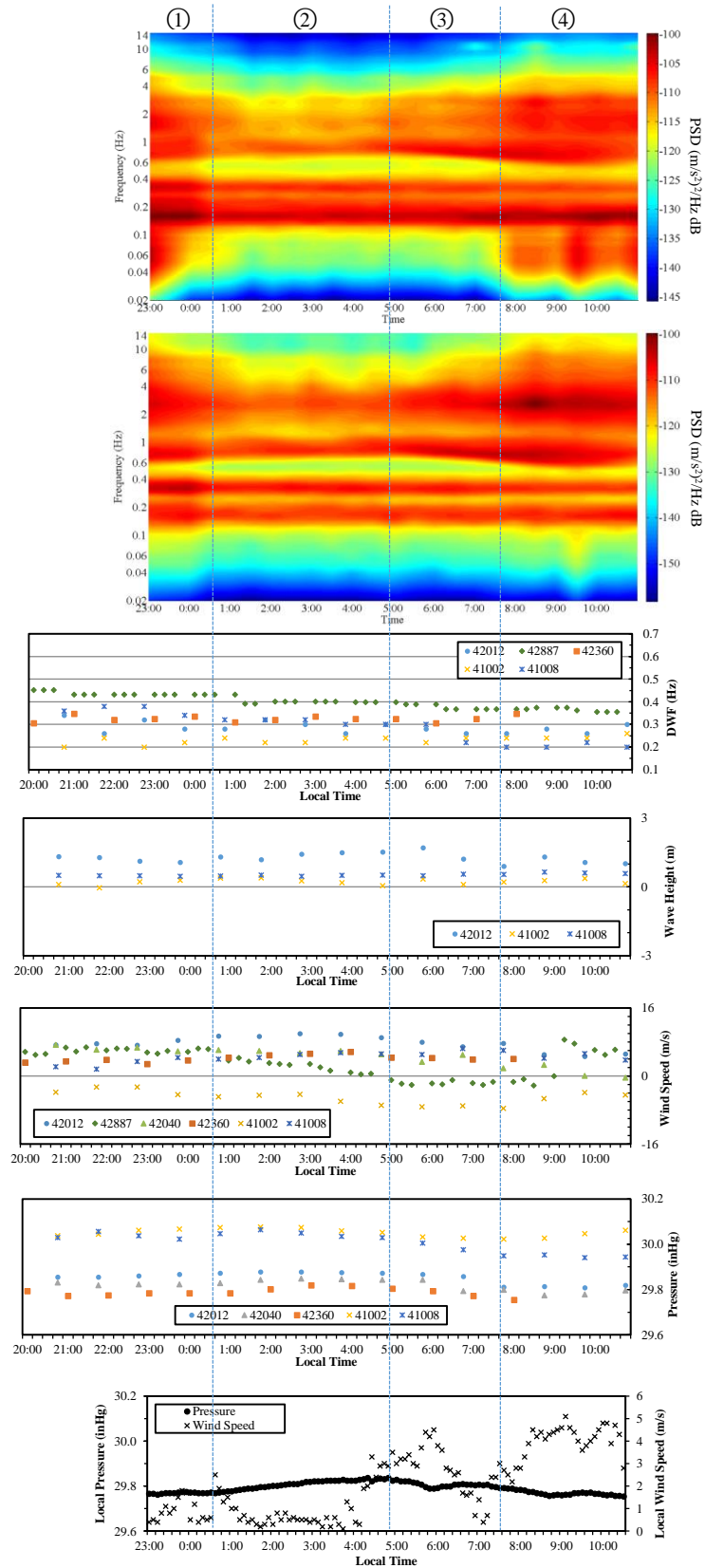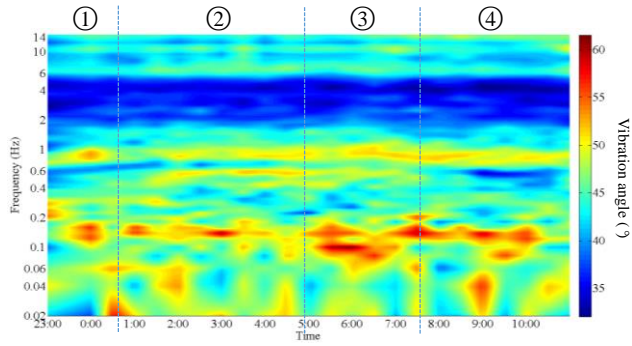
Figure 16.
(1) Color gradient maps in part (a) showing distributions of (i) PSD in horizontal (top) and in vertical (second top) directions in time-frequency (t-f) space at T-2 (a-1) and T-1 (a-2) and (ii) vibration angle in t-f space at T-2 (bottom of a-2);
(2) Color gradient maps in parts (b), (c) and (d) showing distributions of (i) PSD in horizontal (top) and in vertical (second top) directions in t-f space (-1) and (ii) vibration angle in t-f space (top of -2) at OC 37-4, OC 37-6 and LA-1 respectively;
(3) Scatter graphs in parts (a)-1, (b)-1, (c)-1 and (d)-1 showing time histories of (top to bottom) (i) double (ocean) wave frequency peak; (ii) ocean wave height; (iii) wind speed at ocean wave observation stations (see Figure 3 for locations) with reference to the LTR stations; positive and negative values of wave height and wind speed differentiate between the relative orientations of maximum energy wave and wind fields, towards and away from the ambient noise station respectively; (iv) air pressure over the ocean; and (v) local wind speed and pressure during LTRs at T-2, OC 37-4, OC 37-6 and LA1.
(4) Tables in parts (b)-2, (c)-2 and (d)-2 show correlations between ocean data and DF peaks, in which, "+" and "-" represent "positive" and "negative or no" correlation respectively.
Note:
- The ocean data used in this study were all retrieved from the National Data Buoy Center (NDBC) database at http://www.ndbc.noaa.gov/.
- The local wind and pressure data are downloaded from Weather Underground at http://www.wunderground.com/.
- The local pressure and wind speed data at LA 1 (in part d) were recorded at station NWCL1 (30.027 N 90.113 W), which was retrieved from NDBC database.

Wave height

Station	Peak	①	②	③	④
41002	Both	-	-	-	-
41008	Both	-	-	-	-
42012	2nd-DF	-	+	+	+
42887	2nd-DF	+	+	-	-
42360	1st-DF	-	+	+	

Wind Speed

| Station	Peak	①	②	③	④
41002	2nd-DF	-	-	-	-
41008	2nd-DF	-	+	-	-
42012	2nd-DF	-	+	+	+
42040	2nd-DF	+	+	+	+
42887	Both	-	-	-	-
42360	2nd-DF	-	+	+	

Ocean pressure

Station	Peak	①	②	③	④
41002	2nd-DF	-	+	+	-
41008	2nd-DF	+	+	+	+
42012	2nd-DF	-	+	+	-
42040	2nd-DF	-	+	+	-
42360	2nd-DF	-	+	+	

Local

	Peak	①	②	③	④
Pressure	2nd-DF	-	+	+	+
Wind	2nd-DF	-	-	-	-

d)-2

3. *OC 37-6 (*Figure *16c-1&-2)*

In time zone ①, a flat 1st-DF peak appears within a broad frequency band of about 0.13-0.22 Hz. DWFs at stations 41008 and 41048 in Atlantic Ocean are within this band until 6:00, after when they jump to higher frequency around 0.4 Hz. The ocean wave height at station 41008 correlates well with 1st-DF. However, none of the available ocean wave height data correlates well with 2nd-DF.

In time zone ②, 1st-DF peak is still broad and flat without any significant variation in PSD level and correlates well with ocean wave height at stations 41048 in Atlantic Ocean. DWF sharply decreases while wave heights recorded at stations 41002 and 41008 in Atlantic Ocean display a steep and a mild increase respectively. Concurrently, the PSD level of 2nd-DF very slightly decreases and the separation between 1st-DF and 2nd-DF peaks fades away.

In time zone ③, 1st-DF has a clear peak with a high wide shoulder whereas 2nd-DF peak is still narrow. In Atlantic Ocean, ocean wave at stations 41008 and 41048 propagates in opposite directions while in Gulf of Mexico, at station 42012, wind direction and ocean wave direction are almost opposite. During this period, the PSD levels of both 1st- and 2nd-DF peaks are very high.

4. *LA 1 (*Figure *16d-1&-2)*

Variations of the ocean and local weather conditions are not that obvious during this recording period, and DF peaks do not vary significantly. However, slight variations can be observed, for example, in time zones ①, ② and ③, where DWF at stations 42012 and 42360 (Gulf of Mexico), and 41008 (Atlantic Ocean) are close to 2nd-DF.

From time zone ③ to ④, DWF at station 41008 shifts down to around 0.2 Hz and wind directions at stations 42040 and 42887 (Gulf of Mexico) opposes each other although their directions are switched in the second half of time zone ④. Local wind speed strongly fluctuates during these time zones.

2.3.3. 3rd-peak of LTRs

As shown in Figure 16a-d, all $PSD(t,f)$ maps have a similar feature, i.e. a very clear frequency boundary around 0.6-0.8 Hz, above which PSD show daily variations. At OC 37, this boundary is sometimes presented as a low peak especially in horizontal direction. At SM 2 and LA 1, it appears as a clear peak, frequency of which varies with time, where the corresponding PSD level reasonably correlates with the local pressure and wind speed.
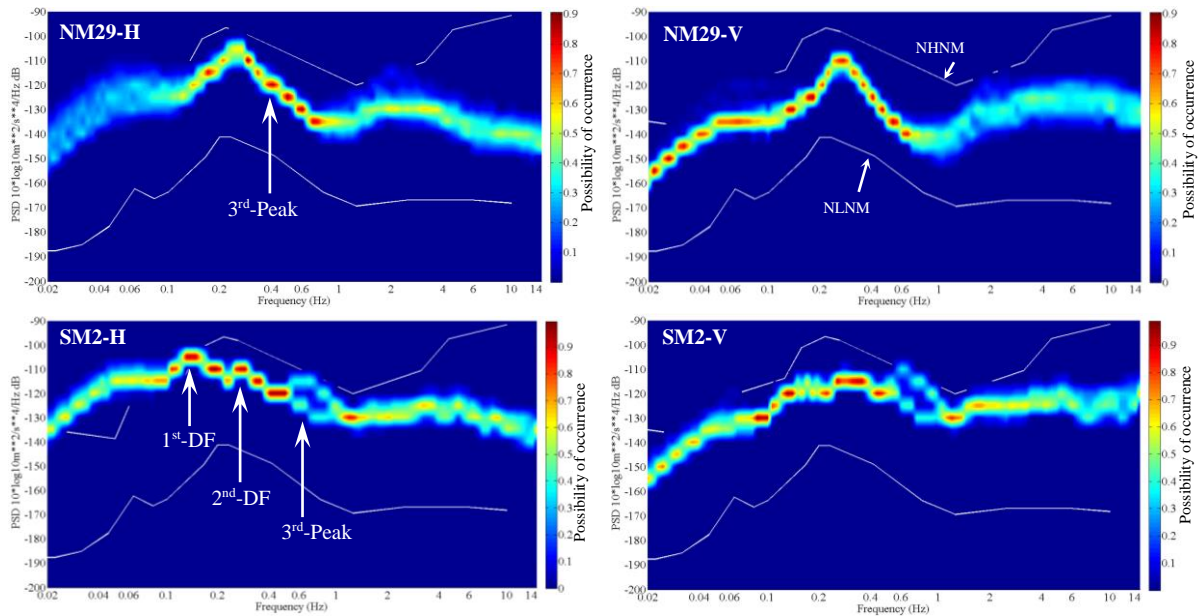

Figure 17. PDF plots of LTRs NM 29 and SM 2 in horizontal (H) and vertical (V) directions.

In ocean seismic observation studies, this frequency range is known as Holu spectrum (0.3-7.5 Hz) which is attributed to short-wavelength local ocean wind waves (McCreery et al,

71

1993; Webb, 1998). In order to distinguish between continental observations of this research and the ocean based observations, this peak is termed 3rd-peak in this paper. This boundary can be observed in all OC 37 recordings at around twice frequency of 2nd-DF peak. This peak does not appear in T-1, T-2 and NM 14 recordings, but in horizontal direction of NM 29 recording, it appears as a narrow shoulder of DF at around 0.4 Hz as shown in Figure 17. In SM 2 recording, this peak appears occasionally in both horizontal and vertical directions at around 0.6 Hz (Figure 17).

2.3.4. Particle motion and vibration angle at DFs at OC 37-6, SM 2 and LA 1

1. Particle motion and azimuth angle

In Figure 18, in each column, first and last pairs of rows exhibit plots of i) particle motion in $V(t)$-$R(t, \varphi_m)$ space and ii) variations of $Ra(\varphi)$ and φ_m (indicated by red arrow) of 1st-DF and 2nd-DF microseisms at the labeled recording station and period. Usually, particle motion plots form clusters rarely with a single elliptical outline and mostly with two centrally symmetric ellipses. The change in the elliptical outline is quantified by a flattening factor f_f calculated by $f_f = (a - b)/a$, where a and b are major and minor axes of the ellipse or centrally symmetric cluster.

For OC 37-6, during the quiet time zone ① (Figure 16b-1 and Figure 18a), Ra of 1st-DF is very comparable to that of 2nd-DF, as they are both very low and nearly independent of azimuth. But in the noisy time zone ③ (Figure 16b-1 and Figure 18b), the maximum energy wave propagation direction in horizontal plane can be easily identified by the high Ra value, where Ra of 2nd-DF is visibly lower than 1st-DF.

72

a) OC 37-6 2014:075:02:00-02:20   b) OC 37-6 2014:076:07:40-08:00
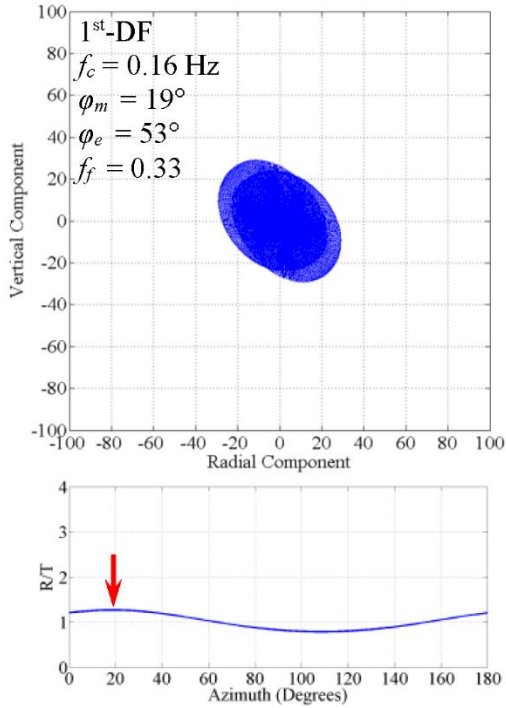
73
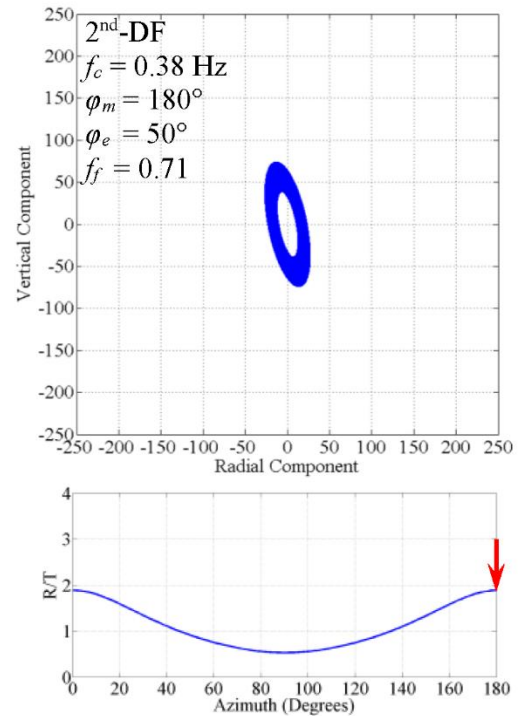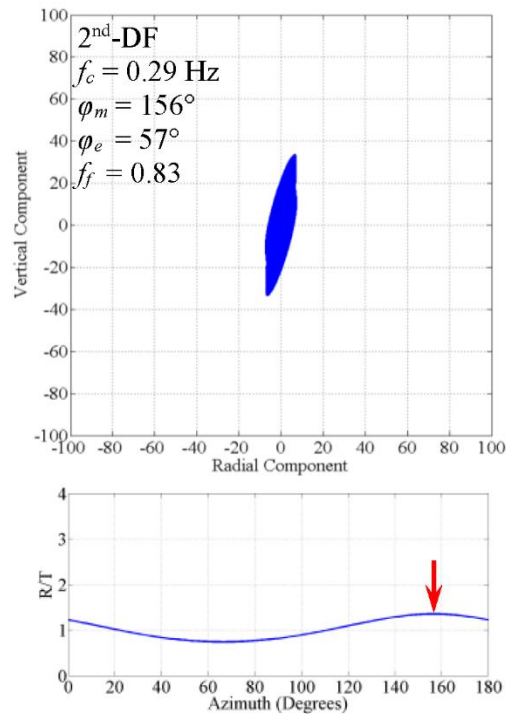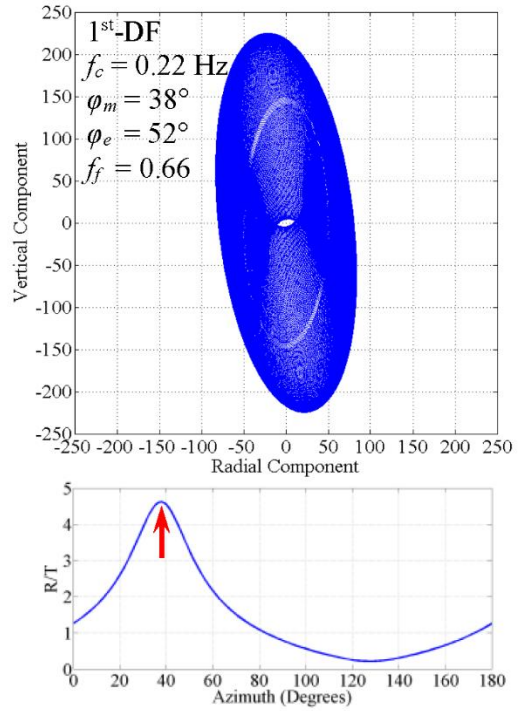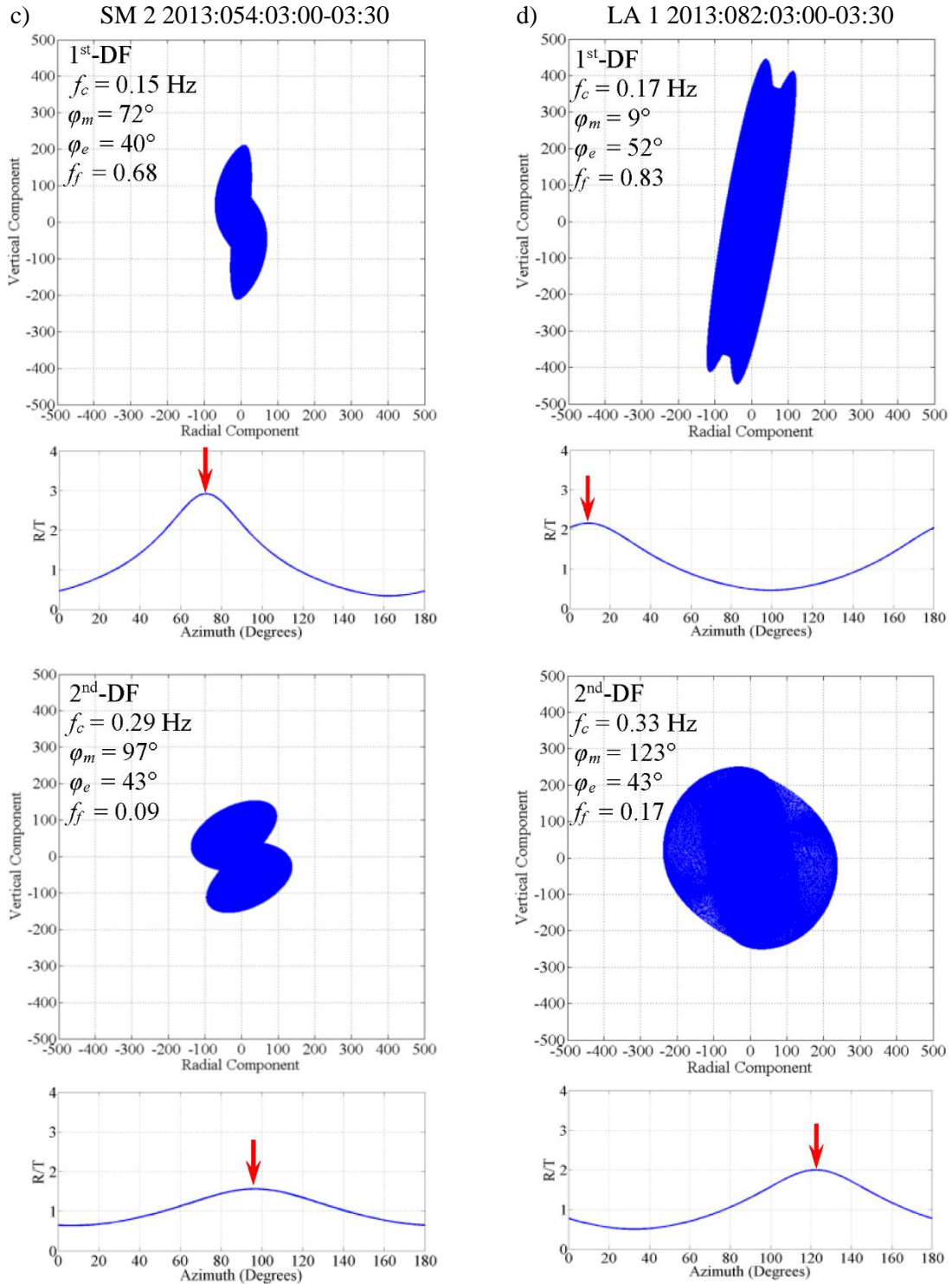
Figure 18. Particle motion patterns traced by plots of vertical vs. radial component at 1st-DF (first row) and 2nd-DF (second row) of LTRs at OC 37-6, SM 2 and LA 1, and variations and peaks of ratios of radial to transverse components (R/T) as a function of azimuth. In each particle motion plot, central frequency of DF peak f_c, azimuth of maximum R/T ratio φ_m, estimated vibration angle φ_e and flattening factor f_f are indicated.

For the 2nd-DF particle motion, the horizontal amplitude of maximum energy wave is almost equal to vertical component (f_f is very low) at the coastal area (SM 2 and LA 1). Also notably, the particle motion plots at 1st-DF at SM 2 and LA 1 have a major axis nearly along vertical direction and the flattening factors at 1st-DF are much higher than those at 2nd-DF.

The φ_m and Ra_m histories of 1st-DF (Figure 19a and c) and of 2nd-DF (Figure 19b and d) are compared at SM 2 (red line) and LA 1 (blue line). The φ_m of 1st-DF shows a 1.5 hour periodic variation, especially during 03:00-08:00, whereas the φ_m period of 2nd-DF is nearly doubled to around 3 hours. Even though SM 2 and LA 1 recordings were taken at different places and time, their φ_m histories show obvious similarity suggesting that the DF microseisms recorded at these points are excited by similar sources and mechanisms noting that the ocean climate over both Atlantic Ocean and Gulf of Mexico were quiet and stable during the ambient noise recording periods (Figure 19e, f and g).

2. Vibration angle

In Figure 18, azimuth angle corresponding to maximum radial to transverse components φ_m (measured from north) and estimated vibration angle φ_e (measured from east) of the DF peaks are noted in each particle motion plot. These angles do not perfectly correlate with each other but they consistently point to the source of vibration.

The $\varphi_e(t,f)$ maps of T-2, OC 37-4, OC 37-6 and LA 1 are presented in the right columns of Figure 16a-2~d-2 Within 2nd-DF bands and 3rd-peak frequency bands, the vibration angles reveal highly frequency dependent variations and correlate well with the energy source characteristics, DWF and ocean wave heights. T-2 and LA 1 recordings display relatively stable vibration angles within 1st-DF band as well. However, vibration angles at OC 37 within 1st-DF

band vary simultaneously with lower frequency band, especially if 1st-DF is within frequency band < 0.2 Hz. A larger collection of vibration angle maps given in Figure 11 and Appendix D reveals that in most Northern Mississippi recordings, vibration angles within frequency band of 1st-DF (< 0.2 Hz) show time-dependency but they are stable within 2nd-DF and 3rd-peak frequency bands.
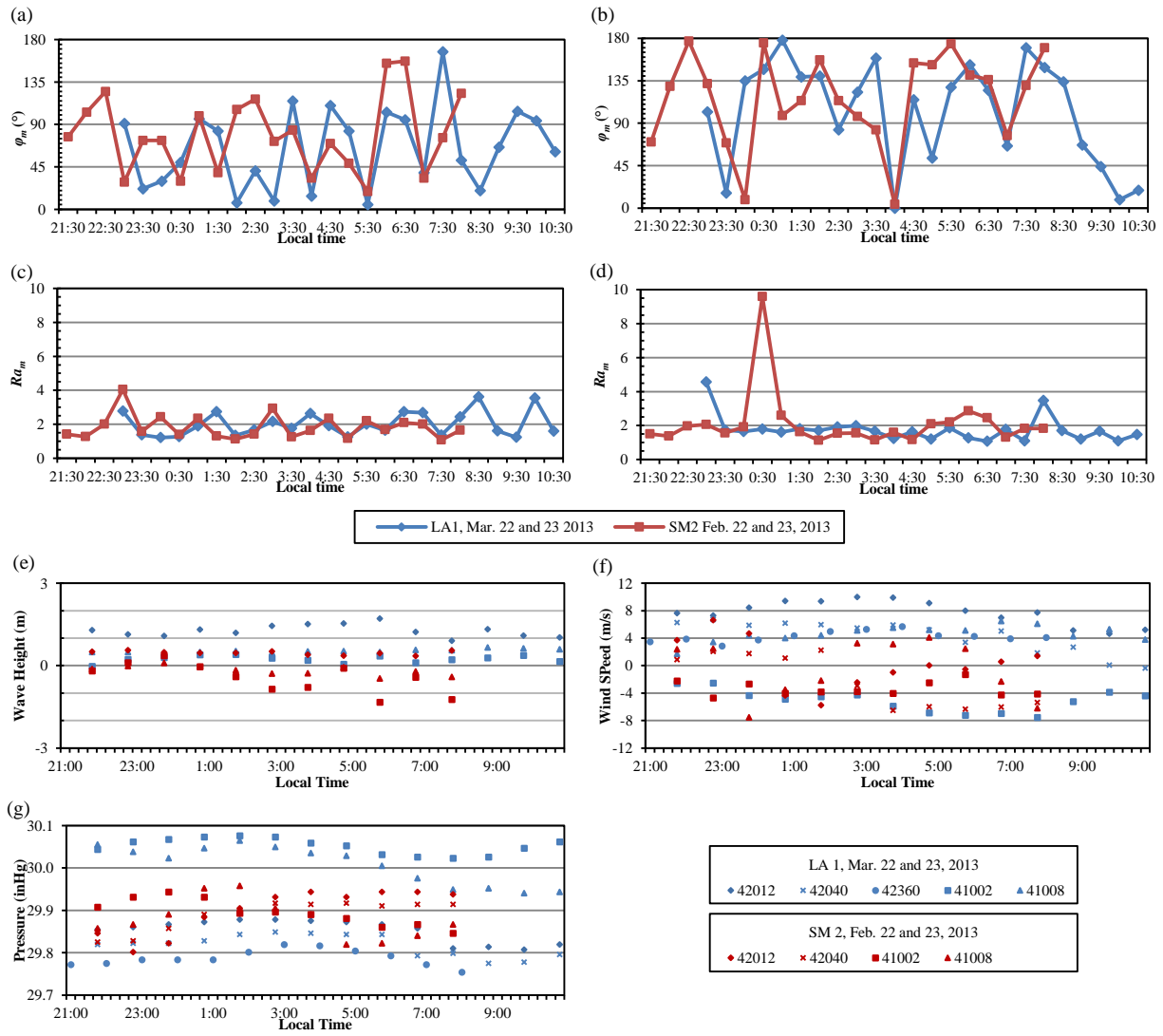

Figure 19. Comparisons of time histories of azimuths at maximum R/T ratio (φ_m) (a and b) and maximum R/T ratios (Ra_m) (c and d) determined at SM 2 (squares) and LA 1 (diamonds) at 1st-DF peak (a and c) and 2nd-DF peak (b and d). Ocean data during these ambient noise recording periods were comparable in (e) wave height, (f) wind speed and (g) pressure above ocean.

The average vibration angle φ_e at 1st-DF and 2nd-DF are calculated and summarized for all LTRs in Table 6. Among Northern Mississippi recordings at T-1, T-2, NM 14 and NM 29, the vibration is primarily in east-west direction since the average vibration angle is smaller than 45 ° but most recordings at OC 37 have mainly north-south direction vibration. This difference might be related to their locations and dominant energy sources as discussed later. Since SM 2 and LA 1 are recorded in the coastal area, the vibration angle is highly related to the ocean activities, especially to the 1st-DF microseism.

2.3.5. Short-term recordings

PSDs of STRs are given in a matrix of graphs with four rows (A-D) and three columns (I-III) in Figure 20. Of these graphs, AI and BI depicts average PSDs in horizontal and vertical directions respectively of STR-I recordings grouped by UST. CI and DI graphs do the same for STR-II recordings. As demonstrated in columns II and III, the DF peaks outlined by red boxes in column I show complex variations with UST and type of recordings.

1. Horizontal direction (Figure 20A and C)

In horizontal direction, differences between the PSD curves of STR-I and STR-II recordings are evident. Within UST range 0-600 m, STR-I (Figure 20AII) displays the DF peaks that are almost unidentifiable due to the high noise in low frequency band (<0.2 Hz). With UST increasing from 600 to 1300 m (Figure 20AIII), while the DF peaks become more identifiable and sharper, they shift from around 0.5 Hz to 0.3 Hz, with the DF peak levels roughly increasing with UST. Compared to STR-I, PSDs of STR-II within UST range 0-600 m (Figure 20CII) present obviously different characteristics: the peaks are all visible, but they shift randomly; and they have much higher PSD values at these peaks within UST range 200-600 m than that within

0-200 m. Note, however, that there is only one STR-II recording in each 100 m interval in 200-600 m UST range (Figure 5) and that two common properties of these STR-II recordings are 1) very high wind speeds, and 2) proximity to a heavy traffic road. Within UST range 700-1400 m, PSDs of STR-II show very clear peaks in every UST range (Figure 20CIII). With UST increasing from 700 m to 1400 m, the peaks shift stably from around 0.3 Hz to 0.2 Hz and their PSD levels increase in general. These changes of peak frequencies and corresponding PSD levels for STR-I and STR-II recordings are summarized in Figure 21 where general trends of DWF and wave height can also be found.

2. *Vertical direction (Figure 20B and D)*

On PSDs of STR-I recordings, the DF peaks are obvious: i) within UST range 0-600 m (Figure 20BII), the peaks are almost fixed around 0.23 Hz; ii) with UST increasing from 0 to 600 m, the PSD values generally decrease; iii) within UST range 600-1300 m (Figure 20BIII), peak frequency and PSD values do not correlate well with UST; iv) the peak PSD values slightly increase with peak frequency; v) the 3rd-peaks visible in Figure 20BIII shift from 0.6 Hz to 0.33 Hz with a general increase in the peak value.

For STR-II, within UST range of 0-200 m, the peaks stay at 0.2 Hz. Within UST range 200-600 m, the peaks shift to a lower frequency and with much higher amplitudes. This change is likely an artifact of limited measurements as it was observed in the horizontal direction. Within UST range of 700-800 m, two DF peaks exist: a higher peak at around 0.2 Hz and a lower one at around 0.35 Hz, which are more easily identified on LTR at OC 37 (Figure 16b-1 and c-1). With UST increasing from 800 m to 1400 m, the peak shifts from 0.31 Hz to 0.22 Hz and the peak PSD value gradually increases. These changes as a function of UST in the peak

frequency and PSD values in vertical direction can be seen in Figure 21c and d. These properties described above are also summarized in Table 7.
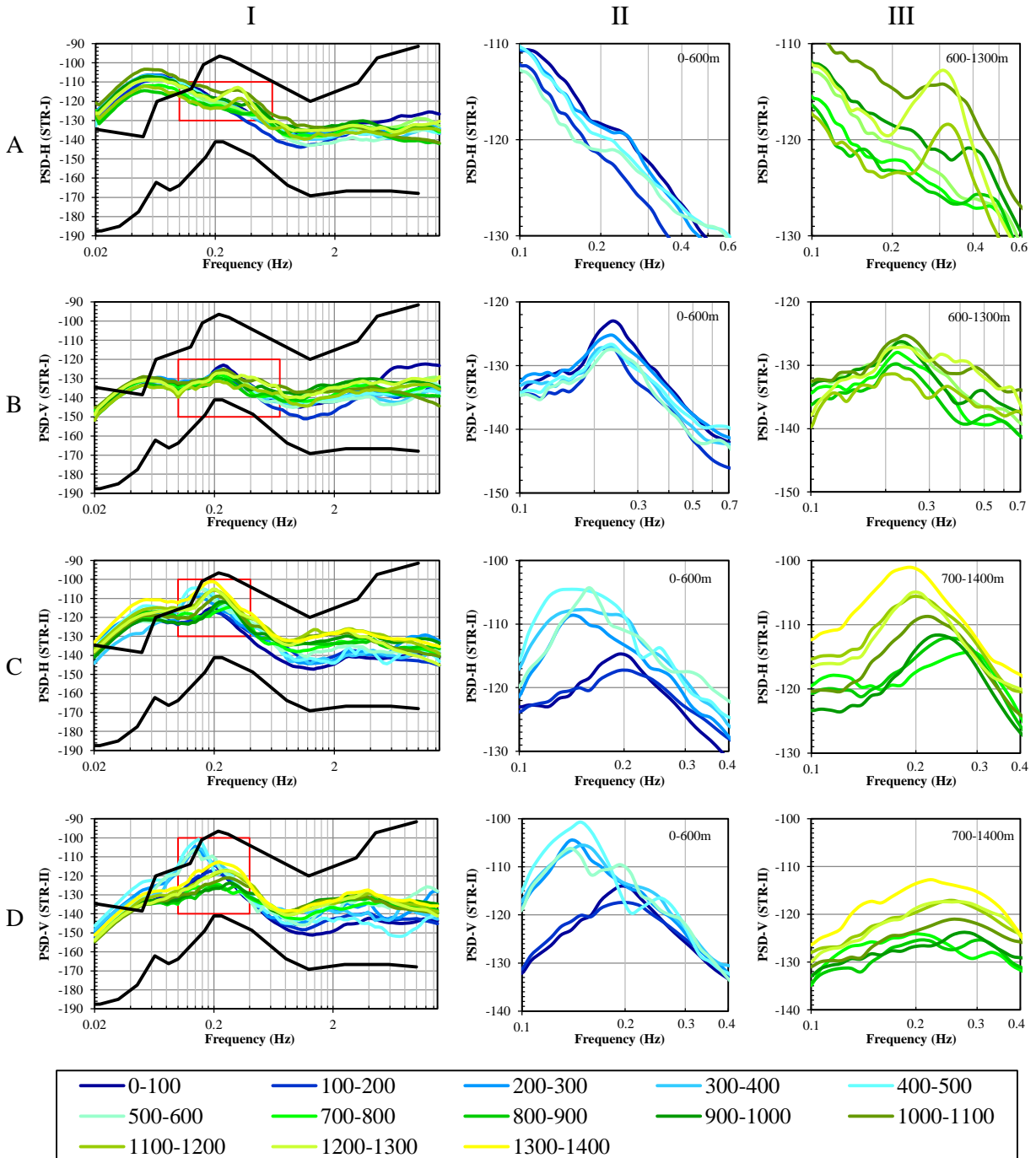

Figure 20. Column I: PSD of STRs grouped by UST; Column II and III: zoomed in curves of the boxed DF peaks in column I. PSD-H and PSD-V are PSD values in horizontal and vertical directions respectively.

2.3.6. DF vs. UST

A closer look into the relationships of peak frequencies (f_p) and PSD levels at DF peaks (PSD@f_p) of horizontal and vertical components with UST (Figure 21) allows the following observations.

In horizontal direction, the f_p value makes a peak at UST of 500 m (Figure 21a). In this figure, the two lines (A-4 and B-4) are the regression curves of predominant frequency (f_0) vs. UST obtained by Nakamura method based on the STR data (Figure 12b). The coincidence of f_0 regression curve and DF plots suggests that in horizontal direction, shear wave resonance in the sediments modifies the DF microseism in thick sediments. With decreasing UST, the f_p trends closer to the original frequency band. Because the resonance frequency of the bedrock is high (> 1.0 Hz, Guo et al, 2014), the DF peaks at the eastern boundary (UST $\approx$ 0 m) are within its expected band. Going west (UST increasing), resonance frequency approaches to the DF band, allowing them to couple. This results in a wider band of values around UST of 500 m. As UST increases further, the stronger peaks always occur at the frequencies where resonance and DF are coupled. The PSD@f_p reaches the lowest value at around UST of 200 m (Figure 21b) because 1) the attenuation of wave energy gets lower in very thin (< 200 m) sediments overlying bedrock; and 2) the shear wave resonance in thick (> 200 m) sediments amplifies the energy in horizontal direction.

As to the f_p and *PSD@fp* variations as a function of UST in vertical direction (Figure 21c and d): i) within UST range of 0-800 m, f_p does not vary with UST, but PSD@f_p forms slightly decreasing large band; and ii) within UST range > 800 m, f_p gets slightly larger, but still without

variation with UST, where PSD@f_p increases as a function of UST. A rough correlation is noted between the 3rd-peak and UST.
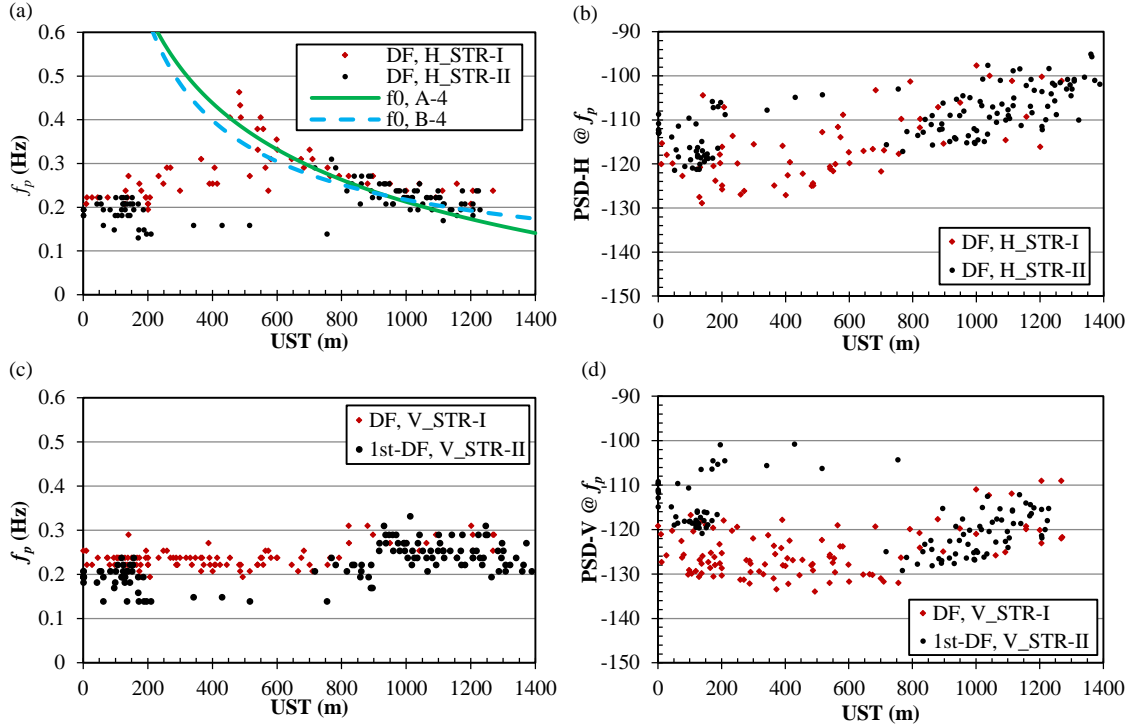
Figure 21. DF peak frequencies and PSD level vs. UST in horizontal (a and b) and vertical (c and d) directions. The two lines in **a** are the regression curves of predominant frequency (f_0) vs. UST obtained by Nakamura method based on the STR data in Figure 12.

Within the UST range > 800 m, STR-I and STR-II recordings do not reveal obvious differences in both f_p and PSD@f_p trends. On the contrary, in UST range < 800 m, f_p and PSD@f_p of STR-II are obviously lower and higher respectively than those of STR-I in both horizontal and vertical directions. This difference is thought to result from: 1) the sensor is very sensitive in detecting tilting of ground or sensor body caused by air flow (Angelis and Bodin, 2012) since sensor was exposed during STR-I recordings; and/or 2) the seasonal variation of ocean wave activities might cause higher DF peaks in the UST range < 800 m. Within low UST range (0-200 m), the DF peaks might be caused by the ocean activities in Atlantic Ocean as

discussed later. Based on this hypothesis, the DF within this area is related to the ocean waves of Atlantic Ocean. The STR-I recordings were made during May-July, 2012 while STR-IIs were during August, 2012-February, 2013 but in this particular area (where UST ranges between 0 and 200 m) during October-November, 2012. The lower band of DWF recorded at station 41002 (Atlantic Ocean) during October and November, 2012 is lower than that during May-July, 2012 when STR-Is were made, and the ocean wave height recorded at the same station during October and November, 2012 were higher than that during May-July, 2012. These observations explain why the PSD levels of STR-IIs are higher than those of STR-Is.

Table 7. Summary of the DF peaks and 3rd-peak of STRs.

Measuring type	Vibration component	Peak name	UST range		Peak frequency (f_{ps}) shift (Hz)		PSD@f_{ps} vs. UST		Referring figures
			From	To	From	To	From	To	
STR-I	Horizontal	DF	0	600	Unidentifiable				Figure 20AII
			600	1300	0.5	0.3	-127	-113	Figure 20AIII
	Vertical		0	600	0.23		-123	-128	Figure 20BII
			600	1300	0.22		-125 ~ -131		Figure 20BIII
		3rd-peak	600	1300	0.6	0.33	-137	-128	
STR-II	Horizontal	1st-DF	0	200	0.19		-115	-117	Figure 20CII
			200	600	Not statistically reliable.				
			700	1400	0.3	0.2	-114	-101	Figure 20CIII
	Vertical		0	200	0.19		-114	-117	Figure 20DII
			200	600	Not statistically reliable.				
			700	800	1st-DF transfer from 0.33 to 0.19.				Figure 20DIII
			800	1400	0.31	0.22	-125	-113	
		2nd-DF	700	800	0.33		-128		
			800	1400	No		No		

2.4. DISCUSSION

2.4.1. Possible causes of DF peaks

McNamara and Buland (2004) in their Figure 11B presented a map of PDF mode noise levels above the NLNM across the United States in frequency band 0.125-0.25 Hz. This map shows that the noise levels in this band, from the east coast to inland, decreases roughly as a function of distance to the coastline. This suggests that the ambient noise within this frequency band is predominantly related to large scale/ubiquitous natural activities in Atlantic Ocean. However their dataset includes only one seismic station in the Northern Mississippi area, which prevents the detailed study of the local ambient noise structure. Considering the shortest distances from Northern Mississippi to Atlantic Ocean and to Gulf of Mexico are around 720 km and 500km, respectively, it is more plausible that the DF peaks might be a combined product of the activities in both Atlantic Ocean and Gulf of Mexico. The qualitative correlation analyses of PSD levels, frequency ranges and vibration angles of DF peaks with ocean and inland weather data presented in this paper provide evidence to support this hypothesis of combined effect where the lack of a complete ocean data set hinders a more definitive view.

As indicted earlier, the DF peak of T-2 correlates well with Atlantic Ocean waves, whereas 1st-DF and 2nd-DF peaks of OC 37-4 are related to Atlantic Ocean and Gulf of Mexico waves respectively. For example, the unusually high wave height and wind speed may explain the higher PSD levels of DF peak at T-2, compared to T-1, SM 2 and LA 1 recordings. Similarly, decreasing wave height at station 41002 in Atlantic Ocean is the most likely cause of decreasing PSD levels at 1st-DF at the beginning of OC 37-4 recording. During a subsequence time zone at OC 37-4, the slight decrease in PSD levels of the 2nd-DF peak seems to be in response to the

sudden change in wave propagation direction and DWF at station 42012 in Gulf of Mexico. Later on during the OC 37-4 recording, increasing wave height (41002 and 41010 in Atlantic Ocean) offers an explanation for increasing PSD level of 1st-DF peak, while increasing wave height in negative direction at 42010 and 42040 in Gulf of Mexico gives a likely cause for increasing PSD level of 2nd-DF peak. Towards the end of this recording period, significant rise of DWF at 42012 seems to have resulted in decreasing PSD level of both DF peaks the despite fact that the wave height was increasing at the same time. Similar correlation can be found at OC 37-6, although they are not as visible as at OC 37-4. In time zone ②, the fading separation between the PSD levels of the 1st and 2nd DF peaks seems to be related to decreasing DWF (shifting 2nd-DF to lower levels) and increasing wave height (closing the gap in PSD levels of DF peaks). In time zone ③, the high PSD levels of 1st and 2nd-DF peaks can be attributed to opposing ocean wave directions in the Atlantic Ocean and to opposing ocean wave and wind directions in the Gulf of Mexico.

At LA 1, in time zones ③ and ④, the increasing PSD levels of 1st DF peak (in both vertical and horizontal directions) may result from opposing wind directions at stations 42040 and 42887 (Gulf of Mexico). This is in contrast to the observations at OC 37-4 and OC 37-6 as summarized above. During these times zones, however, the strong fluctuations in local wind appears to be also reflected in fluctuations of the PSD levels of 1st-DF peak in horizontal direction.

Long axes of the outlines obtained by plotting $Ra(\varphi)$ values calculated at DFs of all LTR segments (Figure 22) represent the directions along which dominant energy is aligned. The patterns of Ra outlines in Figure 22 can be categorized into the following types: 1) two primary

85

vibration directions marked by very sharp tips (T-2); 2) two primary vibration directions marked by two clearly identifiable tips (1st-DF and 2nd-DF of LA 1, and 1st-DF of SM 2); 3) primary vibration zone in which no specific directions may be identified (1st-DF of OC 37-4 and OC 37-6); 4) one primary direction marked by a relatively sharp tip (T-1, NM 14, SM 1, 2nd-DF of SM 2 and OC 37-4, and NM 29). Analysis of these directions provide further support to the proposed hypothesis as listed in the following: i) the DF peaks recorded at T-1, T-2, OC 37-4, and OC 37-6 are perfectly consistent with the hypothesis and the correlations with the ocean weather data; ii) NM14 (located on the eastern boundary of Northern Mississippi) produced a consistent outline with the nearby T-1 and T-2; iii) $Ra(\varphi)$ plots of 1st-DF at SM 2 and LA 1 show two primary directions, E-W and N-S, although these stations are located at the coastal area of Gulf of Mexico (Figure 3). It can be concluded from these observations that Atlantic Ocean generates more energetic and/or efficient waves due to faster deepening of its waters; iv) $Ra(\varphi)$ plots of 2nd-DF at SM 2 and LA 1 exhibit similar primary directions around N137°; v) $Ra(\varphi)$ plot of SM 1 indicates that the primary direction is around N43° implying the combined energy of ocean activities in Gulf of Mexico and Atlantic Ocean; vi) $Ra(\varphi)$ plot of NM 29 exhibits a strong East-West direction, which might be related to the channel flow processes in Mississippi River.

Figure 23 displays $Ra(\varphi)$ vs. φ plots obtained at DFs of STRs which are grouped into UST intervals of 100m. Variations among the patterns of Ra outlines of these groups indicate possible alignments of vibration sources responsible for the DF peaks. These patterns in almost all UST ranges exhibit both N-S and E-W source directions: i) within 0-500 m range, either N-S or E-W is dominant; ii) within 500-700 m, Ra value in N-S and E-W directions are almost equal; iii) within 700-1000 m, E-W and around N45° are the primary directions; iv) within 1000-1200 m, N-S and E-W are both obvious; v) within 1200-1400 m, only E-W is the primary direction;

and vi) for the entire UST range (0-1400 m) (the last plot labeled as "ALL") in addition to N-S and E-W directions, NE-SW direction is prominent. These observations confirm that the DF peaks in Northern Mississippi area is essentially influenced by ocean activities from both Atlantic Ocean and Gulf of Mexico but the lack of systematic variations inhibit evaluation of how UST modifies Ra patterns.
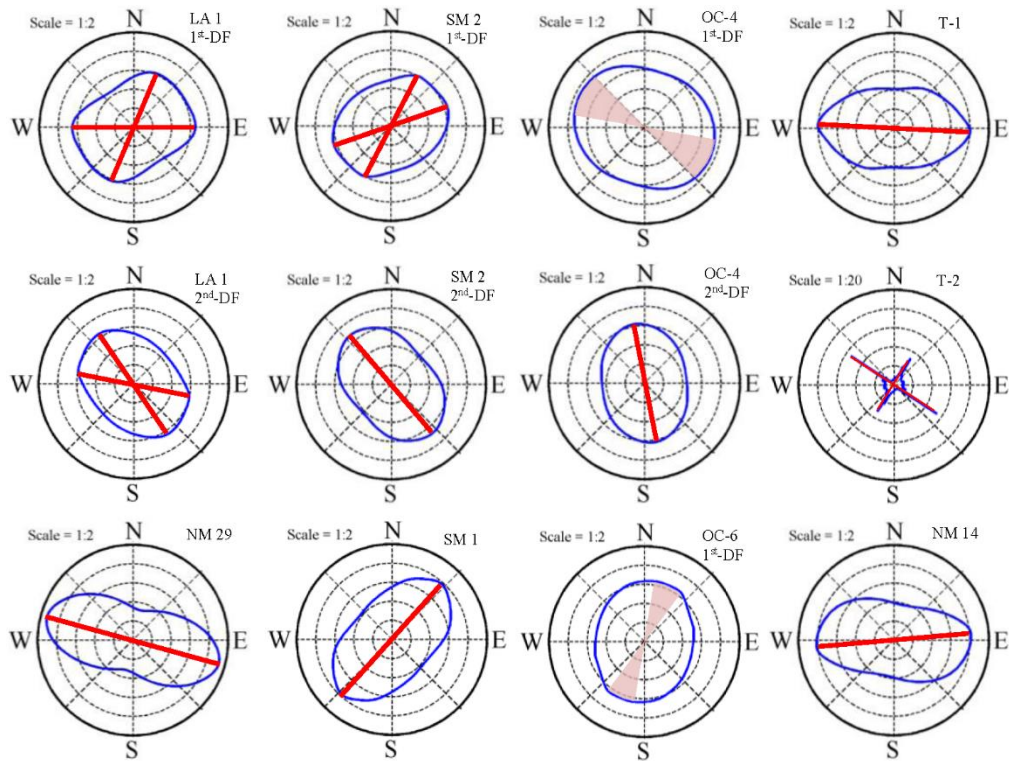

Figure 22. Patterns of average ratios of radial to transvers amplitudes $Ra(\varphi)$ at DF of LTRs (blue lines). The scales show the magnifications factors e.g. at a scale of 1:2, the solid circle has a diameter of 2 units.

From the eastern to the western boundary of Northern Mississippi, both the UST and distance to Atlantic Ocean increase. Starting from the eastern boundary, westward decrease of the PSD level (particularly for the vertical component, Figure 21) and E-W alignment of $Ra(\varphi)$ at DF (Figure 23) suggest that the primary vibration energy originates from Atlantic Ocean. In the central part of Northern Mississippi, the DF is influenced by both Atlantic Ocean and Gulf of

Mexico. On the west, as it gets closer to Mississippi River, higher PSD levels might be related to the flow processes in the Mississippi River channel and to the sediment resonance as discussed below.
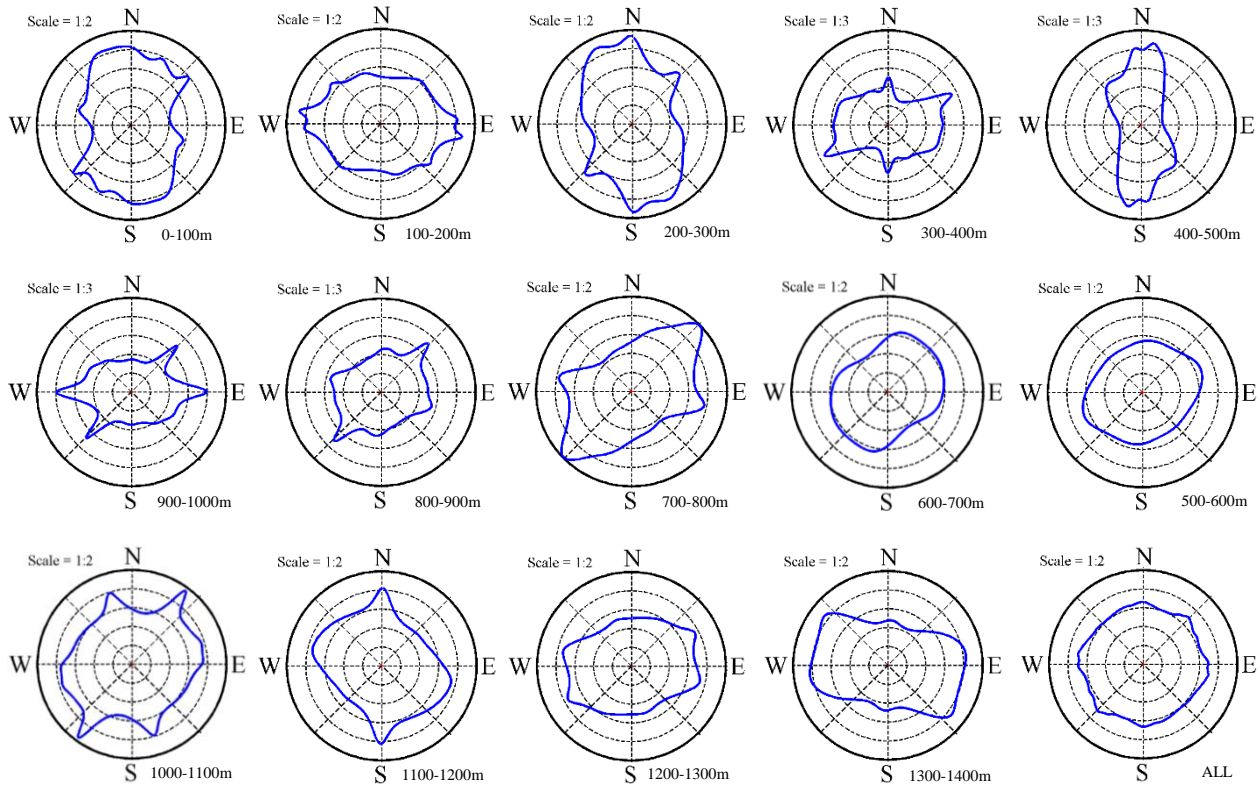

Figure 23. Patterns of average ratio of radial to transvers amplitudes $Ra(\varphi)$ at 1st-DF of STRs grouped by UST (indicated at the right bottom corner of each pattern). The scales show the magnification factors e.g. at a scale of 1:2, the solid circle has a diameter of 2 units.

2.4.2. Resonance and attenuation of DF microseisms propagating in sediments

Because the DF microseisms propagate fundamentally as Rayleigh waves through sediments (Haubrich and McCamy, 1969), attenuation through sediments and shear wave resonance influence their structure as they travel inland. As shown in Table 6, comparing the PSD levels in horizontal (PSD-H) to vertical (PSD-V) components of each LTR, T-1, T-2 and NM 14 recordings produce almost identical values, while for the other LTRs, the PSD-H is obviously larger than PSD-V. This is likely because of stronger shear wave resonance in

horizontal direction in thick sediments. Analysis of the STR data presented in Figure 21 reveals that the resonance effect weakens as sediment thickness is reduced toward the eastern boundary.

The particle motion plots of 2nd-DF peaks of SM 2 and LA 1 (Figure 18c and d) show that in the coastal area, the horizontal amplitude of maximum energy wave is almost equal to that of vertical component, producing a very low f_f. However, further to the north (OC 37), the modification in two directions varies significantly, resulting in very high f_f for the inland recordings.

As shown in Table 6, from coastal LTRs (LA 1 and SM 2) to inland LTRs (SM 1 and OCs), the average PSD level of the DF peaks generally decrease even though the ocean was quieter during coastal recordings. This clearly reveals that the DF microseism is generated by ocean waves and that it strongly attenuates as it propagates through the sediments. The attenuation is more obvious in vertical direction since in horizontal direction the shear wave resonance offsets the attenuation effect on the DF microseism. These observations also provide empirical support to the validity of the Nakamura's horizontal to vertical spectral ratio (HVSR) method for determining the predominant frequency f_0.

The particle motions of 1st-DF and 2nd-DF of OC 37-6 during time zone ③ (noisy) (Figure 18b) suggest that energy of 2nd-DF attenuates faster than 1st-DF in horizontal plane since Ra of 2nd-DF is lower (rather than being very similar) than that of 1st-DF. This can be also seen through f_f of 2nd-DF (in both quiet and noisy times zones, ① and ③) which is much higher than 1st-DF since the major axis of the ellipse is along the vertical direction.

2.5. CONCLUSIONS

This study explored the possibility of estimating the wave climates of Atlantic Ocean and Gulf of Mexico based on long- and short-term inland (Northern Mississippi) and coastal (Gulf of Mexico) recordings of ambient noise in a region potentially influenced by both sources. The analysis utilized a number of modified and novel data processing methods which are clearly explained and applied. In addition to determining PSD, PDF, particle motion and vibration angle parameters, procedures for computing and comparing components of magnitude/direction of wave/wind (measured at NDBC stations) were presented with reference to the ambient noise stations. Correlating PSD levels, frequency ranges and vibration angles at DF peaks with ocean and inland (local) weather data disclosed not only a dual source mechanism for DF microseisms in the study area but also provided further insight into the nature of DF microseisms.

Computing and plotting ratios of the PSD levels of radial to transverse components of ambient noise in the horizontal plane (Ra) enabled determination of dominant energy directions produced further support for the dual source mechanism and shown that Atlantic Ocean waves are more energetic or efficiently coupled with the ground. Lack of systematic variations of Ra with UST reinforced the proposed dual sources for DF peaks. On the other hand, UST was found to regulate the resonance effect.

The results of the analysis presented in this paper also provided strong support to the validity of the Nakamura's HVSR method commonly used in determining f_0. The results was consistent with a well-known fact high frequency waves (2nd-DF in this case) attenuates faster that the slower ones (1st-DF).

PART III:

CORRELATION OF HORIZONTAL TO VERTICAL SPECTRAL

RATIO AND OCEAN WAVE CLIMATE

3.1. INTRODUCTION

As discussed in Parts I and II, the predominant frequencies (f_0) over most of the Northern Mississippi area where UST > 300m are within the expected double-frequency (DF) ranges. Therefore, as DF is closely related to ocean activities, f_0 and HVSR values might also be influenced by ocean activities. This part is dedicated to examining this possibility, through a systematic analysis of correlations between HVSR@f_0 and wave climate, and exploring presence of a consistent transfer function. In order to enable this examination, microtremor is visualized as resultant vectors of three spectral components (V, NS and EW) and these vectors are calculated for 100 narrow frequency bands evenly divided in logarithmic scale within 0.02 Hz and 15 Hz range. These vectors derived from segmented LTRs at each narrow frequency band are projected onto a stereographic net to show time dependent variations of vibration directions and HVSR values simultaneously. The stereographic projections for all frequency bands also show the frequency dependent variations of vibration directions and HVSR values. Based on this analysis, a modified HVSR method by considering the source energy effect is proposed to estimate amplification factor more accurately. STRs in each 100 m-UST group are analyzed in the same manner to show the frequency- and UST-depended variations of the vibration direction and HVSR values.

3.2. DATA PROCESSING

3.2.1. Color gradient map of HVSR in time-frequency domain ($HVSR(t, f)$) for LTRs

As described in Section 1.1, the HVSR spectra of time series segments of LTRs are calculated within the frequency band of 0.02-15.0 Hz, and are plotted in time-frequency (t-f) domain to create the HVSR(t,f) map. The HVSR(t,f) maps of T-1, T-2, OC 37-4, OC 37-6, and LA 1 are shown in Figure *25*, and those of the other LTRs can be found in Appendix C.

3.2.2. Transfer function between HVSR value and ocean data

The transfer function between HVSR value and ocean data is defined as:

$$Tr(t) = \frac{HVSR@f(t)}{X(t)} \tag{13}$$

where HVSR@$f(t)$ is the HVSR value at a certain frequency (f_0 or f_1) as a function of time (t), and $X(t)$ is the ocean data (significant ocean wave height, significant wind speed and atmosphere pressure) as a function of t. It should be noted that unlike the data processing described in Section 2.3.2, where the wave height and wind speed are decomposed into components aligned with the ambient noise stations, the wave height and wind speed data used to calculate the transfer functions are all raw data which are the resultant vectors along their significant traveling directions.

3.2.3. Stereographic projection of vibration vector

A single pick of microtremor time series at three directions (vertical, N-S and E-W) can define a spatial vector $\vec{M}$, where this vector can be projected as a point **A** onto a stereographic net as shown in Figure 24a. For this projection, basically, two angles are needed: 1) β, the angle

from the resultant horizontal vector $\vec{H}$ to the north, and 2) δ, the angle defined in vertical plane

from the resultant horizontal vector $\vec{H}$ to the spatial vector $\vec{M}$.

As discussed before, the spectra obtained by FFT are more meaningful to estimate the vibration direction and HVSR at various frequency bands. For this reason, in this part, the average spectral amplitudes in three directions ($V(f)$, $NS(f)$ and $EW(f)$) of each LTR segment and STR are used for stereographic projection. As the spectral amplitudes are all positive values, the projected points are all located in the first quadrant of a compass. Therefore, the two angles of each STR and LTR segment at each frequency can be estimated by the following equations:

$$\beta(f) = 90° - \varphi_e(f) \tag{14}$$

$$\delta(f) = atan\left(\frac{1}{HVSR(f)}\right) \tag{15}$$

where, $\varphi_e(f)$ is the vibration angle calculated by Eq. (8), and HVSR(f) is the horizontal to vertical spectral ratio of a time series segment calculated by Eq. (7). The angle $\beta(f)$ or $\varphi_e(f)$ reflects the vibration direction as discussed in Section 1.1.6, whereas $\delta(f)$ suggests the HVSR(f) value, i.e. when $\delta(f) < 45°$, HVSR(f) >1, and if $\delta(f) > 45°$, HVSR(f) >1.

For each segment of LTR and complete STRs in every 100m-UST group, the spatial spectral vectors calculated for each frequency band are projected as blue dots forming a cluster; and then the angles (β_R and δ_R) representing the averages of these clusters are calculated according to Eq. (16) ~ (21) (Goodman, 1989) and projected as a red dot as shown in the example in Figure 24b. In this figure, the thick solid gray circles are the isopachs of HVSR or δ values as labeled, and the dashed gray circles are the mid-value of two neighboring ispachs. The dashed gray circle greater than HVSR of 10.0 has a value of 20.0.

In order to calculate the angles (β_R and δ_R) of average spatial vector, firstly calculate the three transform factors l, m and n by Eq. (16) for each segment:

$$l = \cos \delta \cos \varphi_e \quad m = \cos \delta \sin \varphi_e \quad n = \sin \delta \tag{16}$$
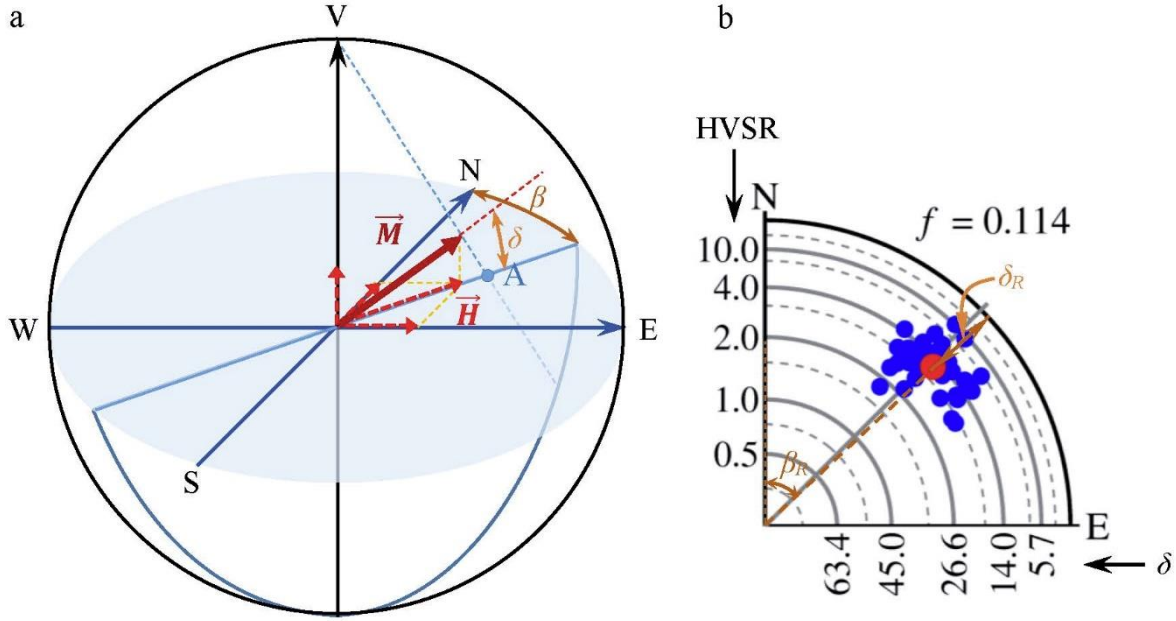

Figure 24. (a) Definition of stereographic projection of a spatial vector, and (b) an example of stereographic projection of a LTR at a specified frequency indicated in the figure.

Then find the resultant transform factors l_R, m_R and n_R:

$$l_R = \frac{\sum l_i}{|\bar{R}|} \quad m_R = \frac{\sum m_i}{|\bar{R}|} \quad n_R = \frac{\sum n_i}{|\bar{R}|} \tag{17}$$

where, i is the number of segments of a LTR, from 1 to N_s, and $|\bar{R}|$ is calculated by:

$$|\bar{R}| = \sqrt{(\sum l_i)^2 + (\sum m_i)^2 + (\sum n_i)^2} \tag{18}$$

Finally, the angles (β_R and δ_R) are given by:

$$\delta_R = arcsin(n_R) \quad 0 \leq \delta_R \leq 90° \tag{19}$$

$$\beta_R = 90° - \varphi_{eR} \tag{20}$$

where φ_{eR} is calculated by:

$$\varphi_{e_R} = arccos\left(\frac{l_R}{cos\ \delta_R}\right) \tag{21}$$

The standard deviation of the vectors of a LTR or STRs in a 100 m-UST group can be calculated as:

$$SD = \sqrt{\frac{N_S - |\bar{R}|}{N_S}} \tag{22}$$

where N_s represents (a) the total number of segments for each LTR and (b) the total number of STRs within each 100 m group.

3.3. RESULTS

3.3.1. Correlation of HVSR peaks with wave climate and local weather

To investigate the influence of ocean wave climate and local weather on HVSR, LTRs at T-2, OC 37-4, OC 37-6 and LA 1 (to be consistent with Figure 16) are selected to present variations in HVSR as shown in the top $HVSR(t,f)$ maps in Figure 16a-d. Again to be consistent, the scatter graphs of ocean wave data and local weather data as well as the time zones are exactly same as those in corresponding parts of Figure 16. The tables in parts (b), (c) and (d) are summary of correlation between ocean and local weather conditions and HVSR peaks in each time zone, in which, well correlated relationship is marked by "+" and lack of correlation is marked by "-".

1. T-1 and T-2 (Figure 25a)

The HVSR at T-1 and T-2 show broad peaks within high frequency ranges (1-4Hz) which are ten times higher than DF, and based on the observations, the correlation between the peaks and the wave climates is not obvious which is expected since their frequency ranges are totally different. Within DF range (0.1-0.6Hz), the HVSRs are very low (around 1) and not correlated with ocean and local weather. This result coincides well with the fact that T-1 and T-2 are located on bedrock where the modifications on vibrations in horizontal and vertical directions are almost identical, thus HVSR does not show any time variation of vibration sources.

2. OC 37-4 (Figure 25b)

The $PSD(t,f)$ of LTR OC 37-4 (Figure 16b and Table 6) has two distinct DF peaks (1st-DF at 0.17-0.24Hz and 2nd-DF at 0.36Hz), while the $HVSR(t,f)$ (Figure 25b and Figure 9g) just

show one sharp peak stably at $f_0 = 0.29$Hz which is within DF ranges. However, the peak value of HVSR (HVSR@f_0) varies with time significantly, which is also correlated well with ocean data and local weather as shown in Figure 25b. Within time zone ③ and ④, the change of ocean wave height, wind speed and pressure might cause the HVSR peak increases significantly.

3. OC 37-6 (Figure 25c)

Same as OC 37-4, the HVSR peak of recording OC 37-6 appears constantly at $f_0 = 0.29$Hz within both quiet time zone ① and noisy time zone ② and ③, while during noisy time, the HVSR@f_0 value is obviously higher than that during quiet time. In addition, a new finding is even though the DF peaks of OC 37-6 are broad and flat sometimes (Figure 16c and Table 6), the HVSR peak at f_0 is always very sharp. This result suggests that the top soil at OC modifies the vibrations by most different ways on horizontal and vertical directions within a very narrow frequency band where f_0 is in, and the time variation of vibration source is presented by the variation of HVSR@f_0.

4. LA 1 (Figure 25d)

At LA 1, several HVSR peaks at various frequency bands can be observed in *HVSR(t,f)* map (Figure 25d), of those the first peak is at $f_0 = 0.130$Hz which is more identifiable during night time (0:00 - 7:00) and the second peak appears at $f_1 = 0.237$Hz which is always clear during the recording time.

Variations of the ocean and local weather conditions are not that obvious during the recording period, and HVSR peaks do not vary significantly. However, slight variations can be observed as well as rough correlation between HVSR@f_0 and ocean and local weather condition.

a) T-1 (left) and T-2 (right)
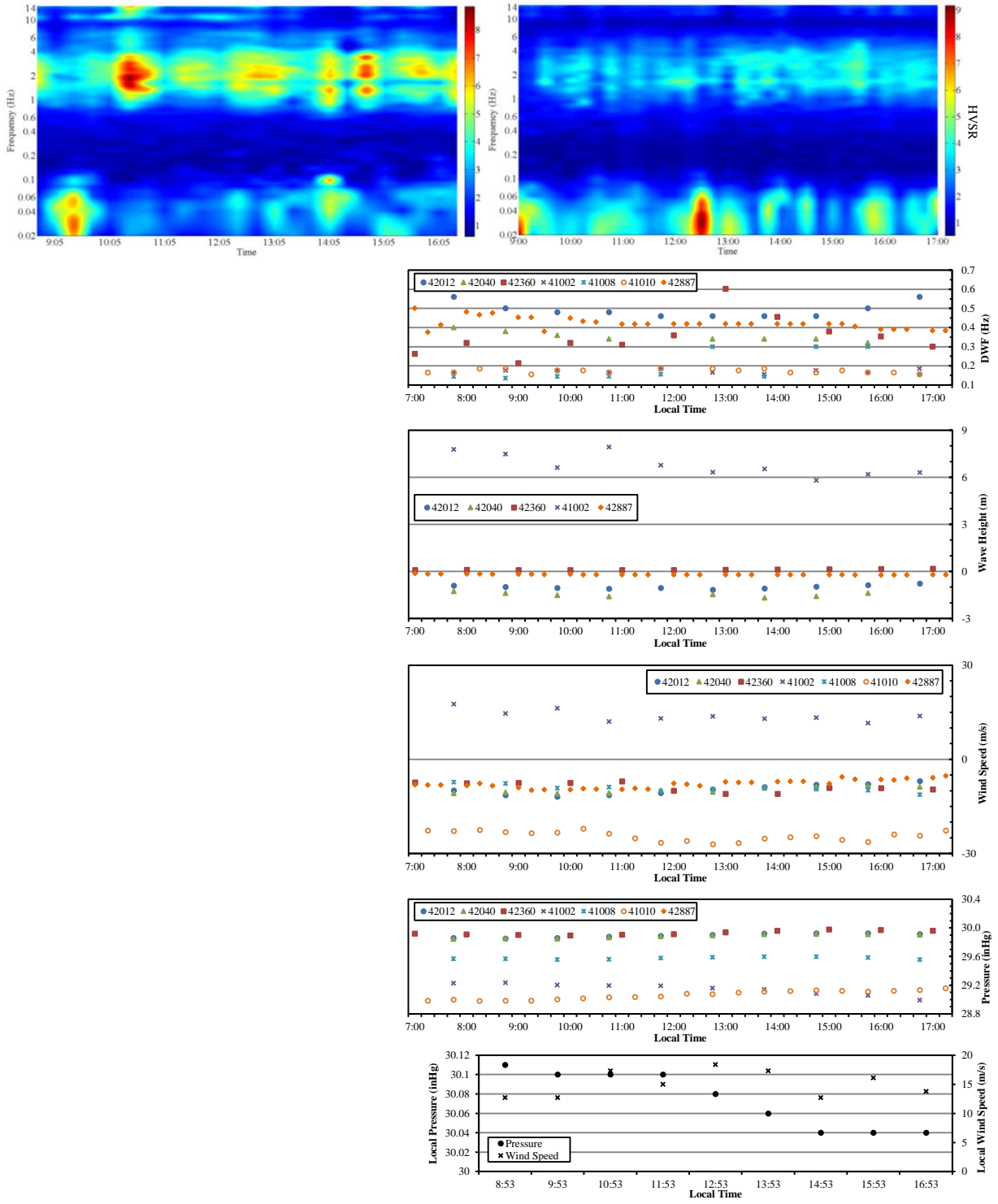
b) OC 37-4
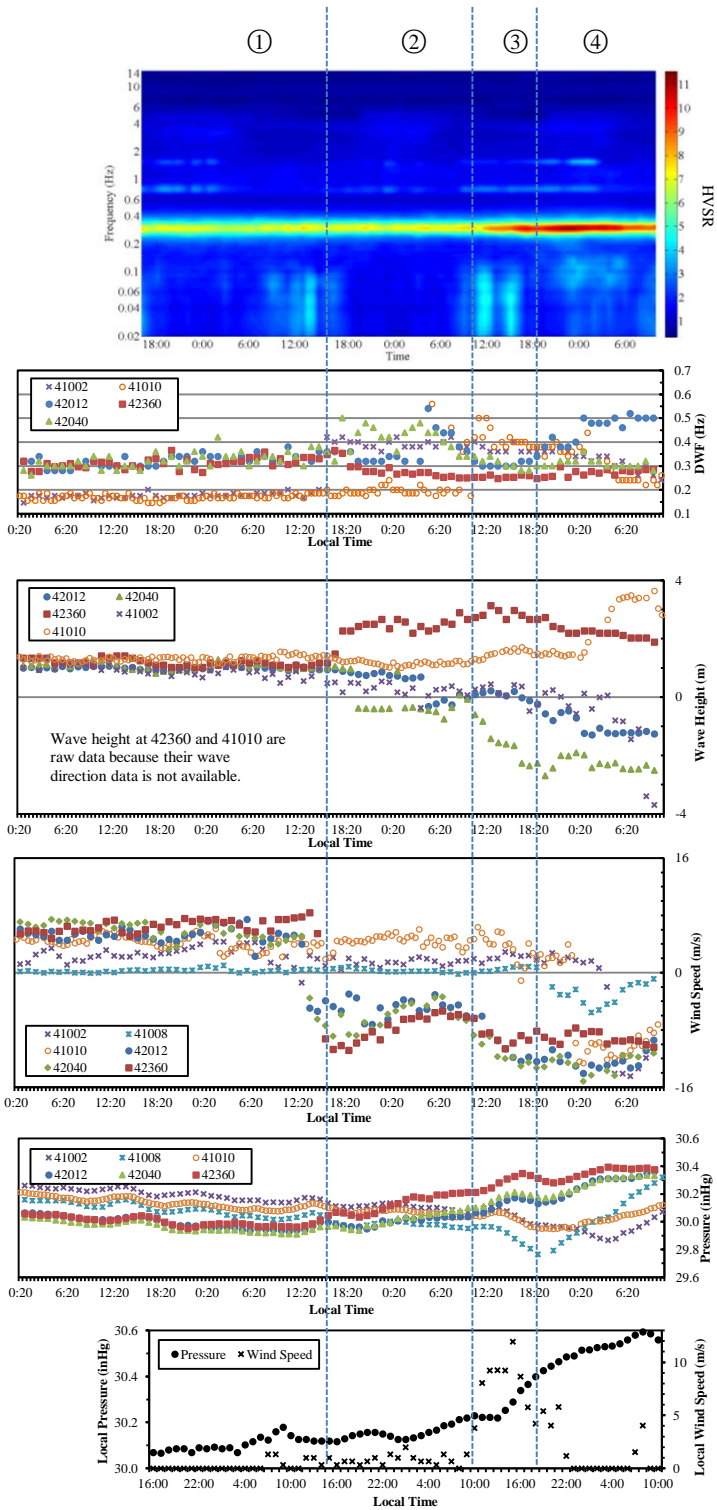
Wave height

Station	①	②	③	④
41002	+	-	-	-
41010	-	-	-	-
42012	+	-	-	+
42040	+	-	+	+
42360	-	+	+	+

Wind Speed

Station	①	②	③	④
41002	-	-	-	-
41008	+	+	+	+
41010	-	-	-	+
42012	+	-	-	-
42040	+	+	+	+
42360	+	+	+	+

Ocean pressure

Station	①	②	③	④
41002	+	+	+	+
41008	+	+	+	+
41010	+	+	+	+
42012	+	+	+	+
42040	+	+	+	+
42360	+	+	+	+

Local

	①	②	③	④
Pressure	+	+	+	+
Wind	-	+	+	-

Wave height at 42360 and 41010 are raw data because their wave direction data is not available.

100

c) OC 37-6
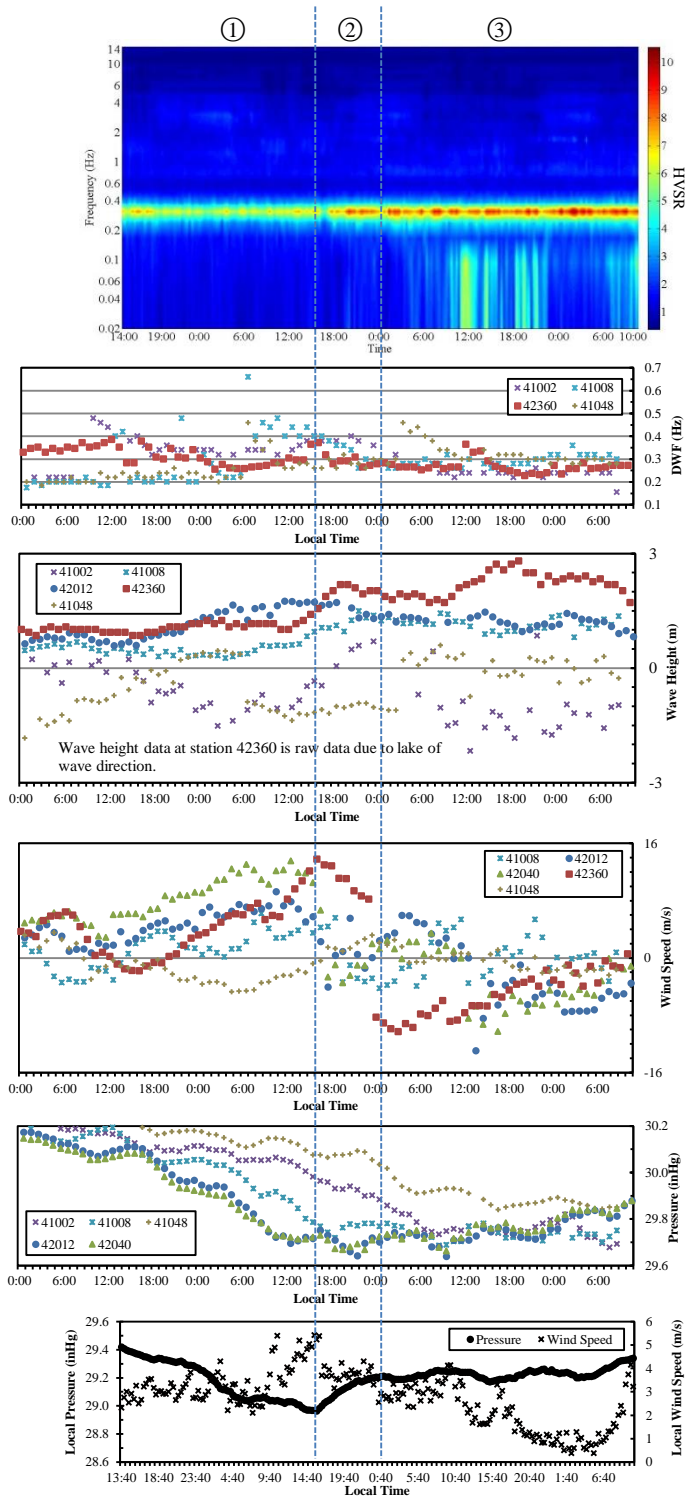
Wave height

Station	①	②	③
41002	-	-	-
41008	+	+	+
41048	-	+	-
42012	-	-	+
42360	+	+	+

Wind Speed

Station	①	②	③
41008	+	+	+
41048	-	-	-
42012	+	+	+
42040	-	-	-
42360	-	-	-

Ocean pressure

Station	①	②	③
41002	+	+	+
41008	+	-	-
41048	+	+	+
42012	+	-	-
42040	+	-	-

Local

	①	②	③
Pressure	+	+	+
Wind	+	-	-

Wave height data at station 42360 is raw data due to lake of wave direction.

101

d) LA 1
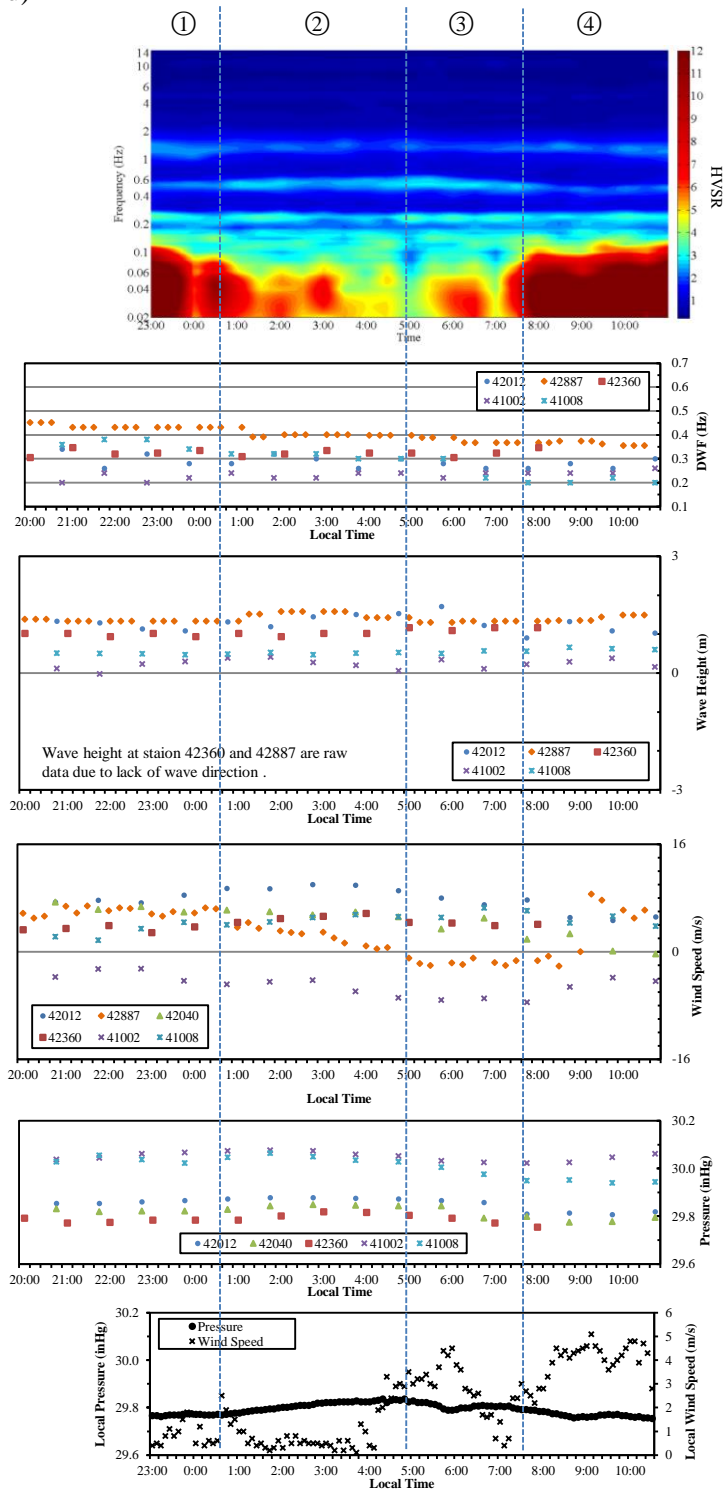
Wave height

Station	Peak	①	②	③	④
41002	f_0	+	+	+	-
	f_1	-	+	-	+
41008	f_0	+	-	-	-
	f_1	+	-	+	+
42012	f_0	+	+	+	-
	f_1	+	-	-	-
42887	f_0	-			
	f_1	+	+	+	+
42360	f_0	-	+	-	
	f_1	+	-	+	

Wind Speed

Station	Peak	①	②	③	④
41002	f_0	+	+	+	+
	f_1	-	-	+	-
41008	f_0	+	+	-	+
	f_1	-	-	-	+
42012	f_0	+	-	-	+
	f_1	-	+	-	-
42040	f_0	+	+	-	-
	f_1	+	-	-	-
42887	f_0	+	-	+	+
	f_1	-	+	+	+
42360	f_0	+	+	-	
	f_1	-	+	-	

Ocean pressure

Station	Peak	①	②	③	④
41002	f_0	+	-	-	-
	f_1	-	+	-	-
41008	f_0	+	+	-	+
	f_1	+	+	-	-
42012	f_0	-	-	-	+
	f_1	+	+	-	+
42040	f_0	+	+	-	-
	f_1	-	-	-	+
42360	f_0	+	+	-	
	f_1	-	+	-	

Local

	Peak	①	②	③	④
Pressure	f_0	+	+	+	+
	f_1	-	+	-	+
Wind	f_0	-	+	-	-
	f_1	-	-	-	+

$f_0 = 0.130\text{Hz}$
$f_1 = 0.237\text{Hz}$

Figure 25. (1) Color gradient maps in part (a) showing distribution of HVSR in time-frequency (t-f) space at T-1 (left) and T-2 (right); (2) color gradient maps in parts (b), (c) and (d) showing distribution of HVSR in t-f space at OC 37-4, OC 37-6 and LA 1 respectively; (3) scatter graphs in parts (a), (b), (c) and (d) and insert tables in parts (b), (c) and (d) are same as those in corresponding parts of Figure 16.

3.3.2. Transfer function between HVSR and ocean data

From Figure 25, it is evident that time variations of HVSR values at f_0 (HVSR@f_0) and/or f_1 (HVSR@f_1) are roughly correlated with ocean data. However it will be more helpful for improving estimates of amplification factor from HVSR values if transfer functions are established. For this reason, Figure 26 is made to present the transfer functions of HVSR values at a) f_0 at OC 37-4, b) f_0 at OC 37-6, c) f_0 at LA 1, and d) f_1 at LA 1 and ocean data (-1: wave height, -2: wind speed and -3: pressure) observed at the selected ocean observation stations.

If HVSR@f_0 is perfectly correlated with ocean data, then the transfer functions become constants with no time variation. Otherwise time variations can be simulated by numerical models, from which the transfer functions are derived. The transfer functions of OC 37-4 are all within relatively narrow bands, which differ with respect to the types of ocean data, and recording locations of microtremor and ocean data. For example, at OC 37-4, the values of transfer functions of HVSR@f_0 and 1) ocean wave height (Figure 26a)-1) are within 2-10; 2) wind speed (Figure 26a)-2) are within 0.5-2; and 3) pressure (Figure 26a)-3) are within 0.2-0.4. Similar observations can be found at recordings OC 37-6 (Figure 26b) and LA 1 (Figure 26c and d). Meanwhile, the transfer functions of HVSR@f_0 and wave height at station 42360 in Gulf of Mexico are very similar between OC 37-4 and OC 37-6.

Within the three ocean wave factors (wave height, wind speed and pressure), pressure is the one for which transfer functions show least variation with location of ocean stations (Figure 26a-3, b-3, c-3 and d-3). Since the ocean wind and wave are all activated due to the change of air pressure and its spatial variation, it is not surprising that the transfer functions of HVSR@f_0 and pressure form narrower bands.

Considering that for a certain type of ocean data, e.g. wave height, the transfer functions are more concentrated during quiet periods (e.g., within time zone ① at OC 37-4 and OC 37-6) regardless of ocean data location, differences between the transfer functions must be largely due to noisy (high ocean activity) periods (as for other time zones at OC 37-4 and OC 37-6).

It can be stated that at large distances from the source(s), changes in HVSR@f_0 can be directly related to variations in the energy of the vibration source, which is ocean waves in this case. It follows that the HVSR@f_0 as a proxy of site amplification factor largely vary with the source energy level at large distances. This variation is shown to be significant in subsequent sections.

3.3.3. Stereographic projections

Stereographic projections of microtremor spectral vectors are carried out at 100 discrete frequencies logarithmically evenly distributed within 0.02-15 Hz range for all LTRs and all STRs in each 100m-UST interval. Examples of these projections at several selected frequencies (covering low, medium and high frequencies) of LTRs and STRs are presented in Figure 27 and Figure 28. (The full projections of all LTRs and STRs are attached in Appendix F.)

1. LTRs

As these projections in Figure 27 shown, in one recording, the clusters formed by the projected points differ in shape and position in different frequency ranges:

- In the low frequency range (< 0.1 Hz), both β and δ angle form wide ranges, which indicates that the vibration sources (estimated according to β angle) and HVSR value (suggested by δ angle) vary significantly with time without an obvious correlation.

- Within the DF range, indicated by blue dashed box in Figure 27, especially at the predominant frequency f_0 (red box in Figure 27), the clusters are more concentrated than the low frequency range, which suggests the presence of a specific energy source. Within the area where UST > 200 m, the cluster forms a wider range in β dimension than in δ dimension, which confirms that location or direction of the vibration source do not noticeably influence the HVSR@f_0 values, but the local geological conditions and source energy levels do (see discussion on the transfer functions).

- Within the "holu" frequency range (around 0.6 Hz), the clusters mostly vary in δ dimension, which suggests that the specified vibration sources changes in their energy levels.

- Within the high frequency range (>1.0 Hz), a) for T-2 recorded on bedrock and only during day time, location and energy of vibration source vary with time, which produces a scattered cluster; b) for the others recorded during night time or during a quiet period of day time, the clusters are mostly very concentrated, probably varying in δ dimension; and c) the vertical amplitude is larger than the horizontal amplitude at most recordings since δ angles are mostly larger than 45 °.

2. STRs

Figure 28 presents stereographic projections for several frequency ranges of STRs grouped by their locations in 100m UST intervals. The following observations can be obtained.

- Within low frequency (<0.1 Hz), similar to LTRs, the clusters formed by the spectral vectors of STRs cover wide range in both β and δ dimensions, which agrees that the vibration sources in this range are uncertain.

- Within the DF ranges, patterns of the clusters vary with UST values. In low UST range, the clusters are more scattered in δ dimension suggesting significant variations in the energy level and a lack of noticeable modification of this energy by the sediments. As UST increases, the energy modification becomes more obvious as the clusters cover a wider range in β dimension while becoming narrower in δ dimension. This supports the notion that the variations in energy level is less important at large UST values, where sediment modification dominates the HVSR values.

- Within the high frequency range, except in the lowest UST ranges (Figure 28a and b) where the f_0 is located at the high frequency range, the clusters show random patterns, indicating that the sediments have a very limited modifying effects on the energy components in this frequency range.

- Furthermore, from these stereographic projections for various frequency bands, the f_0 of each UST range can be identified easily by comparing the locations of these clusters. If these projections are produced on a denser array of discrete frequencies, estimates of f_0 would be more accurate, as shown in Figure F-2 in Appendix F.
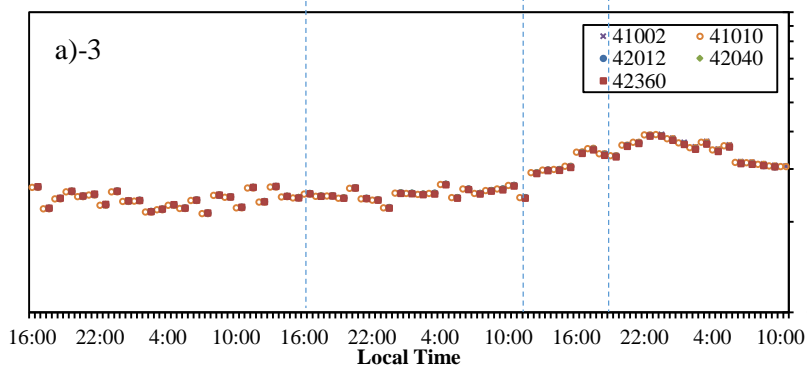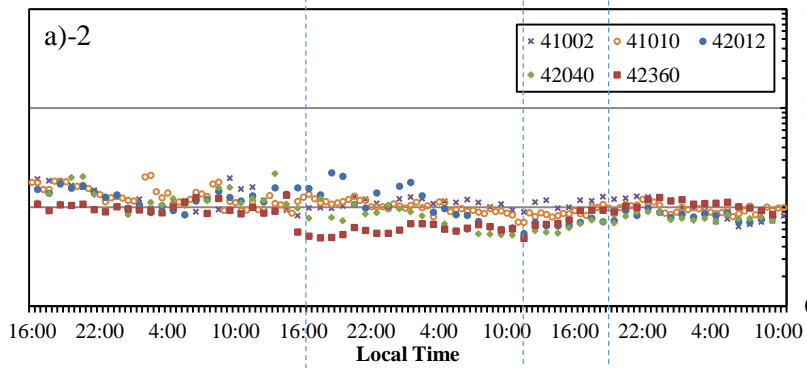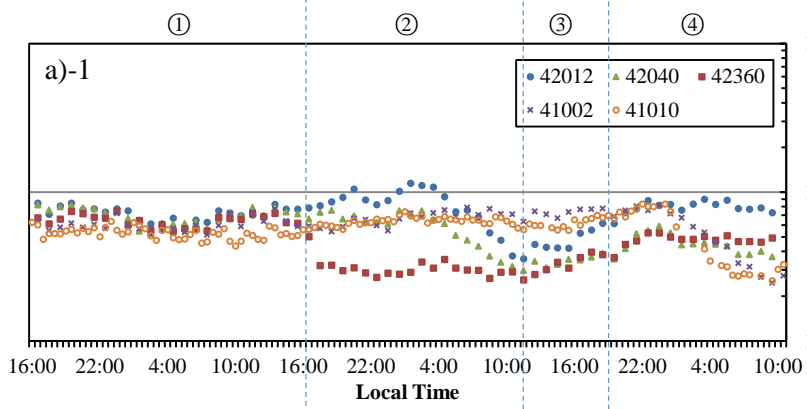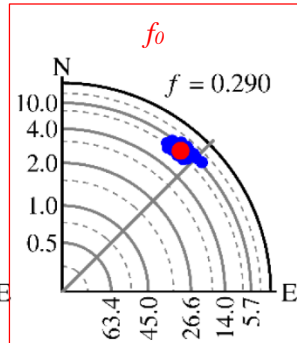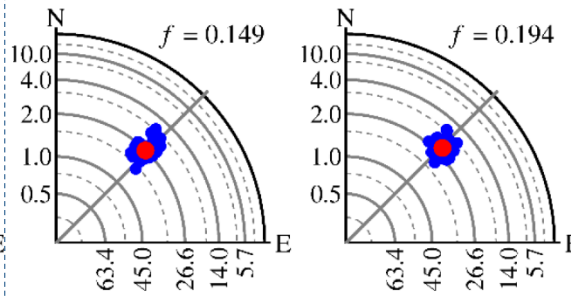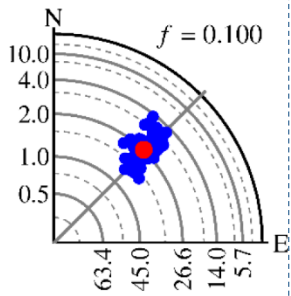
a) OC 37-4, at f_0
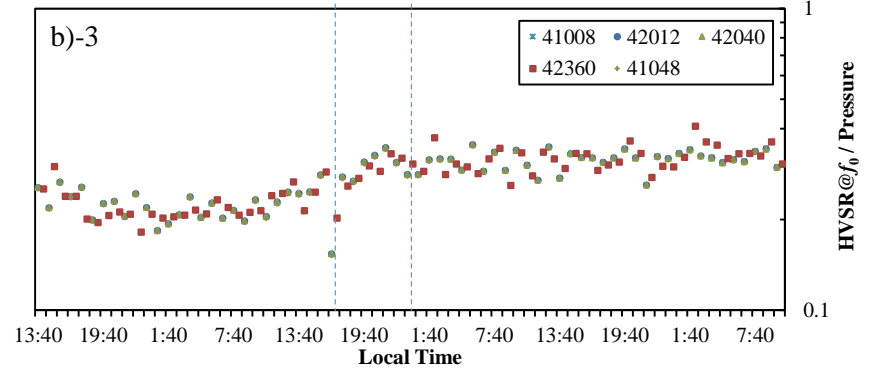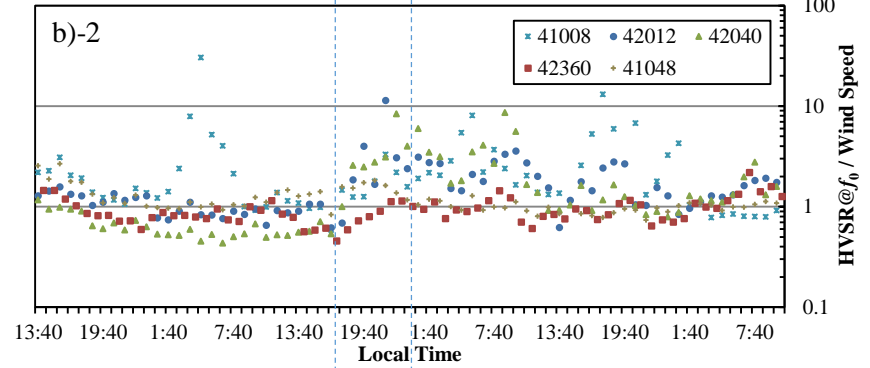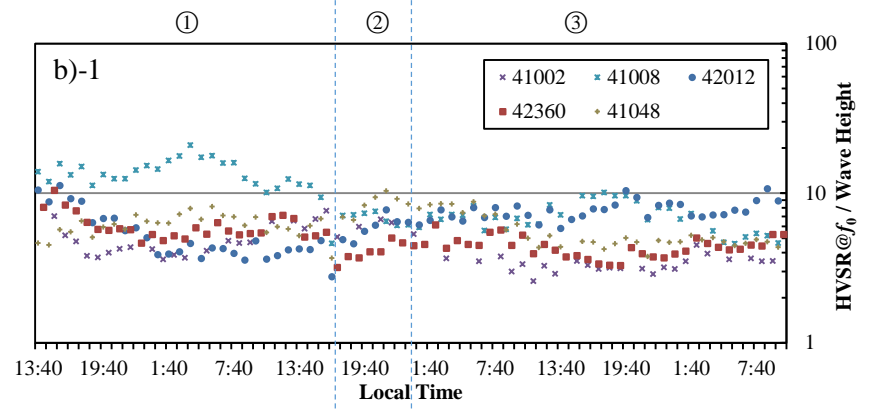
b) OC 27-6, at f_0
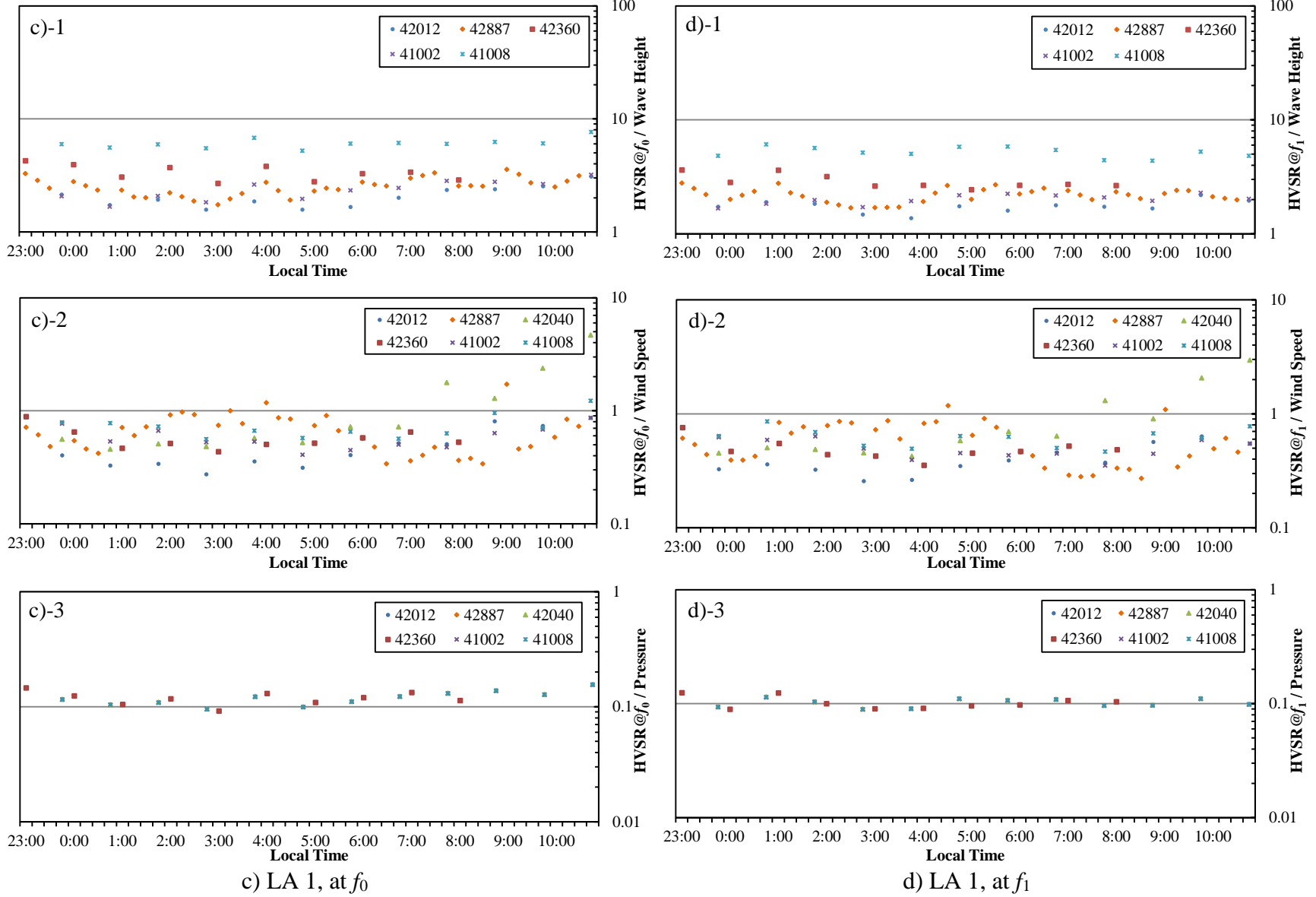
Figure 26. Transfer functions between HVSR@f_0 of (a) OC 37-4, (b) OC 37-6, (c) LA 1, and HVSR@f_1 of (d) LA 1 and ocean data.
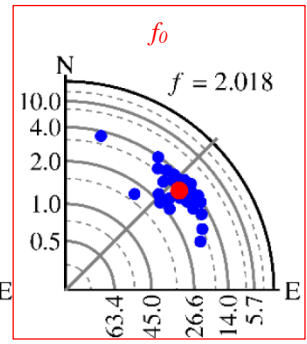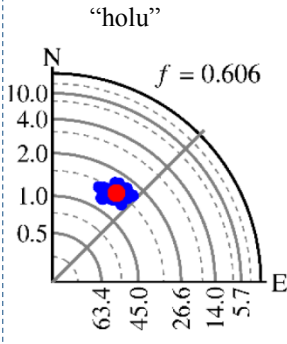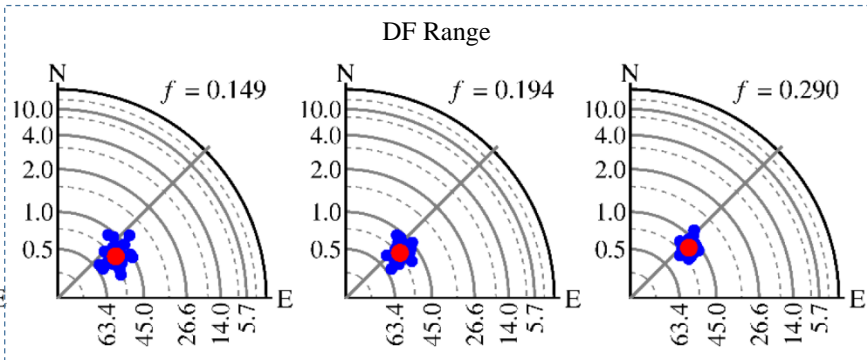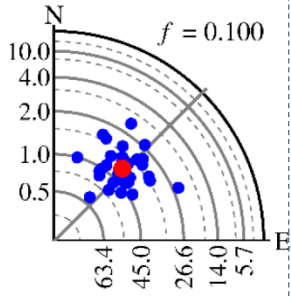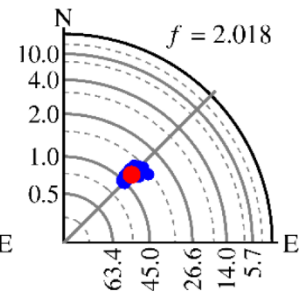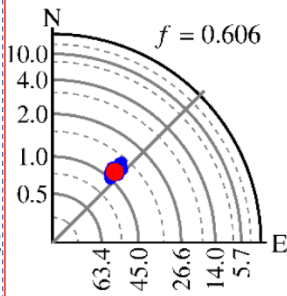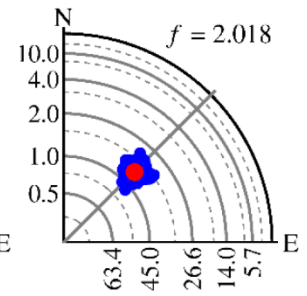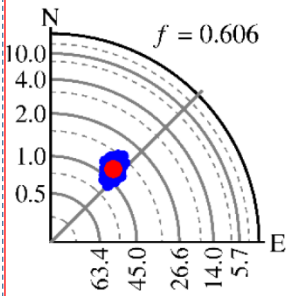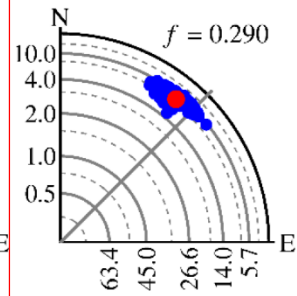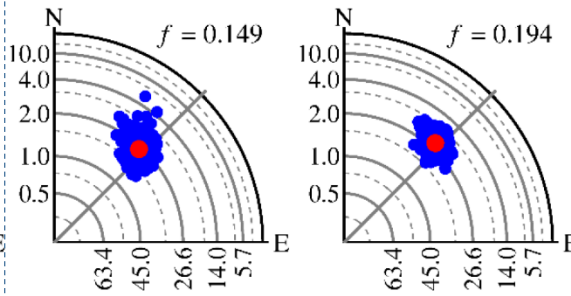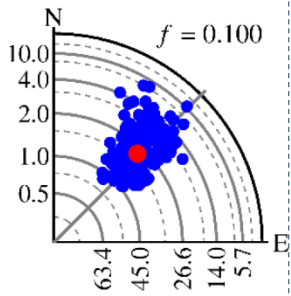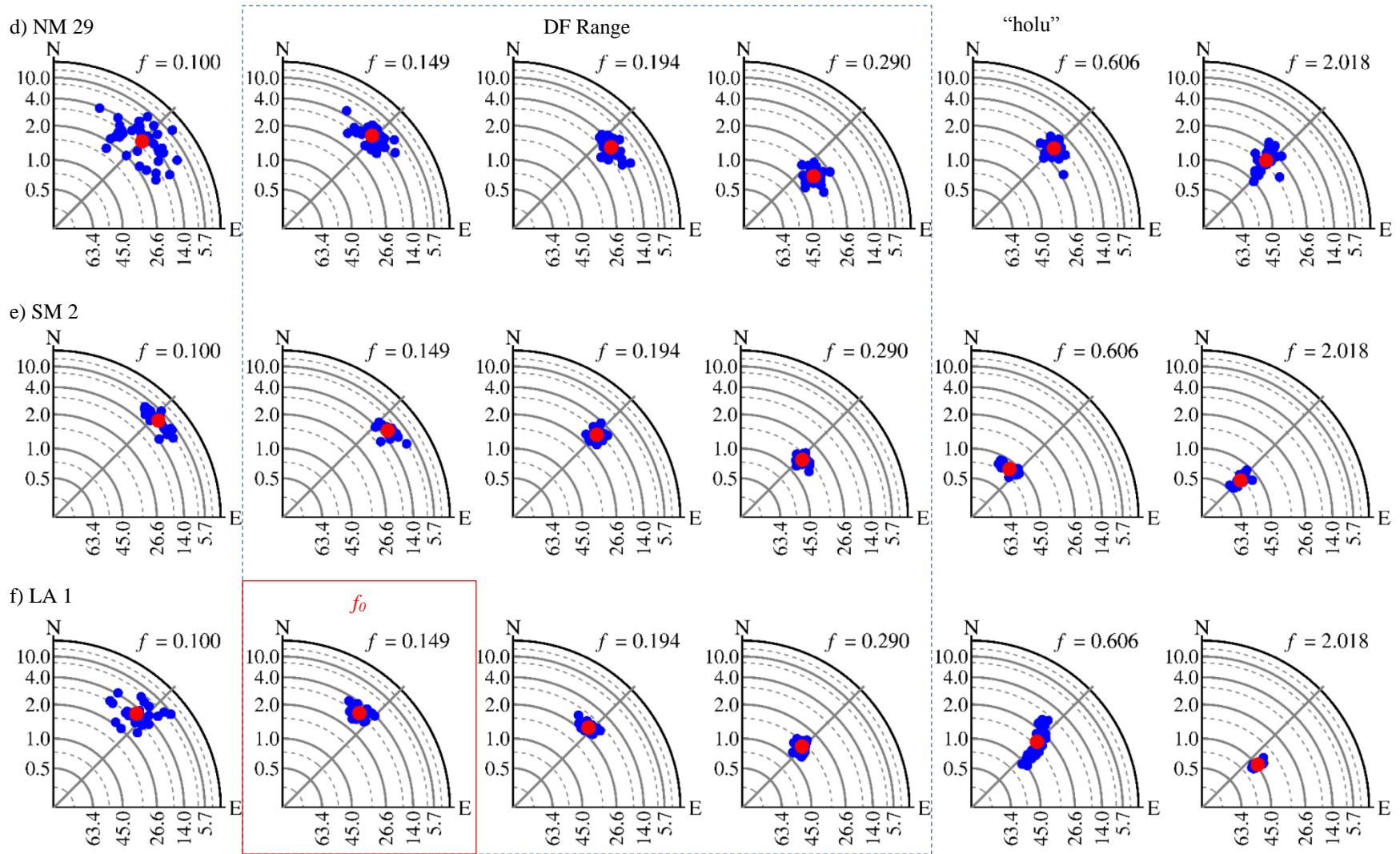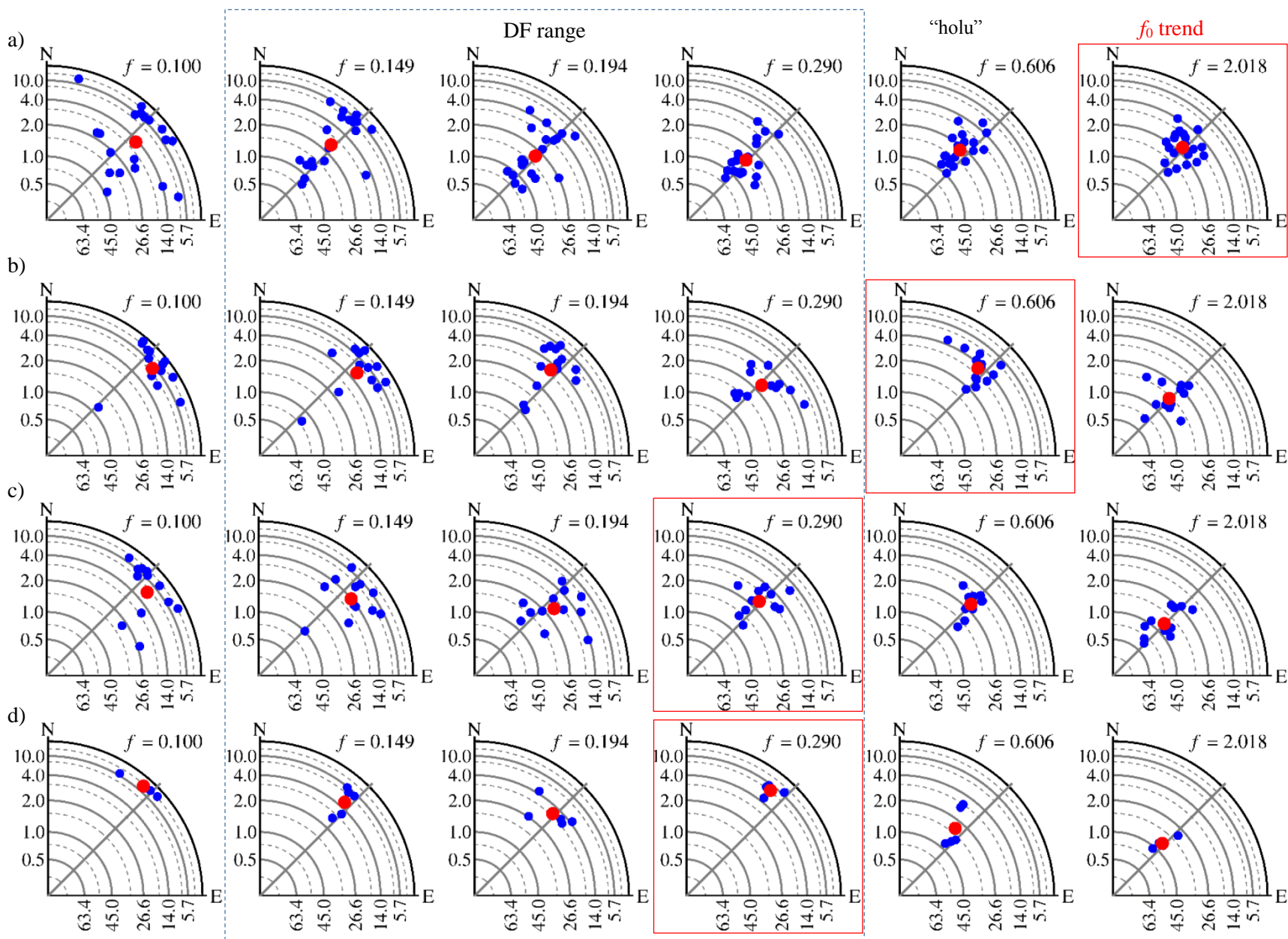
Figure 27. Stereographic projection of LTRs of (a) T-2, (b) OC 37-4, (c) OC 37-6, (d) NM 29, (e) SM 2 and (f) LA 1. The DF range is indicated by dashed blue box and f_0 of each LTR is indicated by red box.
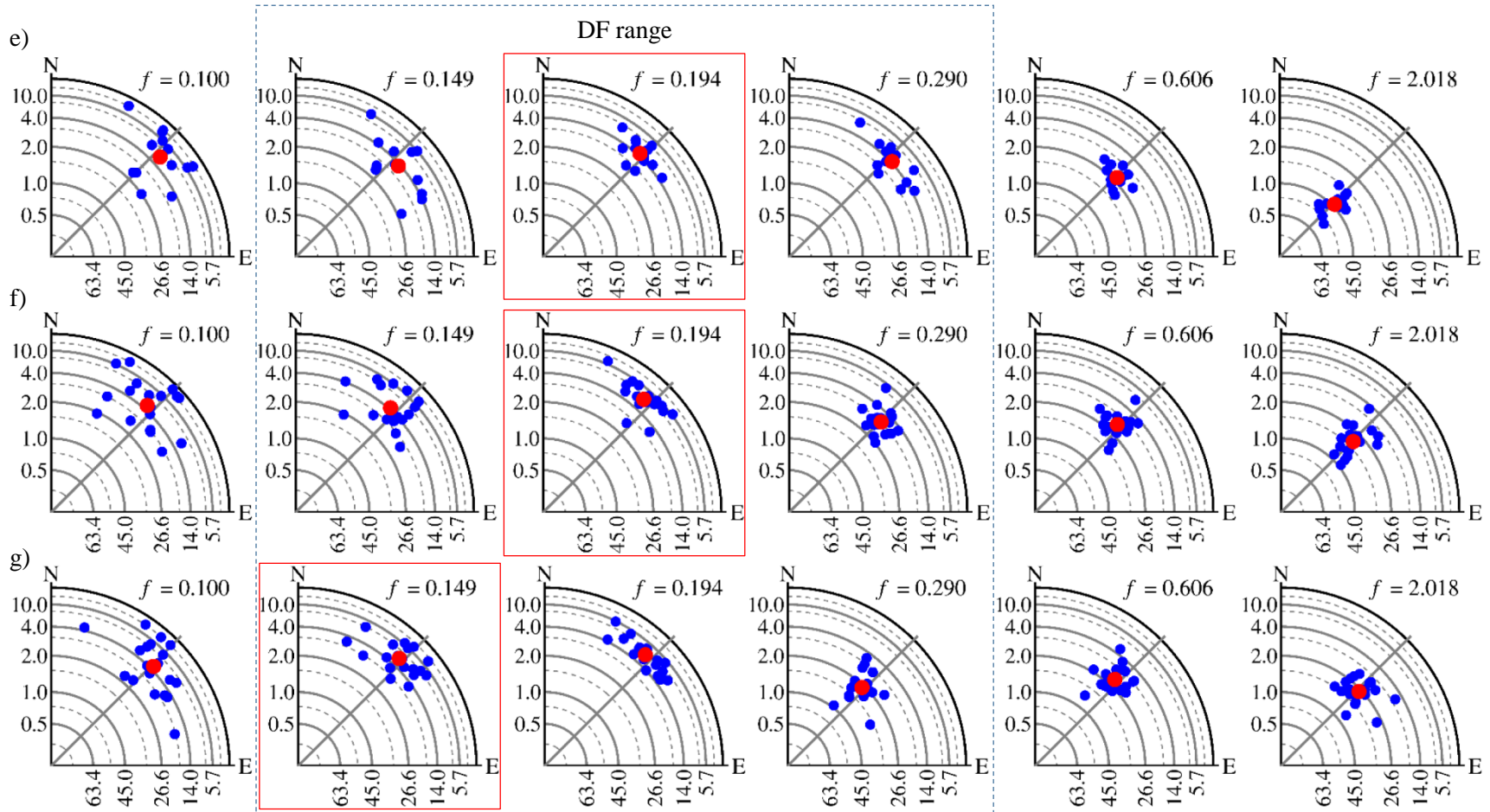
Figure 28. Stereographic projections of STRs grouped by UST range, (a) 0-100m, (b) 200-300m, (c) 400-500m, (d) 600-700m, (e) 800-900m, (f) 1000-1100m, and (g) 1200-1300m.

3.4.   DISCUSSION AND CONCLUSION

As an easy and fast method, HVSR method also proved to be reliable in estimating site effects parameters, especially the predominant frequency, by numerous researchers all over the world. However, this method's estimate of amplification factor is still being questioned but the cause of inconsistencies is not well known. This study revealed that the amplification factor is time-dependent which explains the lack of reliable estimates of this site effect variable.

As the correlation analysis and the transfer function between HVSR@f_0 and wave climate in Sections 3.3.1 and 3.3.2 show, the HVSR@f_0 is related to the energy level of the vibration source (ocean activities) within the area where UST > 300m in Northern Mississippi. However, as shown in Figure 27 and Figure F-1 in Appendix F, the shape of the cluster formed by stereographic projection reflects both time and frequency dependent variations in both vibration direction and HVSR values, which is uniquely helpful in understanding how the vibration source influences the HVSR values, especially HVSR@f_0.

As shown by the stereographic projections of LTRs (Figure 27 and Figure F-1 in Appendix F), even though most clusters at f_0 (indicated by red box) have very narrow ranges in δ dimension, the time variation of δ is still obvious indicating that energy level of the vibration sources vary in time. Therefore, in order to obtain a more accurate estimation of amplification factor, the variation of HVSRs caused by the variation of energy level of vibration source has to be minimized.

Within these clusters, the red dot is the average spatial vector of LTRs, which also takes the source location or direction and the time-dependent variations of the energy level into

consideration. Therefore, the HVSR value estimated by this point is a more reliable and accurate estimation of amplification factor, given by:

$$HVSR_R = \frac{1}{\tan \delta_R} \tag{23}$$

where δ_R is the angle from the resultant horizontal vector to the average spatial vector, calculated by Eq. (19).

Applying this method, the amplification factors for LTRs with identified f_0 values are listed in Table 8, together with the two angles defining average spatial spectral vectors (β_R and δ_R) and the standard deviations (SD) of these vectors.

Table 8. Summary of predominant frequency (f_0) and amplification factors calculated by modified HVSR method.

Recording points		f_0	β_R	δ_R	HVSR@f_{0R}	SD
T-1		2.018	46.4 °	11.5 °	4.92	0.085
T-2		2.466	47.4 °	17.1 °	3.25	0.107
NM 14		0.967	45.3 °	16.6 °	3.35	0.076
OC	37-1	0.290	41.5 °	5.9 °	9.68	0.056
	37-2	0.290	52.1 °	7.1 °	8.03	0.026
	37-3	0.290	38.7 °	7.7 °	7.40	0.051
	37-4	0.290	40.1 °	7.1 °	8.03	0.029
	37-5	0.290	38.4 °	6.0 °	9.51	0.040
	37-6	0.290	39.0 °	7.1 °	8.03	0.052
	38	0.290	35.1 °	7.3 °	7.81	0.031
NM 29		0.170	44.7 °	13.3 °	4.23	0.068
SM 1		0.130	45.5 °	8.4 °	6.77	0.096
LA 1		0.130	38.1 °	16.1 °	3.46	0.046
SD: standard deviation of the vectors of a LTR.						

DISCUSSION AND CONCLUSIONS

4.1. DISCUSSION

4.1.1. Wind effect

Considering the vibration sources within frequency bands related to the objectives of this research, wind plays an important role in defining spectral characteristics as the vibrations are caused either directly or indirectly by wind on land or above the ocean. For the local wind effects (discussed in section 1.3.2), on the other hand, the HVSR show extremely high amplitudes within the low frequency range (< 0.2 Hz). This is mainly because of the direct exposure of the seismometer to wind during field recordings (STR-Is). Even though the seismometer was protected from direct wind by a plastic box during some recordings (STR-IIs), high amplitudes within the low frequency band (< 0.2 Hz), especially in horizontal component, can still be observed. This is believed to be caused also by wind through other mechanisms, as confirmed by good correlations between estimated vibration angles φ_e and wind directions as shown in Figure 11.

Within the double frequency (DF) range, good correlation between the PSD levels of DF peaks and the ocean data (significant wave height, ocean wind speed, atmosphere pressure) supports the notion that the DF microseism is mainly caused by the ocean waves (Figure 16). A strong correlation between the significant ocean wave height and the ocean wind speed is consistent with the fact that ocean wave is excited by ocean wind. This is why the horizontal component of the DF peaks consistently rotates with tracks of ocean storms.

Within the DF range, neither the PSD levels of the DF peaks nor the HVSR@f_0 are correlated well with the local wind speed, but instead with the local atmospheric pressure (Figure 16). Comparing the atmospheric pressures over the microtremor recording locations and the

116

ocean observation stations, it is very obvious that, even though their magnitudes are different, their trends are quite consistent. In this sense, the PSD levels of the DF peaks and the HVSR@f_0 are both correlated with the atmospheric pressures above the ocean and around the recording point. Therefore, variations in the atmospheric pressure might be the main reason for variations of the PSD level at DF peak and HVSR@f_0. However it is difficult to clearly determine the vibration source within this frequency range, as the wind can also play this role due to the difference on land and ocean.

4.1.2. DF microseism and HVSR peak

As discussed in Part II, differences in horizontal and vertical directions of shear wave resonance and attenuation provide empirical support to the validity of the HVSR method for determining the predominant frequency. In Northern Mississippi area where UST > 200 m, the predominant frequency is within the DF range. Even though the frequency and energy level of the DF peak are tightly related to the frequency and energy level of the ocean waves (as it is considered as the energy source of the DF peak), the shear wave resonance in the sediments modifies the frequency of DF peak bringing it closer to the predominant frequency of the sediments in horizontal direction, but not in vertical direction. However this modification does not affect the observations of variations in energy level of ocean wave, which makes it possible to correlate the HVSR@f_0 with the ocean wave. In this sense, it is essential to consider the variation of microtremor source when the amplification factor is being estimated by HVSR method.

4.2. CONCLUSIONS

This study presents 15 continuous long-term microtremor (ambient noise) recordings at 8 (including 6 inland and 2 coastal) locations in Mississippi, Louisiana and Alabama States, and a total of 305 systematic single-point short-term recordings in Northern Mississippi area. On these recordings, (1) horizontal to vertical spectral ratio (HVSR) method is applied to estimate the site effect parameters (predominant frequency f_0 and amplification factor); (2) power spectral density (PSD) is calculated to compare the energy level to the NLNM and NHNM and other recordings at different locations; (3) particle motion and vibration angles at various frequency band are calculated to trace the vibration source; (4) PSD level within double-frequency (DF) and HVSR value at f_0 (HVSR@f_0) are correlated with ocean wave climate (significant wave frequency, significant wave height, ocean wind speed, atmosphere pressure and local wind speed and pressure) to estimate the possible vibration sources at DF and f_0; (5) stereographic projection is used to project the microtremor spatial spectral vectors at various frequency bands and average spectral vector at f0 are calculated to improve the estimation of amplification factor for long-term recordings.

4.2.1. General conclusions

1. Microtremor, as a stationary stochastic process, can provide a stable and reliable estimation of the predominant frequency (f_0). However, the amplification factor estimated by HVSR method fluctuates with the energy level of the vibration sources at f_0. Therefore, a modified HVSR method based on stereographic projection is proposed to eliminate the influence from variation of vibration sources in estimating amplification factor.

2. Wind as a natural source and human activities can significantly influence the HVSR in

low frequency band (< 0.2 Hz). Wind effects caused by direct exposure of seismometer to nature wind can be significantly reduced by preventing direct exposure of the seismometer.

3. Predominant frequency correlates well with unconsolidated sediment thickness.

4. Average shear wave velocity and its variation as a function of UST across a sedimentary basin can be established from systematic microtremor surveys.

4.2.2. Specific conclusions

Specific conclusions that may be valid only for the Mississippi Embayment area and in particular for Northern Mississippi are:

1. High peaks on HVSR curves in low frequency range (0.02-0.2 Hz) are caused by wind and human activities.

2. Vibration direction is strongly frequency-dependent above 0.2 Hz and time-dependent below this value.

3. The observed values of the first and second harmonics of the predominant frequencies are consistent with their theoretical values.

4. Predicted and measured values of average shear wave velocity appear to be more consistent within the UST range of 200-1000 m.

5. The DF microseism is possibly a combined product of both wave climates of Atlantic Ocean and Gulf of Mexico.

6. The shear wave resonance modifies the DF and PSD level at DF more significantly in horizontal direction than in vertical direction in parts of the study area where UST > 200 m.

119

7. The attenuation of the DF microseism in vertical direction is more obvious since in horizontal direction the shear wave resonance may offset the attenuation effect on the DF microseism.

LIST OF REFERENCES

Arai H. and K. Tokimatsu, 2004. S-wave velocity profiling by inversion of microtremor H/V spectrum. *Bulletin of the Seismological Society of America*, 94, 53-63.

Ali, M. Y., K. A. Berteussen, J. Small and B. Barkat, 2010. Low-frequency passive seismic experiments in Abu Dhabi, United Arab Emirates: implications for hydrocarbon detection. *Geophysical Prospecting*, 58, 875-899.

Angelis, S. D. and P. Bodin, 2012. Watching the wind: seismic data contamination at long periods due to atmospheric pressure-field-induced tilting. *Bulletin of the Seismological Society of America*, 102, 1255-1265.

Babcock, J., B. Kirkendall and J. Orcutt, 1994. Relationship between ocean bottom noise and the environment. Bulletin of the Seismological Society of America, 84, 1991-2007.

Bard, P.-Y., 1999. Microtremor measurements: A tool for site effect estimation? In: *Proc. 2nd Int. Symp. on the Effects of Surface Geology on Seismic Motion*, Yokohama, Japan, 1251-1279.

Bard, P.-Y. & SESAME-Team, 2005. Guidelines for the implementation of the H/V spectral ratio technique on ambient vibrations-measurements, processing and interpretations. SESAME European Research Project EVG1-CT-2000-00026, D23.12.

Bendat, J. S. and A. G. Piersol, 1971. Random data: analysis and measurement procedures. Wiley-interscience, New York

Beroya, M.A.A., A. Aydin, R. Tiglao and M. Lasala, 2009. Use of microtremor in liquefaction hazard mapping. *Engineering Geology*, 107,140-153.

Bodin, P., K. Smith, S. Horton, et al, 2001. Microtremor observation of deep sediment resonance in metropolitan Memphis, Tennessee. *Engineering Geology*, 62, 159-168.

Bonnefoy-Claudet, S., S. Baize, L. F. Bonilla, C. Berge-Thierry, C. Pasten, J. Campos, P. Volant, and R. Verdugo, 2008. Site effect evaluation in the basin of Santiago de Chile using ambient noise measurements. *Geophys. J. Int.*, 1-13.

Borcherdt, R. D., 1976. Effects of local geological conditions in the San Francisco Bay region on ground motions and the intensities of the 1906 earthquake. *Bulletin of the Seismological Society of America*, 66, 467-500.

Borcherdt, R. D., G. Glassmoyer, A. D. Kiureghian and E. Cranswick, 1989. Results and data from seismologic and geologic following earthquakes of December 7, 1988 near Spitak, Armenia, S.S.R. *U.S. Geol. Surv. Open-File Rept*. 89-163A.

Bromirski, P. D., R. E. Flick and N. Graham, 1999. Ocean wave height determined from inland seismometer data: Implications for investigating wave climate changes in the NE Pacific. *J. Geophys. Res.*, 104, 20753-20776

Bromirski, P. D., F. K. Duennebier and R. A. Stephen, 2005. Mid-ocean microseisms. *Geochemistry Geophysics Geosystems*, 6, Q04009, doi: 10.1029/2004GC000768.

Brooks, L. A., J. Townend, P. Gerstoft, S. Bannister and L. Carter, 2009. Fundamental and higher-mode Rayleigh wave characteristics of ambient seismic noise in New Zealand. Geophysical Research Letters, 36, L23303.

Cessaro, R. K., 1994. Sources of primary and secondary microseisms. Bulletin of the Seismological Society of America, 84, 142-148.

Chatelain, J.-L., B. Guillier, F. Cara, et al, 2008. Evaluation of the influence of experimental conditions on H/V results from ambient noise recordings. *Bulletin of Earthquake Engineering*, 6, 33-74.

Chevrot, S., M. Sylvander, S. Benahmed, et al, 2007. Source locations of secondary microseisms in western Europe: Evidence for both coastal and pelagic sources. Journal of Geophysical Research, 112, B11301.

Cushing, E. M., E. H. Boswell and R. L. Hosman, 1964. General Geology of the Mississippi Embayment, Department of the Interior. Geological survey professional paper, 448-B, U.S. United States Government Printing Office, Washington

Dorman, L. M., A. E. Schreiner, L. D. Bibee and J.A. Hildebrand, 1993. Deep-water seafloor array observations of seismo-acoustic noise in the eastern Pacific and comparisons with wind and swell. In: *Natural Physical Source of Underwater Sound*, edited by B. Kerman, Springer, New York, 165-174.

Dravinski, M., H. Yamanaka, Y. Nakajima, H. Kagami, R. Keshavamurthy and K. Masaki, 1991. Observation of Long period Microtremors in San Francisco Metropolitan Area. *Fourth International Conference on Seismic Zonation*, Stanford, California, USA, August, 401-407.

Ebeling, C. W., 2012. Inferring ocean storm characteristics from ambient seismic noise: a historical perspective. Advances in Geophysics, 53, doi: http://dx.doi.org/10.1016/B978-0-12-380938-4.00001-X

Essen, H.-H., F. Krüger, T. Dahm and I. Grevemeyer, 2003. On the generation of secondary microseisms observed in northern and central Europe. Journal of Geophysical Research, 108, B10, 2506, doi: 10.1029/2002JB002338.

Goodman, R. E., 1989. Introduction to Rock Mechanics. Wiley New York, 2nd edition, 562 pp.

Guo, Z., A. Aydin and J. Kuszmaul, 2014. Microtremor recording in Northern Mississippi. *Engineering Geology*, 179, 146-157.

Ibs-von Seht, M. and J. Wohlenberg, 1999. Microtremor measurements used to map thickness of soft sediments. *Bulletin of the seismological society of America*, 89, 250-259.

Haubrich, R. A. and K. McCamy, 1969. Microseisms: coastal and pelagic sources. *Review of Geophysics*, 7, 539-571.

Havskov, J. and L. Ottemöller, 2010. Routine data processing in earthquake seismology. Springer New York, 347 pp.

Hough, S. E., R. D. Borcherdt, P. A. Friberg, R. Busby, E. Field and K. H. Jacob, 1990. The role of sediment-induced amplification in the collapse of the Nimitz freeway during the October 17, 1989 Loma Prieta earthquake. *Nature*, 344, 853-855.

Jiang, H., 2005. Study on site effects of stochastic simulation of earthquake ground motions. *Ph.D. degree Thesis*, Institute of Geophysics, China Earthquake Administration, in Chinese

Johnston, A. C., 1985, Recurrence rates and probability estimates for the New Madrid Seismic Zone. *Journal of Geophysical Research*, 90, 6737 – 6753.

Johnston, A. C. and E. S. Schweig, 1996. The enigma of the New Madrid earthquakes of 1811 – 1812. *Annual Reviews of Earth & Planetary Science*, 24, 339 - 384.

Kaláb, Z., and A. Lyubushin, 2008. Study of site effect using mining induced seismic events and ambient noise from Karviná region, Acta Geodyn. *Geomater*, 5, 105-113.

Kanai, K and T. Tanaka, 1954. Measurement of the microtremor. *Bulletin of Earthquake Research Institute*, 32, 199-209.

Kibblewhite, A. C. and K. C. Ewans, 1985. Wave-wave interactions, microseisms and infrasonic ambient noise in the ocean. *Journal of Acoustic Society of America*, 78, 981-994.

Langston, C. A., S. P. Horton, 2011. 3D Seismic velocity model for the unconsolidated Mississippi Embayment sediment from H/V ambient noise measurements. Final Technical Report, USGS MEHRP award G10AP00008.

Lermo, J. and F. J. Chávez-García, 1992. Site effect evaluation using microtremor measurements. A review in three cities in Mexico and results of a new technique. *International Symposium on Earthquake Disaster Prevention*, Mexico, D. F, 18-21 May, P. 144-55.

Lermo, J. and F. J. Chávez-García, 1993. Site effect evaluation using spectral ratios with only one station. *Bulletin of the seismological society of America.* 83, 1574-1594.

Lermo, J. and F. J. Chávez-García, 1994. Are Microtremors Useful in Site Response Evaluation? *Bulletin of the seismological society of America.* 84, 1350-1364.

Longuet-Higgins, M., 1950. A theory of the origin of microseisms, Philosophical Transaction of the Royal Society of London, Series A, 243, 2-36.

Ma, Z., 2009. The study on the seismic response of the Gravel Formation on Chengdu Plain. *Master degree thesis*, Chengdu University of Technology, China, in Chinese

McCreery, C. S., F. K. Duennebier and G.H. Sutton, 1993. Correlation of deep ocean noise (0.4 to 30 Hz) with wind, and the Holu Spectrum – A worldwide constant. *J. Acoust. Soc. Am.*, 93, 2639-2648.

McNamara, D. E. and R. P. Buland, 2004. Ambient noise levels in the continental United States. *Bulletin of the Seismological Society of America*, 94(4), 1517-1527.

MDEQ (Mississippi Department of Environment Quality). Geologic maps and data for Mississippi.

http://www.deq.state.ms.us/MDEQ.nsf/page/Geology_surface?OpenDocument

Mucciarelli, M., M. R. Gallipoli, D. D. Giacomo, 2005. The influence of wind on measurements of seismic noise. *Geophys. J. Int.*, 161, 303-308.

Nakamura, Y., 1989. A method for dynamic characteristics estimation of subsurface using microtremor on the ground surface. *QR of RTRI*, 30, 25 - 33.

Nakamura, Y., 1996. Real-time information systems for seismic hazards mitigation UrEDAS, HERAS and PIC. *QR of RTRI*, 37, 112-127.

Nakamura, Y., 2008a. Basic structure of the H/V spectral ratio. Earthquake Disaster Symposium. *Society of Exploration Geophysicists*, Japan. (in Japanese with English abstract)

Nakamura, Y., 2008b. On the H/V spectrum. The 14th World Conference on Earthquake Engineering, October 12-17, 2008, Beijing, China.

Nuttli, O. W., 1974. New Madrid Earthquakes 1811-1812. *Earthquake Information Bulletin*, 6,

Okada, H., 2003. The Microtremor Survey Method. Society of Exploration Geophysicists with the cooperation of Society of Exploration Geophysicists of Japan & Australian Society of Exploration Geophysicists, 135 pp.

Park, D., Y. M. A. Hashash, 2005. Evaluation of seismic site factors in the Mississippi Embayment. I. Estimation of dynamic properties. *Soil Dynamics and Earthquake Engineering*, 25, 133-144.

Parolai, S., P. Bormann, and C. Milkereit, 2002. New Relationships between V_s, thickness of sediments, and resonance frequency calculated by the H/V ratio of seismic noise for the Cologne Area (Germany). *Bulletin of the Seismological Society of America*, 92, 2521-2527.

Peterson, J., 1993. Observation and modeling of seismic background noise. U.S. Department of Interior Geological Survey, open-file Report, 93-322, Albuquerque, New Mexico

Rhie, J. and B. Romanowicz, 2006. A study of the relation between ocean storms and the Earth's hum. Geochemistry Geophysics Geosystems, 7, Q10004, doi:10.1029/2006GC001274.

Schimmel, M., E. Stutzmann, R. Ardhuin and J. Gallart, 2012. Polarized Earth's ambient microseismic noise. Geochemistry Geophysics Geosystems, 12, Q07014, doi: 10.1029/2011GC003661.

Seht, M.I.-v. and J. Wohlenberg, 1999. Microtremor measurements used to map thickness of soft sediments. Bulletin of the Seismological Society of America, 89, 250-259.

Romero, S. M., and Rix, G. J., 2005. Ground motion amplification in the Upper Mississippi Embayment. Report No. GIT-CEE/GEO-01-1, National Science Foundation Mid America Center, Atlanta.

Rosenblad, B. L., R. Goetz, 2010. Study of the H/V spectral ratio method for determining average shear wave velocities in the Mississippi embayment. *Engineering Geology*, 112, 13-20.

Schweig, E. S., 1996. Neotectonics of the upper Mississippi embayment. *Engineering Geology*, 45, 185-203.

Seo, K., T. Samano, H. Yamanaka, X. Hao and M. Takeuchi, 1990. Comparison of ground vibration characteristics among several districts mainly with microtremor measurement. *Proc. of 8th Japan Earthquake Engineering Symp.*, Japan, 685-690.

Seed, H. B., H. M. EERI, M. P. Romo, J. I. Sun, A. Jaime and J. Lysmer, 1988. The Mexico earthquake of September 19, 1985-Relationships between soil conditions and earthquake ground motions. *Earthquake Spectra*, 4, 687-729

Singh, S. K., J. Lermo, T. Dominguez, M. Ordaz, J. M. Espinosa, E. Mena, and R. Quaas, 1988a. A study of amplification of seismic waves in the Valley of Mexico with respect to a hill zone site (CU). *Earthquake Spectra*, 4, 653-673.

Singh, S. K., E. Mena, and R. Castro, 1988b. Some aspects of the sources characteristics and the ground motion amplifications in and near Mexico City from the acceleration data of the September, 1985, Michoacan, Mexico earthquakes. *Bulletin of the Seismological Society of America*, 78, 451-477.

Stephen, R. A., K. R. Spiess, J. A. Collins, J. A. Hildebrand, J. A. Orcutt, K. R. Peal, F. L. Vernon and F. B. Wooding, 2003. Ocean seismic network pilot experiment. *Geochemistry Geophysics Geosystems*, 4(10), 1092, doi: 10.1029/2002GC000485

Sun, T., M. Xue, K. P. Le, et al, 2013. Signatures of ocean storms on seismic records in South China Sea and East China Sea. *Marine Geophysics Research*, 34, 431-448.

Stover, C. W. and J. L. Coffman, 1993. Seismicity of the United States. USGS Professional Paper 1527, 418p.

Traer, J., P. Gerstoft, P. D. Bromirski and P. M. Shearer, 2012. Microseisms and hum from ocean surface gravity waves, Journal of Geophysical Research, 117, B11307, doi: 10.1029/2012JB009550.

Webb, S. C., 1998. Broadband seismology and noise under the ocean. *Review of Geophysics*, 36, 105-142.

Wenzel, H. and G. Achs, 2006. Determination of site effects by ambient vibration monitoring. *First European Conference on Earthquake Engineering and Seismology*, Geneva, Switzerland, 3-8 September.

Xu, J., 2003. Study on the component of frequency spectrum of microtremor and response of dynamics of site soil. *Master degree Thesis*, University of Fuzhou, P. R. China, in Chinese

Young, A. P., R. T. Guza, M. E. Dickson, W. C. O'Reilly and R. E. Flick, 2013. Ground motions on rocky, cliffed, and sandy shorelines generated by ocean waves. *Journal of Geophysical Research: Oceans*, 118, 6590-6620.

Zaharia, B., B. Grucu, M. Radulian, M. Popa and D. Paulescu, 2007. H/V spectral ratios technique-application for Bucharest area. *International symposium on strong Vrancea Earthquake and risk mitigation*, Oct. 4-6, Bucharest, Romania

LIST OF APPENDIX

APPENDIX A:

FIELD DESCRIPTION FORM OF RECORDING POINT

Table A-1. Description of survey points in Northern Mississippi.

Date:1   /   /   **Time:**2 _____ : _____am/pm   **County:**3   Urban/Suburban 4

NO. 5		GPS 6	W:		N:		H:		
Weather7		**Atm. 8 Pressure**				**Wind** 9	Speed		
							Direction		
Lunar phase 10		**Stream** 13	Width			**Tree** 14	Name		
Air Temp. 11			Depth				Height		
Ground Temp. 12			Speed				Diameter		

Record time15	Local time	Starting		Ending			Lasting
	UTC time	Starting		Ending			

Terrain 16	**Macro**	Altitude	slope	**Micro**	Height	Slope	At Peak/valley	Other description	No. of Photo

Soil 17	Color	Grain size	%	Dry/wet		Hardness		Porosity	%	No. of Photo
				Very dry		Very hard		Loose		
				Dry		Hard		Porous		No. of sample
				Medium		Medium		Medium		
				Wet		soft		Compact		

Remark 18**:**

Recorded by: Page   of   at this point

Instruction of table A-1:

Requirements:

1. This table must be filled totally in the field (maybe by hand firstly and then typed into computer);

2. Every blank must be filled; if some blanks are not be able to be filled, write down the clear reason;

3. Take as much remarks as possible to describe the place and the factors that may influence the recording.

Introduction to each item:

1. **Date:** Mostly, the measurements are taken on the midnight and early morning, so be careful the date;

2. **Time:** The time when the equipment starts recording stably;

3. **County:** The name of the county where the point is;

4. **Urban/Suburban**: Circle one to describe the location;

5. **NO.**: The number of the designed survey points;

6. **GPS:** The GPS coordinates read from the GPS connect to REFTEK;

7. **Weather**: Clear, cloudy, foggy, humidity;

8. **Atm. Pressure**: Atmosphere Pressure, read from other website;

9. **Wind**:

   Speed: fill the general term according to the table A-2 below:

Table A-2. General wind classifications.

Beaufort scale	10-minute sustained winds (knots)	General term	Beaufort scale	10-minute sustained winds (knots)	General term
0	**< 1**	**Calm**	10	48–55	Whole gale
1	**1–3**	**Light air**	11	56–63	Storm
2	**4–6**	**Light breeze**	12	64–72	Hurricane
3	**7–10**	**Gentle breeze**	13	73–85	
4	**11–16**	**Moderate breeze**	14	86–89	
5	**17–21**	**Fresh breeze**	15	90–99	
6	22–27	Strong breeze	16	100–106	
7	28–29	Moderate gale	17	107–114	
	30–33			115–119	
8	34–40	Fresh gale		> 120	
9	41–47	Strong gale	1 knot = 0.514 m/s = 1.852 km/h = 1.151 mph = 1.688 ft/s		

The best recording time is when there is no wind, but it is really difficult to have that perfect time to make measurement. Therefore **Fresh Breeze** is tolerable.

Direction: Use a stick with a light handkerchief tied on the top, and measure the direction by a compass.

10. Lunar Phase: write the date of Chinese lunar calendar.

11. Air. Temp.: read from REFTEK;

12. Ground Temp.:

13. Stream: if have to make recordings near a stream, describe the width, depth and speed of water flow in the stream;

14. Tree: since the recording is done in Mississippi, it is very necessary to describe the trees around the recording spot if the recording spot is surrounded by trees or even though hundreds meters away from trees because even a light wind can make the tree shake and influence the microtremor;

15. Record time: fill the **starting time** and **ending time** of the record in both local time and UTC time due to the time in RTCC is in UTC. And also record the **lasting** in second as the unit.

16. Terrain:
Macro: *Altitude*: the height above or below the sea level, read from topography map or roughly from GPS; the altitude in north Mississippi is from 200 ft to 600 ft; *Slope*: in a large scale, the changing of altitude;
Micro: *Height*: the relief: *Slope*: the slope in a small area, for example the slope of a small hill; All the four parameters should be record in 4 directions; **At Peak/valley**: where does the recording point locate in, the peak of a small hill or in the valley between two hills;

17. Soil: Grain size: USCS;

18. Remark: record the weather 3 days before and after the recording day according to the official weather report; all the necessary details (especially the ground type and the possible noise) during the recording should be recorded.

APPENDIX B:

RECORDING CONDITIONS AND SITE EFFECTS PARAMETERS

OF STRS

Table B-1. Summary of recording conditions and site effect parameters of STRs in Figure *2*.

ID	Lat.	Lon.	UST(m)	GT[1]	RT[2]	f_0(Hz)	HVSR @f_0	f_1(Hz)	HVSR @f_1	φ_e@f_0 (°)	f_1/f_0	V_S (m/s)
MEM1	-89.80400	35.09100	847.641	A	I	0.237	7.933	0.740	3.200	47.427	3.117	805.046
MEM2	-89.78700	35.20000	812.985	A	I	0.237	10.210	0.692	3.573	47.009	2.915	772.131
MEM3	-89.73000	35.09400	815.556	A	I	0.254	6.194	0.846	2.921	44.155	3.332	828.139
MEM4	-90.01600	35.14000	992.124	A	I	0.194	7.975	0.647	2.445	39.848	3.332	770.996
MEM5	-89.98100	35.04500	973.380	C	I	0.194	9.409	0.566	2.573	41.837	2.915	756.429
SD 1	-89.79688	34.40553	830.345	GG	I	0.254	12.924	0.692	11.250	43.088	2.727	843.155
SD 2	-89.80637	34.41272	839.653	GG	I	0.237	13.136	0.692	12.651	46.098	2.915	797.459
SD 3	-89.87305	34.40165	881.956	A	I	0.237	8.585			44.955		837.647
SD 9	-89.79800	34.40400	830.345	GR	I	0.237	7.481	0.740	2.567	46.672	3.116	788.685
SD 6	-89.58362	34.53925	743.450	S	I	0.290	8.496	0.740	2.505		2.550	862.943
SD 7	-89.58068	34.54043	743.450	C	I	0.290	7.525	0.791	1.899		2.727	862.943
SD 8	-89.58300	34.54700	743.450	S	I	0.290	7.507	0.791	2.135		2.727	862.937
NM 1	-89.32400	34.30700	572.686	GR	I	0.355	6.733			48.698		812.400
NM 2	-89.05090	34.25800	413.829	GG	I	0.433	4.137			59.466		717.460
NM 3	-89.01173	34.25333	387.419	A	I	0.433	5.303			60.583		671.673
NM 4	-88.91723	34.24268	299.184	S	I	0.495	3.646			49.447		592.922
NM 5	-88.82502	34.23228	232.763	S	I	0.530	6.304			41.489		493.190
NM 6	-88.74410	34.25507	192.833	A	I	0.606	5.482			51.430		467.049

NM 7	-88.57183	34.27123	149.784	A	I	0.740	5.611			45.883		443.375
NM 8	-88.40320	34.23828	110.209	A	I	1.778	6.871			42.430		783.901
NM 9	-88.26412	34.23717	73.227	A	I	1.351	3.216			48.523		395.679
NM 10	-88.14588	34.44232	0.100	A	I							
NM 11	-88.19395	34.64500	9.134	GG/S	I	1.034	2.394			51.154		37.772
NM 12	-88.20433	34.80342	44.434	A	I	1.351	4.037			41.347		240.096
NM 13	-88.41203	34.86378	102.605	A	I	0.692	3.146			43.733		284.074
NM 15	-88.62900	34.93700	173.043	GG	I	0.846	3.931			49.138		585.518
NM 16	-88.77102	34.93735	248.033	GR	I	0.606	7.381			42.230		600.747
NM 17	-88.90035	34.94613	346.370	GR	I	0.530	8.467			56.976		733.906
NM 18	-88.96727	34.96060	390.685	S	I	0.495	6.787			62.347		774.258
NM 19	-89.14637	34.94735	515.175	GG	I	0.379	10.241			48.190		781.358
NM 20	-89.24887	34.95350	564.206	A	I	0.355	6.279			45.616		800.371
NM 21	-89.44340	34.94798	682.813	C	I	0.290	12.164	0.791	2.658	46.581	2.727	792.560
NM 23	-89.65993	35.02438	791.410	C	I	0.254	9.484			56.304		803.620
NM 24	-90.02457	35.08227	999.719	A	I	0.208	7.641			33.341		830.622
NM 25	-90.15235	34.95273	1040.631	A	I	0.194	8.827			44.444		808.691
NM 26	-90.31402	34.81970	1111.485	A	I	0.194	7.016	0.495	3.109	40.458	2.550	863.753
NM 27	-90.37682	34.69198	1205.472	A	I							
NM 27-1	-90.37680	34.69207	1205.472	A	I	0.149	15.090			38.803		716.933
NM 27-2	-90.37500	34.68400	1205.472	C	II	0.170	7.981			47.267		819.518

NM 28	-90.46797	34.42362	1267.916	A	I							
NM 28-1	-90.47005	34.42347	1267.916	A	I	0.149	14.044			34.725		755.592
NM 30	-90.27360	34.25910	1156.703	A	I	0.182	10.352			40.338		840.748
NM 30-1	-90.27425	34.25945	1156.703	C	I	0.182	6.376			50.908		840.794
NM 31	-89.95010	34.31100	948.779	A	I	0.222	9.171			40.568		842.815
NM 32	-89.84265	34.31553	879.466	GG	I	0.222	6.299			48.703		781.244
NM 33	-89.74295	34.34047	822.470	C	I	0.254	10.280			32.062		835.159
NM 34	-89.61300	34.35500	763.821	A	I	0.271	8.057	0.647	2.090	47.191	2.385	829.244
NM 35	-89.29883	34.42548	539.314	A	I	0.355				30.156		765.059
NM 35-1	-89.29853	34.42312	539.314	S	I	0.379	8.454			48.331		817.968
NM 36	-89.15281	34.45517	485.778	F	I	0.400	6.787			46.983		777.245
NM 36-1	-89.15667	34.45247	493.421	F	I	0.405	3.911			51.094		800.118
NM 37	-89.06508	34.48972	423.283	C	I	0.530	3.629			50.577		896.873
NM 38	-89.00352	34.48565	392.108	C	I	0.566	5.774			50.436		888.273
NM 39	-88.94640	34.44497	363.552	S	I	0.405	5.752			55.236		589.525
NM 40	-88.87570	34.40678	291.230	A	I	0.463	4.216			59.512		539.826
NM 41	-88.77055	34.37870	205.725	C	I	0.566	5.370					466.044
NM 42	-88.68070	34.37582	173.742	A	I	0.647	5.140			42.900		449.912
NM 43	-88.52700	34.38600	139.411	GR/S	I	0.566	8.736			56.125		315.820
NM 44	-88.48208	34.42842	136.529	C	I	0.904	4.100			45.332		493.916
NM 45	-88.32202	34.50575	94.548	C	I	0.967	3.531			42.626		365.698

NM 46	-88.22648	34.55893	26.427	A	I	0.904	3.912			63.131		95.605
NM 47	-88.21048	34.51020	10.903	A	I	2.157	4.997			45.097		94.081
NM 48	-88.31813	34.36402	105.440	GR	I	0.967	4.624					407.827
NM 49	-89.16460	34.35067	487.194	GR	I	0.405	3.232			67.157		790.020
NM 50	-89.02377	34.35057	406.193	C	I	0.405	6.095			51.133		658.672
NM 51	-88.91172	34.54393	331.139	A	I	0.433	9.191			48.081		574.100
NM 52	-88.83663	34.56787	287.774	C	I	0.566	6.204			57.347		651.917
NM 53	-88.72727	34.50653	200.298	A	I	0.495	5.702			43.435		396.950
NM 54	-88.61160	34.50847	158.214	GR	I	0.566	8.009			56.547		358.415
NM 55	-88.47037	34.56432	139.738	A	I	0.606	6.492			51.986		338.451
NM 56	-88.26680	34.66228	80.737	A	I	1.351	4.839			50.514		436.260
NM 57	-88.22448	34.73155	74.991	C	I	1.351	2.419			44.374		405.213
NM 58	-88.30512	34.72970	118.695	A	I	0.967	4.270			45.147		459.092
NM 59	-88.31500	34.84100	97.229	GR	I	1.765	5.584			45.071		686.492
NM 60	-88.42878	34.76092	128.305	C	I	0.740	5.448			44.574		379.793
NM 61	-88.60435	34.75777	176.959	GR	I	0.647	4.025			48.277		458.242
NM 62	-88.67520	34.78907	200.000	GR	I	0.606	4.576			41.911		484.409
NM 63	-88.77925	34.82742	258.561	A	I	0.647	6.485			44.278		669.554
NM 64	-88.87918	34.84450	318.006	S	I	0.566	8.300			55.477		720.404
NM 65	-88.96548	34.83977	372.420	A	I	0.463	3.521			54.679		690.322
NM 66	-89.05832	34.81755	409.188	GR/S	I	0.433	7.128			48.885		709.415

NM 67	-89.25623	34.84188	553.226	F	I	0.379	10.713			21.599		839.069
NM 68	-89.31863	34.91678	600.610	A	I	0.355	7.291			51.209		852.014
NM 69	-89.39653	34.86295	665.191	A	I	0.332	8.352			44.585		882.591
NM 70	-89.45595	34.75135	709.299	A	I	0.310	7.490			40.154		880.240
NM 71	-89.56588	34.88295	755.839	A	I	0.271	8.115			48.840		820.578
NM 72	-89.68930	34.87267	821.635	A	I							
NM 72-1	-89.69468	34.87280	831.770	A	II	0.254	8.078			55.102		844.602
NM 73	-89.82918	34.96123	896.576	A	I	0.237	5.368			48.711		851.522
Nm 73-1	-89.82533	34.96048	889.858	A	II	0.237	6.486			39.621		845.141
NM 74	-90.03428	34.95655	1000.080	A	I							
NM 74-1	-90.03100	34.95803	1000.080	A	II	0.194	5.497	0.647	2.540	47.630	3.332	777.179
NM 75	-90.21538	34.90483	1061.806	C	I	0.182	8.043			36.683		771.772
NM 75-1	-90.21535	34.90490	1061.806	C	II	0.194	10.720			37.107		825.147
NM 76	-90.24168	34.77237	1091.381	F	I	0.159	14.137			48.374		693.965
NM 76-1	-90.23713	34.77277	1091.381	F	II	0.182	7.507			44.463		793.268
NM 77	-90.33920	34.56865	1200.354	F	I	0.182	5.882			53.158		872.475
NM 77-1	-90.33973	34.56848	1205.813	F	II	0.222	7.015			55.174		1071.143
NM 78	-90.19512	34.50342	1140.167	A	II	0.208	7.572	0.606	3.596	48.064	2.915	947.315
NM 79	-90.25303	34.39480	1173.447	A	I							
NM 79-1	-90.25380	34.39478	1173.447	GR	II	0.194	9.535			47.460		911.904

NM 80	-90.05680	34.43905	1040.358	A	II	0.159	7.012			34.744		661.668
NM 81	-89.91750	34.43818	916.863	A	II	0.222	8.044	0.791	3.014	46.031	3.563	814.464
NM 82	-89.82765	34.50952	860.185	A	II	0.254	8.980	0.606	2.214	50.799	2.385	873.456
NM 83	-89.71228	34.58355	838.214	A	II	0.237	9.752	0.740	3.518	58.954	3.117	796.092
NM 84	-89.57128	34.65747	781.037	A	II	0.271	8.079	0.740	3.208	52.670	2.727	847.934
NM 85	-89.45823	34.64615	700.466	C	I	0.271	3.505	0.846	2.565	44.347	3.117	760.462
NM 86	-89.50323	34.50285	644.871	C	I	0.310	9.250	0.740	2.639	57.370	2.385	800.285
NM 87	-88.21077	34.26843	54.867	C	II	2.466	3.368			31.517		541.195
NM 88	-88.88325	34.32237	277.969	GR	I	0.495	3.486	2.819	2.784	47.701	5.689	550.878
NM 89	-88.44253	34.66813	137.304	A	I	0.904	3.377			51.644		496.721
NM 90	-88.55688	34.65590	164.020	A	I	0.606	3.130			53.718		397.263
NM 91	-88.66358	34.71178	200.198	GR	I	0.692	6.019			53.924		554.273
NM 92	-88.80873	34.71297	269.420	C	I	0.433	6.250			46.960		467.097
NM 93	-89.48723	34.38543	674.248	A	I	0.310	7.323	0.740	2.307	52.014	2.385	836.742
NM 94	-89.41658	34.43773	580.650	GR	I	0.310	6.691			68.696		720.586
NM 95	-89.35120	34.50747	556.431	GR	I	0.405	7.965			44.694		902.294
NM 96	-89.30023	34.54208	540.379	A	I	0.379	5.247			41.993		819.584
NM 97	-89.11940	34.55635	444.250	C	I	0.433	6.576			55.399		770.202
NM 98	-89.38972	34.58763	598.396	A	I	0.332	6.657			56.667		793.966
NM 99	-89.28957	34.64530	549.050	A	I	0.405	9.172			44.340		890.323
NM 100	-89.18798	34.61554	482.085	A	I	0.433	6.107			52.107		835.796

NM 101	-89.02605	34.67003	364.354	C	I	0.495	6.271			60.100		722.076
NM 102	-89.00428	34.59922	367.854	C	I	0.379	7.970	0.791	3.866	40.422	2.087	557.918
NM 103	-88.94508	34.72495	335.879	C	I	0.495	4.751			66.188		665.643
NM 104	-88.84047	34.64213	287.537	A	I	0.495	5.223			54.092		569.839
NM 105	-88.68532	34.62690	193.824	C	I	0.566	6.165	2.636	2.706	69.847	4.655	439.084
NM 106	-88.60323	34.57988	166.075	C	I	0.530	5.815			48.545		351.887
NM 107	-89.08330	34.74902	400.333	A	I	0.463	5.156	1.444	2.805	48.731	3.117	742.060
NM 108	-89.17947	34.70860	453.627	C	I	0.433	6.471			60.419		786.458
NM 109	-88.20563	34.36195	41.476	C	II	3.014	2.541			34.546		499.995
NM 110	-88.07752	34.45018	1.000	C	II	5.146	3.700			41.531		20.582
NM 111	-88.84507	34.48902	290.289	GR	I	0.530	3.715			48.348		615.079
NM 112	-88.51883	34.84128	130.512	F	I	0.967	6.479			37.324		504.802
NM 113	-88.64280	34.87312	179.345	C	I	0.846	4.311			56.067		606.844
NM 114	-89.56458	34.78905	767.893	C	II	0.271	6.316	0.791	2.442	47.583	2.915	833.665
NM 115	-89.71757	34.78812	860.829	A	II	0.271	5.719	0.904	2.313	51.643	3.332	934.561
NM 116	-89.83033	34.86498	915.219	A	II	0.222	5.935	0.606	3.250	58.318	2.727	813.004
NM 117	-89.99902	34.82212	992.892	A	II	0.208	6.786	0.606	2.586	49.637	2.915	824.950
NM 118	-90.14015	34.83055	1033.653	A	II	0.194	6.347	0.566	3.215	47.661	2.915	803.269
NM 119	-90.12248	34.69837	1004.138	A	II	0.208	6.013			48.599		834.294
NM 120	-90.24028	34.67067	1103.617	GR	II	0.182	7.100	0.692	2.954	40.628	3.809	802.162
NM 121	-90.20978	34.59437	1099.535	GR	II	0.208	5.445	0.530	2.876	51.318	2.550	913.555

NM 122	-90.08240	34.61907	991.567	A	II	0.208	8.705	0.692	2.305	52.785	3.332	823.849
NM 123	-90.05658	34.55013	1024.489	GR	II	0.222	6.256	0.530	3.020	54.848	2.385	910.070
NM 124	-89.93820	34.51247	946.477	A	II	0.222	6.823	0.606	2.544	53.089	2.726	840.838
NM 125	-89.96967	34.59837	973.785	A	II	0.222	4.933	0.606	2.389	41.363	2.726	865.099
NM 126	-89.97540	34.68701	968.428	A	II	0.222	6.256	0.740	2.601	51.406	3.332	860.270
NM 127	-90.02460	34.76040	994.583	F	II	0.222	4.647	0.740	2.734	42.145	3.332	883.504
NM 128	-89.87342	34.76725	934.905	S	II	0.208	4.808	0.606	2.674	46.294	2.915	776.771
NM 129	-89.87348	34.69883	930.350	A	II	0.237	6.433	0.606	2.789	48.467	2.550	883.598
NM 130	-89.83737	34.60068	890.985	A	II	0.237	7.399	0.647	2.070	51.265	2.727	846.211
NM 131	-89.74982	34.69288	882.689	GR	II	0.237	8.181	0.647	2.871	53.501	2.727	838.332
NM 132	-89.63942	34.71767	815.153	GR	II	0.254	7.773	1.034	3.631	60.262	4.072	827.729
NM 133	-89.48062	34.71078	715.892	S	II	0.310	5.602	0.740	2.008	45.499	2.385	888.421
NM 134	-90.45665	34.31995	1270.861	C	I	0.159	11.743			43.025		808.090
NM 135	-90.31128	34.47712	1216.749	GR	II	0.208	7.321	0.530	2.976	48.153	2.550	1010.943
NM 136	-90.45498	34.52428	1250.621	S	II	0.182	6.056	0.495	2.350	46.574	2.727	909.011
NM 137	-90.63928	34.35923	1321.081	A	II	0.149	6.004	0.463	4.618	42.314	3.117	785.689
AR 001	-90.62597	34.54507	1296.308	A	II	0.182	10.275			39.995		942.219
NM 138	-87.99518	34.54548	0.100	A	II	6.772	2.441					2.709
NM 139	-87.93143	34.59717	0.100	A	II	11.480	3.389					4.592
NM 140	-87.86198	34.68600	0.100	C	II	7.686	7.696			46.019		3.074

NM 141	-87.81280	34.72172	0.100	C	II	10.043	9.163			47.336		4.017
NM 142	-87.97217	34.75750	0.100	C	II	7.189	7.320			44.533		2.875
NM 143	-88.07778	34.68105	0.100	B	II							
NM 144	-88.14415	34.72693	0.100	GR/S	II							
NM 145	-88.25795	34.92543	50.433	S	II	6.724	6.765			50.050		
NM 146	-88.38427	34.72727	127.722	A	II	0.791	8.200	2.636	3.541	49.982	3.332	404.215
NM 147	-88.35828	34.64570	122.562	S	II	0.904	5.871	2.306	5.110	52.345	2.550	443.390
NM 148	-88.37652	34.57082	118.224	S	II	0.740	3.062	2.466	2.794	42.610	3.332	349.953
NM 149	-88.39975	34.48197	123.040	S	II	2.018	4.198			48.314		993.042
NM 150	-88.52653	34.74845	150.559	GR	II	0.740	6.027	2.466	2.622	47.969	3.332	445.669
NM 151	-88.48713	34.61583	144.435	S	II	0.791	3.768	2.819	1.655	46.405	3.563	457.108
NM 152	-88.51797	34.50722	144.016	GR	II	0.740	6.523			54.429		426.299
NM 153	-88.59857	34.44325	155.622	A	II	0.692	4.350	2.636	2.954	58.608	3.809	430.858
NM 154	-88.61075	34.34182	153.052	A	II	0.740	4.304	2.636	2.455	58.518	3.563	453.049
NM 155	-88.49158	34.32097	129.234	C	II	1.034	3.517	5.501	1.943	49.816	5.321	534.424
NM 156	-88.39753	34.38237	122.231	A	II	1.651	3.781			42.093		807.197
NM 157	-90.63432	34.24845	1339.125	F	II							
NM 158	-90.72173	34.26558	1358.656	A	II							
NM 159	-90.78065	34.14940	1387.639	C	II	0.159	8.551	0.463	2.842	63.395	2.915	882.344
NM 159-1	-90.69142	34.20795	1361.985	S	II	0.170	11.678	0.647	5.670	39.794	3.809	925.921

NM 160	-90.67685	34.11930	1370.800	C	II	0.170	8.767	0.463	2.560	44.014	2.727	931.914
NM 161	-90.54363	34.27502	1306.525	GR/S	II							
NM 162	-90.51962	34.36540	1293.686	A	II	0.149	9.760	0.463	3.839	47.004	3.117	769.397
NM 163	-90.33733	34.32398	1205.470	GR	II	0.170	12.799	0.530	3.227	51.418	3.117	819.517
NM 164	-88.37608	34.97498	82.718	A	II	1.544	6.257			49.254		510.920
NM 165	-88.45650	34.93213	100.041	C	II	0.791	7.060	2.157	2.053	51.405	2.727	316.609
NM 166	-88.38583	34.78505	119.069	A	II	0.791	8.783	2.466	2.284	51.492	3.117	376.831
NM 167	-88.25743	34.44525	61.825	GR	II							
NM 168	-88.32517	34.42492	106.227	A	II	1.105	3.457			51.502		469.665
NM 169	-88.52745	34.26842	137.403	A	II	1.263	4.029	4.210	1.106	49.070	3.332	694.429
NM 170	-88.32315	34.29043	97.897	A	II	1.105	3.415			44.510		432.834
NM 171	-88.38725	34.32358	117.934	GR	II	0.530	4.745			38.522		249.885
NM 172	-88.69565	34.45163	185.548	A	II	0.566	4.346			46.893		420.338
NM 173	-88.44535	34.50855	132.321	A	II	0.692	7.730	2.306	3.136	63.233	3.332	366.347
NM 174	-88.65355	34.52507	169.378	A	II	0.566	5.196			56.075		383.706
NM 175	-88.67375	34.31858	171.665	C	II	0.904	3.188	2.819	1.881	42.953	3.117	621.026
NM 176	-88.94772	34.32133	341.015	C	II	0.495	2.804	1.263	1.485	49.540	2.550	675.822
NM 177	-88.78957	34.29997	195.189	C	II							
NM 178	-88.67387	34.24203	187.458	A	II	0.647	3.205			49.910		485.431
NM 179	-89.05040	34.42595	429.015	A	II	0.433	2.428			54.546		743.788
NM 180	-89.23593	34.25613	514.704	C	II	0.310	4.629	0.967	2.689	37.442	3.117	638.748

NM 181	-89.52667	34.27385	753.835	C	II	0.237	6.800	0.495	2.544	51.501	2.087	715.953
NM 182	-89.71393	34.21478	857.164	C	II	0.234	7.036	0.740	3.938	48.538	3.164	801.815
NM 183	-88.51495	34.16195	135.166	A	II	1.263	2.536	4.813	1.902	56.735	3.809	683.125
NM 184	-88.60292	34.18945	168.967	A	II	0.904	2.493	6.289	1.837	29.467	6.953	611.266
NM 185	-88.72082	34.18840	209.221	C	II	0.495	2.027			49.081		414.633
NM 186	-90.14997	34.39330	1098.089	F	II	0.237	8.480	0.791	3.021	51.034	3.332	1042.908
NM 187	-90.11233	34.29442	1050.361	A	II	0.208	8.194	0.692	3.764	43.827	3.332	872.699
NM 188	-90.39697	34.24063	1244.977	A	II	0.194	9.728	0.405	3.650	63.779	2.087	967.492
NM 189	-90.35900	34.31685	1222.953	GR	II	0.208	4.520			42.733		1016.098
NM 190	-90.21648	34.33302	1116.693	GR	II	0.194	6.527			37.290		867.800
NM 191	-90.46800	34.22980	1282.720	A	II	0.222	4.769	0.530	4.011	59.032	2.385	1139.460
NM 192	-89.94778	34.21443	959.336	C	II	0.208	7.702	0.606	4.452	49.004	2.915	797.070
NM 193	-90.13635	34.17347	1064.627	C	II	0.170	4.402	0.740	3.754	37.348	4.354	723.767
NM 194	-90.38907	34.48595	1237.984	F	II	0.149	6.798	0.495	4.856		3.332	736.269
NM 195	-90.00352	34.37257	978.973	A	II	0.170	6.391			44.021		665.537
NM 196	-88.34612	34.18095	95.507	C	II	1.444	4.476			49.449		551.757
NM 197	-88.25035	34.17857	61.811	A	II	2.466	2.015			65.289		609.687
NM 198	-90.12143	35.05007	1018.640	A	II	0.222	8.830	0.692	3.156	55.657	3.117	904.875
NM 199	-89.91063	34.96040	936.107	A	II	0.222	6.830	0.606	2.694	45.191	2.727	831.559
NM 200	-90.08070	34.87582	1016.253	C	II	0.237	12.657			51.933		965.184

NM 201	-90.44115	34.64073	1227.264	A	II	0.170	7.041			54.335		834.334
NM 202	-90.31118	34.62795	1181.016	C	II							
NM 203	-90.54475	34.48688	1285.627	C	II	0.149	5.627			45.837		764.604
NM 204	-89.86065	35.03300	894.307	A	II	0.222	6.164	0.791	2.963	53.921	3.563	794.427
NM 205	-90.30720	34.75173	1135.570	GR/S	II	0.170	7.666			58.605		771.997
NM 206	-90.39585	34.78162	1170.412	S	II	0.182	9.131	0.566	2.934	46.672	3.117	850.712
NM 207	-90.14797	34.77535	1035.051	S	II	0.194	12.329			66.775		804.355
NM 208	-90.23885	34.85423	1074.799	A	II	0.208	8.677	0.566	3.020	57.845	2.727	893.004
NM 209	-89.91968	34.90065	956.680	A	II	0.208	9.577	0.606	2.731	52.235	2.915	794.863
NM 210	-90.49883	34.15165	1299.953	GR	II	0.194	5.738	0.647	5.454	34.796	3.332	1010.214
NM 211	-90.16852	34.25377	1079.465	GR	II	0.182	9.346	0.647	3.417	48.652	3.563	784.607
NM 212	-90.28000	34.18568	1168.417	GR	II							
NM 213	-90.21210	34.17237	1114.089	GR	II							
NM 214	-90.39032	34.15978	1245.531	GR	II	0.194	5.661					967.922
NM 215	-90.43535	34.59927	1234.499	A	II	0.170	5.530	0.405	3.529	35.965	2.385	839.252
NM 216	-90.04002	34.24937	1011.374	A	II	0.194	5.963	0.846	2.785	46.699	4.354	785.955
NM 217	-90.44593	34.41830	1262.827	A	II	0.182	6.348			48.967		917.883
NM 161-1	-90.54398	34.27512	1306.525	GR	II	0.182	5.813			42.760		949.645
NM 212-1	-90.27450	34.20460	1156.245	C	II	0.194	4.421	0.530	3.260	47.073	2.727	898.537
NM 213-1	-90.21268	34.17203	1114.089	S	II	0.194	4.923	0.495	2.901	46.568	2.550	865.777

AL 02	-86.81000	33.92700			I							
AL 03	-87.11200	33.94400			I							
SM-3	-90.15155	32.21450			II							

Abbreviations: UST: unconsolidated sediment thickness; GT: ground type; RT: recording type; φ_e: estimated vibration angle; Vs: average shear wave velocity.

1) Ground type: A-Asphalt; C-Concrete; GG-Grass ground; GR-Gravel road; S-Soil; F-Farmland; B-Bedrock.
2) Recording type: I: STR-1, sensor exposed to wind; II: STR-II, sensor protected by a plastic box from wind.

Table B-2. Summary of recording conditions and site effect parameters of STRs in Oxford campus in Figure 4

ID	Lat.	Lon.	UST(m)	f_0 (Hz)	HVSR@f_0	f_1(Hz)	HVSR@f_1	f_1/f_0
OC1	-89.537	34.371	716.944	0.290	12.323	0.846	1.727	2.915
OC2	-89.540	34.370	716.944	0.290	9.488	0.740	1.531	2.550
OC3	-89.541	34.369	716.944	0.290	7.953	0.740	3.418	2.550
OC4	-89.543	34.368	726.004	0.290	10.638	0.740	2.553	2.550
OC5	-89.546	34.367	733.208	0.290	8.694	0.904	2.205	3.117
OC6	-89.544	34.365	733.208	0.290	8.505	0.740	3.504	2.550
OC6-1	-89.543	34.366	726.004	0.290	10.710	0.740	2.818	2.550
OC7	-89.542	34.367	726.004	0.290	10.154	0.740	3.213	2.550
OC8	-89.539	34.369	716.944	0.290	9.732	0.740	2.538	2.550
OC9	-89.538	34.370	716.944	0.290	8.858	0.740	2.424	2.727

OC10	-89.536	34.370	716.944	0.290	8.765	0.740	2.089	2.550
OC11	-89.534	34.371	716.944	0.290	9.811	0.740	1.758	2.550
OC12	-89.530	34.370	716.944	0.290	10.573	0.740	1.585	2.550
OC14	-89.532	34.368	716.944	0.310	8.913	0.791	1.921	2.727
OC15	-89.534	34.369	716.944	0.310	8.781	0.791	1.971	2.727
OC16	-89.536	34.368	716.944	0.290	6.555	0.791	2.170	2.727
OC17	-89.538	34.367	726.004	0.290	9.232	0.740	5.235	2.550
OC18	-89.541	34.367	726.004	0.290	12.323	0.791	2.022	2.727
OC19	-89.542	34.366	726.004	0.290	10.035	0.791	3.251	2.727
OC20	-89.543	34.365	726.004	0.290	10.940	0.846	3.242	2.915
OC21	-89.542	34.365	726.004	0.290	9.875	0.846	1.862	2.915
OC22	-89.540	34.366	726.004	0.290	8.148	0.846	2.087	2.915
OC23	-89.536	34.367	726.004	0.290	9.132	0.846	3.717	2.915
OC24	-89.535	34.368	726.004	0.290	9.488	0.846	2.819	2.915
OC24-1	-89.533	34.367	726.004	0.290	7.776	0.791	2.576	2.727
OC25	-89.529	34.367	726.004	0.290	9.508	0.791	4.206	2.727
OC26	-89.528	34.366	718.799	0.290	7.659	0.791	4.692	2.727
OC27	-89.530	34.365	726.004	0.290	8.564	0.846	2.788	2.915
OC27-1	-89.531	34.367	726.004	0.290	8.704	0.846	2.414	2.915
OC28	-89.532	34.365	726.004	0.310	5.936	0.740	2.249	2.550
OC28-1	-89.534	34.366	726.004	0.290	8.787	0.740	1.732	2.385

OC29	-89.535	34.365	726.004	0.290	9.850	0.846	2.420	2.915
OC30	-89.536	34.365	726.004	0.290	7.797	0.846	2.214	2.915
OC31	-89.539	34.365	726.004	0.290	7.675	0.791	1.953	2.727
OC32	-89.540	34.364	726.004	0.290	8.163	0.791	2.049	2.550
OC33	-89.542	34.362	726.004	0.290	9.923	0.740	2.361	2.550
OC33-1	-89.543	34.361	726.004	0.290	7.040	0.791	3.074	2.727
OC34	-89.544	34.359	733.208	0.290	10.394	0.846	2.408	2.727
OC35	-89.541	34.362	726.004	0.290	8.232	0.846	2.624	2.915
OC35-1	-89.539	34.363	726.004	0.290	8.734	0.791	1.983	2.727
OC36	-89.538	34.364	726.004	0.290	8.605	0.740	2.348	2.550
OC37	-89.536	34.364	726.004	0.290	8.520	0.740	2.144	2.385
OC37-1	-89.534	34.364	726.004	0.290	8.983	0.740	2.381	2.550
OC38	-89.532	34.364	726.004	0.290	7.936	0.740	1.971	2.550
OC39	-89.529	34.364	726.004	0.310	9.165	0.791	1.817	2.727
OC40	-89.532	34.363	726.004	0.290	7.089	0.846	1.884	2.727
OC41	-89.536	34.363	726.004	0.290	7.566	0.791	1.887	2.727
OC42	-89.538	34.362	726.004	0.290	8.500	0.740	1.907	2.550
OC42-1	-89.539	34.360	726.004	0.271	7.022	0.692	2.111	2.385
OC43	-89.541	34.358	726.004	0.290	10.144	0.846	2.517	3.563
OC44	-89.540	34.358	726.004	0.290	7.784	0.740	2.002	2.550
OC45	-89.536	34.360	726.004	0.290	7.596	0.791	1.968	2.727

OC46	-89.534	34.361	726.004	0.310	7.147	0.791	1.816	2.727
OC47	-89.538	34.360	726.004	0.237	5.919	0.740	1.470	2.550
OC48	-89.530	34.361	726.004	0.290	7.462	0.791	2.216	2.727
OC49	-89.534	34.359	726.004	0.290	7.894	0.791	2.141	2.727

APPENDIX C:

COLOR GRADIENT MAP OF HVSR OF LTRS
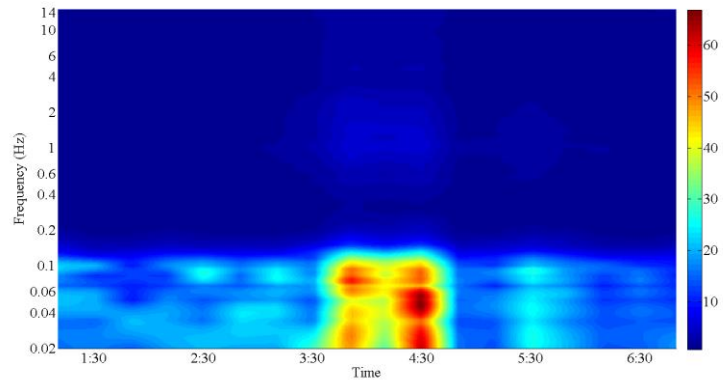
a) AL 1
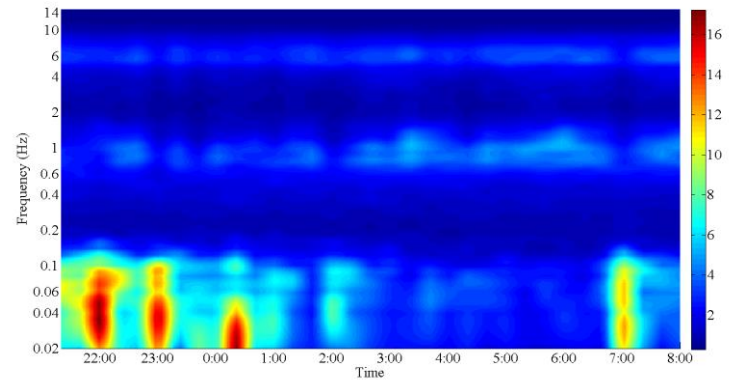
b) NM 14
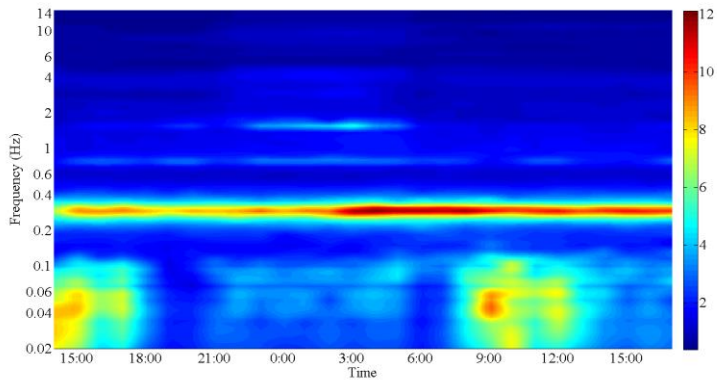
c) OC 37-1
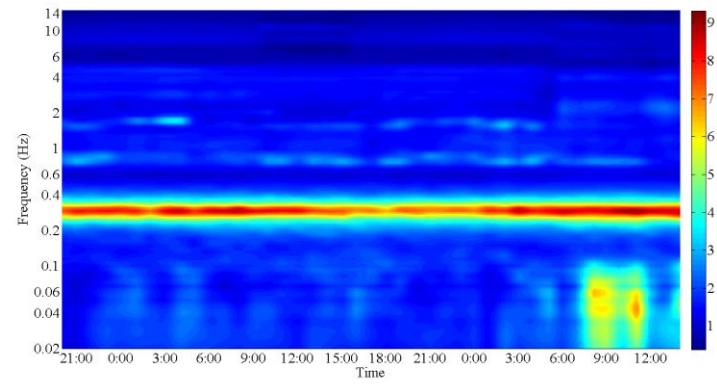
d) OC 37-2
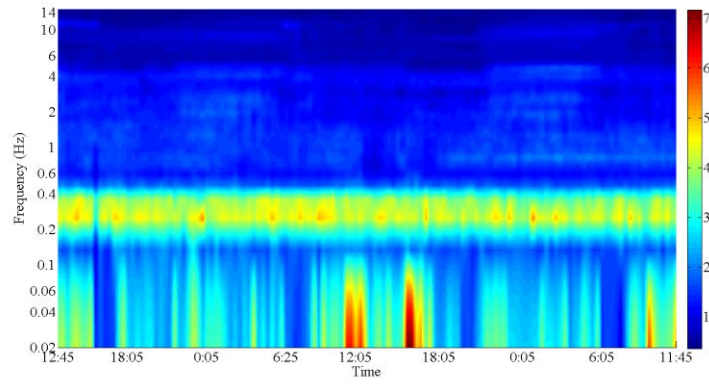
e) OC 37-3
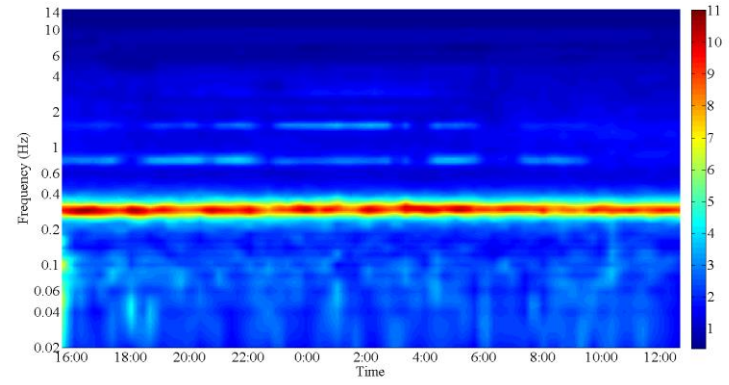
f) OC 37-5
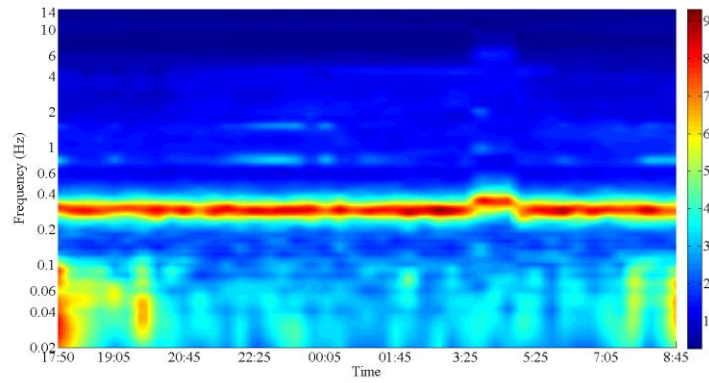
g) OC 38
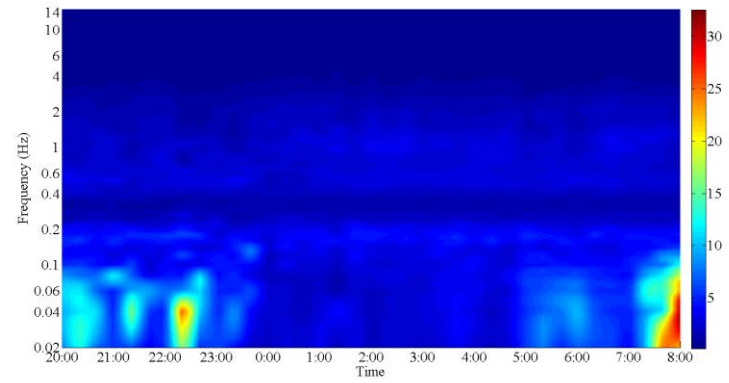
h) NM 29
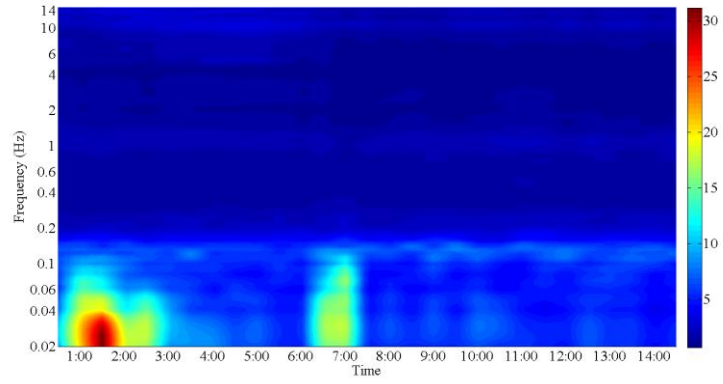
i) SM 1
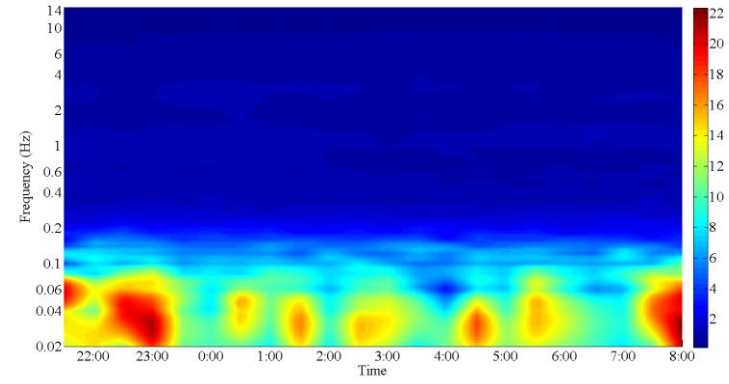
j) SM 2

Figure C-1. Color gradient map of HVSR of LTRs. See Figure 25a), b), c) and d).for T-1 and T-2, OC 37-4, OC 37-6 and LA 1.

APPENDIX D:

COLOR GRADIENT MAP OF ESTIMATED VIBRATION ANGLE φ_e
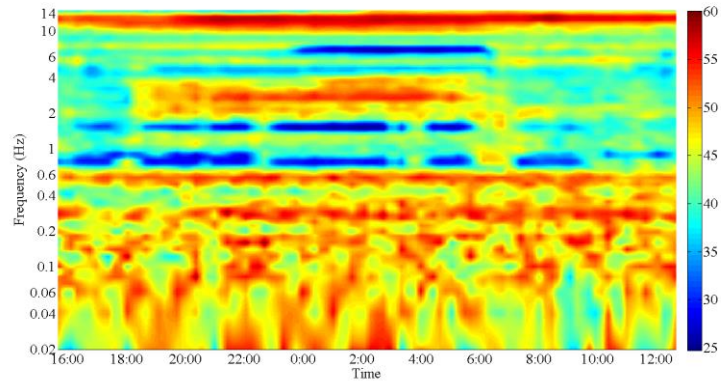
OF LTRS

a) OC 37-5
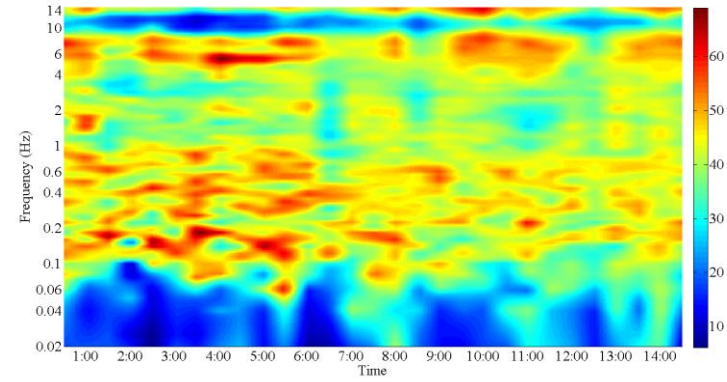
b) SM 1
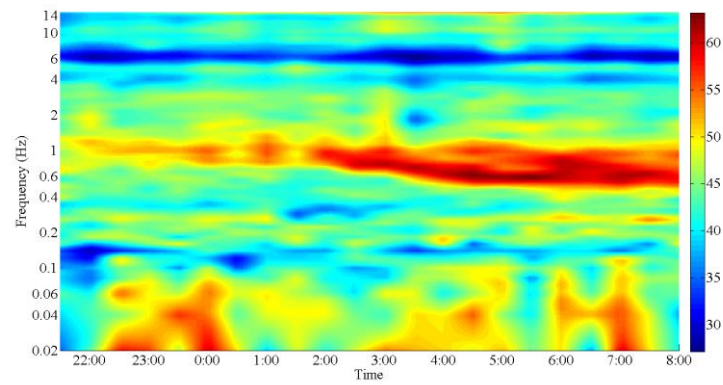
c) SM 2

Figure D-1. Color gradient map of estimated vibration angle φ_e of LTRs. (See Figure 11 for LTRs of AL 1, NM 14, T-1, T-2, OC 37-1, OC 37-2, OC 37-3, OC 37-4, OC 38 and NM 29, and see Figure *16*b)-2 and c)-2 for OC 37-4 and OC 37-6)

APPENDIX E:

COLOR GRADIENT MAP OF PSD AND PDF OF LTRS
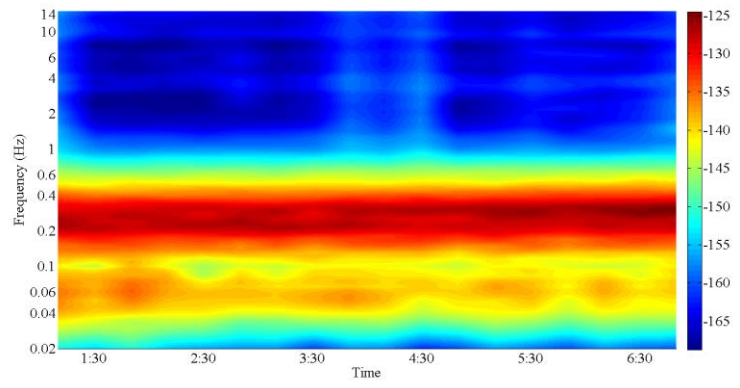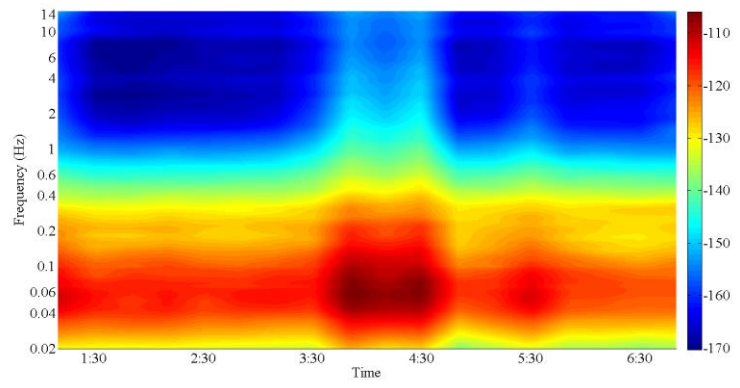
a) AL 1 in horizontal (left) and vertical (right) directions
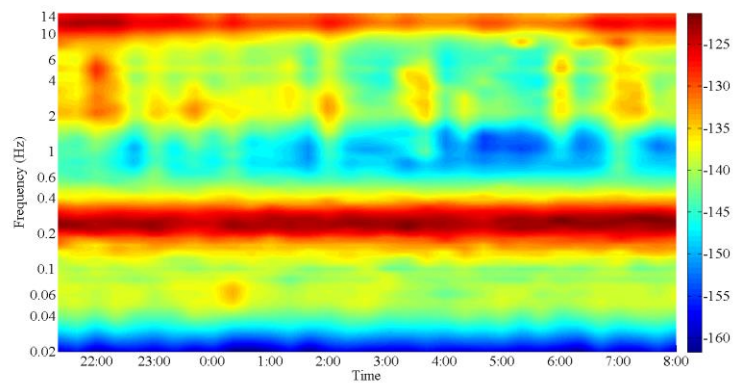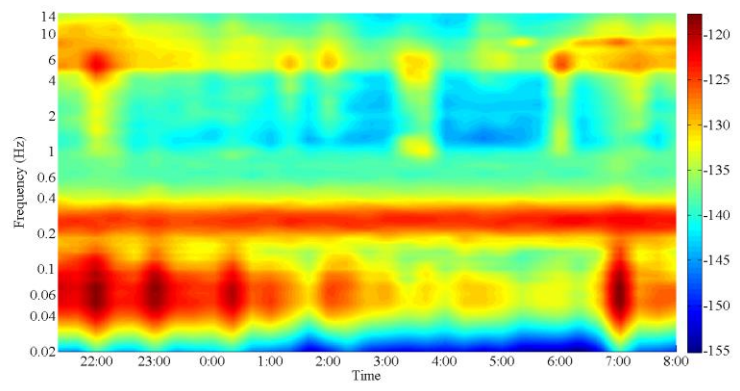
b) NM 14 in horizontal (left) and vertical (right) directions
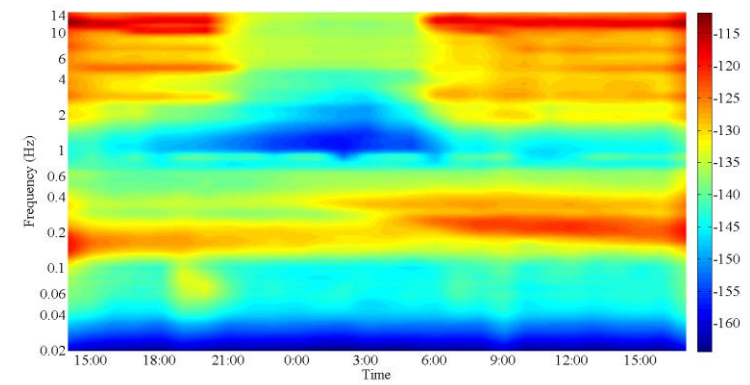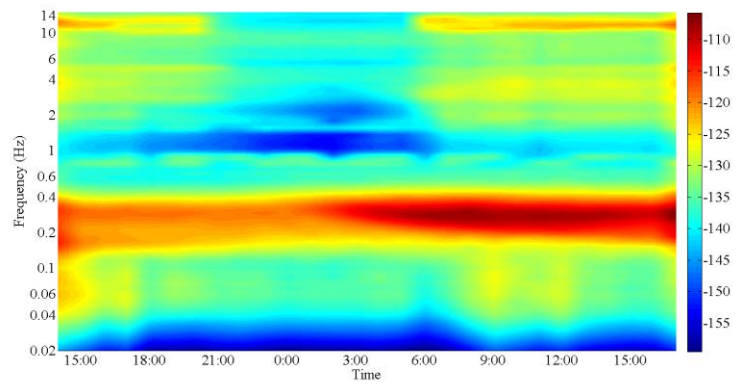
c) OC 37-1 in horizontal (left) and vertical (right) directions
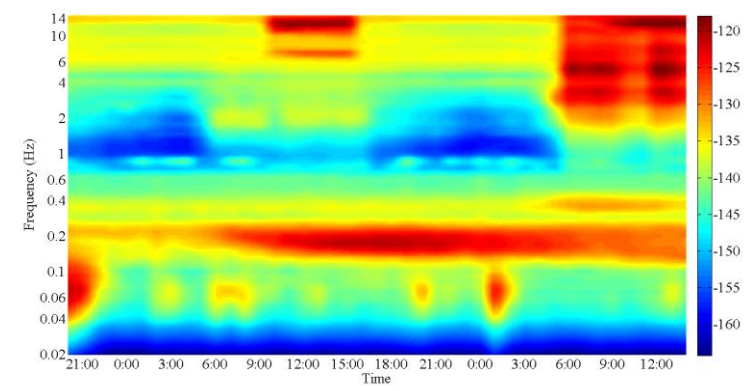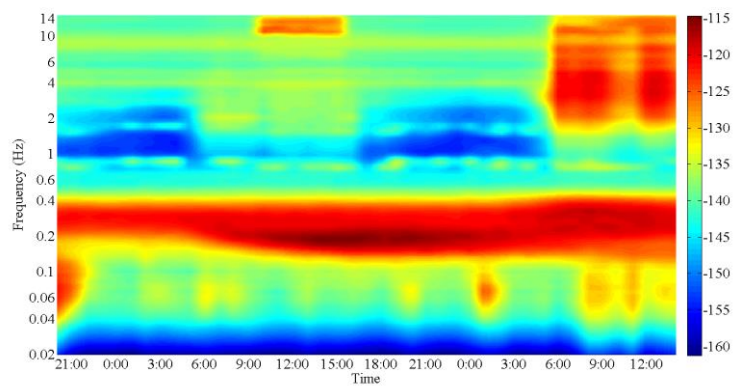
d) OC 37-2 in horizontal (left) and vertical (right) directions
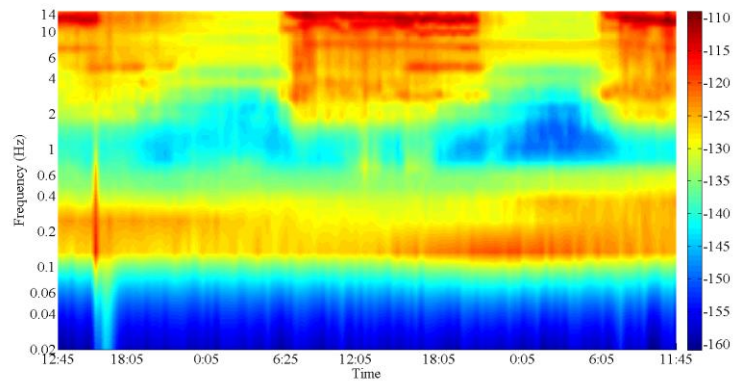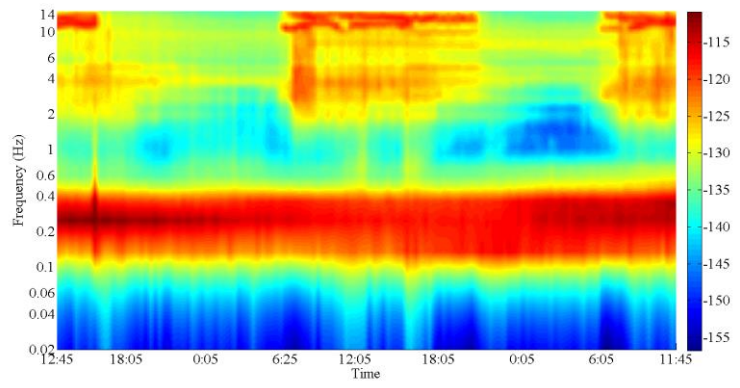
e) OC 37-3 in horizontal (left) and vertical (right) directions
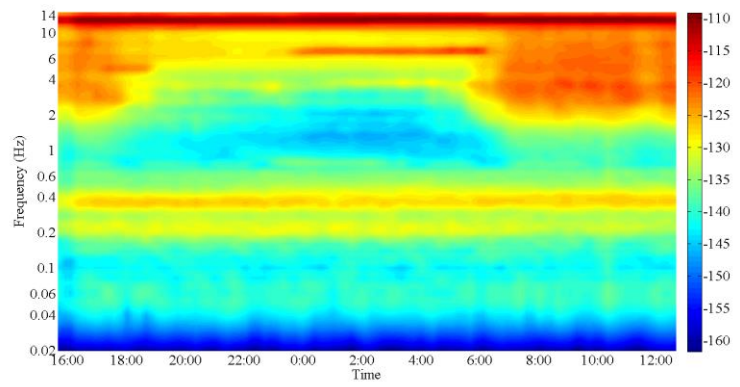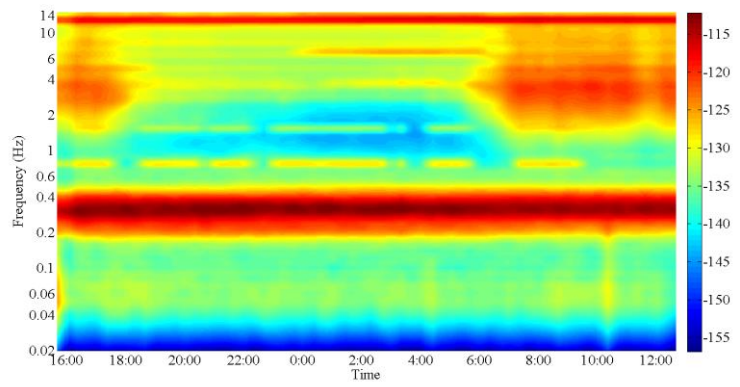
f) OC 37-5 in horizontal (left) and vertical (right) directions
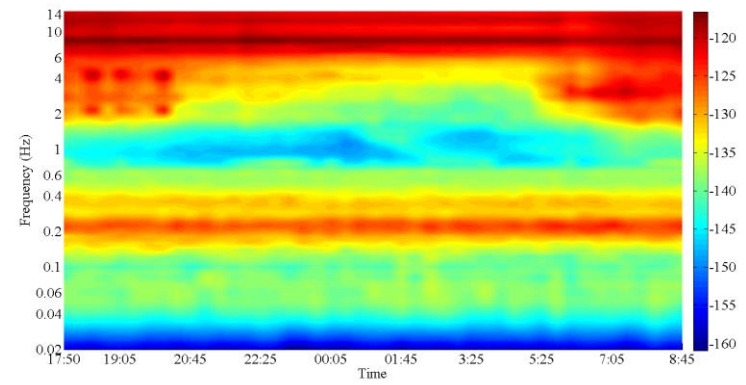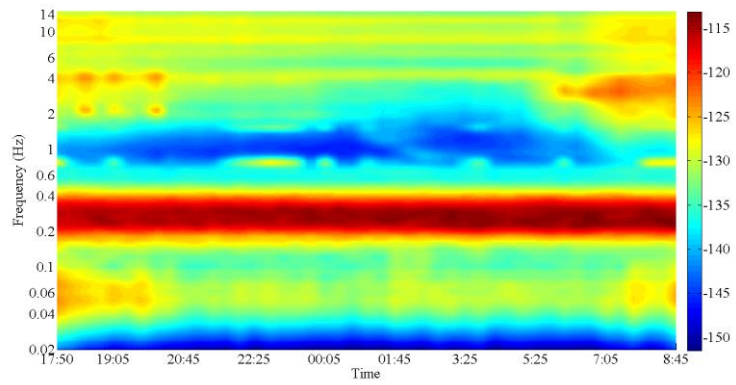
g) OC 38 in horizontal (left) and vertical (right) directions
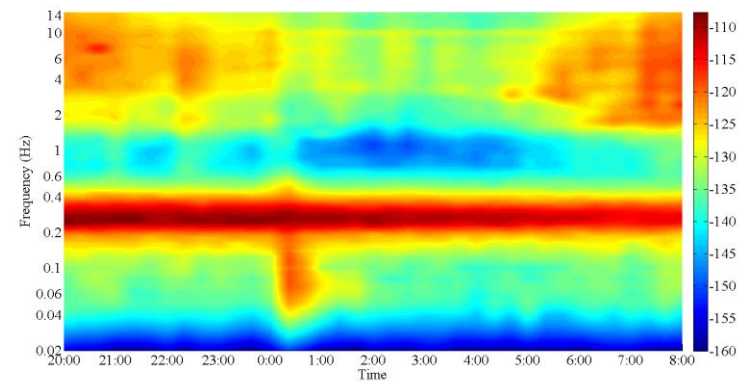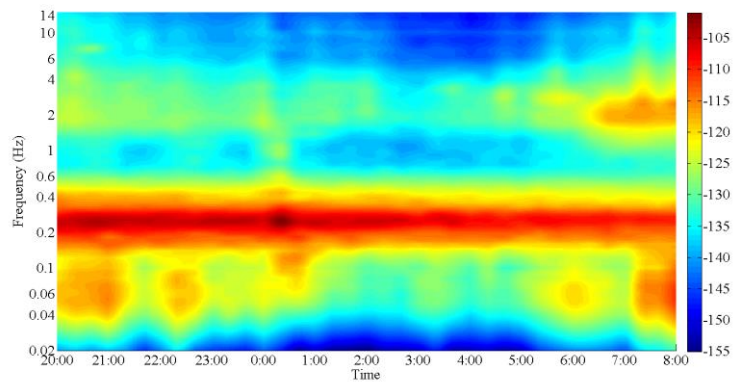
h) NM 29 in horizontal (left) and vertical (right) directions
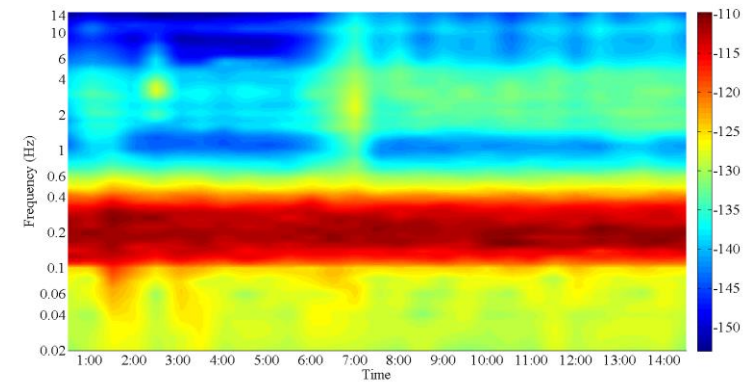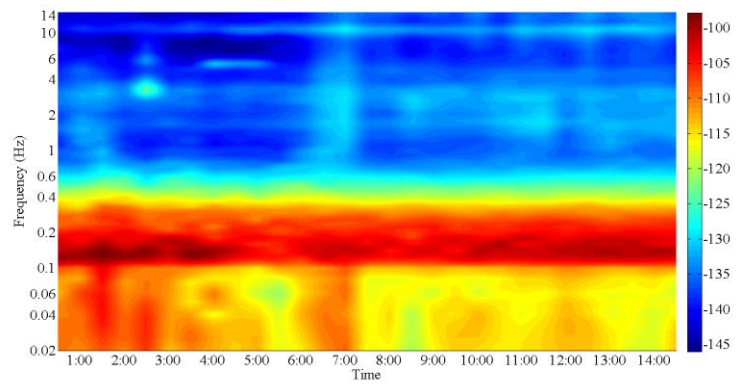
i) SM 1 in horizontal (left) and vertical (right) directions
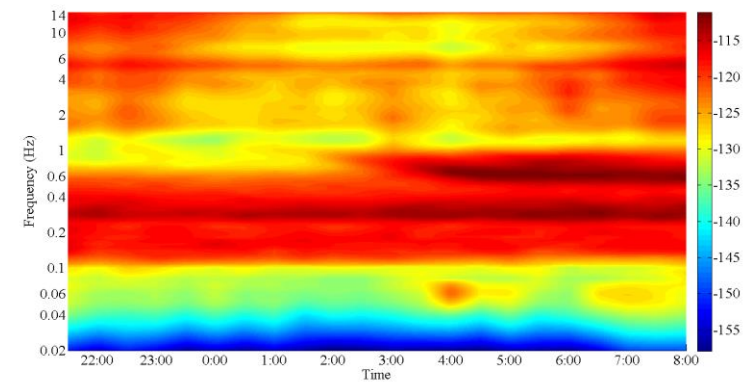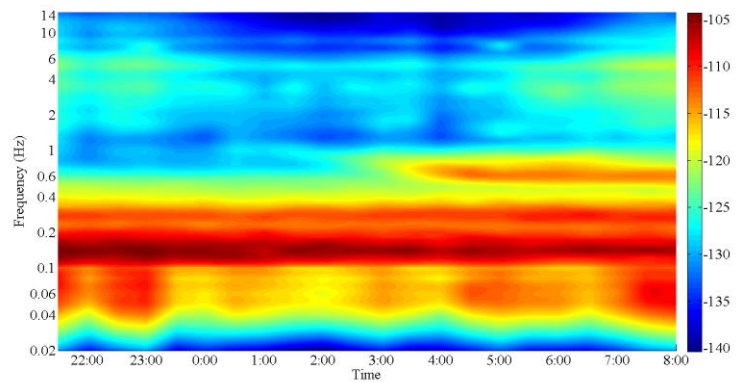
j) SM 2 in horizontal (left) and vertical (right) directions

Figure E-1. Color gradient map of PSD of LTRs. See Figure 16 for T-1 and T-2, OC 37-4, OC37-6 and LA 1.
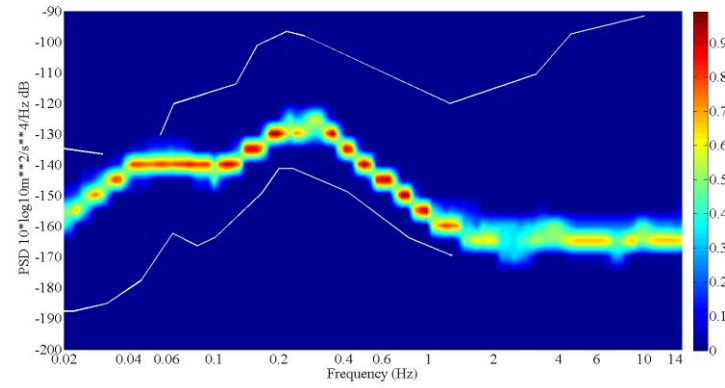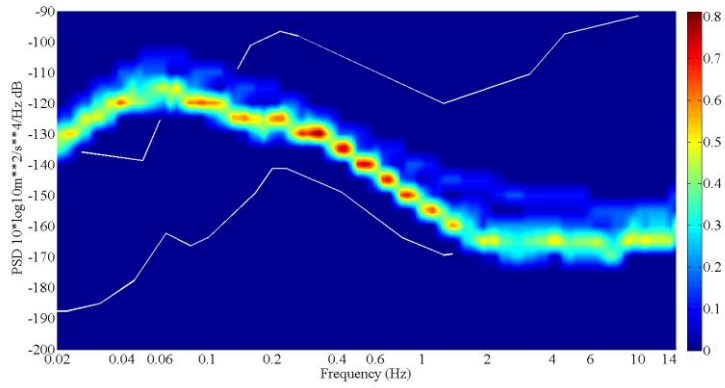
a) AL 1 in horizontal (left) and vertical (right) directions
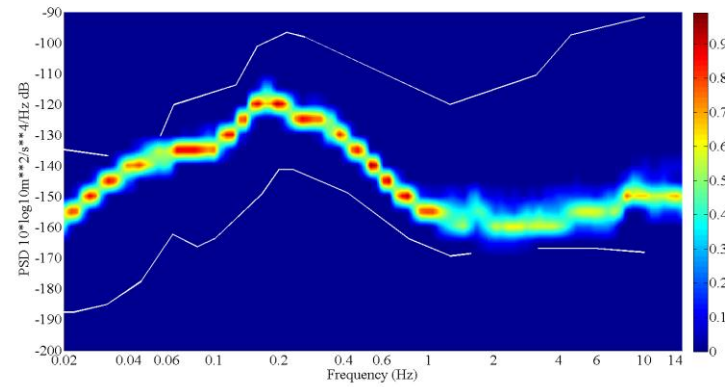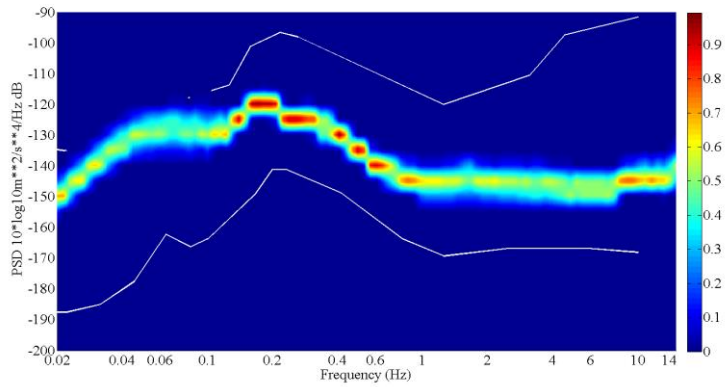
b) T-1 in horizontal (left) and vertical (right) directions
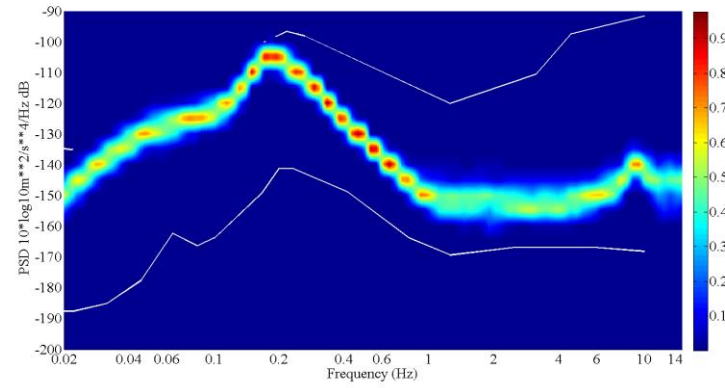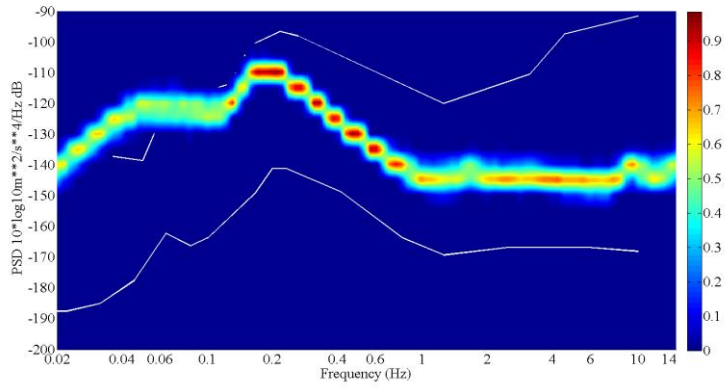
c) T-2 in horizontal (left) and vertical (right) directions
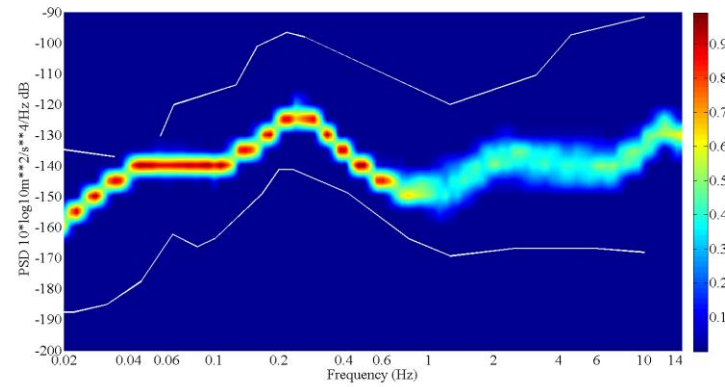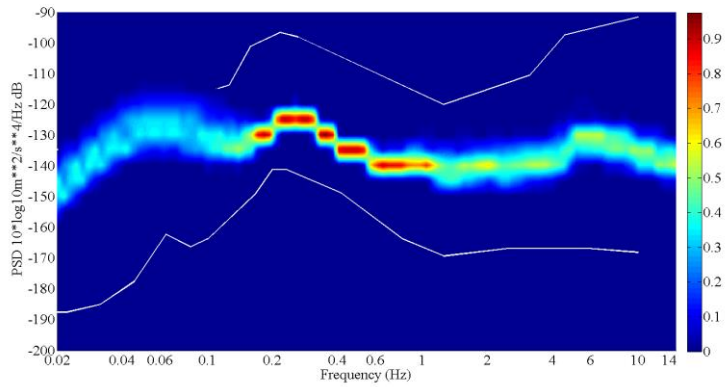
d) NM 14 in horizontal (left) and vertical (right) directions
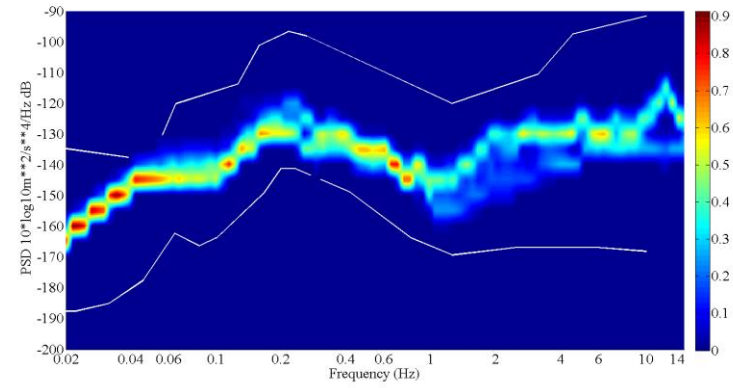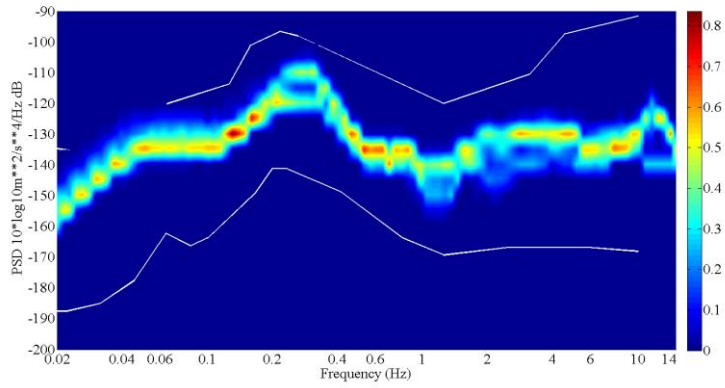
e) OC 37-1 in horizontal (left) and vertical (right) directions
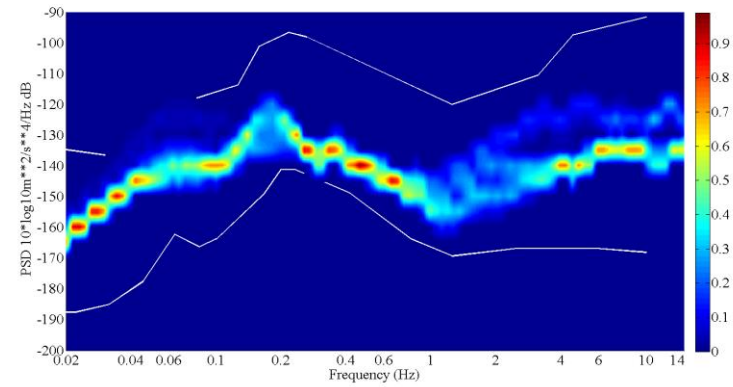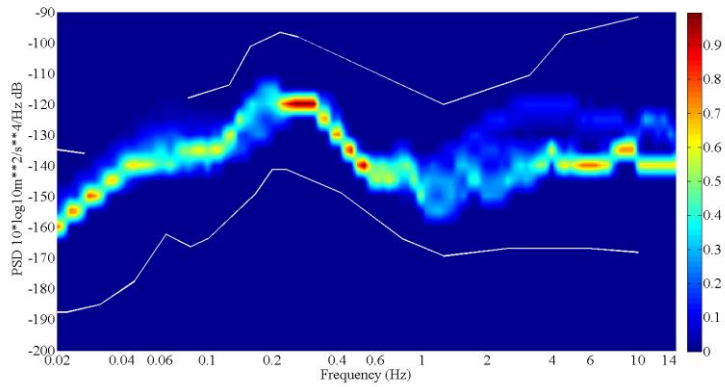
f) OC 37-2 in horizontal (left) and vertical (right) directions
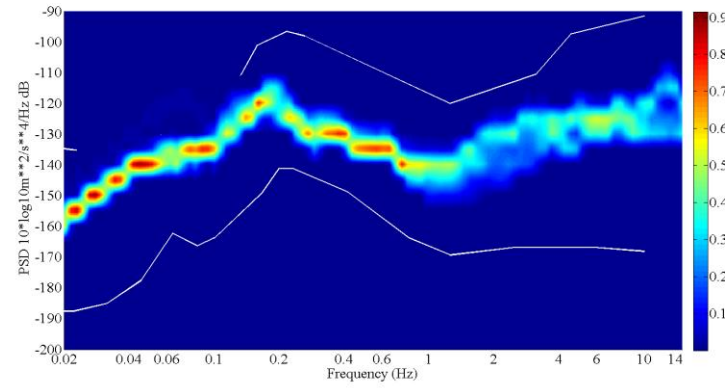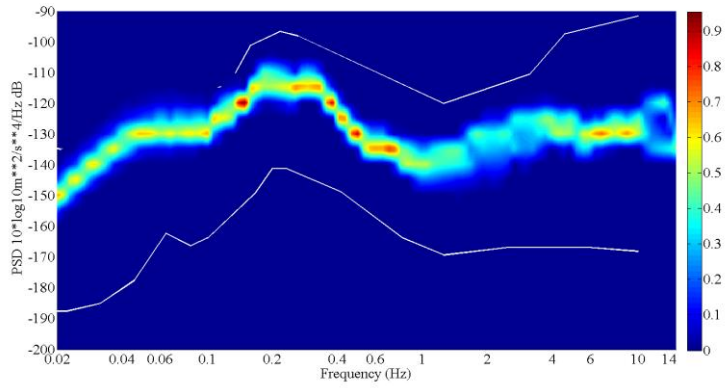
g) OC 37-3 in horizontal (left) and vertical (right) directions
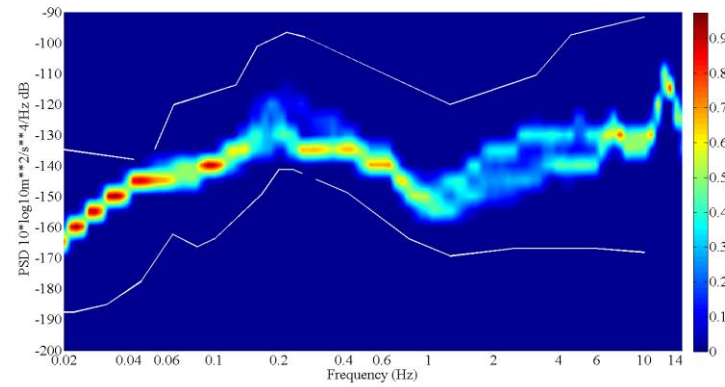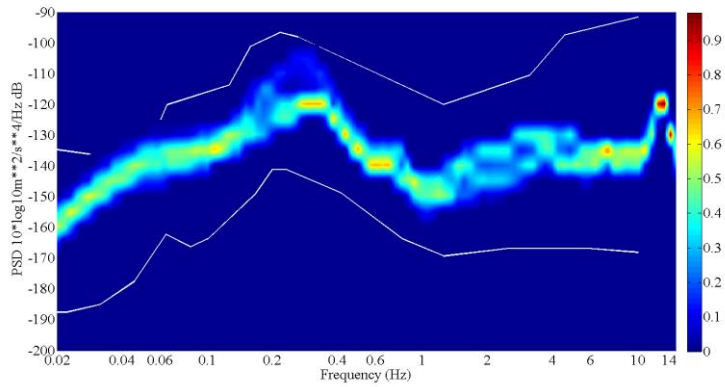
h) OC 37-4 in horizontal (left) and vertical (right) directions
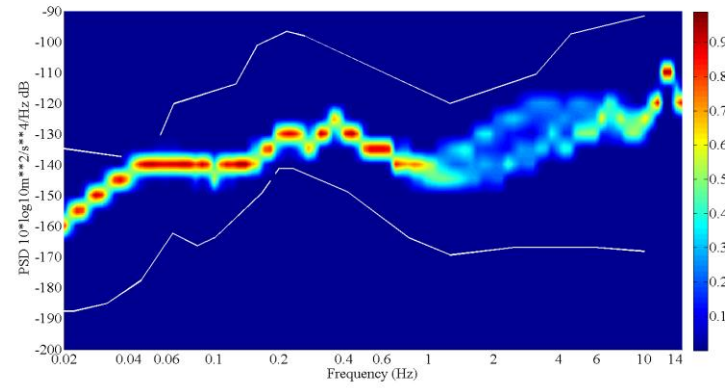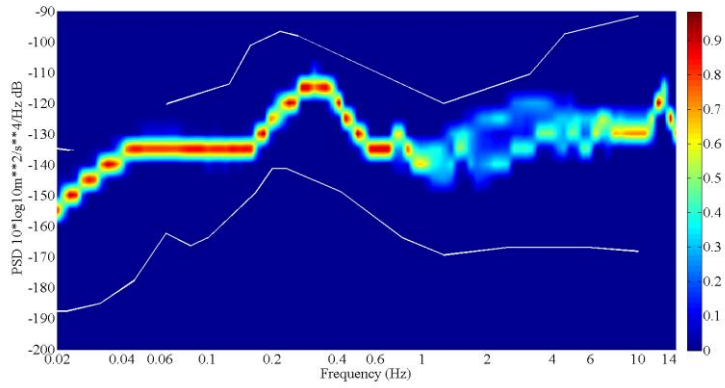
i) OC 37-5 in horizontal (left) and vertical (right) directions
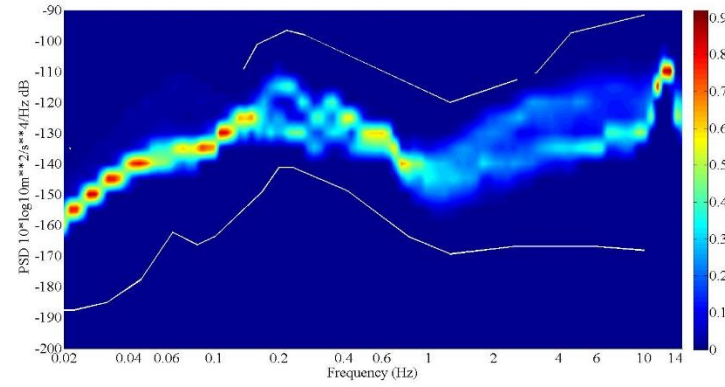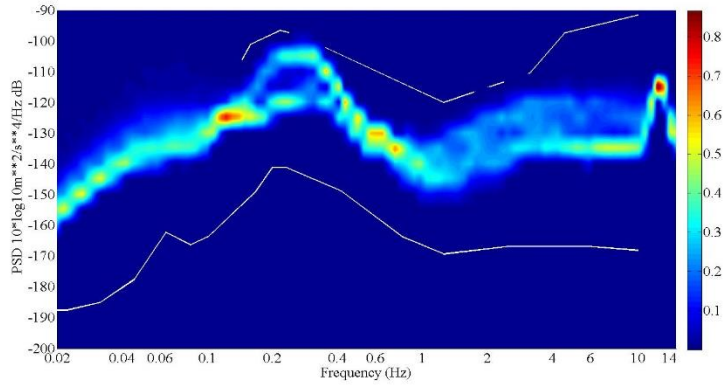
j) OC 37-6 in horizontal (left) and vertical (right) directions
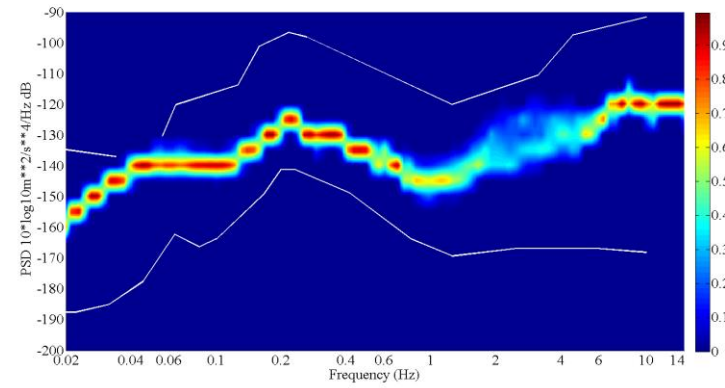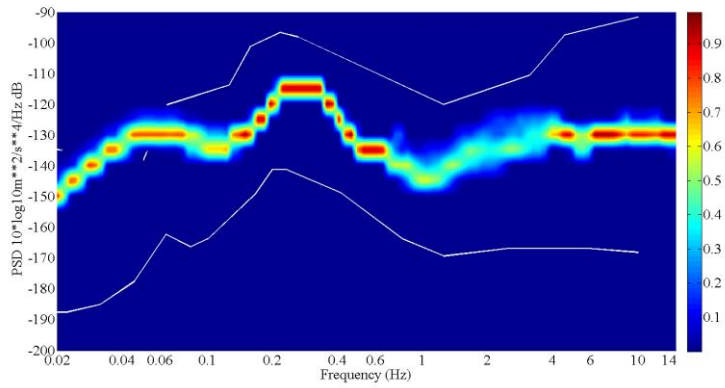
k) OC 38 in horizontal (left) and vertical (right) directions
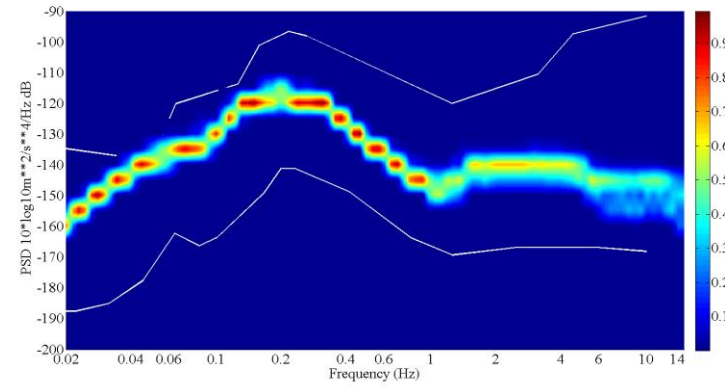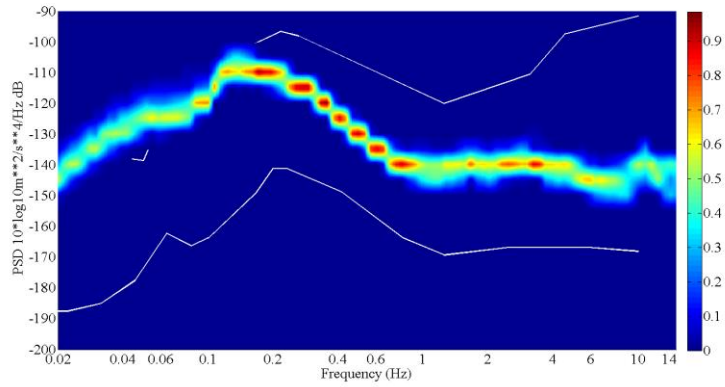
l) SM 1 in horizontal (left) and vertical (right) directions
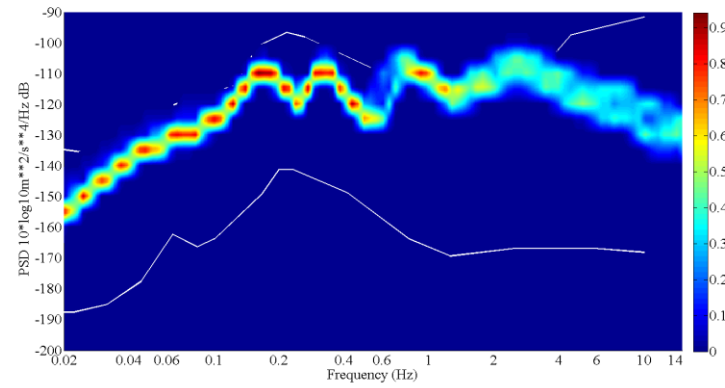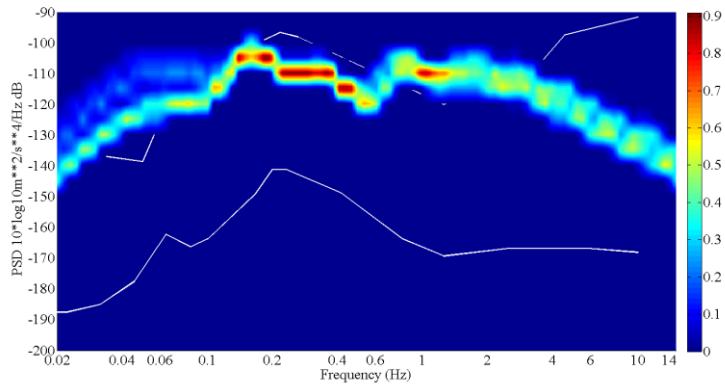
m) LA 1 in horizontal (left) and vertical (right) directions

Figure E-2. Color gradient map of PDF of LTRs. See Figure 17 for NM 29 and SM 2.

APPENDIX F:

STEREOGRAPHIC PROJECTION OF LTRS AND STRS

a) AL 1

b) T-1

c) T-2

d) NM 14

e) OC 37-1

f) OC 37-2

g) OC 37-3

h) OC 37-4
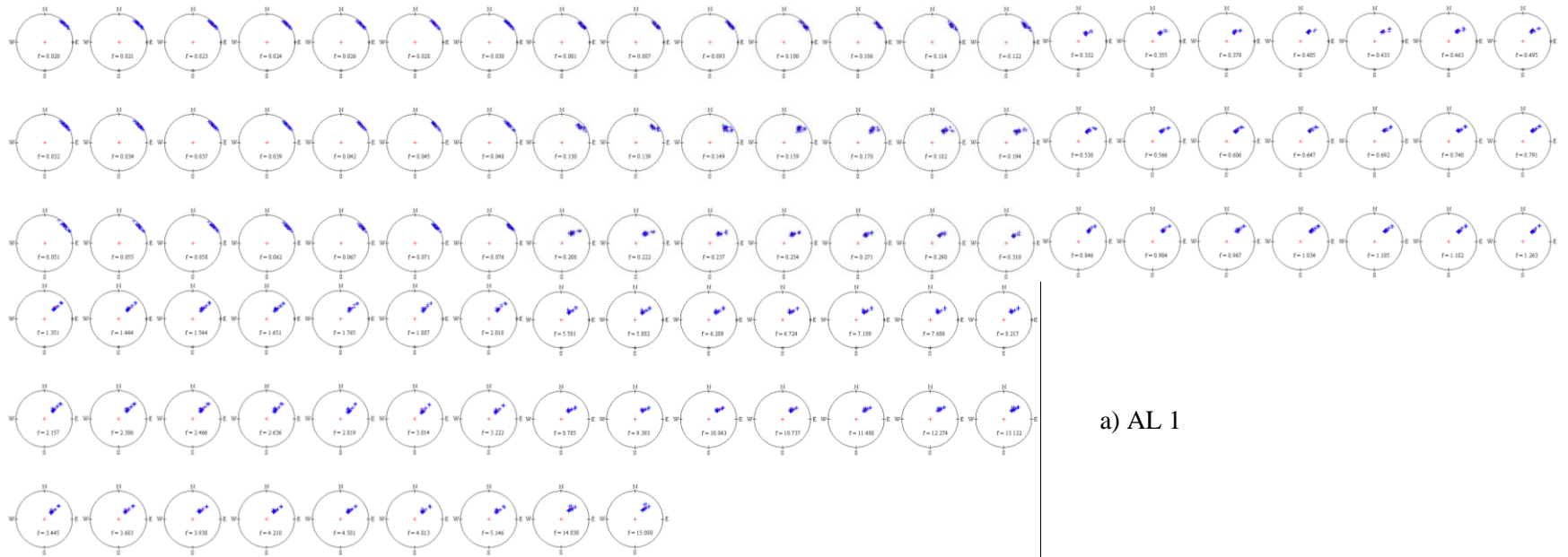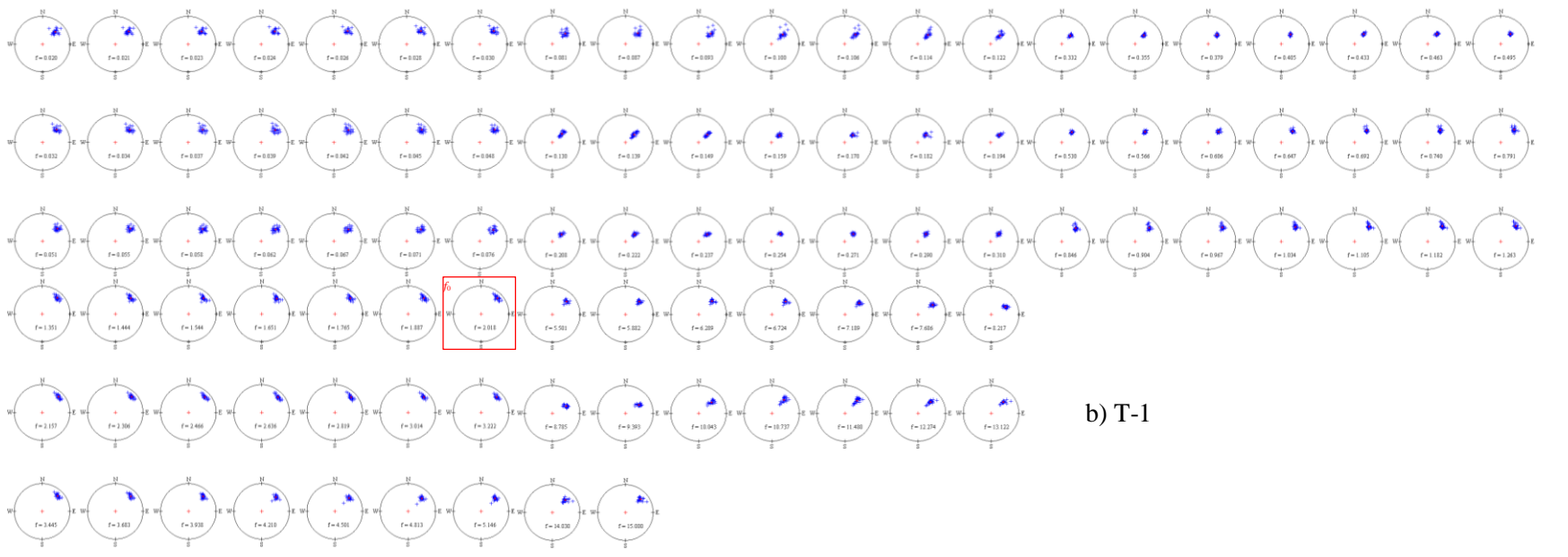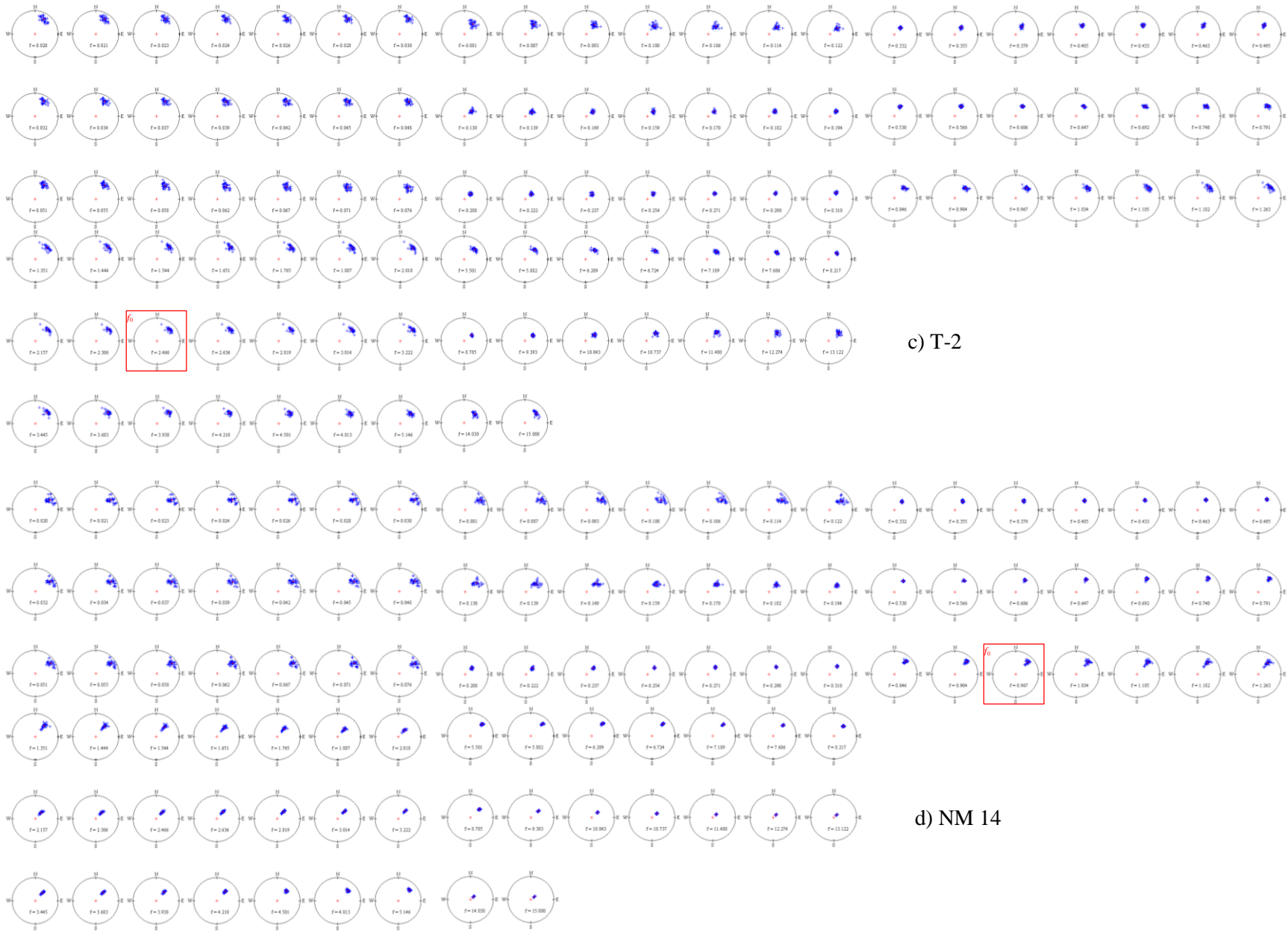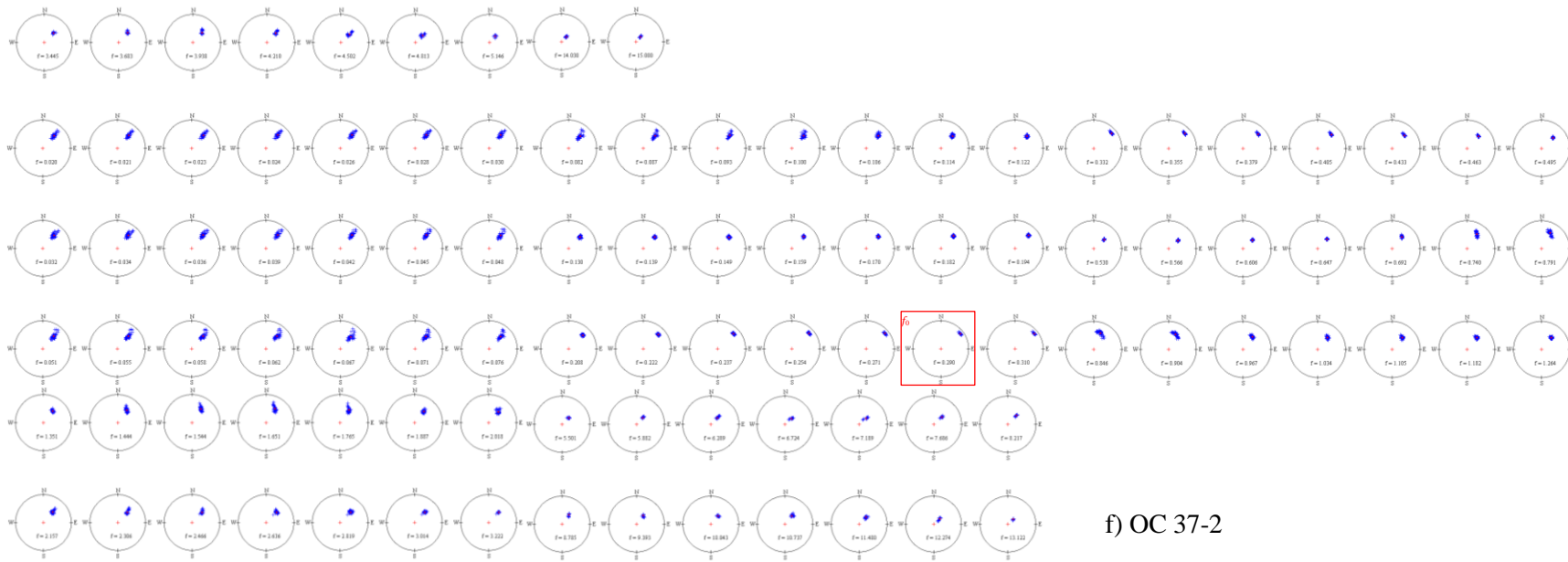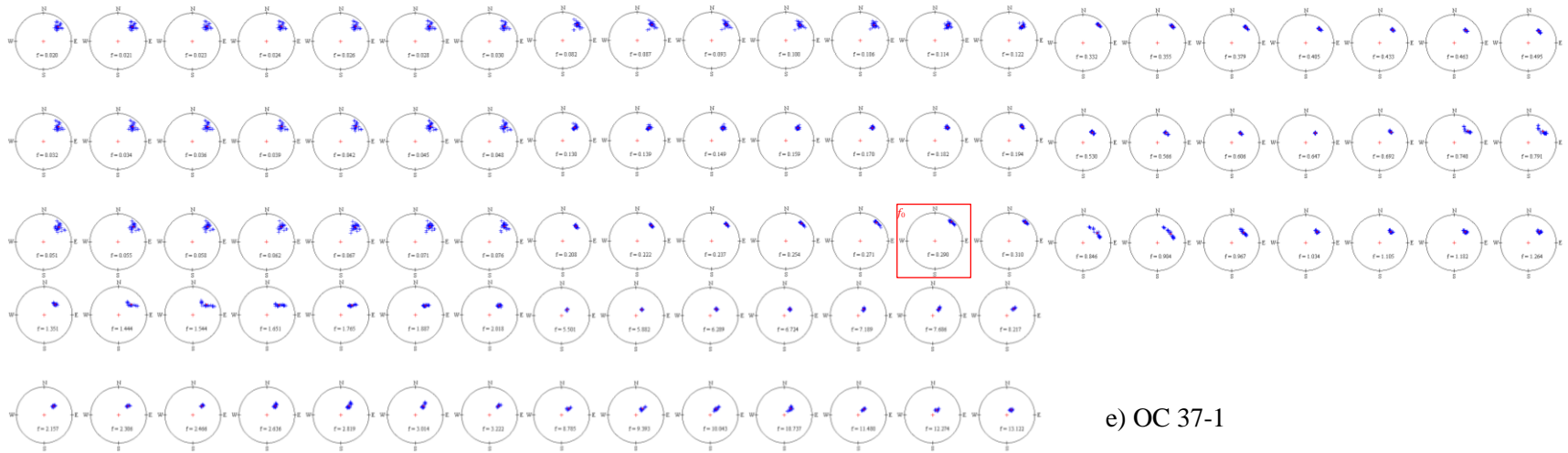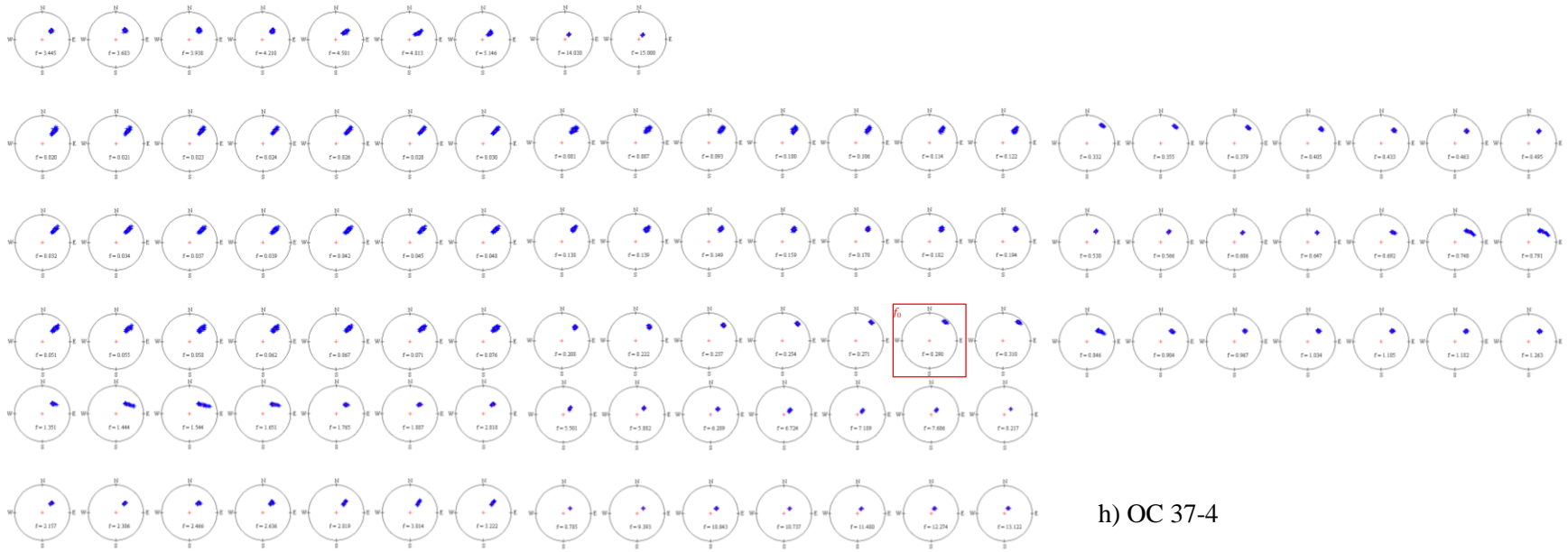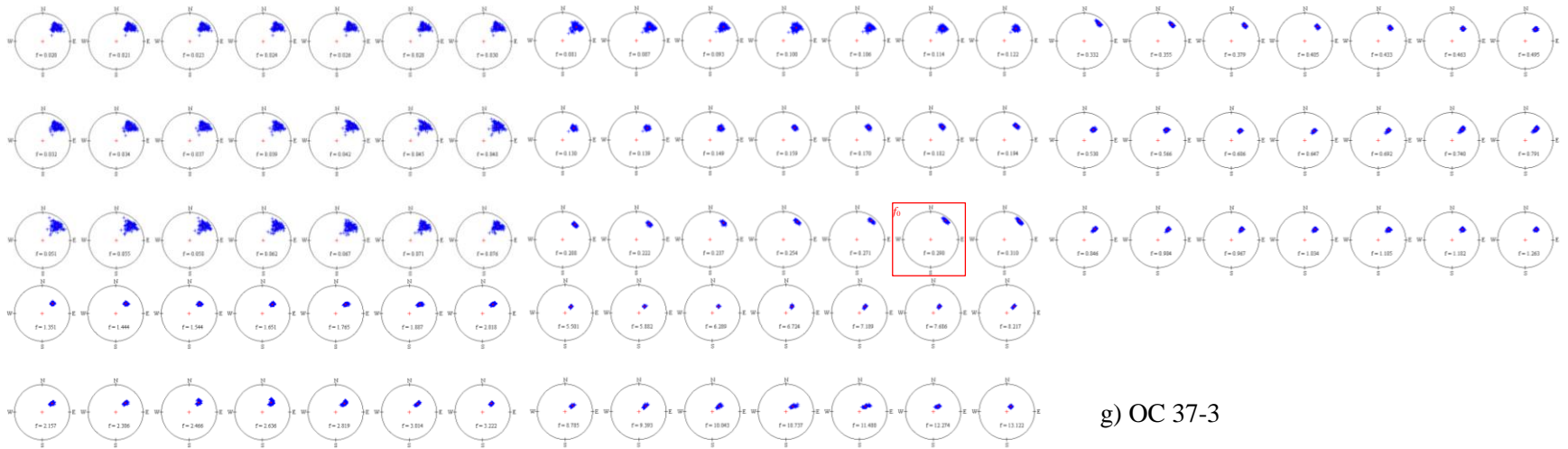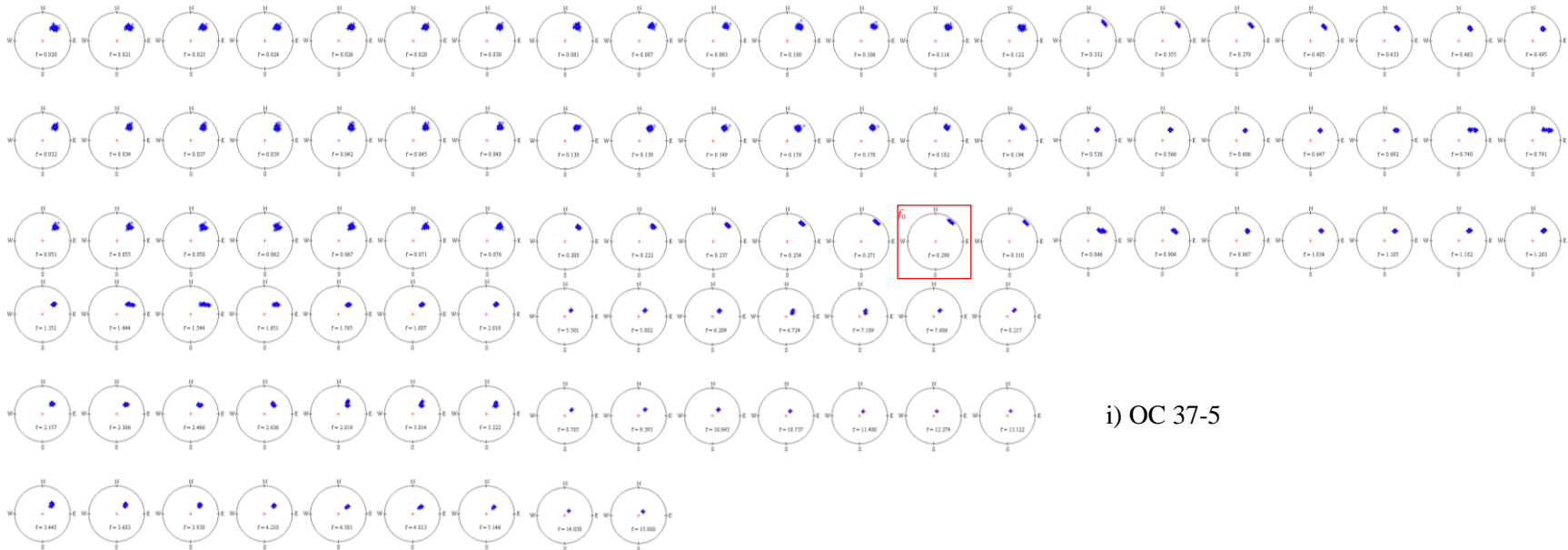
i) OC 37-5
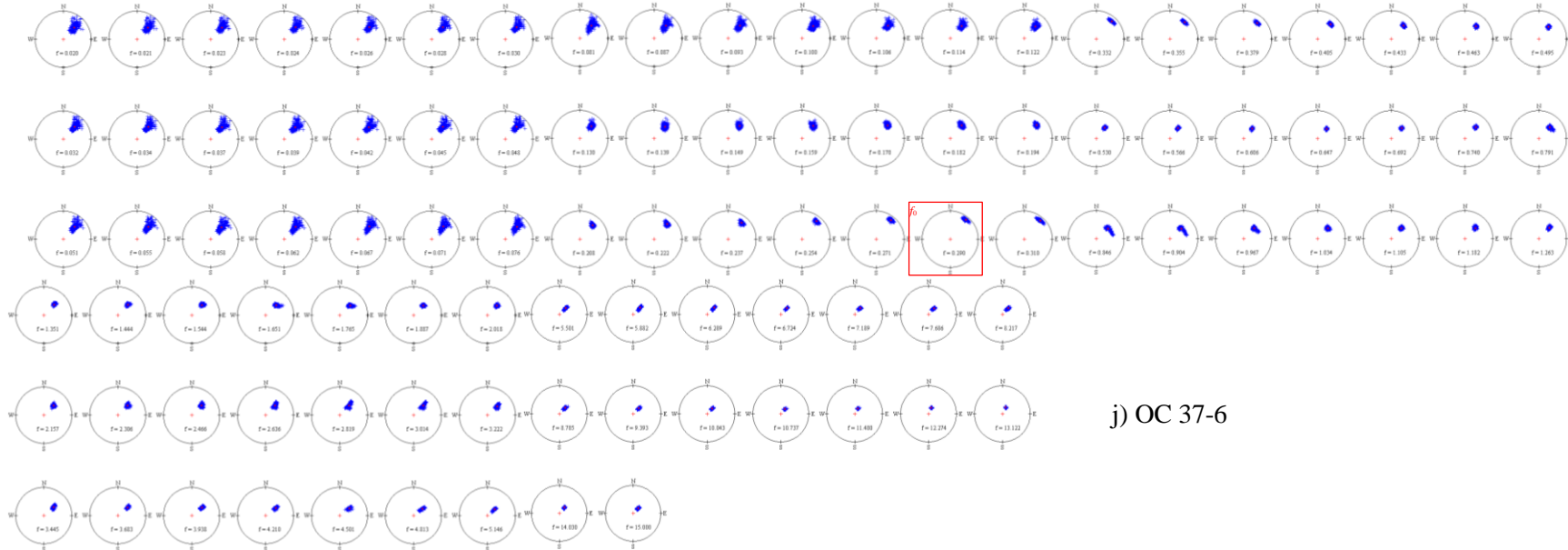
j) OC 37-6
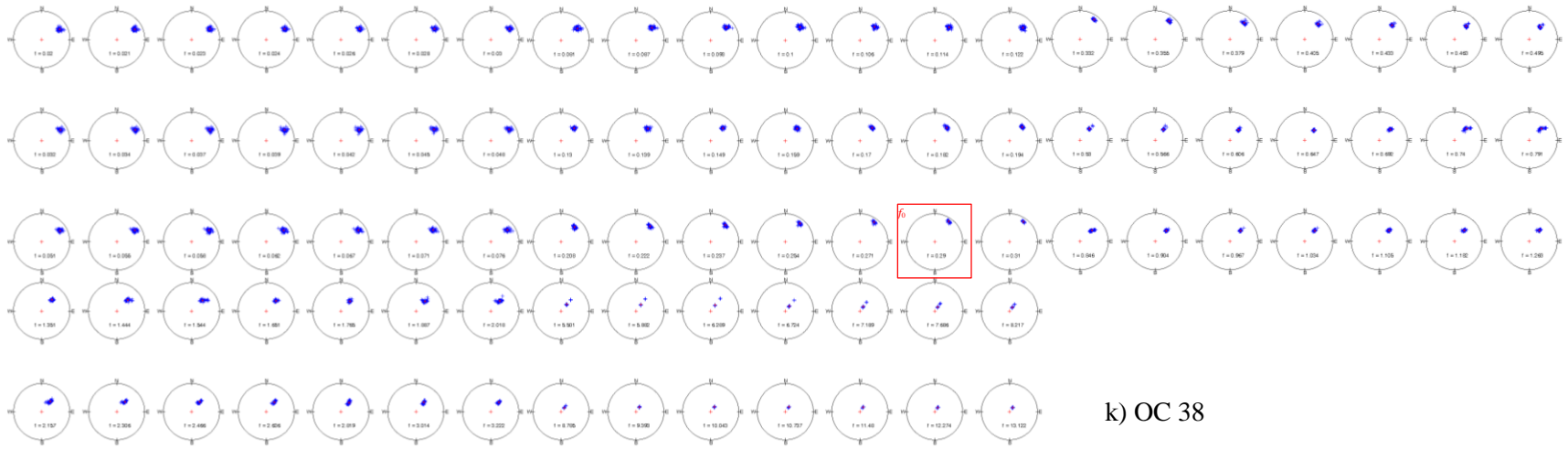
k) OC 38
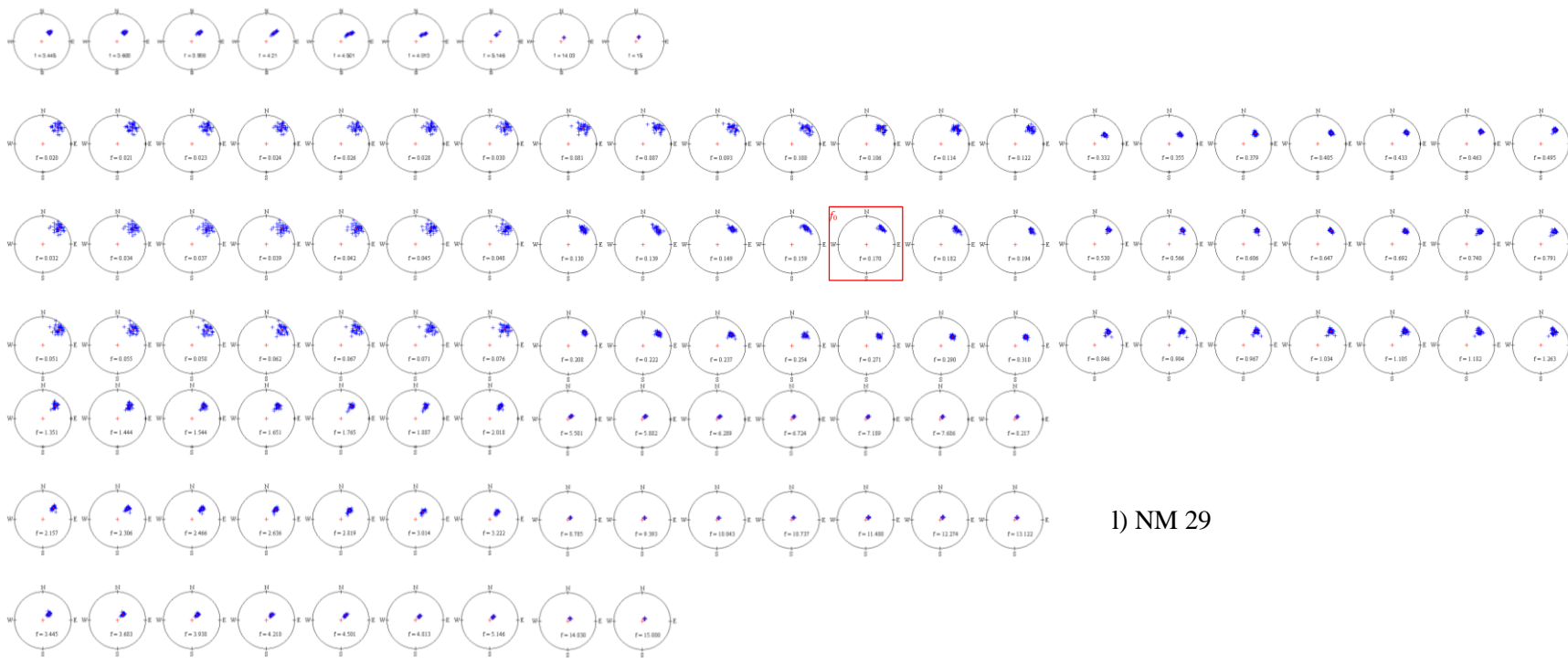
l) NM 29
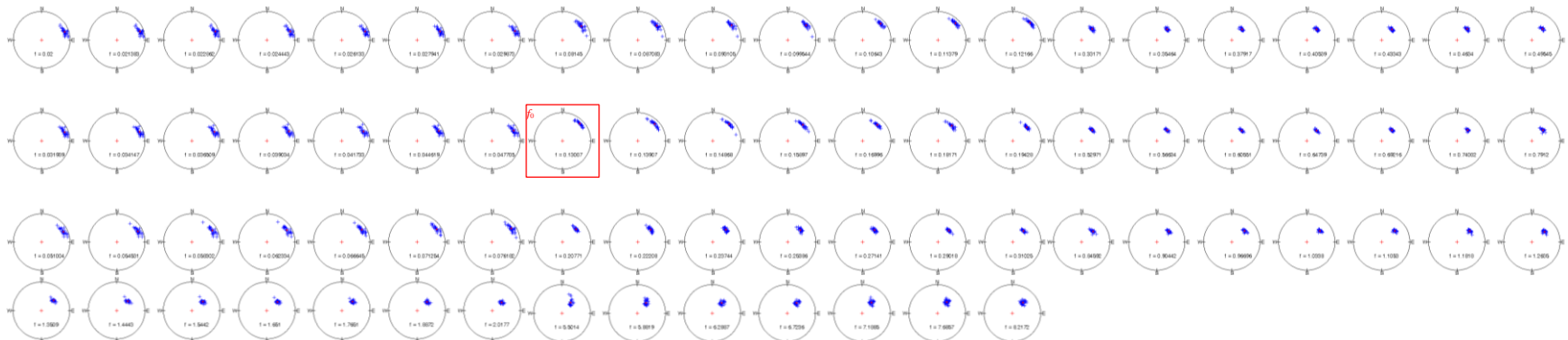
m) SM 1
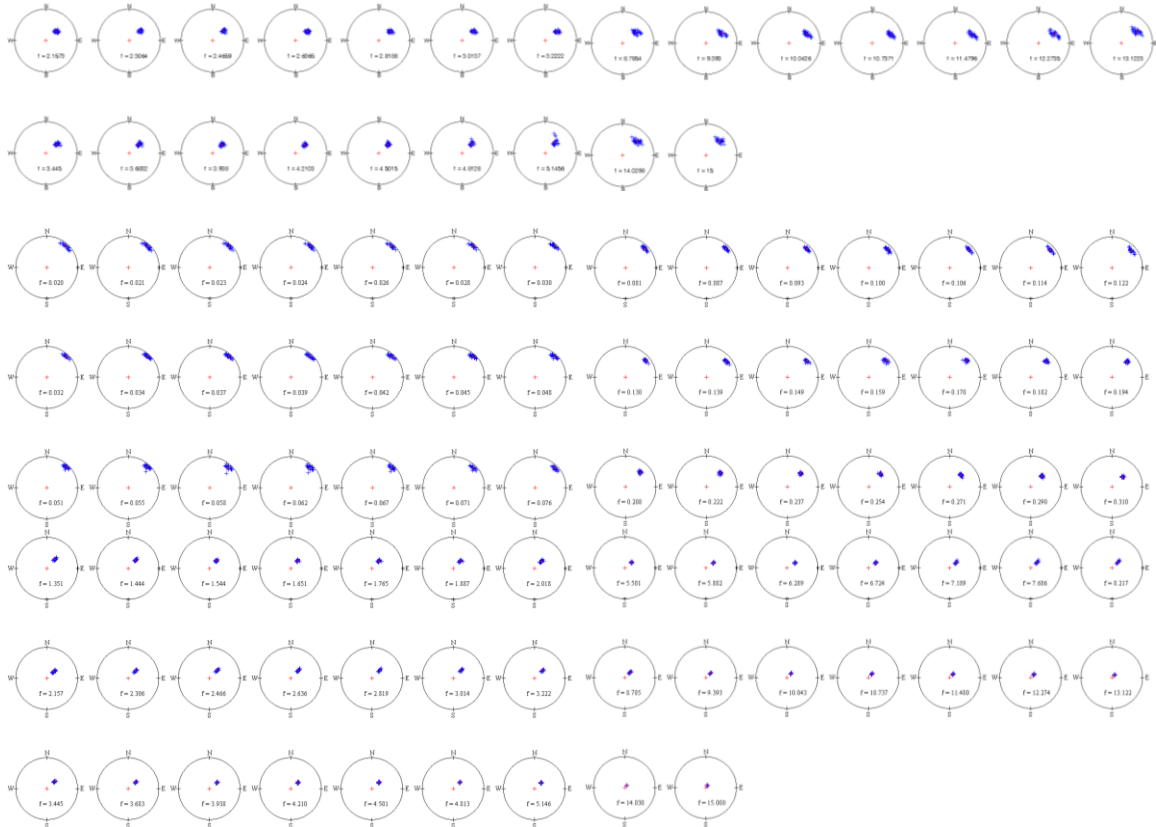
n) SM 2
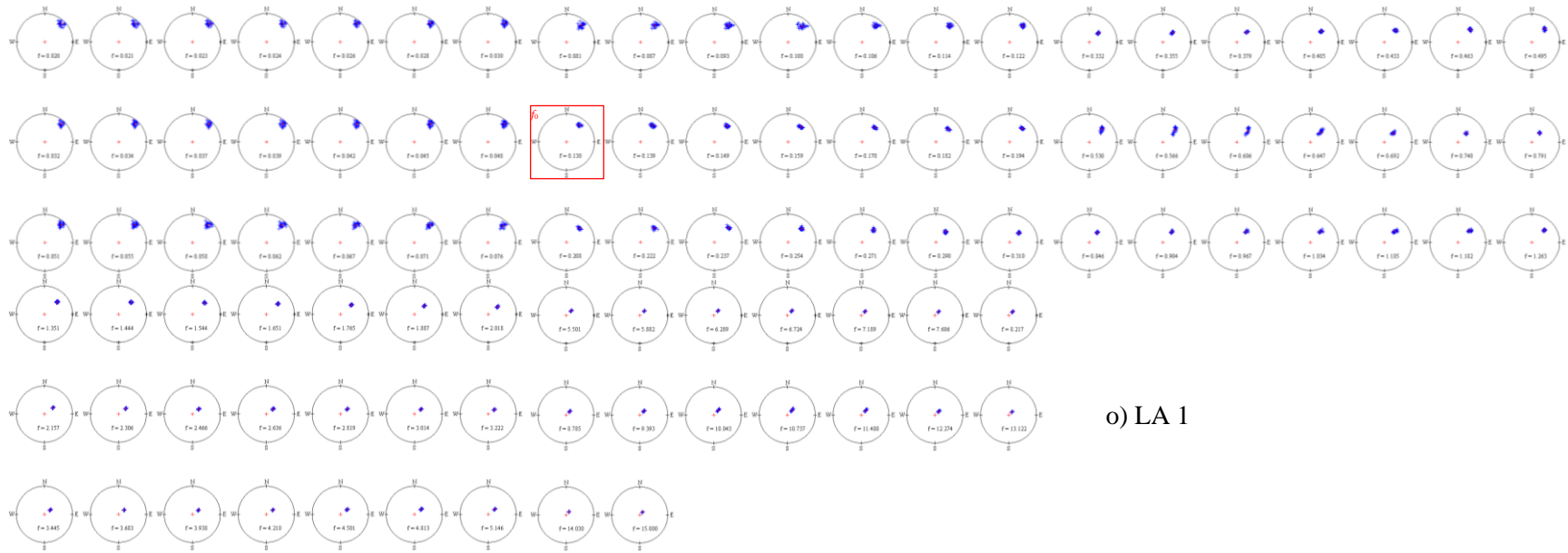
Figure F-1. Stereographic projections of LTRs
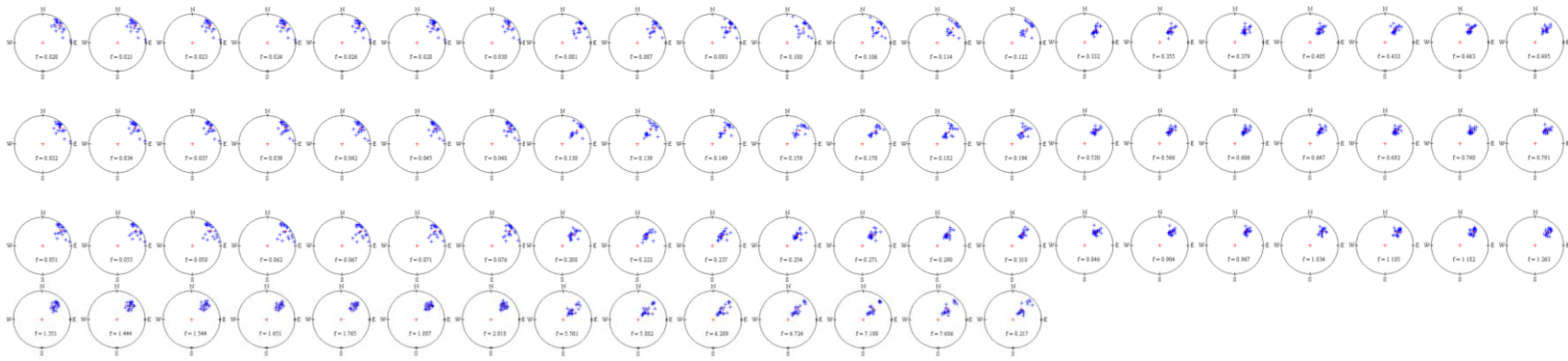
a) UST: 0-100m
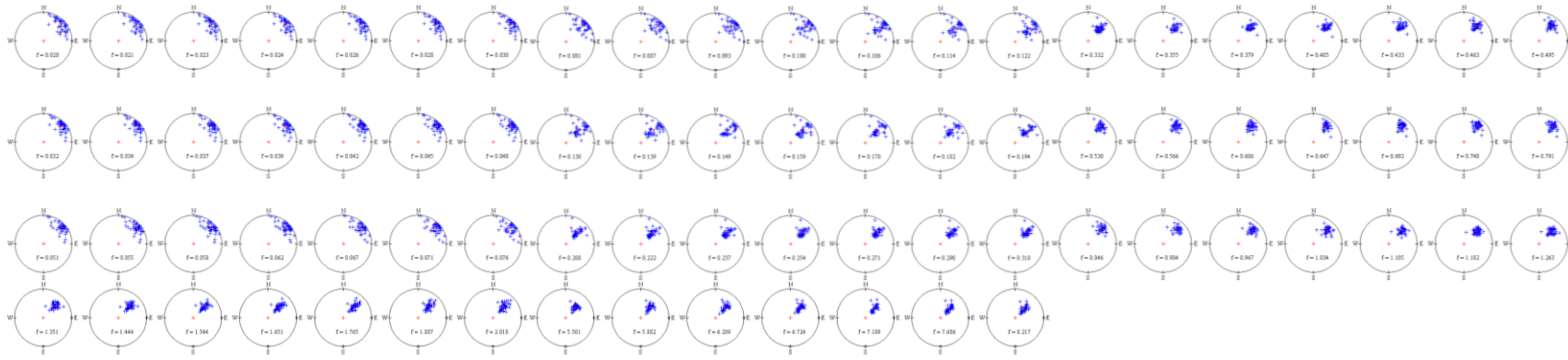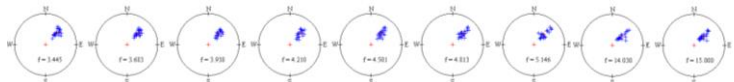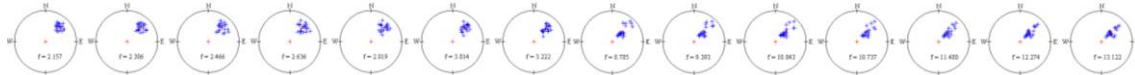
b) UST: 100-200m
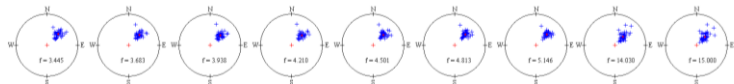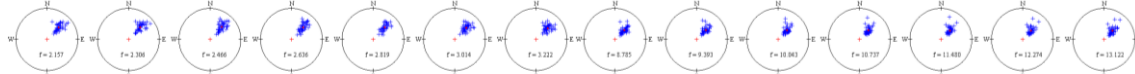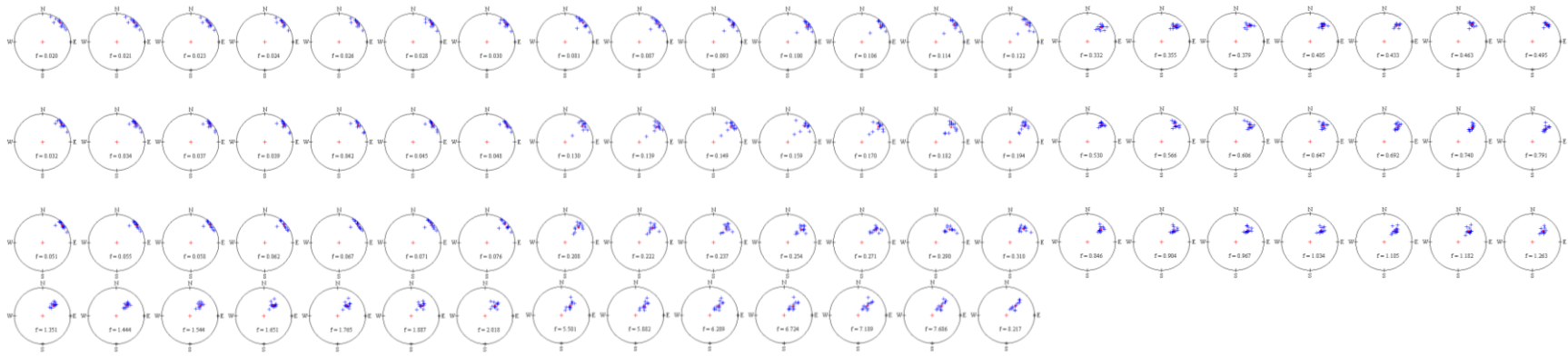
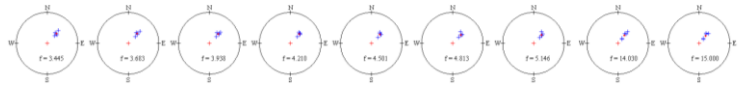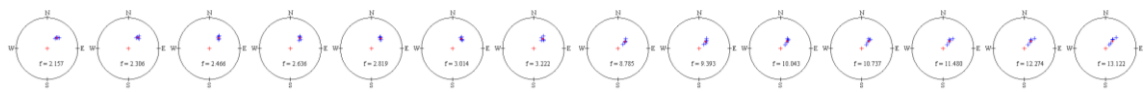c) UST: 200-300m
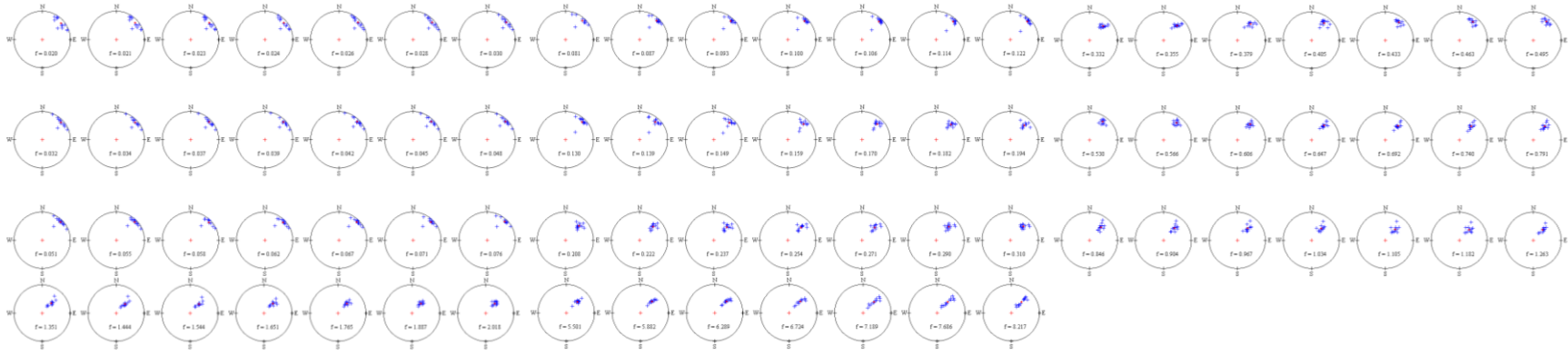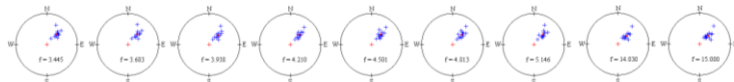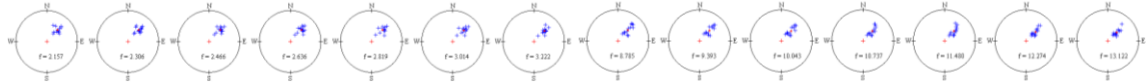
d) UST: 300-400m
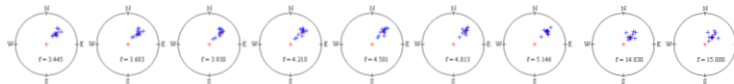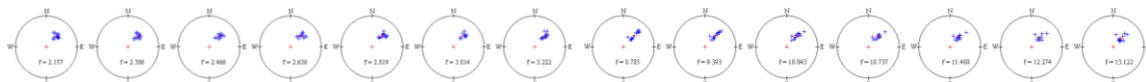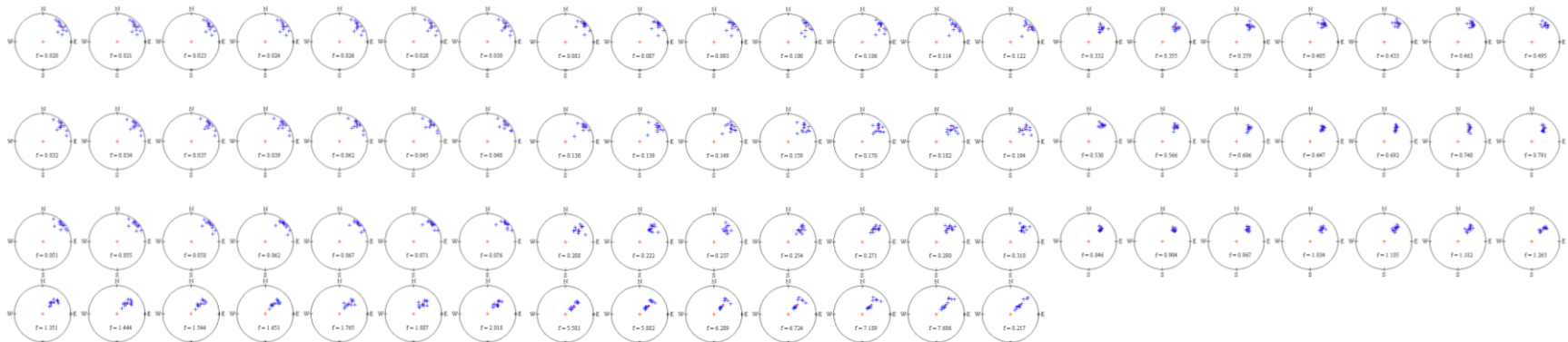
e) UST: 400-500m
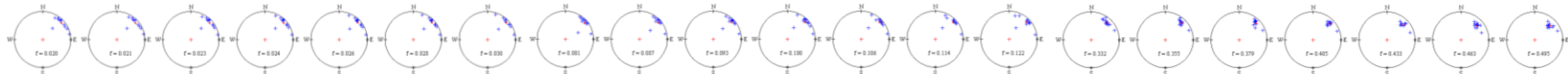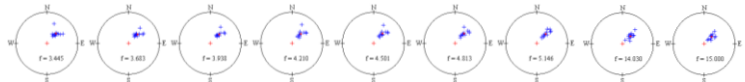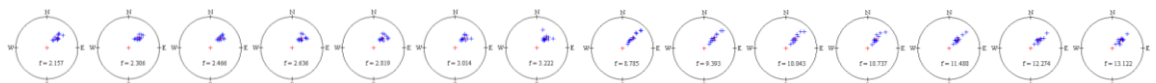
f) UST: 500-600m
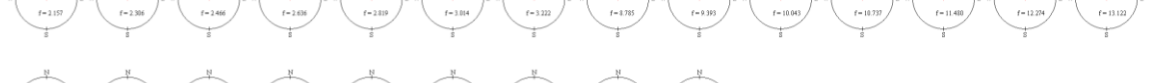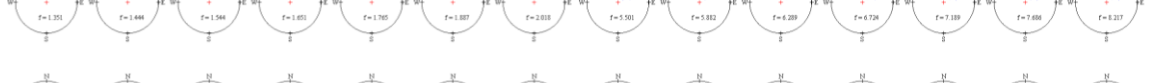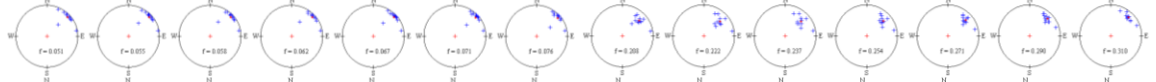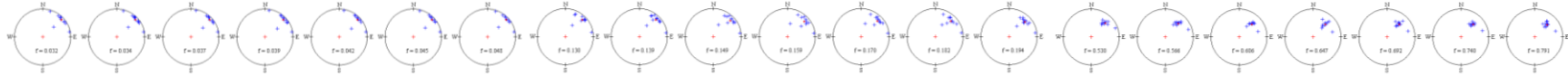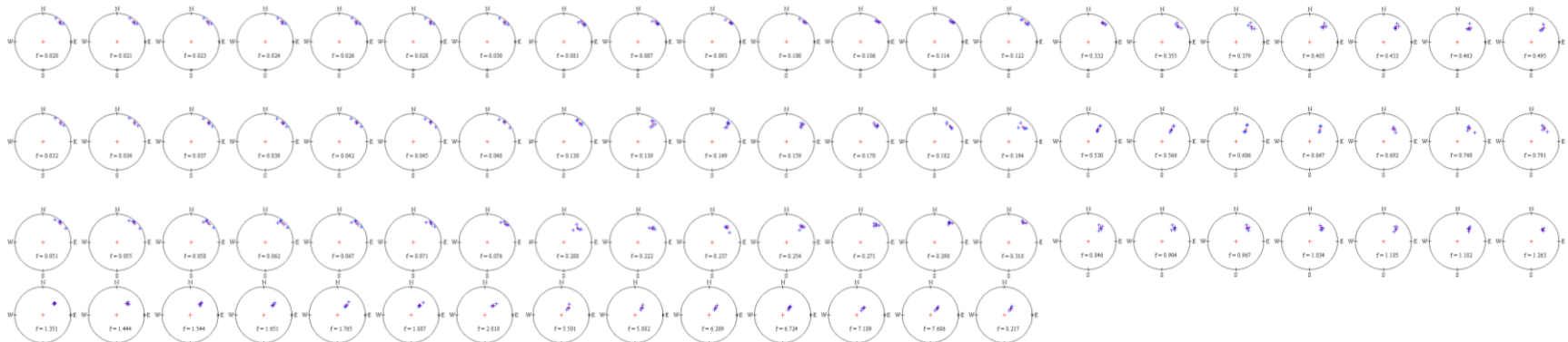
g) UST: 600-700m

h) UST: 700-800m

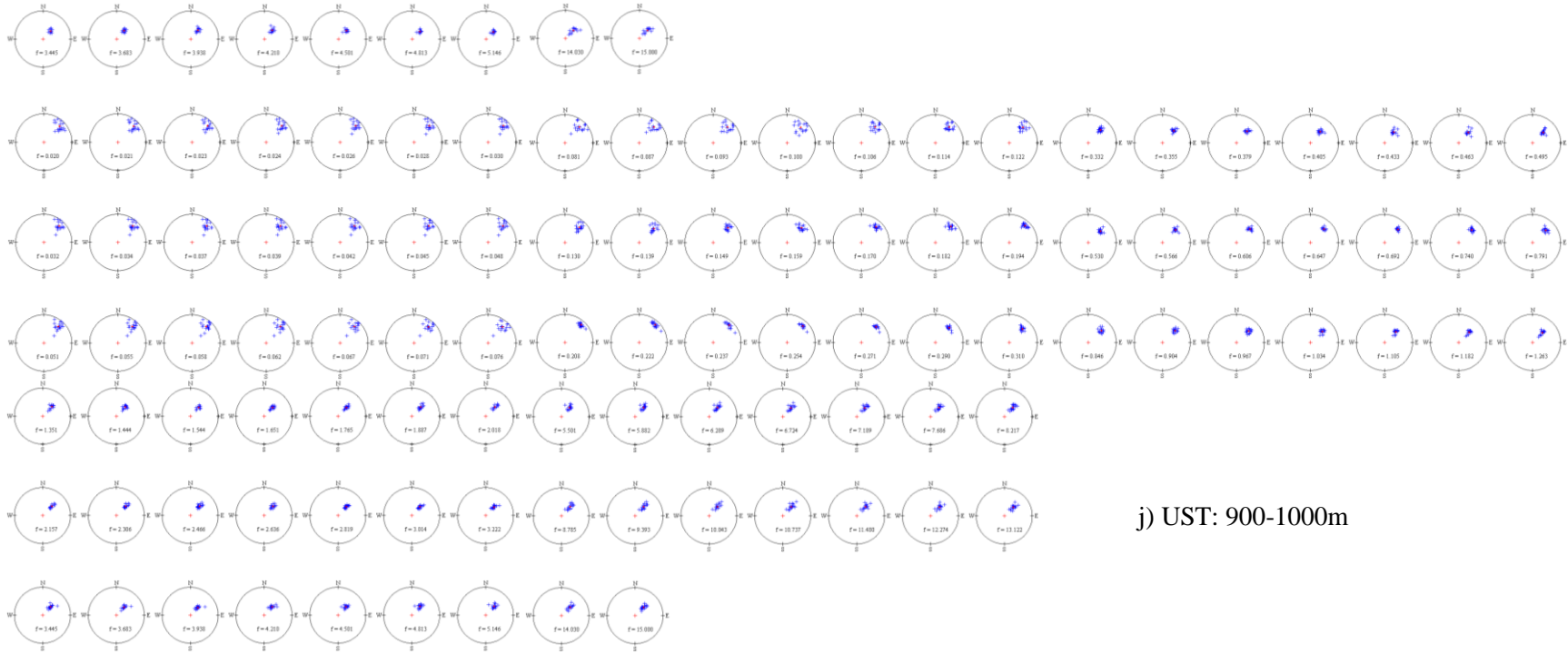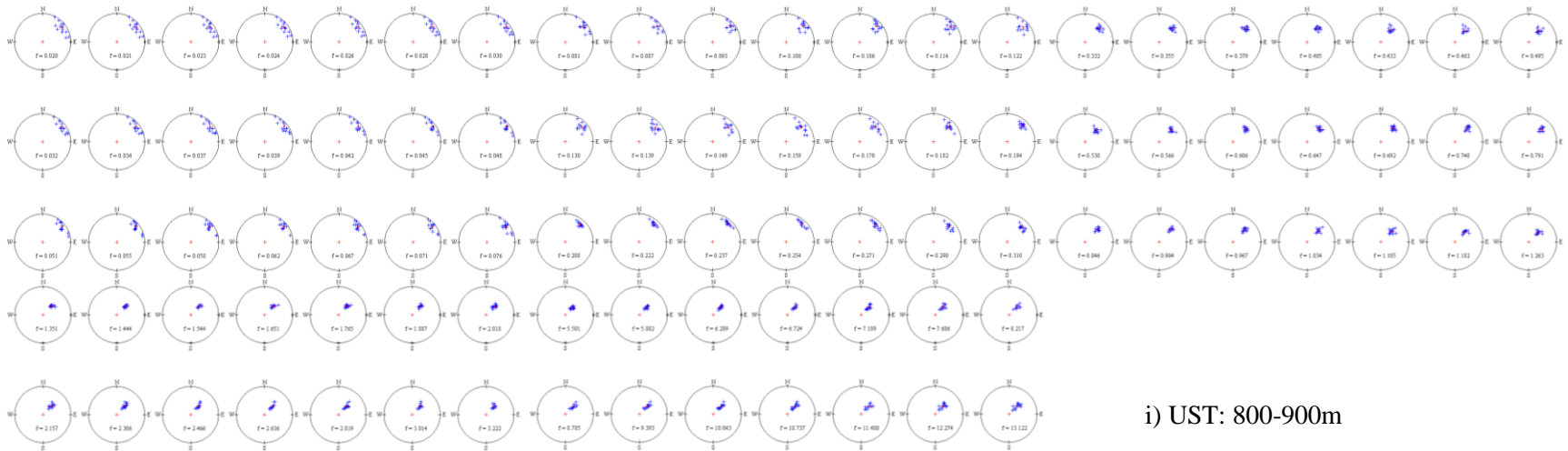i) UST: 800-900m
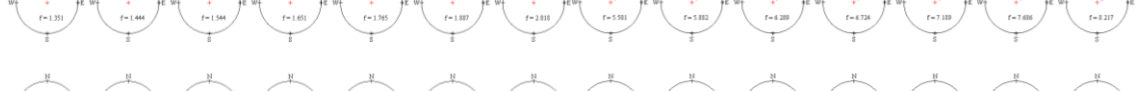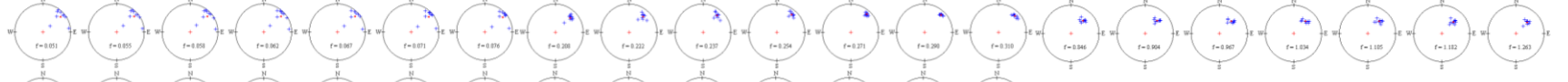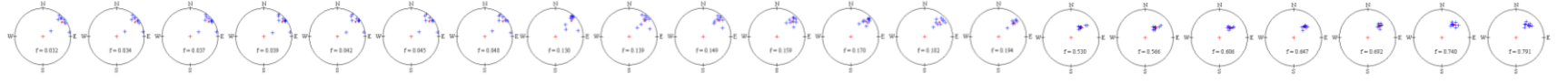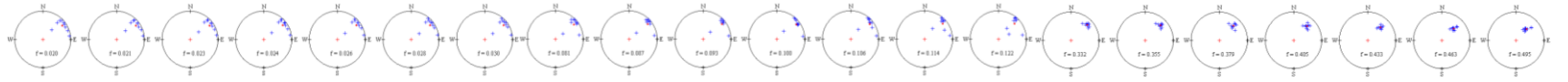
j) UST: 900-1000m

k) UST: 1000-1100m

k) UST: 1100-1200m

l) UST: 1200-1300m
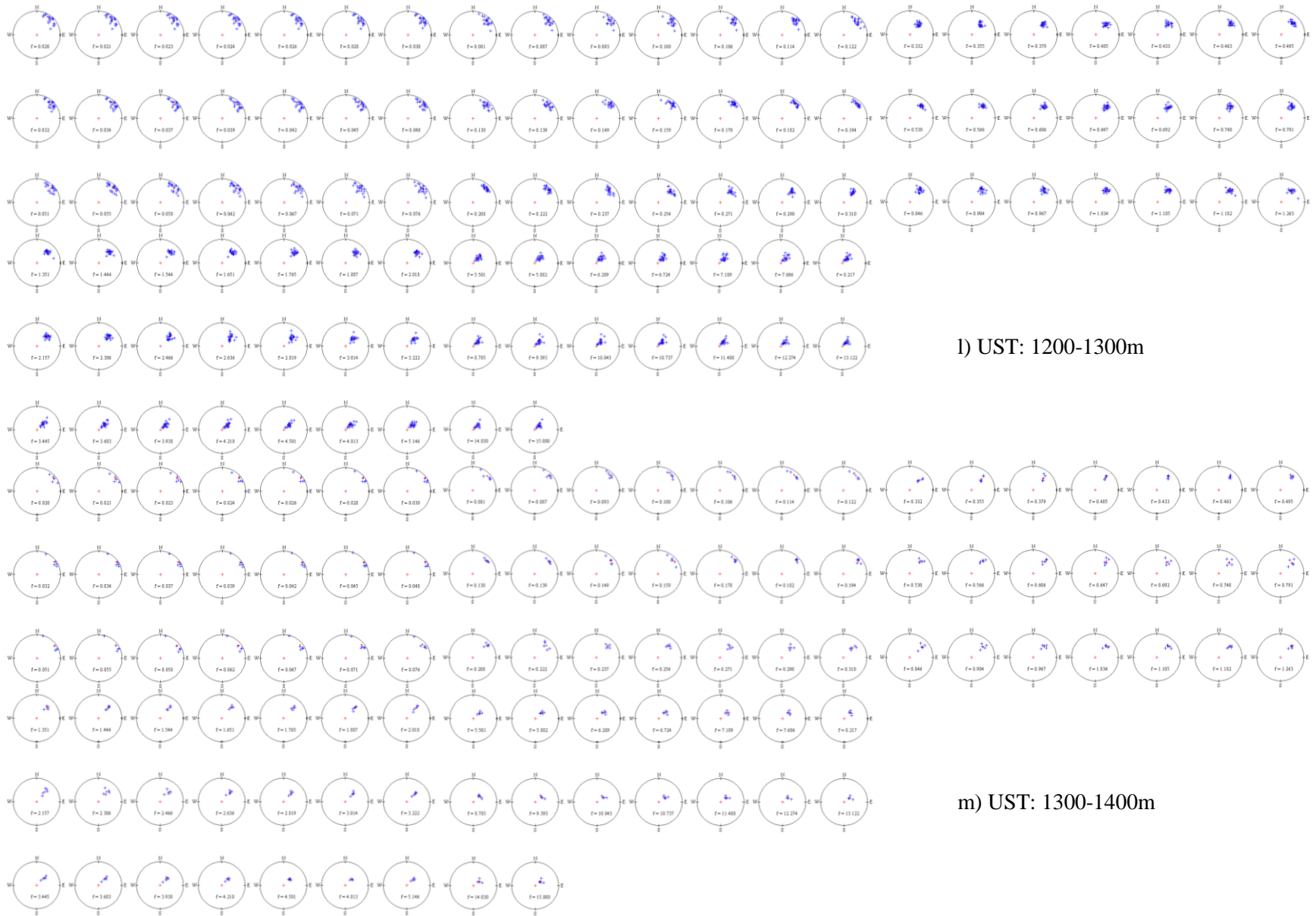
m) UST: 1300-1400m

Figure F-2. Stereographic projections of STRs grouped by 100m UST range

CURRICULUM VITA

ZHEN GUO

EDUCATION

Ph.D., Engineering Science, University of Mississippi, (GPA: 4.0/4.0), to be awarded May 2015
    Concentrations: Geological Engineering, Geophysics
    Dissertation: Microtremor Recordings in Northern Mississippi: Evaluating Site Effect and Correlating with Wave Climate

M.Sc., Geotechnical Engineering, Jilin University (JLU), P.R. China, June 2011
    Concentration: Geotechnical Engineering
    Thesis: Reliability Analysis of Weak Rock Slope in Laohuding Mining Area, Jixian County, Tianjin City

B.Sc., Civil Engineering, JLU, P.R. China, (Major GPA: 3.5/4.0), June 2007

RESEARCH EXPERIENCE

➢ Site effects evaluation of Northern Mississippi, Supported by Graduate Student Council Research Grant, University of Mississippi, 2012-2013

➢ The investigation and evaluation of the mud-rock flow in Wudongde hydropower reservoir area, in Sichuan province, China, 2008

➢ Engineering geological evaluation of the stability of new excavated rock slope in 1000KV transformer substance in Norhtern Zhejiang province, China, 2008

➢ The geological investigation of the current situation and the controlling measurements of the mud-rock flow in Dongwopu, Jixian County, Tianjin City, China, 2008

➢ The engineering geological surveying and mapping of the nuclear power plant in Jingyu County; and engineering geological evaluation of the stability of high and steep rock slope in the nuclear power plant in Jingyu County, Jilin province, China, 2007

➢ Engineering geological evaluation of the rock slope stability in the reclamation of the Laohuding mining area in Jixian County, Tianjin City, China, 2007

PUBLICATIONS

- **Zhen Guo**, and Adnan Aydin, 2015. Double-frequency microseisms in ambient noise recorded in Mississippi. *Bulletin of the Seismological Society of America*, 105(3), doi: 10.1785/0120140299

- **Zhen Guo**, Adnan Aydin and Joel Kuszmaul, 2014. Microtremor measurements in Northern Mississippi. *Engineering Geology*, 179, 146-157.

- **Zhen Guo**, Adnan Aydin, 2013. Site effect evaluation of Northern Mississippi, Mississippi Academy of Science (MAS) 77th annual meeting, Feb. 21-22 in Hattiesburg, MS. Abstract and oral presentation

- **Zhen Guo**, Adnan Aydin, 2011. Microtremor measurements at the Oxford campus of University of Mississippi. 2011 AGU fall meeting, Dec. 5-9 in San Francisco, CA. Abstract and Poster presentation

- **Zhen Guo**, Adnan Aydin, Jianping Chen, 2010. Reliability analysis of slope stability: a parameter study. 2010 AEG annual meeting, Sep. 20-26 in Charleston, SC. Abstract and Poster presentation, student volunteer

- **Zhen Guo** and Jianping Chen, 2009. Sensitivity analysis on influence factors of debris slope's stability. *Journal of Jilin University (Earth Science edition)*, 39(Sup.):15-19, in Chinese

ACADEMIC EXPERIENCE

Teaching Assistant, 2010-2015

> Department of Geo. & Geol. Engr., University of Mississippi
- Courses in classroom:
  G E 405/577: Engineering Geophysics/Geophysics I;
  Engr 453/G E 413: Probability and Statistics in Engineering Design;
  G E 440: Rock Mechanics;
  ENGR 207: Graphic I;
  ENGR 340: Engineering Geology;
- Courses grading assignments:
  G E 450: Hydrogeology;
  Geol 104: Environmental Geology-Hazards;
  Geol 105: Environmental Geology-Resources;

Instructor, 2012-2013

> Department of Geo. & Geol. Engr., University of Mississippi
> Geol 114: Environmental Geology - Hazards laboratory;
> Geol 115: Environmental Geology - Resources laboratory.

AWARDS

- **Outstanding Graduate Student** of Department of Geo. & Geol. Engr., University of Mississippi, 2013-2014 and 2014-2015.

- **Charles Dunbar King Memorial Scholarship** of University of Mississippi, 2014.

- Second place among 2nd-year group in 6th South Central America Japanese Speech Contest (SCAJSC), Apr. 5, 2014, at Tougaloo College, MS.

- First place among 1st-year group in 5th SCAJSC, March 30, 2013, at Tulane University, New Orleans, LA.

- **Best Student Presentation** award in the Geology and Geography Division in the MAS 77th Annual Meeting, Feb. 22nd, 2013, at USM in Hattiesburg, MS.

- **Outstanding Teaching Assistant** of Department of Geo. & Geol. Engr., University of Mississippi, 2010-2011

- **Outstanding Undergraduate Thesis** of JLU, China, 2007.

- **First place for Scholarship** of JLU, China, 2006.

- **Third place in Mathematical Modeling** Contest, JLU, China, 2005 and 2006.

- **Dongrong Scholarship** of JLU, China, 2005.

- **Second place for Scholarship** of JLU, China, 2004 and 2005.